UNIVERSITY OF OXFORD

DEPARTMENT OF ENGINEERING SCIENCE

Inkjet and Electrohydrodynamic Printing of Liquid Crystal Droplets for Functional Optical Elements

---

Mengmeng Li
Mansfield College

A thesis submitted for the degree of

Doctor of Philosophy

in the Department of Engineering Science

Trinity Term 2024

Declaration

This thesis entitled "INKJET AND ELECTROHYDRODYNAMIC PRINTING OF LIQUID CRYSTAL DROPLETS FOR FUNCTIONAL OPTICAL ELEMENTS" was supervised by:

1) Stephen M. Morris – Professor of Engineering Science

2) Steve J. Elston – Professor of Engineering Science

3) Alfonso A. Castrejón-Pita – Professor of Engineering Science

I confirm that the work submitted herein is entirely my own, and to the greatest extent of my knowledge, it does not include any material previously published or written by someone else, except for those instances specifically acknowledged. Most of the materials utilized for this thesis are directly sourced from my published works where I hold the position of lead author, as itemized below:

1) Mengmeng Li, Waqas Kamal, Andrew C. J. Orr, Alfonso A. Castrejón-Pita, Steve J. Elston, and Stephen M. Morris. "Printed Polymer-Stabilized Chiral Nematic Liquid Crystal Privacy Windows." *Macromolecular Chemistry and Physics* **223**, 2200154 (2022).

2) Mengmeng Li, Steve J. Elston, Chao He, Xuke Qiu, Alfonso A. Castrejón-Pita, and Stephen M. Morris. “Printed Liquid Crystal Optical Vortex Beam Generators.” *Advanced Optical Materials* 2400450 (2024)

3) Mengmeng Li, Chao He, Steve J. Elston, Bohan Chen, Xuke Qiu, Alfonso A. Castrejón-Pita, and Stephen M. Morris. “Inkjet Printed Liquid Crystal Droplet for Complex Beam Manipulation.” (in submission)

Abstract

Inkjet and Electrohydrodynamic Printing of Liquid Crystal Droplets for Functional Optical Elements

By Mengmeng Li

This thesis investigates the use of Drop-on-Demand (DoD) printing methodologies for the fabrication of optical components using liquid crystal (LC) mixtures. The two DoD printing methodologies considered in this thesis are inkjet and electrohydrodynamic (EHD) printing. Together, these methodologies facilitate the precise deposition of LC-related mixtures across a wide range of length scales, spanning droplets that vary in size from 1 micron to several hundred microns in droplet diameter. The processes relating to inkjet printing and EHD printing were simulated using COMSOL Multiphysics with the objective being to deepen our understanding of the operational mechanisms inherent to each printing method, with a particular emphasis on EHD printing.

Using these printing technologies, three different optical elements are presented in this thesis. The first photonic device that is demonstrated is a printed polymer stabilized chiral nematic LC (PSCLC) smart window, which can function in either a conventional mode (scattering to transparent) or reverse mode (transparent to scattering) with the application of an electric field. Inkjet-printed droplets of the PSCLC mixture, with diameters of the order of 100–200 μm at the glass substrate and with LC layer thicknesses of ≈10–15 μm, are characterized in terms of their transmission of light as a function of the electric field amplitude and the response times for switching into and out of the scattering state. It is found that the printed droplets, and arrays thereof, exhibit similar electro-optical properties to analogous thin-film devices, but with the ability to incorporate bespoke features such as images and decorative patterns.

A DoD printed optical vortex beam generator is then demonstrated, which, upon the application of an electric field of suitable amplitude, can generate a vortex beam in the far-field. Both simulations and experiments are carried out to determine the optical characteristics of the printed LC devices and the resulting far-field patterns for different polarizations of light. The study showcases the versatility of the generator in

that it can produce both vortex beams and vector fields, the choice of which is simply determined by the polarization of the input light.

The next element that is presented is a printed LC droplet that can be used as a key component in a single-shot Stokes polarimeter for the measurement of the state of polarization of light. The use of a printed LC droplet simplifies the optical assembly requiring only the addition of a lens, a polariser and a CCD as a receiver. This polarimeter functions as a division of wavefront polarimeter which can enable single-shot measurements with an error margin of less than 1% in the determination of Stokes parameters. This accuracy highlights the effectiveness of the printed LC device in analyzing the polarization of unknown light sources.

In the Future Work, the thesis introduces two possible future applications facilitated by the deposition of LC droplets via inkjet and EHD printing: LC gratings and optical Skyrmions. The application of LC gratings primarily leverages the capability of EHD printing to produce LC droplets with diameters as small as 1μm. Regarding the application of optical Skyrmions, the devices created through inkjet printed LC droplets demonstrate versatility in generating diverse types of Skyrmions.

Acknowledgments

I extend my deepest gratitude to my supervisors, Professor Steve J. Elston, Professor Stephen M. Morris, and Professor Alfonso Castrejón-Pita, for their unwavering support and unparalleled assistance throughout my DPhil journey. Their guidance has been invaluable, and I am profoundly thankful for their dedication and commitment to my academic and personal growth. Thank you, Steve E, for your unconditional support and guidance in navigating the intricacies of research work. I will forever cherish the memory of my arrival in the UK during the challenging times of COVID-19, feeling lost, panicked, and overwhelmed. Your kindness in acquainting me with the city of Oxford, the structure of our lab, and even providing me with directions from my accommodation to the department was a beacon of light in those uncertain times. Your patience in laying the foundation of my knowledge of liquid crystals and optics was truly commendable. In research, you guided me to think scientifically, a priceless treasure that has greatly enriched my academic journey. Whenever I encountered difficulties, I knew I could always turn to you. With you, I never felt alone; you cared for me not just academically but also took an interest in my future work and mental well-being. No matter the challenge, you were always there to support me, offering invaluable advice on all aspects of my studies and life, even in areas where I fell short. I could never have imagined myself to be so fortunate to have a supervisor as patient, serious, caring, and supportive as you. Your help will never be forgotten! I will always treasure all the moments with you! Thank you, Steve M, for providing ample research facilities throughout my study! Your meticulous guidance and assistance in revising all of my papers, reports, and thesis have been immensely educational. I am profoundly grateful for every piece of patient feedback you have provided. I sincerely appreciate the thorough and detailed training you arranged for me upon my entry into the group, which enabled me to quickly familiarize myself with the research topics and laid a solid foundation for my subsequent experimental work. Beyond research work, you reminded me of the importance of engaging with college life and facilitating a smoother integration into life at Oxford. Your responsiveness to every email and your positive support through various challenges have been invaluable. You have created numerous opportunities for us to engage with and understand a broader array of topics related to optics, such as participating in photonic days, attending optical seminars, and being part of the British Liquid Crystal Conference! Thank you, Alfonso, for your steadfast support concerning the research facilities, and for providing me with the necessary laboratory space and relevant experimental equipment.

Whenever I sought your advice, you consistently offered very clear guidance that enabled me to make more rational decisions. Your invitation for the whole group to the Royal Oak was a thoughtful gesture to help us unwind and momentarily escape the disappointment of unfavourable experimental results.

I am deeply grateful to all the members of the Soft Matter Photonics Group! I feel incredibly fortunate to have studied and worked in such a friendly and supportive research group. I extend my heartfelt thanks to Waqas, whose valuable training introduced me to printing techniques and the use of printing equipment, swiftly bringing me up to speed with printing-related research. I am thankful to Lake for helping me understand the research group when I first joined. I appreciate Yihan, who offered me considerable assistance with housing and life in the UK even before my arrival. My gratitude goes to Alva for patiently and meticulously guiding me through the bespoke printing system. I thank Peng for his immense help and support both in research and life, boosting my confidence, objectivity, and passion for life. I am grateful to Bohan for his emotional support and encouragement during tough times, and for the delicious food he shared. I thank my peers, Guanxiong, Zimo, and Zipei, for their advice and assistance. I am indebted to Xuke and Linpei for their unconditional support, encouragement, and help during my difficult times, making me feel warmly embraced during my most challenging moments. I thank Nathan, Camron, Alec, and Urban for their help while attending conferences in the USA. My appreciation extends to Qihao, Jinge, Zhiyu, Ji, Runchen, Aldi, Bradley, Junseok, Yunuen, and many others for enriching and brightening my DPhil journey. Thank you to Dr. Chao He and Yifei for their support and assistance in my research. I am thankful to the entire Fluid Dynamics Group for the relaxing conversations and discussions at the Royal Oak. My thanks also go to Tom for his support and guidance in the lab.

I am grateful for my friends in Oxford. Thank you, Haopeng, for always understanding me, helping me, offering kindness, and providing warmth that helps me relax during exhausting times. Thank you, May, for being my strongest support; I feel completely at ease discussing anything with you. Thank you, Minyi, for being my friend for over six years. It's a wonderful twist of fate that we've spent so many joyful times together in Oxford. I'm so happy to have your companionship and support. Thank you, Xiaoyun, for making my life in Oxford happier; you always listen to my troubles seriously, helping me ease my mind. Thank you, Guanqi, despite your busy schedule, you always show up when I need help, doing your utmost to cheer me up. Thank you, Yuqing, your encouragement brings me peace. Thank you, Feng, you always gave me much care. Thank you, Ning, for your kind support and joyful companionship. Additionally, I'd like to extend my thanks to my previous friends, Jiaqi, Yiping, Qiaoxuan, Ke, and Xin, for their substantial support from a distance, even though we are miles apart.

I also wish to express my gratitude to my family: my mother, father, grandparents, uncles, aunts, brothers, and sister. I feel that my family is always my strongest support, giving me the confidence to face any difficulty or challenge. No matter the circumstances or problems I encounter, they always stand by me, protecting and supporting me, allowing me to confront any challenge without burden. Throughout my journey of growth, they have provided me with immense support and love. I hope that I can be their support in the future as well.

Finally, I wish to extend gratitude to myself for embodying courage, strength, and unwavering confidence. Throughout this journey, despite facing numerous challenges, moments of sorrow, and disheartenment, I never surrendered. Each obstacle was met with resilience, instilling a profound sense of pride and commendation within myself. This sense of achievement bolsters the belief that, in the future, I will navigate through life's hurdles with the same fortitude displayed thus far. I am convinced of my excellence and capability!

Publications

Thesis-related

1. **Mengmeng Li**, Chao He, Xuke Qiu, Alfonso A. Castrejón-Pita, Steve J. Elston, and Stephen M. Morris **Inkjet Printed Liquid Crystal Droplet for Optical Skyrmion Generator and Stokes polarimeter** [*in submission*]

2. **Mengmeng Li**, Steve J. Elston, Chao He, Xuke Qiu, Alfonso A. Castrejón-Pita, and Stephen M. Morris **Printed Liquid Crystal Optical Vortex Beam Generators** *Advanced Optical Materials* 2400450 (2024)

3. Waqas Kamal, **Mengmeng Li**, Thomas Syke, Alfonso A. Castrejón-Pita, Steve J. Elston, and Stephen M. Morris **Drop-on-Demand Electrohydrodynamic Printing of Nematic Liquid Crystals** *Advanced Engineering Materials* 2400245 (2024)

4. **Mengmeng Li**, Waqas Kamal, Andrew C. J. Orr, Alfonso A. Castrejón-Pita, Steve J. Elston, and Stephen M. Morris **Printed Polymer-Stabilized Chiral Nematic Liquid Crystal Privacy Windows** *Macromolecular Chemistry and Physics* **223**, 2200154 (2022).

5. Waqas Kamal, **Mengmeng Li**, Jia-De Lin, Ellis Parry, Yihan Jin, Steve J. Elston, Alfonso A. Castrejón-Pita, and Stephen M. Morris **Spatially Patterned Polymer Dispersed Liquid Crystals for Image-Integrated Smart Windows** *Advanced Optical Materials* 2101748 (2021)

Not related to thesis

1. Yihan Jin, Steve J. Elston, Julian A. J. Fells, Bohan Chen, **Mengmeng Li**, Waqas Kamal, Zimo Zhao, and Stephen M. Morris **Backflow-Assisted Time-Resolved Phase Modulation in Nematic Liquid Crystal Pi-Cells** *Optics & Laser Technology* **156**, 108596 (2022).

2. Bohan Chen, Peng Xie, Zimo Zhao, Patrick S. Salter, **Mengmeng Li**, Linpei Xue, Xuke Qiu, Martin J. Booth, Steve J. Elston, and Stephen M. Morris **Ultrafast Laser-Writing of Liquid Crystal Waveguides** *Ultrafast Science* (2024)

Conference

Oxford Photonics Day 2022

(University of Oxford)

Oxford, United Kingdom – October 2022 ***(Poster)***

“Printed Polymer-stabilized Chiral Nematic Liquid Crystal Privacy Windows”

Oxford Photonics Day 2023

(University of Oxford)

Oxford, United Kingdom – October 2023 ***(Poster)***

“Printed Liquid Crystal Vortex Beam Generators”

SPIE Photonics West 2024

San Francisco, United States – January 2024 ***(Oral)***

“Printed of liquid crystal droplets for functional optical components”.

British Liquid Crystal Society Annual Meeting 2024

Worcester College, Oxford, United Kingdom – April 2024 (Poster)

“Printed Liquid Crystal Vortex Beam Generators”

Table of contents

List of abbreviations

AM	Amplitude Modulated
CIJ	Continuous Inkjet
CLC	Chiral nematic Liquid Crystal
DoAmP	Division of Amplitude Polarimeter
DoAP	Division of Aperture Polarimeter
DoD	Drop-on-demand
DoFP	Division of Focal plane Polarimeter
DoWP	Division of Wavefront Polarimeter
DSA	Diffractive Spiral Axicon
DOLP	Degree of the Linear Polarization
DOCP	Degree of Circular Polarization
EHD	Electrohydrodynamic
GRIN	Gradient-Index
GPLC	Grid-Patterned Liquid Crystal
ID	Inner Diameter
IPA	isopropyl alcohol
ITO	Indium tin oxide
LC	Liquid Crystal
LCLV	Liquid Crystal Light Valve
LCP	Left Circularly Polarized
LP	Linear Polarizer
LS	Level Set
MM	Mueller Matrix

ND	………………….	Neutral Density
NOA	………………….	Norland Optical Adhesive
OD	………………….	Outer Diameter
OV	………………….	Optical vortex
PDLC	………………….	Polymer Dispersed Liquid Crystals
PSG	………………….	Polarization State Generator
PSA	………………….	Polarization State Analyser
PSLC	………………….	Polymer Stabilized Liquid Crystals
PSCLC	………………….	Polymer Stabilized Chiral nematic Liquid Crystal
PVA	………………….	Polyvinyl alcohol
PZT	………………….	Piezoelectric Transducer
QWR	………………….	Quarter Wave Retarder
RCP	………………….	right circularly polarized
SLM	………………….	Spatial Light Modulator
SOP	………………….	State of Polarization
UV	………………….	Ultraviolet
VOF	………………….	Volume of Fluid
VOF-Gen	………………….	Vector Optical Field Generator

CHAPTER 1: Introduction

With the development of advanced printing methodologies, notably inkjet printing and electrohydrodynamic (EHD) printing, the landscape of device fabrication is witnessing a remarkable transformation. Inkjet printing was first invented by William Thomson and Abbe Nollet in 1858[1]. By the help of the discovery of the piezoelectric effect by Pierre and Jacques in 1880, piezoelectric inkjet printing was developed in the late 1940s[2], which has already been used in many different fields including tissue engineering[3-5], electronics[6-8], biopharmaceuticals[9-10] and more.

However, the resolution for inkjet printing is around 12 μm in diameter and may vary according to the properties of the printed ink[11]. In this circumstance, EHD printing, on the other hand, involves the application of a large amplitude electric field between the nozzle and the substrate to pull the ink out of the nozzle instead of pushing the ink out as is the case for the inkjet printing system. This mechanism leads to the formation of a Taylor cone that results in the deposition of printed droplets with a smaller diameter than that achievable using inkjet printing. The resolution in EHD printing is even smaller than 1 μm[12]. These methodologies, celebrated for their precision and multifaceted material deposition capabilities, are emerging as robust tools, enabling swift, cost-efficient, and mass production of optical devices, thereby propelling advancements in the realm of photonic technologies.

The primary objective of this thesis is to demonstrate the application of advanced techniques in the fabrication of optical devices using liquid crystal (LC) materials. LCs are unique substances that exhibit properties between those of solid and liquid states, making them particularly suitable for the printing processes discussed in this research. These materials possess significant optical anisotropy, resulting in birefringence, which is advantageous for optical device applications. An exploration of the operational process of inkjet and EHD printing is undertaken, supported by an evaluation of their benefits and possible constraints. Moreover, an examination of the specificities of these methodologies for optical device creation is conducted, with emphasis on the use of LC, the complexities of the printing process, and the resultant attributes of the printed optical devices.

1.1 Aim and motivation

This research aims to demonstrate the practical potential of inkjet printing and EHD printing when applied to LCs and their mixtures in the fabrication of optical devices. Previous research in this area has focused on the printing of LC mixture for sensing devices such as microscopic protein sensor[13], Alcohol sensor[14], time-temperature sensor[15] and so on.

Recognizing the transformative power of advanced printing technologies and their potential use with LC-based materials, this study aims to explore the possibilities that may arise from this combination. To achieve these objectives, the research focuses on the fabrication of three primary optical components using printing techniques. This thesis will emphasize the shape of the printed LC droplet, as the surface tension of the droplet influences the alignment of the LC director, resulting in varying optical properties. These include two operational modes of printed LC smart windows, a printed LC vortex beam generator, and a printed LC device designed specifically for Stokes polarimetry.

Each of these optical components showcases the unique applications of advanced printing technologies in optical device fabrication using LCs. Each component will be examined in the separate subsequent chapters, providing an understanding of the fabrication processes and their resultant properties. The following section outlines the content of this thesis and provides detailed information on each chapter.

1.2 Layout of the thesis

Chapter 2 will introduce the necessary background on LCs, focusing mainly on the nematic phase, chiral nematic phase, and their respective physical and electro-optical properties. LC polymer composites will also be introduced including both polymer dispersed liquid crystals (PDLC) and polymer stabilized liquid crystals (PSLC), which are of importance for Smart Windows.

In Chapter 3, I will provide an overview of the experimental procedures employed in the thesis along with a presentation of the printing systems. There are two different printing techniques used in this D.Phil thesis, which are inkjet printing and EHD printing. The inkjet printing system includes a bespoke printing system and a commercially available printing system (Microfab Jetlab II).

For the EHD printing system, this has been developed by a previous D.Phil student and myself. The system was designed to accommodate interchangeable printing nozzles—both glass capillary and metal types—thereby allowing for customization based on specific project needs through the straightforward modification of the printhead within the apparatus. Additionally, this system was engineered to function with minimal quantities of LC ink. Incorporating a heating element and a control module, the system facilitates the precise thermal management of the printed material.

Chapter 4 will introduce the modelling that has been carried out on inkjet printing and the EHD printing processes. For this work, the COMSOL Multiphysics commercial software package has been used, which is based on finite element modelling. This EHD simulation model has been used to verify the possibility of printing LC and LC-polymer compositions even though they are not conductive materials, which are traditionally employed in EHD printing. Simulations have also been conducted to compare and understand the printing process.

This simulation has been added to the paper ‘Drop-on-Demand Electrohydrodynamic Printing of Nematic Liquid Crystals’ which has been developed in cooperation with another senior D.Phil student. This work has been published in the journal *Advanced Engineering Materials* 2400245 (2024) where I am the second author.

Drop-on-demand (DoD) printing of polymer stabilized chiral nematic liquid crystal (PSCLC) privacy windows is demonstrated in Chapter 5. These printed windows can function in either a conventional mode (scattering to transparent) or reverse mode (transparent to scattering) with the application of an electric field. The results show that the printed droplets, and arrays thereof, exhibit similar electro-optical properties to analogous thin-film devices, but with the ability to incorporate bespoke features such as images and decorative patterns. This work has been published in the peer-reviewed journal paper ‘Printed Polymer-Stabilized Chiral Nematic Liquid Crystal Privacy Windows’ *Macromolecular Chemistry and Physics* **223**, 2200154 (2022) where I am the primary author. In this chapter, I will also present the research that I carried out together with another D.Phil student to demonstrate printed PDLC smart windows. This work led to the publication ‘Spatially Patterned Polymer Dispersed Liquid Crystals for Image‐Integrated Smart Windows’ *Advanced Optical Materials* 2101748 (2021). I am a co-author of this manuscript.

Chapter 6 then introduces another potential application of printed LC droplets in the form of optical vortex beam generators. These unique features make vortex beams important in many photonics applications such as optical tweezers, optical communication, and more. Results are then presented that demonstrate that using inkjet printing in the fabrication process provides a fast and simple process for forming high order vortex beam generators or arrays. Furthermore, the vortex beam can be switched on or off. This work has been published in the paper ‘Printed

Liquid Crystal Optical Vortex Beam Generators' *Advanced Optical Materials* 2400450 (2024), where I am the primary author.

The focus of Chapter 7 is on the development and demonstration of a printed LC droplet device for a new Stokes Polarimeter. The printed LC droplet functions as a microlens, exhibiting radial refractive index variability and serves as a rotating waveplate in the azimuth direction, while undergoing birefringence variation in the radial direction, thereby facilitating simultaneous measurement of the Stokes parameters. This instrument, owing to its compact and sleek design, can be assimilated into various optical systems without compromising the accuracy of measurements. The fabrication procedure, analysis, working principle and experimental results will be described in detail in this chapter. This work has been written up for publication.

Finally, Chapter 8 summarizes the key conclusions from the previous chapters before providing general conclusions for the entire D.Phil thesis. Potential areas for future work are discussed for each of the avenues of research presented in the thesis. This is then followed by a presentation of two further potential applications of printed LC droplets: diffraction gratings using EHD printing, which could provide a printed diameter as small as 1 μm, and printed optical skyrmions. By utilizing LC droplets of varying diameters and combining them with different thin-film-based half-wave and quarter-wave plates, it is possible to fabricate an array showcasing various optical skyrmionium configurations.

CHAPTER 2: Background

In this thesis, liquid crystals (LCs) are the principal material employed in all of the chapters. This unique state of matter, straddling between a crystalline solid and an isotropic liquid, exhibits the fluidity of liquids and the orderliness of solids. The molecules in LCs can self-arrange in specific structures, altering in response to applied electric fields. These distinctive traits make LCs an invaluable asset in technology development, extensively used in a wide range of electronic devices, including optical devices.

2.1 Liquid crystal phases

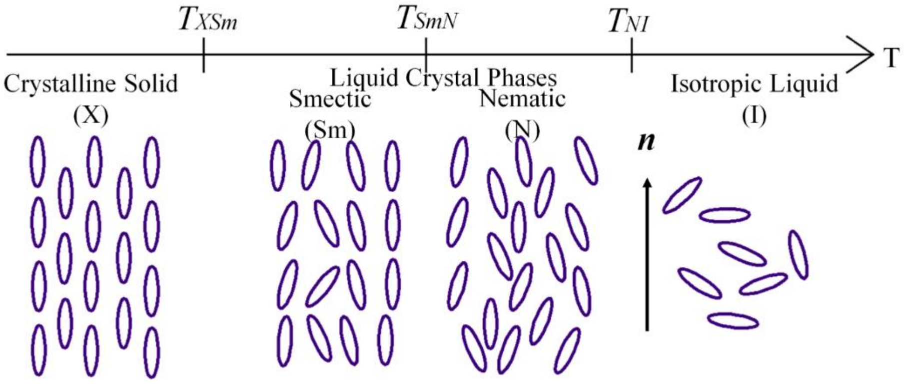

Figure 2.1 An example of the possible phase transitions of a thermotropic LC upon heating to the isotropic liquid phase. The melting temperature is defined as the transition temperature from the crystalline solid to the LC phase whereas the clearing temperature refers to the transition temperature into the isotropic liquid phase.

Crystalline solids refer to a structure that exhibits a certain regularity in terms of a spatial arrangement of the atoms (or molecules) to form a periodic structure. The liquid state, on the other hand, cannot maintain a stable structure, so its composition naturally has no regularity. Liquid crystals (LCs), which were first observed in 1888 by Friedrich Reinitzer [16], are a state of matter that exists between the solid crystalline and isotropic liquid phases. These LC mesophases can exhibit orientational order and, in some cases, positional order as well. LCs can be divided into two classes: thermotropic and lyotropic. Thermotropic LCs refer to the type of materials whereby the mesophase appears upon a change in the temperature (see for example **Figure 2.1**). Lyotropic LCs, on the other hand, are formed with the addition of a solvent, which is controlled both by the concentration of the solvent and temperature [17]. This thesis considers thermotropic LCs only as these are the materials that are used in optoelectronic technologies such as in the displays industry. Aside from the separate classifications, LC phases are also characterized by the type and degree of order that is present e.g. the nematic, chiral nematic (sometimes referred to as cholesteric), and smectic phases.

2.1.1 Nematic phase

The nematic phase is the least ordered LC phase as it possesses orientational order only, but no positional order. It is also the most popular LC phase in terms of commercial technological applications. The molecules that form a nematic phase typically exhibit a rod-like shape and consist of a rigid aromatic core and a flexible alkyl chain. A unit vector known as the director, **n**, is usually employed to characterize the overall orientation of the LC molecules. It is obtained by averaging the orientation of the long axis of the molecules, as shown in Figure 2.1. Nematic LCs can be considered to possess three main features: (1) They have long-range orientational order, which is described by the scalar order parameter, *S*, defined as

$$S = \frac{1}{2}\left\langle 3\cos^2\theta - 1 \right\rangle \tag{2.1}$$

where θ is the angle between the director **n** and the long axis of the molecules. The brackets (< >) denote an average over all the molecules in the nematic phase.

For the crystalline phase, $S \approx 1$ when at absolute zero temperature. Values for S in the nematic phase are lower than 1 because of the lack of perfect order and are observed to decrease with increasing temperature. $S = 0$ in the isotropic phase corresponds to a lack of any orientational order. (2) The nematic phase has no positional order, meaning that the molecules are not arranged in layers and only maintain approximately parallel distribution in terms of the direction of the long axis of the molecules. (3) Nematic LCs exhibit a similar degree of fluidity to ordinary isotropic liquids.

2.1.2 Chiral nematic phase

Chiral nematic LCs (or cholesteric LC as they are often known because the first discovery was in cholesteryl-based derivatives) differ from a nematic LC in terms of the formation of a macroscopic helical arrangement of the molecules as a result of the presence of chirality, as shown in **Figure 2.2**. For chiral nematic LCs that are formed through the addition of chiral additives, the handedness of the helical structure is determined by the handedness of the chiral additive. The director **n** in the macroscopic chiral structure rotates either clockwise or anticlockwise depending upon the handedness of the chiral dopant. The distance over which the director rotates a full 360° is defined as the pitch, p. However, due to the invariance in the physical properties when viewed along either **n** or **-n**, the period of the structure is half of the pitch. The magnitude of the pitch depends upon the concentration of the chiral dopant and the helical twisting power (β). The higher the value of β the smaller the value of the pitch for a given concentration. The relationship between the pitch, the concentration and β is given by

$$p = \frac{1}{\beta c} \tag{2.2}$$

where c is the concentration of the chiral dopant [18-19]. An example of how the pitch varies with temperature for a chiral nematic LC with an underlying Smectic A phase is shown in **Figure 2.3**. As can be seen in the figure, with increasing temperature the LC phase changes from Smectic A to chiral nematic before clearing into the isotropic liquid phase. The pitch of the chiral nematic LC diverges upon approaching the smectic A phase in order to be compatible with the layered structure of the smectic A phase [20].

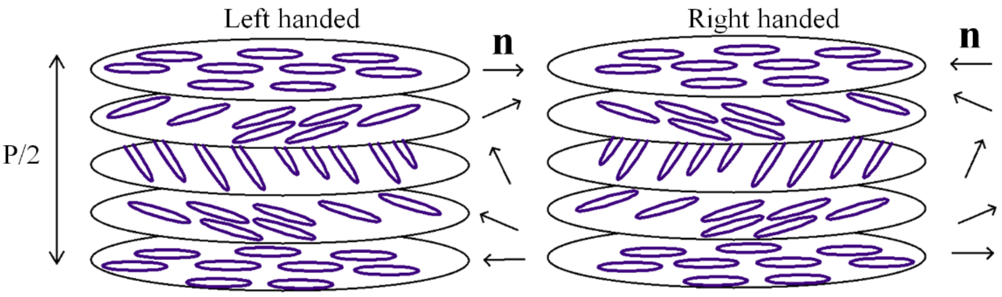

Figure 2.2 Configurations of either a left-handed or right-handed chiral nematic LC.

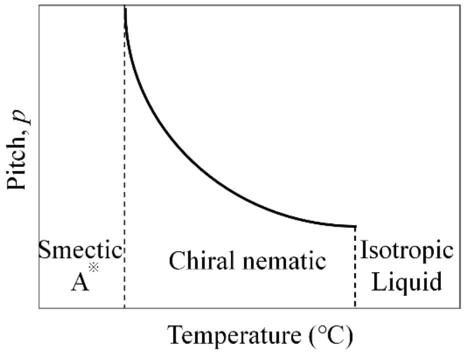

Figure 2.3 The pitch of a chiral nematic LC as a function of temperature [18]. Reproduced with permission from ref [18], © **Copy right 2017**, Informa UK Limited, trading as Taylor & Francis Group http://www.tandfonline.com . DOI: 10.1080/1358314X.2017.1279443.

2.2 Physical properties

The physical properties described in this chapter mainly focus on calamitic (rod-like) nematic LCs. The anisotropy inherent in LC phases makes them an ideal material for many technological applications requiring direct control over the propagation of light. The optical and electrical properties can be quite different for the different alignment configurations, which are described in more detail in the following section.

2.2.1 Optical anisotropy (Birefringence)

Light is an electromagnetic wave with oscillating electric and magnetic fields perpendicular to the propagation direction. Light travels at different speeds when it encounters different refractive indices and for LCs two principal refractive indices correspond to orientations of the oscillating electric field being either parallel or perpendicular to the optic axis. For the case of an aligned nematic LC, the optic axis is an axis that is colinear with the director. The refractive index perpendicular to the optical axis is called the ordinary refractive index (n_o) and the refractive index along the optical axis is called the extraordinary refractive index (n_e) as shown in **Figure 2.4** (a).

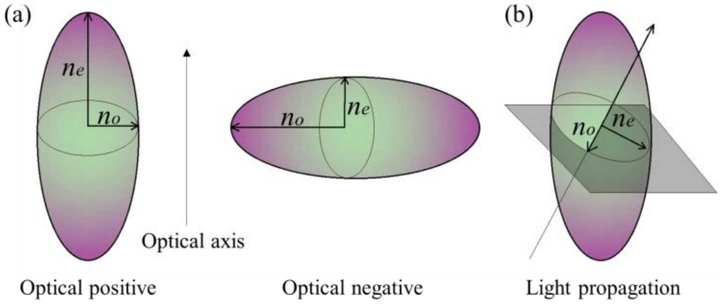

Figure 2.4 (a) Schematic of optically positive (left) and optically negative (right) LC (b) Schematic of light passing through an LC [20]. Reproduced with permission from Springer Nature, from Sengupta, A. (2013). *Liquid Crystal Theory* (Chapter of Topological Microfluidics Nematic Liquid Crystals and Nematic Colloids in Microfluidic Environment).

If the light propagation direction is at an angle, φ, to the optic axis it will split into components that experience n_e and n_o, given by

$$n_e = \frac{n_{\parallel} n_{\perp}}{\sqrt{n_{\parallel}^2 \cos^2(\varphi) + n_{\perp}^2 \sin^2(\varphi)}} \tag{2.3}$$

$$n_o = n_{\perp} \tag{2.4}$$

where $n_{\parallel}$ is the refractive index along the optical axis and $n_{\perp}$ is the refractive index perpendicular to it. The effective birefringence is defined as $\triangle n = n_e - n_o$, which determines the phase difference between the ordinary and extraordinary rays. The phase retardation, δ, can be defined as

$$\delta = \frac{2\pi}{\lambda}\left(n_e - n_o\right) d \tag{2.5}$$

where d is the thickness of the LC layer.

In a chiral nematic LC, the combination of the helical structure and the optical anisotropy leads to the appearance of a bandgap in the transmission spectrum. When the pitch is of the order of the wavelength of light, this bandgap can appear within the visible spectrum. The relationship between the bandwidth of the bandgap ($\Delta\lambda$), the pitch of the helix and the birefringence is given by

$$\Delta\lambda = \Delta n \cdot p \tag{2.6}$$

The band gap can be observed directly from the reflected colour of the chiral nematic LC and with the aid of a UV-Vis spectrometer, as shown in **Figure 2.5**. The edges of the band gap can be calculated by λ and the refractive index along the two directions which are $\lambda \cdot n_o$ and $\lambda \cdot n_e$.

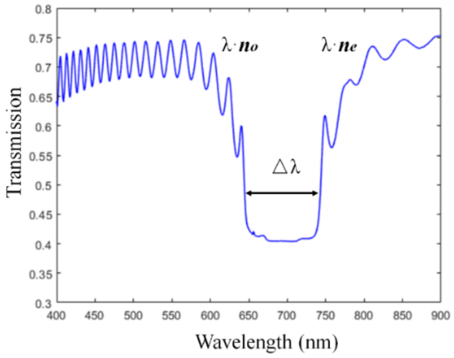

Figure 2.5 Transmission spectrum for white light propagating through a chiral nematic LC film.

2.2.2 Viscosity

LCs are anisotropic fluids that have different viscosities depending upon the different directions of flow [20]. To represent this anisotropy, three viscosity coefficients are typically defined, as shown in **Figure 2.6**. In this case, the bottom plate is fixed whilst the top plate is free to move towards the x-direction according to the applied shear force, Fx. If the LC director is parallel to the flow direction, the viscosity coefficient that is measured is referred to as η_1 (Figure 2.6 (a)). If the director is parallel to the flow gradient, on the other hand, this coefficient is called η_2 (Figure 2.6 (b)). Finally, η_3 (Figure 2.6 (c)) represents the viscosity coefficient corresponding to the case when the director is perpendicular to both the flow direction and the gradient of the flow. In addition, the rotation of the LC director could also influence the viscosity of the LC, which can be evaluated by the rotational viscosity coefficient γ.

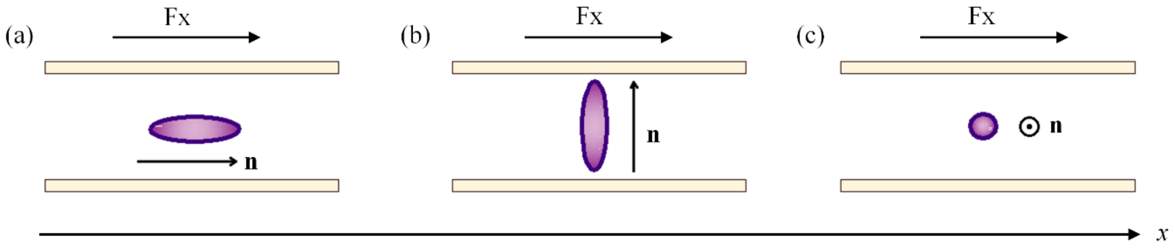

Figure 2.6 Schematic representation of the three different viscosity configurations.

The viscosity influences the flow of the LC, which is of significance for the printing process considered in this work. The viscosity also varies significantly with temperature [21]. **Figure 2.7** demonstrates how these viscosity coefficients typically vary with temperature for a nematic LC. It can be seen that the three viscosity coefficients collapse to a single coefficient (h$_{iso}$) in the isotropic liquid phase, which is of importance when printing LCs and is therefore discussed later in this thesis.

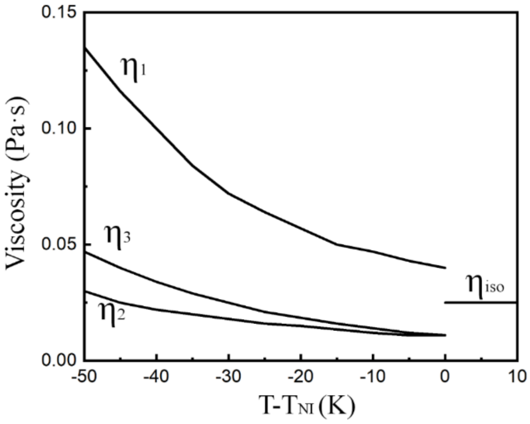

Figure 2.7 The variation of the three viscosity coefficients with temperature. T$_{NI}$ is the nematic-isotropic phase transition temperature [21]. Reproduced from *Introduction to Liquid Crystals Chemistry and Physics* by INFORMA UK LIMITED, ISBN: 9780748406432, page 18, with permission of The Licensor through PLSclear. © INFORMA UK LIMITED.

2.2.3 Surface Anchoring and Alignment

The surface alignment of an LC phase has a significant influence on the properties of the resulting LC film. For nematic LCs, there are typically three types of director alignment: planar, tilted, and homeotropic (or perpendicular). Two angles are typically used to represent the alignment of the LC director as shown in **Figure 2.8**(a): the azimuthal angle φ and the polar angle θ. For a uniform planar alignment as shown in Figure 2.8(b), θ = π/2 and φ = constant whereas for a homeotropic alignment (c) θ = 0 and φ is undefined. For Figure 2.8(d), which represents a degenerate planar alignment θ = π/2 and φ is arbitrary whilst (e) illustrates a tilted alignment of the director whereby θ ranges between 0 and π/2 and φ = constant [20, 22].

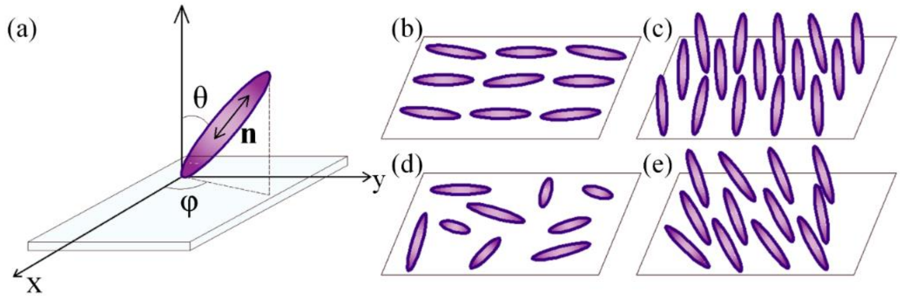

Figure 2.8 (a) Schematic illustration of the anchoring angle, (b) uniform planar alignment, (c) homeotropic alignment, (d) degenerate planar alignment, and (e) tilted alignment.

One way to align a nematic LC is to deposit a planar alignment layer such as polyimide or PVA solution by spin-coating the materials onto the surface of a substrate. A rubbing machine is then used to rub the layer in the desired direction, forcing the LC to align preferentially in a planar orientation. Alternatively, homeotropic alignment is typically achieved through the use of chemical surfactants such as lecithin, which forms a thin layer on the substrate. This kind of surfactant usually contains two parts: a hydrophilic head group and a hydrophobic hydrocarbon chain, resulting in the LC director aligning perpendicular to the substrate. Photoalignment is also a method that can be used to align LC phases, especially for more sophisticated patterning of the LC orientation.

The bulk alignment of an LC phase is also influenced by the elastic free energy as well as from the surface treatment. The Ericksen number (E_r) [23] is used to describe the degree to which the flow of the LC influences the resulting macroscopic alignment. It is defined as the ratio of viscous to elastic forces [24-25],

$$E_r = \frac{\eta \nu L}{K} \tag{2.7}$$

where η is the average flow viscosity coefficient as described before, v is the flow velocity, L is a typical length scale, and K is the elastic constant. If the E_r number is greater than unity, then the main factor influencing the distribution of the LC director is flow. However, for small values of E_r, the surface treatment plays the main role in the director alignment.

2.2.4 Elastic properties

Continuum theory considers the elastic free energy, which describes the relationship between energy and director distortion caused by any other external condition. The free energy per unit volume of an achiral nematic LC can be defined as follows,

$$F_V = \frac{1}{2}K_1[\nabla \cdot \mathbf{n}]^2 + \frac{1}{2}K_2[\mathbf{n} \cdot (\nabla \times \mathbf{n})]^2 + \frac{1}{2}K_3|\mathbf{n} \times (\nabla \times \mathbf{n})|^2 \tag{2.8}$$

where K_1, K_2, and K_3 are constants representing the three fundamental distortions of the director: K_1 relates to splay (**Figure 2.9**(a)), K_2 relates to twist (Figure 2.9(b)), and K_3 relates to bend (Figure 2.9 (c)). These three constants describe the "rigidity" of the LC to director distortion.

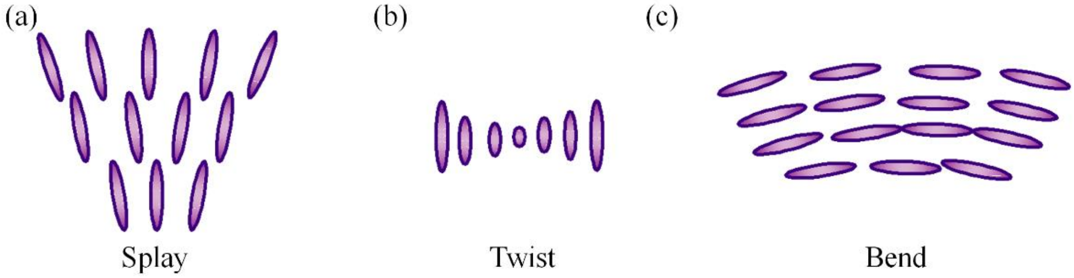

Figure 2.9 Three fundamental distortions of a nematic LC: (a) splay, (b) twist, and (c) bend.

2.2.5 Response to an electric field

The orientation of the nematic LC director can rotate when the LC layer is subjected to an external field. **Figure 2.10** shows a planar-aligned nematic LC sandwiched between two pieces of Indium tin oxide (ITO)-coated glass slides. A voltage is applied and the distance between the substrates is *d*. For a nematic LC, the dielectric response is characterised by two principal dielectric permittivities, which are $\varepsilon_{//}$ measured along the LC director and $\varepsilon_{\perp}$ measured perpendicular to the LC director. For a nematic LC with a positive dielectric anisotropy, $\Delta\varepsilon = \varepsilon_{//} - \varepsilon_{\perp}$ takes a positive value [26]. When a voltage is applied to the LC, the positive dielectric anisotropy means that the director will tend to align parallel to the electric field, whereas for a negative dielectric anisotropy LC the director will align perpendicular to the electric field. However, the electric field needs to be sufficiently large enough such that it overcomes the elastic force. This results in a threshold voltage that can be defined as follows,

$$V_{th} = \sqrt{\frac{\pi^2 K_1}{\varepsilon_0 \triangle \varepsilon}} \tag{2.9}$$

For the case illustrated in Figure 2.10, only K_1 is relevant at the threshold as it corresponds to a splay distortion [27].

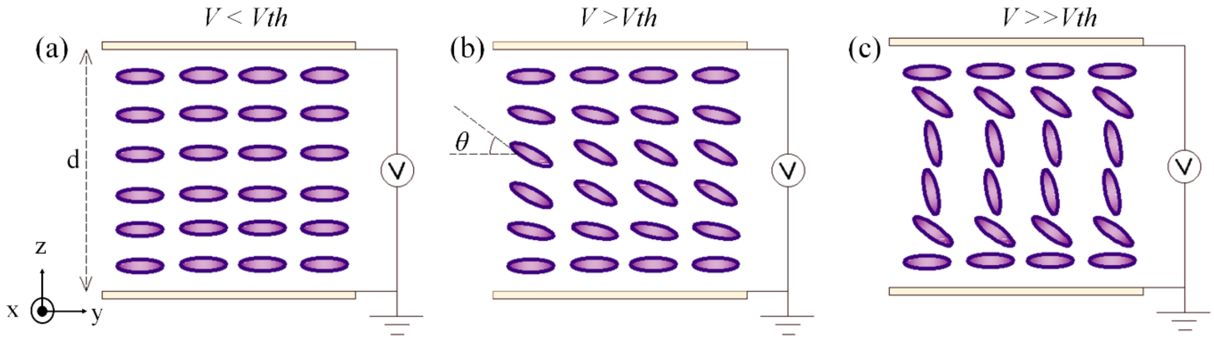

Figure 2.10 Orientation of the nematic LC director (positive dielectric anisotropy) with different applied voltage amplitudes.

With an increasing voltage applied to the LC layer, the tilt angle θ will increase from 0° to 90°, as shown in **Figure 2.11**(a). In the meantime, the permittivity of the layer increases from $\varepsilon_{\perp}$ to $\varepsilon_{\parallel}$ (Figure 2.11(b)) with the application of a voltage. Figure 2.11(c) shows the optical transmission curve for light propagating through a nematic LC layer between crossed polarizers. Equation 2.10 represents the relationship between the optical transmission and the effective birefringence $\triangle n$, which in turn depends upon the applied voltage[27-29].

$$T = \frac{I_{out}}{I_{in}} = \sin^2(2\chi)\sin^2(\frac{\pi\Delta nd}{\lambda}) \qquad (2.10)$$

where I_{in} is the input transmission intensity and the I_{out} is the output transmission intensity, χ is the angle between the optic axis of the LC layer and the transmission axis of the polariser, λ is the wavelength, and d is the thickness of the LC layer.

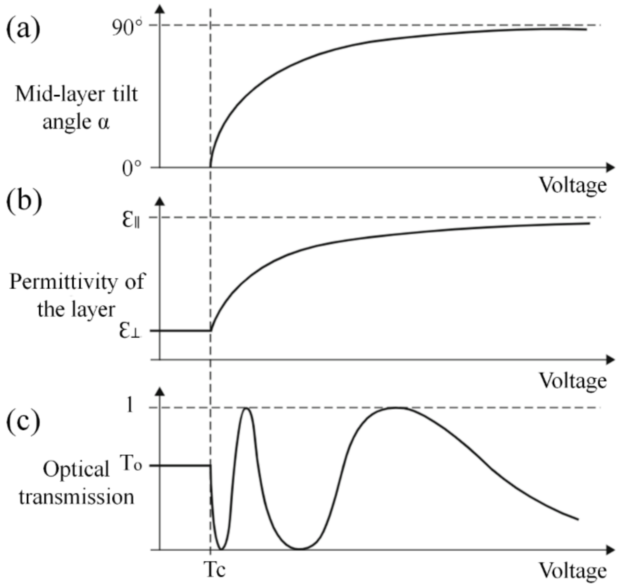

Figure 2.11 (a) the tilt angle, (b) the permittivity of the layer, and (c) the optical transmission through the LC layer between crossed polarisers as a function of the applied voltage.

The rubbing direction of the alignment layers influences the LC director alignment which has a big influence on the electro-optic behaviour of the LC device with different director alignments. Anti-parallel rubbing results in an alignment configuration as shown in **Figure**

2.12 (a). If the rubbing direction is parallel, the LC director adopts a director configuration as shown in Figure 2.12(b), which is called a nematic π(pi) cell.

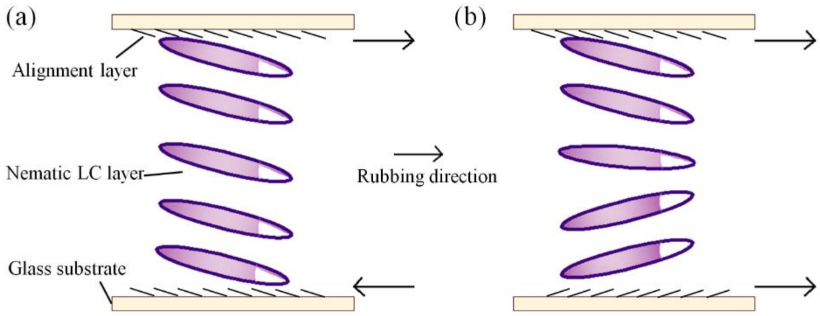

Figure 2.12 Nematic LC cells with anti-parallel rubbing (a) and parallel rubbing (b).

2.3 Liquid crystal polymer composites

For this thesis, LC polymer composites will play an essential role. The purpose of studying these materials is that the addition of a polymer either in the form of a binder or a network provides mechanical stability to the printed materials. Furthermore, by forming LC-polymer composites a wider range of electro-optic properties can be explored as well as the potential for creating components that respond to other external stimuli such as mechanical stress. The two main types considered in this work include: polymer dispersed LCs and polymer-stabilized chiral nematic LCs.

2.3.1 Polymer dispersed liquid crystals (PDLC)

Polymer dispersed liquid crystals (PDLC) are mixtures of LC and polymer that phase separate to form droplets of LC dispersed in a polymer binder. The size of the LC droplets typically ranges from several microns to tens of microns depending upon the phase separation process that is employed. These materials are interesting for devices as they can switch from an opaque scattering state to a transparent state with the application of a voltage across the PDLC layer. The phase separation of the polymer and the LC can be triggered using different processes including photopolymerization-induced phase separation, solution-induced phase separation, and temperature-induced phase separation. Photopolymerization-induced phase separation is used in this work [30].

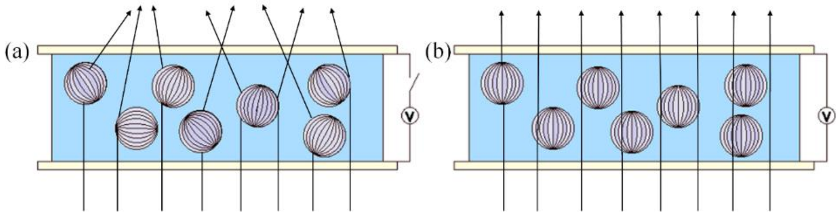

Figure 2.13 PDLC (a) scattering state without a voltage applied. (b) transparent state with a voltage applied.

An illustration of the concept of a PDLC device is shown in **Figure 2.13**(a). In this state, there is a mismatch between the refractive indices of the LC droplets and the polymer binder (n_p). This leads to the scattering of light and an opaque state. When a voltage of sufficient amplitude is applied to the PDLC layer, the director inside the droplets aligns parallel to the electric field, which allows the light to pass through the film (Figure 2.13(b)). In this state, the ordinary refractive index component of the LC droplets (n_o) is matched to the refractive index of the polymer binder (n_p). Therefore, there is no scattering of light, and the device appears transparent when viewed at normal incidence. Due to this switching mechanism, PDLCs are of interest for a range of applications including smart windows [31-32], light shutters [33-34], displays [35-36], and gas flow and pressure sensors [37-38].

2.3.2 Polymer stabilized liquid crystals (PSLC)

Polymer stabilized chiral nematic LCs combine a chiral nematic LC with reactive mesogens (RMs) (an example chemical structure is shown in **Figure 2.14**) that crosslink to form a polymer network when exposed to ultraviolet light. The type of RM used in this work is RM257, which is a widely used RM material. The chemical structure of a reactive mesogen is similar to that of a conventional low molar mass LC in that it contains an aromatic core and flexible terminal chains, but it differs in that there are one or more reactive functional groups, which cross-link in the presence of free-radicals to form a polymer network. A small concentration of photoinitiator (e.g., IR819 in Figure 2.14) is also required in addition to the RMs, which convert to free radicals under UV illumination (wavelength 254 ~ 365 nm) [39]. Through the use of RMs, it is possible to lock in the LC director alignment at the moment of photopolymerization. If the concentration of polymer is large enough, the LC alignment will be fully locked in, meaning that even in the presence of an electric field the LC director will not reorient. In contrast, the director can still reorientate for lower concentrations of RMs. This work will focus on mixtures with a low concentration (by weight) of RMs.

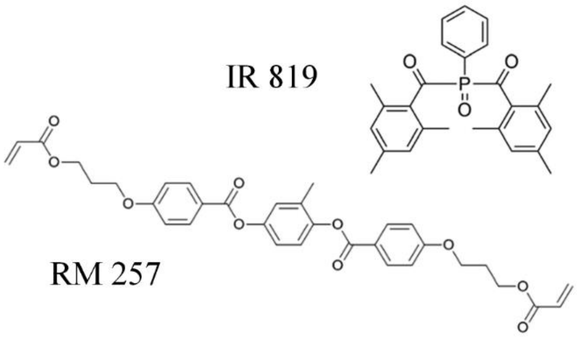

Figure 2.14 the chemical structure of RM257 and IR819[40].

2.4 Printing techniques

In this work, printing processes are used to fabricate new LC devices, including inkjet printing and electrohydrodynamic printing. The two main forms of inkjet printing are continuous inkjet printing (CIJ) and drop-on-demand printing (DoD). An example of a CIJ printing system is shown in **Figure 2.15**(a), a continuous set of droplets form and pass through an electric field. The droplets charged by the electric field are deflected and then collected by a reservoir for reuse. The other droplets that are not influenced by the electric field will be deposited onto the substrate. In contrast, a DoD printing system forms a single droplet due to a volume change and the droplet will then be ejected and printed directly onto a substrate [41]. DoD printing systems can be divided into two types due to the different ways in which the pressure waves are generated inside the nozzle. As shown in Figure 2.15(b), a thermal inkjet generates a bubble through the use of a thin film heater, which will push the liquid inside the nozzle out to form a droplet. The piezoelectric inkjet, however, forms the droplet through the use of a piezoelectric transducer (PZT) (**Figure 2.16**(a)). The inkjet printing used in this thesis focuses on piezoelectric transducer DoD printing [11].

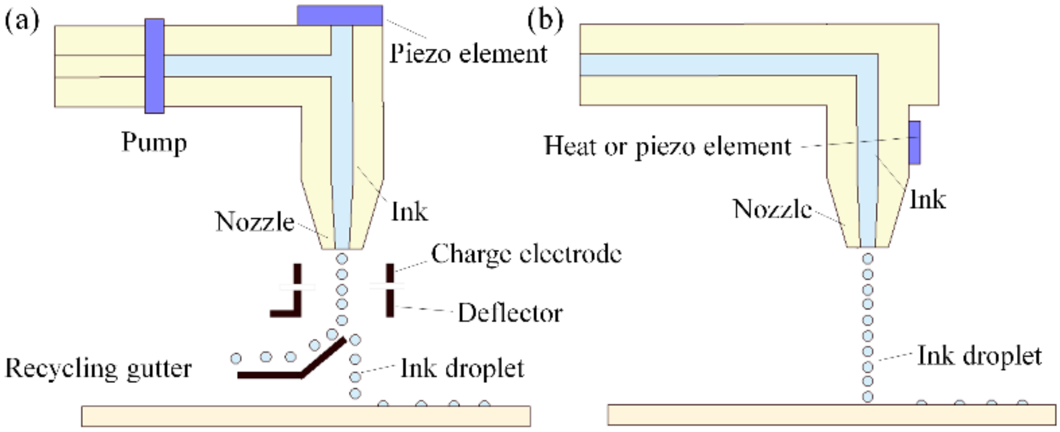

Figure 2.15 Illustration of (a) continuous printing (CIJ) and (b) drop-on-demand printing (DoD).

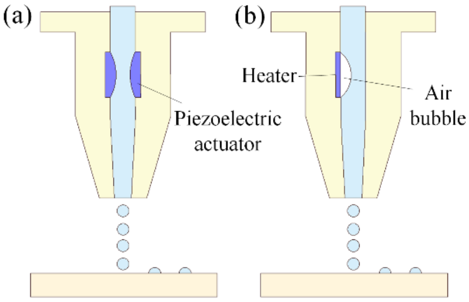

Figure 2.16 (a) piezoelectric DoD mode and (b) thermal DoD mode.

2.4.1 Inkjet printing

Liquid properties

Three main dimensionless parameters are often considered when it comes to printing liquids: the Reynolds number, Weber number, and Ohnesorge number. The Reynolds number [42] is used to describe the balance between the inertial and viscous forces, which is defined as,

$$R_e = \frac{\rho d v}{\eta} \tag{2.12}$$

where ρ is the liquid density, v is the velocity of the droplet out of the nozzle, η is the viscosity, and d is the diameter of the nozzle. The viscosity has to be carefully controlled because a viscosity that is too low will result in the liquid column being easily destroyed whereas a high viscosity will prevent the droplet from being ejected out of the nozzle.

The Weber number [43] defines the influence of the inertial force and surface tension,

$$W_e = \frac{\rho d v^2}{\sigma} \tag{2.13}$$

where σ is the surface tension that controls the shape of the droplet. The final parameter is the Ohnesorge number [44-45], which is a non-dimensional metric, that provides insight into the harmonious interrelation of viscous, inertial, and surface tension forces, proving integral in the advanced analyses of fluid dynamic phenomena.

$$Oh = \frac{\sqrt{We}}{R_e} = \frac{\eta}{\sqrt{\sigma \rho d}} \tag{2.14}$$

N. Reis and B. Derby [46] have defined an additional parameter, $Z = 1/Oh$ and have proposed that the liquid can form stable droplets if Z is in a range of 1 to 10.

Droplet formation process

In the drop formation process, boundary conditions should be considered. The printhead typically comprises a nozzle and a squeeze tube, the latter of which contains an internal piezoelectric actuator. One end of the squeeze tube is connected to the reservoir to supply the printed material, while the other end is connected to the nozzle for the actual printing process. The squeeze tube connected to the reservoir is open-ended since the reservoir diameter is larger than the squeeze tube. On the other hand, the squeeze tube that is connected to the nozzle side is considered a closed end since the nozzle diameter is small compared with the squeeze tube diameter. If a pressure wave travels to an open end, it will reflect in the opposite direction with the opposite sign. However, for a pressure wave traveling to a closed end, it will also reflect in the opposite direction but with a positive sign [47]. **Figure 2.17** shows the whole process of wave generation. The expansion and contraction of the PZT can form pressure waves. During an increase in the voltage, the PZT expands, and a positive pressure is generated which splits into two parts that travel in opposite directions.

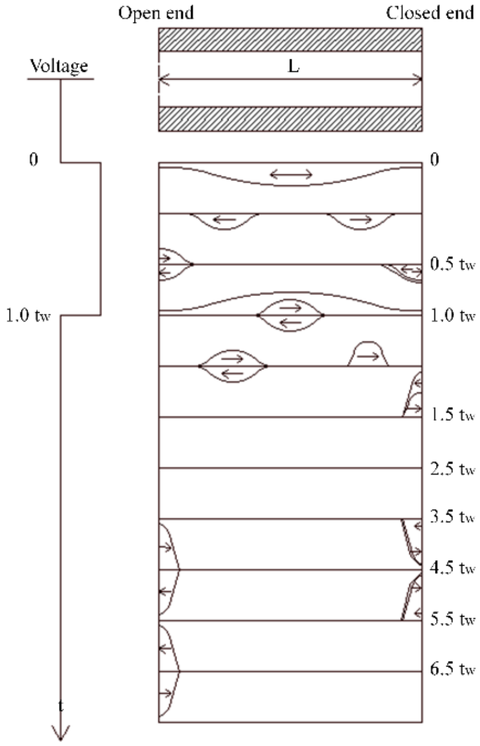

Figure 2.17 Pressure wave generated during the printing process.[48] Reproduced from ref [48], with permission of The Japan Institute of Metals and Materials. © 2004 The Japan Institute of Metals and Materials.

The time for a pressure wave to travel along a length of squeeze tube *L* can be defined as,

$$t_w = \frac{L}{v_{liq}} \qquad (1.15)$$

where v_{liq} is the pressure wave traveling in the liquid. Each wave component takes $0.5t_w$ to reach the open end or closed end and then travels back according to the process described previously. The relative resulting pressure at the nozzle side is illustrated in **Figure 2.18** [48].

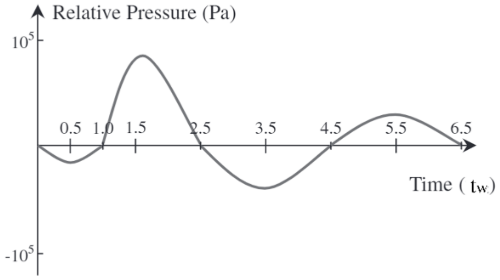

Figure 2.18 Relative pressure generated as a function of time [48]. Reproduced from ref [48], with permission of The Japan Institute of Metals and Materials. © 2004 The Japan Institute of Metals and Materials.

At time 1.5 t_W, the pressure is the highest in the single pulse process, and this condition leads to the generation and ejection of a droplet. However, the printing process highly depends on the generated pressure wave, and the pressure wave is caused by the voltage waveform applied inside the nozzle. Therefore, in addition to the pulse waveform, as shown in **Figure 2.17**, there are different types of waveforms that can be used to optimize the printing process, such as the avoidance of satellite droplets [49-50].

2.4.2 Electrohydrodynamic printing (EHD)

Electrohydrodynamic (EHD) printing is another type of DoD printing process, but with a potentially higher resolution than inkjet printing. **Figure 2.19** shows a typical EHD assembly. The difference between the EHD printing system and the inkjet printing system is the electric field formed between the nozzle and the substrate. The electric field causes the droplet to be pulled out instead of it being pushed out, forming a much smaller droplet size compared to the nozzle's inner diameter and that formed through conventional DoD inkjet printing.

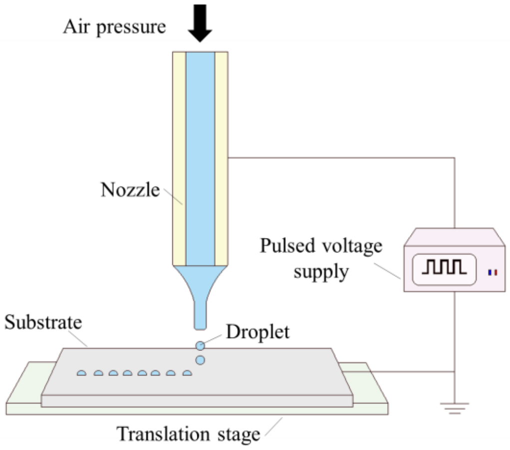

Figure 2.19 An example of an EHD printing system.

There are seven different printable modes in EHD printing depending on the operating conditions, as shown in **Figure 2.20**. Among these modes, the multi-jet, multi-spindle, and irregular fragments that are formed from several droplets combined together are typically not suitable for forming sophisticated patterns. The drop, droplet, and spindle modes form relatively large droplets, reducing the pattern's resolution. The jet mode, also called the cone-jet, is the most stable and uniform and is thus the most widely used.[51-52] This work aims to focus on this model. In this mode, the droplet is held on the tip of the nozzle due to the surface tension of the liquid. With increasing electric field, the charges accumulate on the surface which causes an electric field and a resultant force that stretches the meniscus to form a Taylor cone. More detail is provided in Chapter 5, Section 5.1.

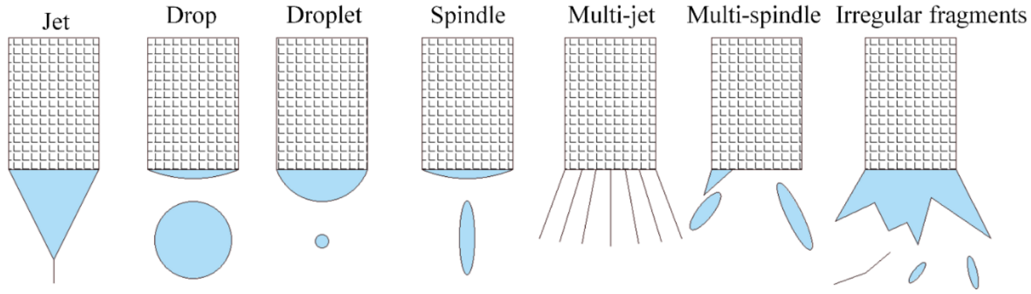

Figure 2.20 The different modes of EHD printing.

Similar to inkjet printing, the liquid properties of the fluid play an important role aside from the electric field strength, nozzle diameter, printing temperature, etc. The liquid properties of importance include the viscosity, density, and surface tension [53] whereas the relevant electrical properties include the conductivity and dielectric properties [54-55]. All these parameters together influence the printing process and cannot be considered in isolation. Overall, higher surface tension makes the printing process more challenging [56].

The droplet formation process

The droplet formation process is more complex than the conventional inkjet printing process. As shown in **Figure 2.21**, the liquid around the nozzle is under the influence of multiple forces simultaneously: the surface tension, gravity, viscosity, and the coulomb force caused by the electric field applied, including both the normal and tangential coulomb forces. When all the forces are in a stable state, the liquid can move towards the substrate continuously and steadily.

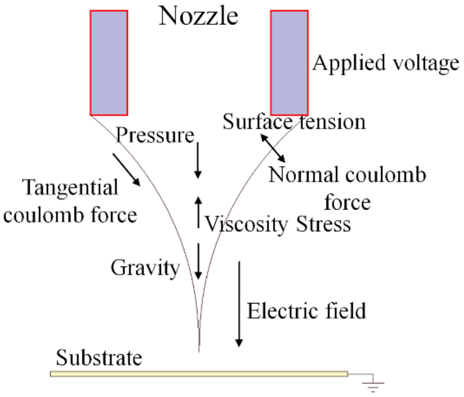

Figure 2.21 Schematic diagram of the formation of a Taylor cone.

The printing process is treated as a cone-jet process. A pre-pressure or initial velocity will be applied to the liquid to form a meniscus on the top of the nozzle. Then a voltage is used, which increases the volume of the meniscus and a Taylor-cone forms. Jetting starts on the top of the Taylor-cone and lasts for a while, making the droplets accumulate on the substrate, as **Figure**

2.22 shows. A period of the jetting process then ends, and a new one will begin according to the next pulse.

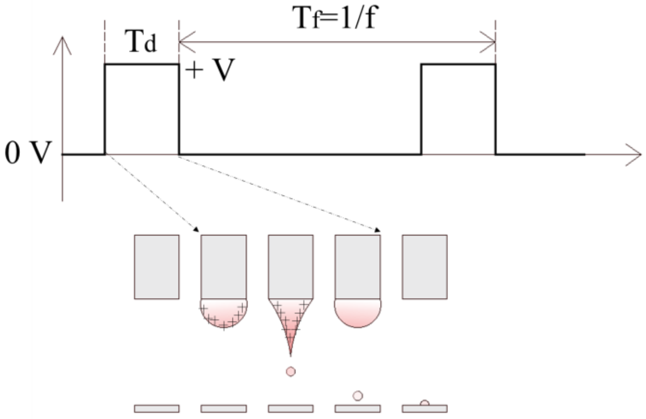

Figure 2.22 Droplet formation in the EHD printing process [57]. Reproduced from ref [57], with permission of John Wiley and Sons. © John Wiley and Sons.

2.5 Summary

This provides a summary on liquid crystals (LC) and printing techniques that are necessary for the following chapters. The chapter has introduced the different LC phases, their physical properties, their role in polymer composites, and the different printing techniques. The discussion was initiated with an analysis of the primary LC phases, namely the nematic phase and the chiral nematic phase, which form the basis for the subsequent studies. The chapter then introduced the various physical properties of nematic LC, including the optical anisotropy (birefringence), viscosity, surface anchoring and alignment, elastic properties, and response to an electric field.

The latter part of this chapter focused on LC polymer composites, including the formation and functionality of PDLCs and PSLCs, and understanding how the properties of LCs can be optimally used in a composite form for a range of applications. This chapter then introduced the main printing technologies used in this thesis, specifically inkjet and EHD printing. The inkjet printing section covered critical aspects such as the prerequisite liquid properties and the droplet formation process, while the EHD printing section focused on the operating principles and the droplet printing process.

CHAPTER 3: Experimental Procedures

This chapter presents a detailed overview of the various experimental procedures employed throughout this thesis. The processes encompass liquid crystal (LC) sample preparation, polarized optical microscopy, and the utilization of inkjet printing and EHD printing systems. Within the domain of inkjet printing, we introduce two distinct printing systems. One is a bespoke system, assembled by a senior member of our team, equipped with a high-speed camera that captures the process of droplet landing on the substrate. The other is a commercially available, automated system (Microfab jetlabII), capable of printing intricate patterns with high precision. For the EHD printing system, the setup was jointly constructed by another senior team member and myself, primarily equipped to print LC. Enhancements were subsequently made to this system by integrating temperature and positional control modules, facilitating the printing of smaller droplet sizes without altering the size of the printing head and enabling the creation of basic patterns.

3.1 Liquid crystal sample preparation

Throughout this thesis, our investigation primarily utilizes two mixtures— the nematic LC mixture denoted as E7 (sourced from Synthon Ltd), and polymer-stabilized chiral nematic LC mixtures (PSCLC). The concentration details of the PSCLC mixture used will be further expounded upon in Chapter 5, while the general methodology for LC sample preparation is outlined in the current discussion.

In this study, all the LC droplets based on optical components have been printed onto variously treated glass slides. Preparatory to the printing process, these slides, whether composed of plain glass or indium tin oxide (ITO) coated glass, are subjected to a rigorous cleaning regime. This procedure involves a sequential cleaning with acetone, an isopropyl alcohol (IPA) solution, and deionized (DI) water. Following the cleaning process, the slides are then dried either on a hot stage or simply in ambient air conditions. This is a precursor step to the spin coating of other solutions for surface alignment.

The fabrication process of different optical devices addressed in this thesis involves varying techniques and specific details. These variations and the particulars of each optical device fabrication will be explained and elaborated in the corresponding chapters.

3.2 Polarized optical microscopy

In the specific scope of this thesis, the application of polarized optical microscopy (POM) is used primarily in transmission mode. This facilitates the investigation of printed droplets under two key conditions—parallel polarizers and crossed polarizers. Utilizing parallel polarizers, incident light is transformed into polarized light upon passing through the first polarizer. As the polarized light propagates through the LC, it encounters the material's birefringent properties, which may change the polarization and phase of the light. Subsequently, as the modified light propagates through the second polarizer, only those light waves whose polarization axes align with the polarizer's polarization axis can pass. This selective transmission results in varying brightness across different regions of the LC. Such differential illumination facilitates enhanced observation of the LC’s characteristics. On the other hand, with crossed polarizers, the birefringent optical properties of the sample dramatically affect the polarization state of the transmitted light, offering a means to observe and understand the inherent anisotropy within the printed droplets. In essence, the use of POM in these two configurations provides a methodology to study the unique optical characteristics of printed LC droplets, contributing significantly to our comprehension of their behaviour and potential applications in this research.

3.3 Inkjet printing systems

3.3.1 Bespoke printing system

The Bespoke printing system consists of a print head, heater, slide holder, translation stage, LED light source, USB Camera, two motors (X and Y) that are used to control the X and Y direction movement, two motors, a power supply for the heaters, and two motors to drive the two u Steppers, as shown in **Figure 3.1**. For the signal part, there are three triggers in total. The first one is to trigger the JetDrive III, which drives the microfab nozzles with the various trapezium voltage waveforms. The following trigger is for the LED light source, and this trigger is delayed by a couple of microseconds since the droplets need time to generate and drop out of the nozzle as described in Chapter 2 at 1.5 t_W. The final trigger is required to tell the camera when to take the pictures.

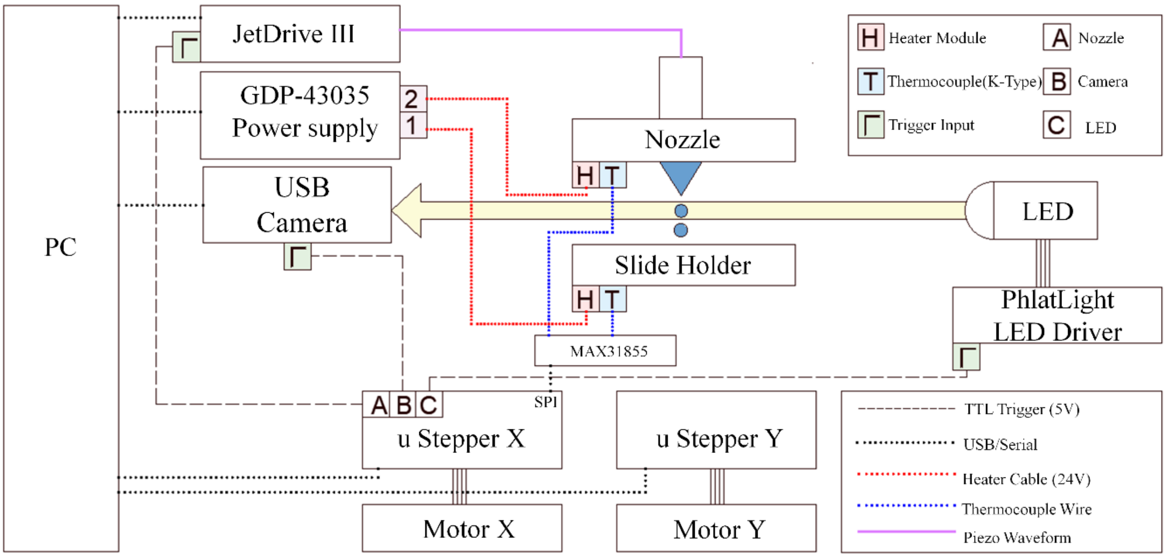

Figure 3.1 Layout of the bespoke printing system developed in the research group.

The waveform used to generate the pressure waves can be modified in the software for the JetDrive III, which was provided by the Microfab company. To begin with, the material needs to be filled into the print-head reservoir and back pressure applied to make the material fill the entire nozzle. The position of the substrate is then adjusted using the translation stage so that the material can be deposited at the desired location. The heater around the nozzle allows the temperature of the LC material to be increased, which results in a lower viscosity. For some LC materials, the increase in temperature is sufficient to cause a transition into an isotropic liquid phase. A photograph of the printing facility is shown in **Figure 3.2**. The versatility provided with this printing system enables us to study the printing process for the LC materials. **Figure 3.3** shows an example of droplets of nematic LC printed using the Bespoke printing system which shows a uniform circular profile. The printed LC droplet is around 100 μm in diameter.

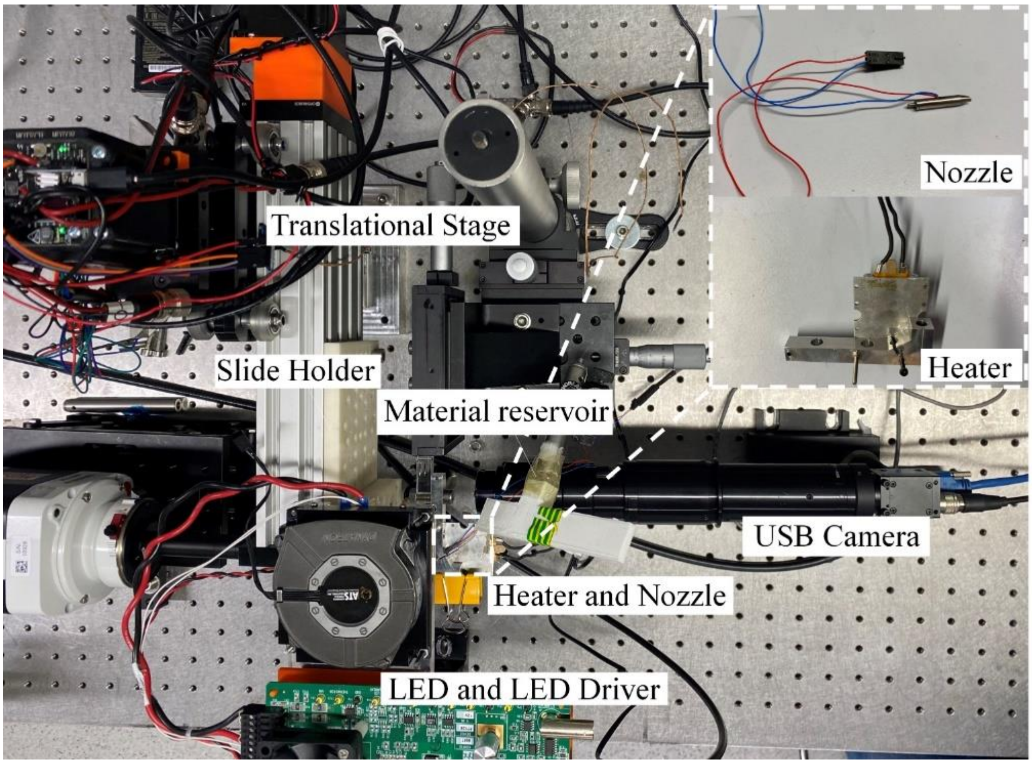

Figure 3.2 The Bespoke printing system.

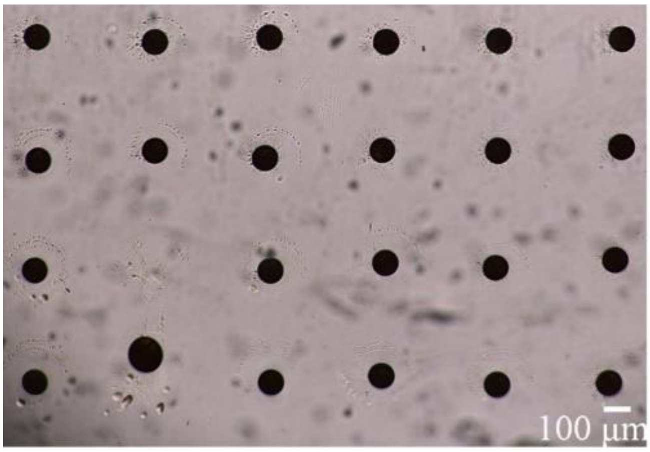

Figure 3.3 The printed droplet with the Bespoke printing system under parallel polarisers and 4× magnification. The printed droplet consists of a polymer-stabilized chiral nematic liquid crystal in the focal conic state, which will be described in detail in Chapter 5.3.1. The bespoke system used in this study was designed for preliminary experiments conducted prior to the main experiment. This system requires only a small amount of the printed material, enabling us to test whether the mixture is suitable for the printing process while minimizing material waste.

3.3.2 Jetlab II printing system

The Microfab Jetlab-II is a commercially available printing system, which is shown in **Figure 3.4**. The Jetlab-II includes a drop inspection camera that can help us better visualize the printing location on the substrate, especially when printing at precise locations is required, such as between in-plane ITO electrodes. The JetLab-II is also equipped with four ink reservoirs and dispensers, which enables us to print up to 4 different materials on the same substrate simultaneously or sequentially. A key functionality that differentiates the JetLab-II from the bespoke printer built by the research group is the highly automated control of the translation stages, which allows us to print complex patterns and features using the LC inks. **Figure 3.5** shows an example of an array of droplets printed with the Microfab Jetlab-II printing system. The diameter of the printed LC droplet is around 100 µm. The gap between the droplets can be adjusted via computer control.

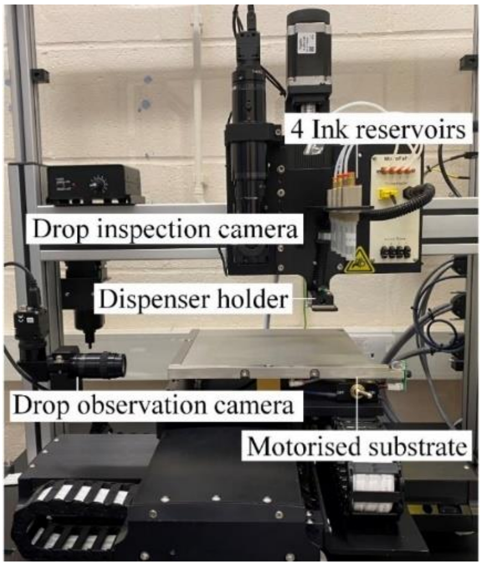

Figure 3.4 The Microfab Jetlab-II printing system.

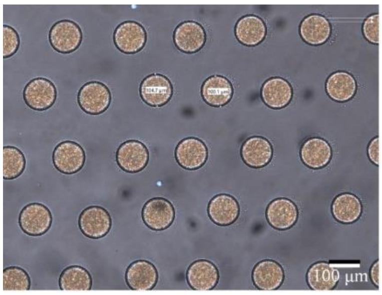

Figure 3.5 Microscope image of an array of printed LC droplets formed with the Microfab Jetlab-II printing system. The image was taken for printed droplets placed between parallel polarizers and using a 4× microscope objective. The mixture used in the printed droplet is a polymer-stabilized chiral nematic liquid crystal in the Grandjean state, which will be discussed in detail in Chapter 5.3.1. The microfab system facilitates the creation of customized patterns with precision and adaptability.

3.3.3 Printheads

The Microfab dispensers (printheads) operate via piezoelectric activation, the structure of which is shown in **Figure 3.6**. A doughnut-shaped piezoelectric (PZT) unit, characterized by radial polarization, is affixed to a glass conduit incorporating a nozzle and orifice. This glass conduit, shielded within a protective enclosure, is joined at the supply terminus to a holder fitted inside the printing system.

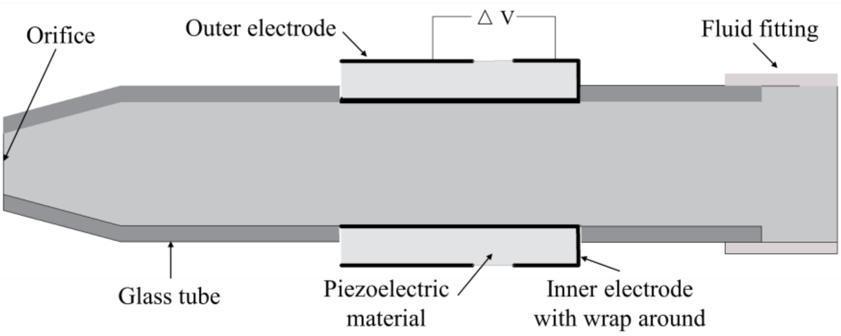

Figure 3.6 Schematic representation of the glass dispensers by MicroFab.

The toroidal piezoelectric actuator, utilized in the printheads, encompasses electrodes on its peripheral and central surfaces. The internal electrode is extended around onto the external surface, which allows the electrical coupling process. A minuscule, demetallized region on the external surface functions to segregate the two electrodes by the piezoelectric material (Figure 3.6). To facilitate connection, slender gauge wires are soldered to the peripheral electrode and the wrap-around portion of the internal one. These wires, loosely intertwined, are housed in a connector that is connected to the output cable of the MicroFab's JetDrive^{TM} electronics system. In this thesis, the Microfab dispensing device selected was the MJ-AT-01, which has an 80 microns nozzle diameter, as shown in **Figure 3.7**.

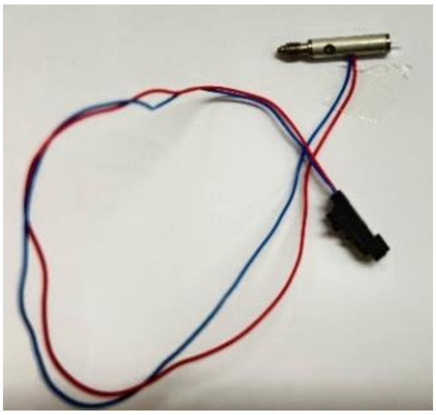

Figure 3.7 Print head with wires and connector.

3.4 EHD printing system

Here the EHD printing system that was constructed in-house is discussed, with particular emphasis on the assembly process and subsequent optimization strategies. In our bid to enhance automation, a thermal controller and position controller have been incorporated into the system. The addition of these features not only enhances the system's performance but also optimizes its efficacy.

3.4.1 Design of the EHD printing system

The EHD printing system, co-developed with a senior group member, comprises key elements that collectively enable a high-precision and high-efficiency fabrication processes. A schematic diagram of the system is shown in **Figure 3.8**. The crux of the EHD printing system revolves around the interaction between the nozzle and the substrate. The design of this arrangement caters to the generation of the electric field, which is imperative for the droplet ejection process.

A function generator serves as the source of electric signals for this operation. These signals require amplification, achieved via a 1000× amplifier working in conjunction with a high voltage power supply, to yield an electric field of sufficient magnitude. The applied electric field is visually represented on an oscilloscope for verification against the prescribed parameters, ensuring the exactitude of the electric field application between the nozzle and the substrate. A syringe pump furnishes the requisite back pressure, prompting the ejection of the print material through the nozzle.

Finally, a high-speed camera monitors the droplet formation process in detail, functioning under the radiance of a dedicated light source to capture the key aspects of the process. A distinguishing feature of our EHD printing system lies in its ability to handle dynamic printing processes. Before printing, the nozzle is adjusted in the z-direction to establish an optimal position for printing. However, once printing commences, the nozzle remains static while the two-directional translation stage manipulates the substrate, facilitating the creation of complex droplet arrays and patterns.

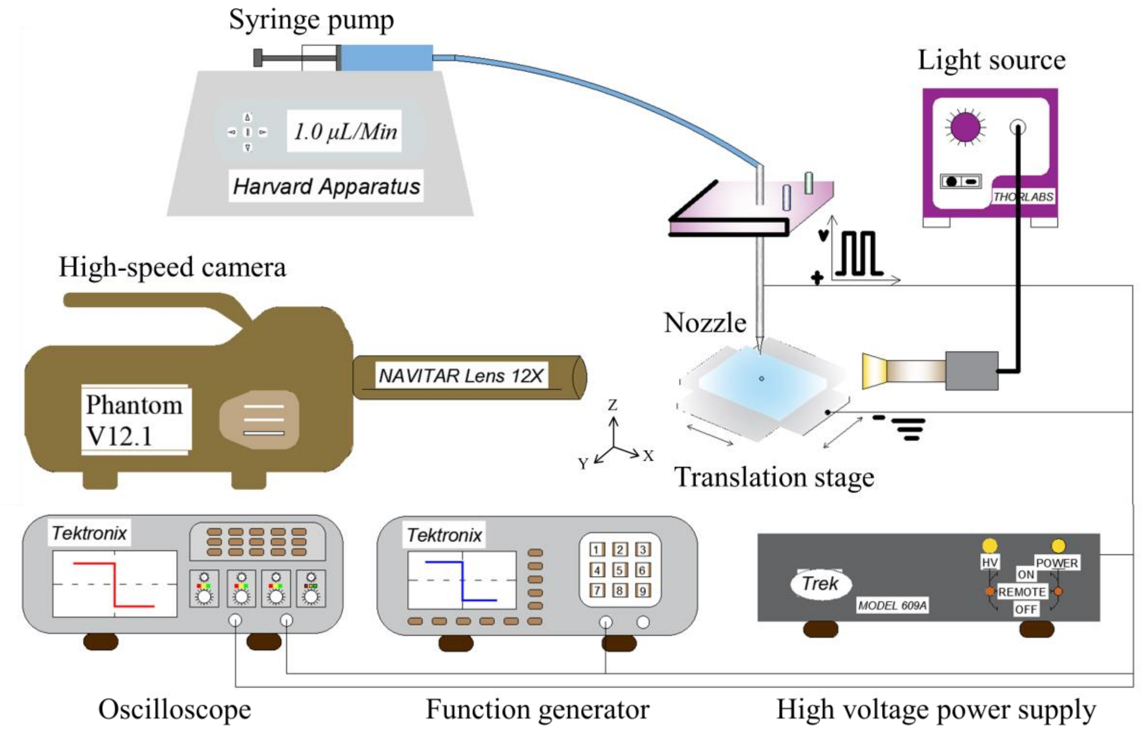

Figure 3.8 Pictorial representation of the EHD Printing system developed in-house. In the EHD printing process, two types of nozzles were utilized. For the metal nozzle, the distance between the nozzle and the substrate was approximately 500 µm, whereas for the glass nozzle, the distance was around 100 µm. The variation in distance is due to the significant influence of the nozzle's outer diameter on the shape of the Taylor cone formed during printing. The nozzle-to-substrate distance must be sufficient to ensure proper Taylor cone formation.

Figure 3.9 illustrates the actual assembly deployed in our study. Two MT1-Z8 Thorlabs translation stages were utilized, allowing bi-directional (*x* and *y*) movement spanning a range of 12 mm × 12 mm. These translation stages were managed by a standalone motion controller (KDC101 Thorlabs) which was computer interfaced. This controller provided diverse operation modes, enabling both the activation of the translation stage and the transmission of an output signal to the function generator for external input. Upon reception of this signal, the function generator (AFG 2021 Tektronix) produced and transmitted a pre-defined wave signal to the amplifier, thereby initiating the application of an electric field between the nozzle and the substrate. The amplifier (Trek 609A) was capable of magnifying the input signal a thousand-fold, thereby facilitating an output range of 0 – 10 kV. The resultant output signal can be visualized and analysed using an oscilloscope (TBS 1000C Tektronix), ensuring the fidelity of the signal amplification process.

The substrate was positioned on a silver sheet measuring 61 mm × 61 mm × 3 mm, connected to the ground. This silver sheet, in turn, was affixed to the translation stage with an interposed insulator, a 3D printed plastic block with the same dimensions and a thickness of 6 mm. The vertical (z-direction) movement of the nozzle was managed via a manual translation stage (PT1 Thorlabs). This precise control mechanism ensured the optimal positioning of the nozzle for efficient and high-quality printing outcomes. The nozzle holder was also fabricated with a 3D printer.

During the printing process, the LC was contained in the glass tip, the specifics of which will be described in the following part of this chapter. To ensure efficient usage of the material, only a modest quantity was loaded into the nozzle. A PTFE microbore tubing linked the glass tip to a 100 ml plastic syringe that functions as an ink reservoir. This plastic syringe was mounted onto a syringe pump (PHD-70-3009, Harvard apparatus), where its plunger was designed to move inside the syringe, inducing a push-pull action on the ink within the tubing. As a result, the LC ink was successfully drawn from the nozzle, offering a controllable, efficient, and wastage-minimizing mechanism for the printing process.

A high-speed camera (Phantom V12.1) was used for the visualization of the droplet formation process with the shadowgraph method. The shadowgraph technique is an elegant optical method employed to elucidate flow characteristics in transparent media. This approach capitalizes on refractive index variations within the fluidic environment, which subsequently results in slight deviations in light direction, thereby engendering observable shadows. In a typical shadowgraph configuration, a point light source is directed through the fluid medium of interest. Fluctuations in refractive index, instigated by temperature or density gradients, precipitate light refraction. The consequential pattern of alternating light and dark regions, colloquially referred to as "shadows," is then captured by an imaging device - in this context, the high-speed camera. The utility of this method lies in its ability to offer a granular visualization of the droplet formation process. The differential light intensities registered by the high-speed camera correlate directly with the various stages of the LC droplet formation, providing insights into the EHD printing process.

The components were mounted on a honeycomb-style optical breadboard with a substantial thickness of 60 mm. This breadboard was positioned on vibration-damping legs, atop a sturdy wooden laboratory bench, to mitigate any vibrational disturbances that might potentially interfere with the accuracy of the printing process. Safety was of paramount consideration in this system. All components were securely attached using plastic sheets that functioned as insulators, reducing the risk of accidental electrical discharge. Moreover, complete insulation was applied to all wires, eliminating the possibility of inadvertent electrical contact and enhancing the overall safety of the experiment. To further bolster the safety measures, we employed plastic washers for all mounting needs and grounded the optical table to safely disperse any residual electrical charge. This attention to safety ensured a robust, reliable, and secure environment for the implementation of our EHD printing process.

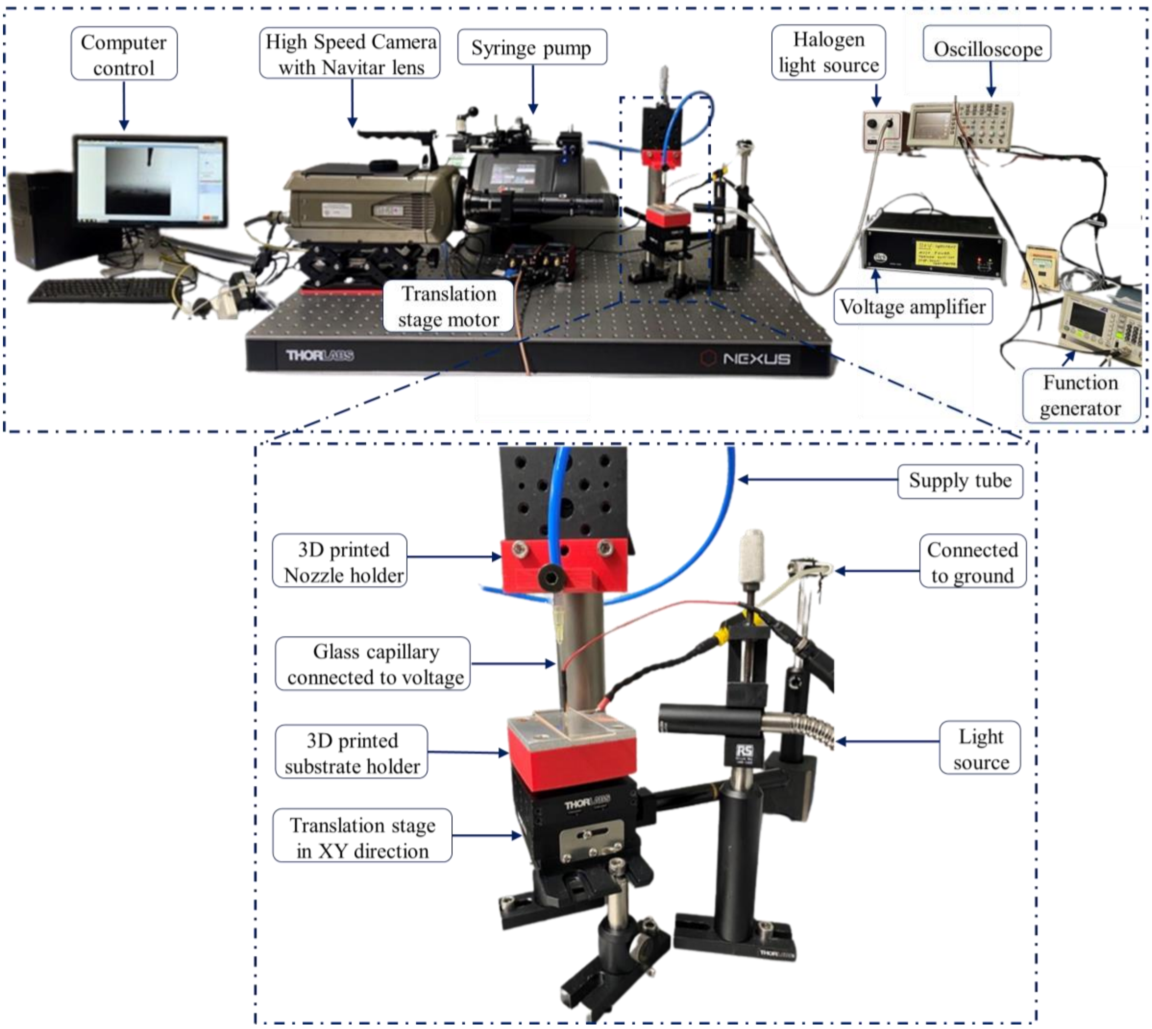

Figure 3.9 The EHD printing system built within the group. All the components used are labelled in the figure. The printing system comprised of three primary components: the printing module, the visualization module, and the electric field application module.

3.4.2 EHD Printheads

This EHD printing system employed two primary printheads: a glass capillary nozzle (TIP1TW1-L, World Precision Instruments) and a metal nozzle, each presenting its distinct advantages and potential drawbacks. The glass capillary nozzle allows a broad spectrum of inner diameter selections, enabling substantial versatility in droplet size manipulation. In the context of this thesis, a diameter of 1 μm was utilized. A challenge to consider when using the glass capillary nozzle, however, lies in its non-conductive nature, necessitating additional procedures as it must interface with the electric field. Conversely, the metal nozzle offers inherent conductivity, ensuring a direct, efficient connection to the electric field. However, this option presents limitations in the minimum attainable inner diameter, which at 159 μm, exceeds that of the glass capillary nozzle and consequently results in larger printed LC droplets. The outer diameter of the metal nozzle was 312 μm. Ultimately, the choice of nozzle depended on the requirements of the specific application, balancing droplet size, conductivity, and the need for additional treatment procedures.

As depicted in **Figure 3.10**(a), we utilized glass capillary nozzles acquired from World Precision Instruments (TIP1TW1-L) in our printing system. These nozzles possess an internal diameter (ID) ranging from 0.1 to 10 µm, efficiently catering to a multitude of printing requirements. For our research, we specifically selected a glass capillary nozzle with an ID of 1 µm. A noteworthy feature of these nozzles is their Luer lock fitting, a standard design feature enabling integration with a variety of syringe types and barrels. This attribute contributes to the system's operational flexibility, thus enabling the fulfilment of diverse printing needs.

To render these nozzles compatible with our printing system, we employed an electric connection treatment, facilitated by copper tape. This configuration is also illustrated in Figure 3.10 (b). The selection of copper tape as a conductive material to assist with the generation of the electric field was primarily driven by its ease of use and effective performance. Previous attempts to utilize an evaporation process for coating the glass capillary with a thin layer of metal proved to be suboptimal. Given the fragility of the glass nozzle, the process often led to irregular heating, resulting in the destruction of the glass nozzle. Copper tape application, however, is a straightforward procedure that does not subject the glass capillary to any significant stress or strain. It involves cutting a small segment of the tape and adhering it to the exterior of the glass capillary. Following this, a suitable sleeve was selected to fit over the copper tape-clad glass nozzle. Subsequently, the sleeve ias melted to secure its firm adhesion to the nozzle, thereby serving a dual role: insulating the nozzle and holding the copper tape in place. The copper tape wass then linked to a connector using a conductive wire. The final setup of the treated glass capillary nozzle is illustrated in Figure 3.10 (c). The glass capillaries exhibit an outer to inner diameter ratio of 1.33:1, as per the supplier's specifications.

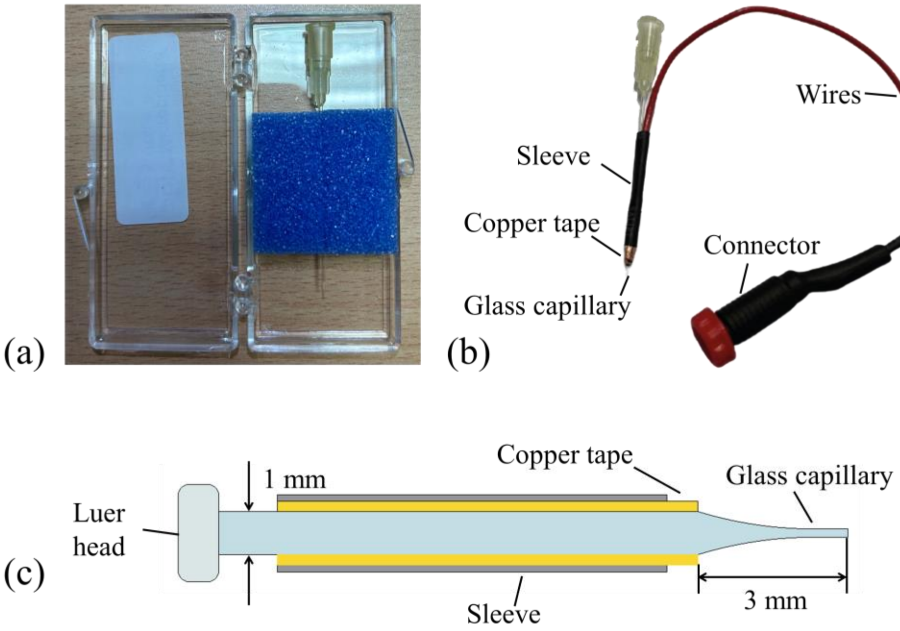

Figure 3.10 The EHD printing nozzle. (a) a depiction of the glass capillary nozzle, (b) an image showcasing the printing nozzle covered with copper tape for added functionality, and (c) an illustration of the dimensions and scale of the glass capillary.

Figure 3.11 shows examples of LC droplets printed utilizing a glass capillary. The smallest observed droplet diameter approximates to around 1 µm. Nonetheless, an increase in droplet diameter was observed in specific instances. This variation can be attributed to the simultaneous deposition of multiple droplets at the same location, or changes in printing parameters, such as the electric field intensity between the nozzle and the substrate. Figure 3.11 demonstrates the variation in the diameter of LC droplets, all printed using an identical glass capillary but under varying printing conditions. These observations highlight the capability of the EHD printing system to easily modulate the diameter of LC droplets.

Shadowgraph images of the printing process involving a glass capillary nozzle are depicted in **Figure 3.12**. Even with the aid of a 10× microscope lens, the small diameter of the nozzle makes the visualization of Taylor cone formation during the printing process challenging. The high-speed camera was only partially successful in detecting the printed droplets deposited on the substrate. Therefore, an alternative approach was adopted to confirm the efficacy of the printing process. Instead of direct observation of the nozzle, we fine-tuned the input waveform parameters while translating the printhead over the substrate. Subsequently, an optical microscope was employed to inspect the morphology of the printed droplets. This approach proved instrumental in ensuring accurate control over the printing process, overcoming the observation difficulties imposed by the minuscule nozzle and droplet dimensions.

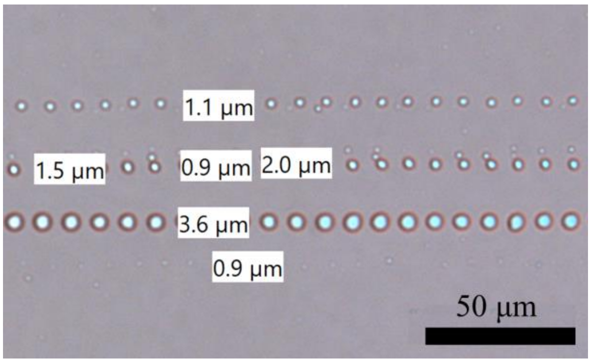

Figure 3.11 Printed LC droplets with different diameters (0.9 µm, 1.1 µm, 1.5 µm, 2 µm and 3.6 µm) printed using the EHD system.

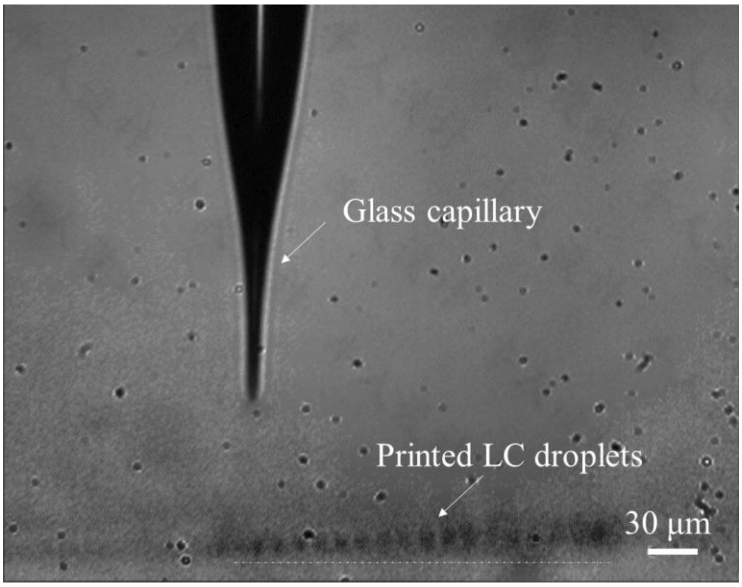

Figure 3.12 Shadowgraph image of the EHD printing process with a 1 µm inner diameter glass capillary.

In terms of the metal nozzle, we selected one with a Luer lock for enhanced system adaptability, since the system was designed with a holder compatible with the Luer lock mechanism facilitating easy compatibility with various nozzle types. These metal nozzles are part of a standardized series, their dimensions specified by a gauge value. According to this system, a higher gauge value corresponds to smaller inner and outer diameters. Specifically, we employed a 30G precision general purpose tip boasting an inner diameter of 250 μm and an outer diameter of 305 μm. Notably, this nozzle demonstrates superior conductivity compared to its glass capillary counterpart. The same method was employed in terms of combining copper tape for conductivity and insulator tape for electrical isolation. **Figure 3.13** presents the structure of the metal nozzle, including an optical microscope image and a photograph depicting the nozzle after the electric wire attachment. This arrangement allows for the interchange of nozzles as per specific printing requirements.

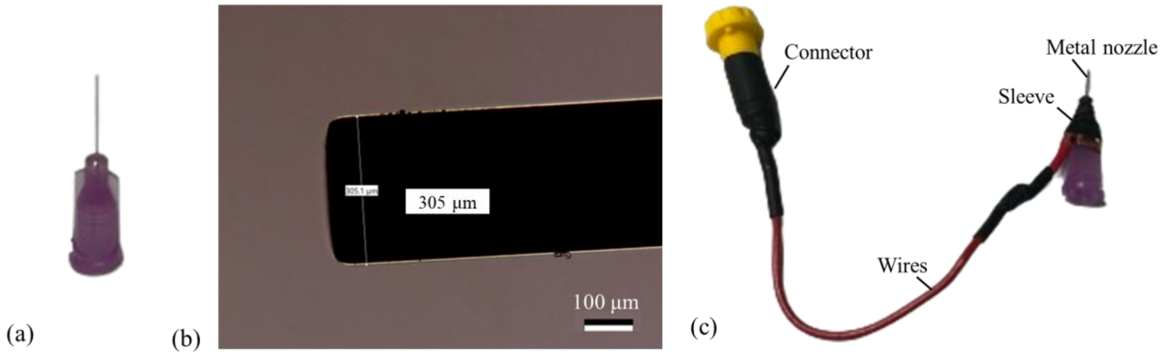

Figure 3.13 (a) Image of the metal nozzle used in the EHD printing process. (b) The metal nozzle viewed on a microscope with an outer diameter of 305 μm. (c) The metal nozzle with electric wire attachment.

Figure 3.14 shows representative shadowgraph images recorded during the printing process utilizing a metal nozzle. The notably larger diameter of the metal nozzle compared to the glass capillary enables a clear observation of droplet formation throughout the process. Initially, the syringe pump propels the material, causing it to protrude from the nozzle and form a meniscus at its tip. Following this, a suitably configured electric field was established between the nozzle and the substrate, inciting the meniscus to undergo morphological changes.

With the sustained application of the voltage, the meniscus distorts into a characteristic 'Taylor cone' shape. The apex of the emerging material becomes progressively narrower. Under the influence of the electric field, the elongating fluid filament 'grows' towards the glass substrate, maintaining its shape due to a balance between the applied electric field's force and the fluid's surface tension. The continuous supply of fluid from the syringe pump sustains this growth. Upon the removal of the electric field, the majority of the material retracts back into the nozzle due to surface tension forces overtaking the dissipating electrostatic forces. A minuscule quantity of the material, however, remains adhered to the glass substrate, forming a printed LC droplet. This withdrawal and deposition process fine-tunes the droplet's size and shape, contributing to precise control over the printed droplet characteristics. Therefore, an understanding of the Taylor cone formation and the interplay between electric and surface tension forces is critical to manipulating the droplet formation process to meet specific printing requirements in the device fabrication process.

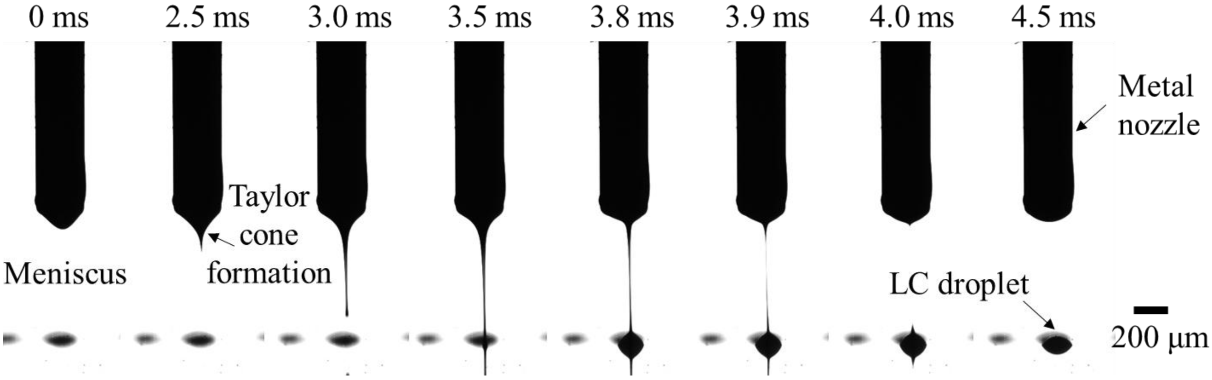

Figure 3.14 Example high-speed shadowgraph images of the EHD printing procedure with a metal nozzle. The distance between the metal nozzle and the substrate is around 500 μm. The voltage pulse is applied at around 2 ms and removed after 3.8 ms.

3.4.3 Thermal control

As described in Chapter 2, temperature profoundly impacts the LC mixture's state, particularly its viscosity, a critical parameter in the EHD printing process. Specifically, the employed LC mixture in this study, E7, undergoes a transition from a nematic phase to an isotropic liquid phase when the temperature exceeds 60°C[58]. Consequently, the integration of thermal control module into the EHD printing system becomes imperative to enhance the system's performance.

The thermal control module primarily involves three components: a cartridge heater (SKU: C-HEAT-12V 40W Cartridge Heater), a sensor cartridge (SKU: HE-E3D-PT100), and a controller board (SKU: RAMPS-S-MEGA2560). To ensure efficient heat transfer to the LC mixture, the module was engineered to heat the nozzle via the cartridge heater. However, this setup presents a challenge, as the initial nozzle holder was fabricated from plastic to attain maximal electrical insulation. Consequently, the transition to a metal nozzle holder, given its superior thermal conductivity, was necessitated. This switch to a metallic holder enabled efficient and rapid heating of the nozzle, enhancing the EHD printing system's overall effectiveness and performance.

Constructing the entirety of the nozzle holder from metal, while advantageous from a heat transfer perspective, invites potential hazards due to the high electric field present in the system. Thus, it became imperative to minimize this risk by limiting the contact area made of metal to what is strictly necessary for effective thermal conductivity.

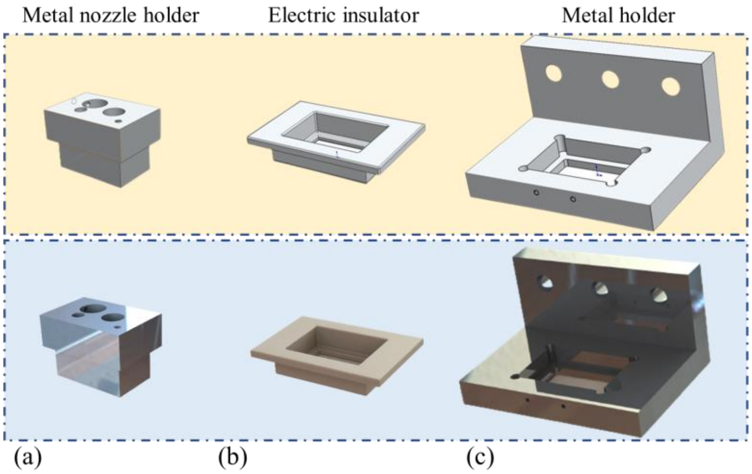

Figure 3.15 The separate components of the optimized nozzle holder. (a) the metal nozzle holder for the convenient generation of the electric field and the heating transfer. (b) the electric insulator between two metal holders. (c) the metal holder for the secure positioning of the nozzle.

While a fully plastic composition for the remaining parts of the holder ensures electrical insulation, it could compromise the mechanical robustness required to stably support the nozzle holder. This shortcoming could result in severe deformation during the heating process, adversely affecting the distance between the nozzle and the substrate during printing. Any changes in this distance could alter the electric field established between them, impacting the diameter of the printed droplets and ultimately compromising the quality of printing. Addressing these challenges required a balanced approach. Consequently, the final design of the nozzle holder comprises three components (**Figure 3.15**): a metal part that facilitates excellent thermal conduction; a plastic element serving as an electrical insulator; and a final metallic component to provide robust mechanical strength. This structure ensures optimal heat transfer, sufficient electrical isolation, and the necessary structural integrity, mitigating the risk of deformation during heating that could disrupt the printing process. **Figure 3.16** presents an overview of our optimized thermal control module. This assembly incorporates the cartridge heater, sensor cartridge, and nozzle, each precisely fitted into the holder. We've tailored this setup specifically for metal nozzles, as the inherent fragility of glass capillary nozzles and the difficulty in inserting them into the small opening of the holder preclude their use. In operation, both the cartridge heater and the sensor cartridge interface with a central control unit — a computer-regulated RAMPS 1.4 Controller Board. This vital component of the thermal control module was responsible for regulating the system's temperature. The interaction between the controller board, the cartridge heater, and the sensor cartridge formed a feedback control loop that maintained the nozzle's temperature within a predetermined range. The cartridge heater, under the control of the RAMPS 1.4 Controller Board, supplied the necessary heat to the nozzle. Concurrently, the sensor cartridge, functioning as a temperature sensor, monitored the nozzle's temperature and relayed this data back to the controller board. In this process, the controller board adjusts the power supply to the cartridge heater, thereby achieving precise temperature control. This temperature regulation process was pivotal in scenarios demanding temperature control, such as the transformation from LC phase to isotropic phase — a critical element of our printing process.

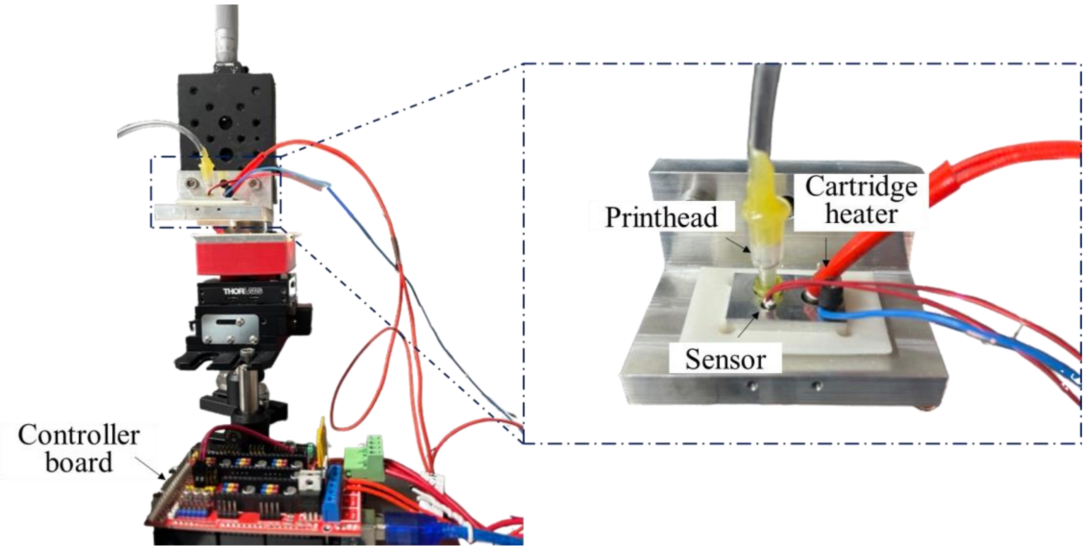

Figure 3.16 Photograph of the optimized thermal control module composed of a cartridge heater, a sensor and a controller board.

Figure 3.17 presents comparative results of LC droplet printing, both with and without the integration of the thermal control module. The significant alteration in the diameter of the printed LC droplets underscores the influential role of the thermal control module. This module allows EHD printing to produce a wider range of droplet sizes, without necessitating modifications of other experimental conditions, such as nozzle dimensions or established printing parameters. Thus, the thermal control module served as a crucial tool for enhancing the versatility and adaptability of EHD printing system. The initial sequence of printed LC droplets was produced using the thermal control module, resulting in a diameter of approximately 125 μm. In contrast, the subsequent series, printed without the thermal control module, exhibited a larger diameter of around 260 μm. Both sequences were printed using the same metal printing nozzle. The significant change in droplet sizes between the two processes demonstrates the substantial impact of the thermal control module on the dimensions of printed LC materials. This capability enables the production of smaller LC droplets without necessitating alterations to the size of the metal nozzle.

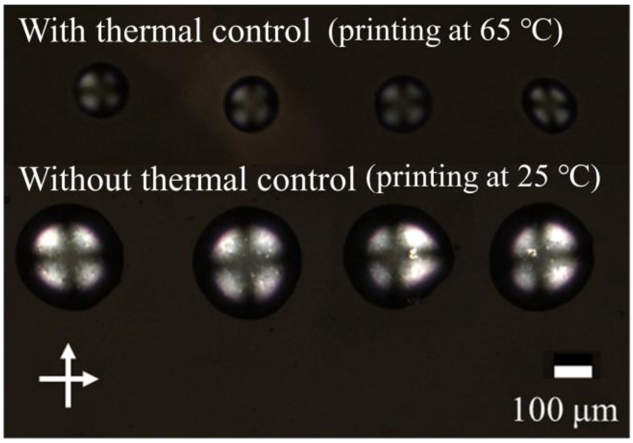

Figure 3.17 Printed LC droplets with and without the thermal control module viewed on a microscope with crossed polarizers. The first row is the printing results with a thermal control module with the diameter of the printed LC droplets of around 125 μm. The second row is the printing results without a thermal control module with a diameter of approximately 260 μm.

3.4.4 Automatic position control

In our initial setup, we could link two motors to a computer and use the software provided by Thorlabs to regulate the motion of the translation stage. Despite its capabilities, this approach primarily facilitated the automatic printing of arrays or the manual crafting of simple patterns. However, for a more intricate and precise pattern generation, an automated control system was highly desirable. To address this need, we incorporated AutoCAD software into our setup. The appeal of AutoCAD lies in its capability to generate .dxf files, a format that defines complex geometric patterns with high fidelity. These .dxf files can be seamlessly imported into MATLAB, where a dedicated script reads the file and instructs the translation stage to move according to the pre-set pattern defined within the file as **Figure 3.18** shows.

In the process, MATLAB could read the lines, polygon lines, circles, arcs and points forming different shapes. By parsing the coordinate information of the vertices, starting points, endpoints, and radii of these shapes contained in the pattern and storing it, the used Thorlab motor was then identified and connected by the MATLAB program through its serial number. The position information stored above was sent to the motor to move it according to the set pattern. However, due to the movement limitations of our translation stage (12 mm in each direction), the pattern needs to be designed within a 12 mm × 12 mm square area. This approach enhances the precision and complexity of patterns that can be generated by our system, marking a significant upgrade from the manual and semi-automatic methods previously utilized.

Figure 3.18 Printed nematic LC droplets of ‘OXFORD’ characters with the modified automatic position control in the EHD printing system.

3.5 Summary

In conclusion, this chapter outlined the essential experimental procedures integral to this thesis, providing a detailed examination of the preparation and analysis of LC samples, and the implementation of two key printing technologies—inkjet and EHD printing. The unique features and capabilities of the two inkjet printing systems, the bespoke system and the commercial Microfab JetlabII, have been considered. Furthermore, the construction and progressive enhancement of an EHD printing system capable of effectively printing LC droplets has been described. The developments of temperature and positional control modules have notably extended the capabilities of this system. By detailing these procedures, this chapter lays the foundation for the ensuing investigation into the innovative applications of these technologies in the fabrication of optical devices.

CHAPTER 4: Modelling of Liquid Crystal Printing Processes

In this chapter, we will delve into the modelling of liquid crystal (LC) printing procedures, encompassing both the inkjet printing and Electrohydrodynamic (EHD) printing processes, employing the COMSOL Multiphysics software for simulation and analysis. COMSOL Multiphysics is a versatile simulation software package designed for modelling complex physics-based systems across multiple disciplines [59]. Its strength lies in its ability to handle simultaneous interactions of different physical phenomena, enabling realistic modelling of real-world systems. With modules dedicated to various applications, from acoustics [60-63] to heat transfer [64-66], robust geometry creation [67-68] and meshing capabilities, it offers a flexible, tailored approach to diverse simulation needs. Additionally, its interoperability with other software, parameterized modelling, and optimization capabilities enhances its value for both academic and industrial settings.

4.1 The COMSOL model

Presented in this chapter is the application of four key modules from the extensive suite within COMSOL Multiphysics: the Electrostatics, Laminar Flow, Level Set, and Multiphysics modules. Primarily, the Electrostatics model [69-71], a critical component of the Electric Currents interface, is employed to explore and simulate static electric fields where the charge movement is typically negligible. This module is indispensable in analyzing components such as capacitors [72-74], insulators [75-77], MEMS [78-81], and electrostatic actuators [82-84], and permits efficient computation of quantities like the electric potential distribution, electric field strength, and electric displacement. In the thesis, this module is utilized to establish an electric field between the nozzle and the substrate within the EHD simulation process.

Secondly, the Laminar Flow module is also used [85-86], which has been designed to model and scrutinize fluid flow situations characterized by steady, slow flow and low Reynolds number. This scenario emerges when viscous forces dominate, rendering turbulence negligible. The module facilitates the analysis of various laminar flow facets, including creeping flows, Stokes flow, and Hele-Shaw flows. Its applications are diverse, ranging from microfluidic device design [87-89] to studying biomedical flows in minuscule blood vessels [90]. In our context, we deploy this module to categorize the properties of the LC as a fluid and to apply a volume force.

Following this, the Level Set module is then used [91-94], which is a crucial tool in COMSOL for monitoring the progression of interfaces, boundaries, or fronts in spatial models, irrespective of their dimensionality. This proves especially beneficial when the location of the interface is undefined beforehand. The module caters to problems involving two-phase flow, phase transitions, and the spread of species, chemicals, or populations. It also affords the flexibility to combine with other physics models to tackle complex Multiphysics simulations such as fluid-structure interaction and mass transfer across interfaces. In our case, we employ this module to define the interface between the LC and air.

Lastly, we incorporate the Multiphysics module [95], a foundational component of COMSOL, which facilitates the coupling of multiple physical phenomena to emulate real-world systems with high fidelity. This model supports both predefined Multiphysics interfaces and user-defined ones, offering flexibility in modelling. The module aids in the resolution of complex physics scenarios involving not only fluid dynamics, acoustics, electromagnetism, and heat transfer, but also others. By providing a holistic view of the system under investigation, it is used across diverse sectors, spanning from bioengineering[96-98] and chemical engineering[99-100] to geophysics[101] and microelectronics[102-103].

In this chapter, I implement a unified model of the above to simulate both EHD and inkjet printing techniques, distinguished only by their initial conditions for the velocity and voltage pulses used in this study. Within the EHD printing framework, an initial velocity pulse is deployed, succeeded by a voltage pulse interpreted as a back pressure, a concept elaborated on in subsequent sections. On the other hand, inkjet printing simulations solely employ a velocity pulse. This nuanced alteration in the applied initial conditions confers upon our model the versatility to simulate both EHD and inkjet printing mechanisms. This approach simplifies the simulation protocol while concurrently broadening the operational scope of our model, underscoring its wide-ranging utility.

4.2 Simulations of EHD printing of nematic liquid crystals

In this system, an electric field is established between the electrode and the substrate through the electronics segment, with the capacity to design and modify pulse waves to meet our specific needs. The fluid characteristics, relating to density and dynamic viscosity, are outlined within the dimension of the laminar flow module. The Multiphysics module, which encompasses two-phase flow and the wetted wall, describes the boundary conditions and the interactions between the two phases (air and the printing material for this project).

To track the gas-liquid interface, the level set method is employed. Various interface tracing methodologies, such as Volume of Fluid (VOF) [104-106], Level Set (LS) [107-110], Front Tracking [111-112], Phase-field [113-115], and coupled Volume-of-Fluid and Level Set method (VOSET) [116-119], exist. However, only VOF and LS are supported by COMSOL, with LS being the method of choice for this simulation. The fundamental concept of LS in COMSOL is the level set function φ, which operates as a smoothed step function that holds a value of zero in one domain and one in another, as illustrated in **Figure 4.1**.

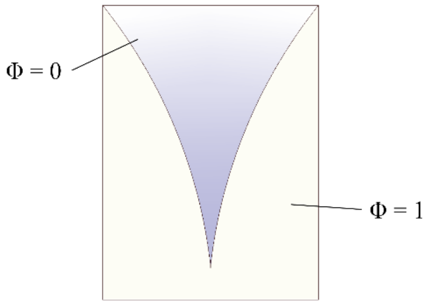

Figure 4.1 Example of the two domains divided by an interface used in the level set method.

The Level Set Model meshes with the chosen shape and each node of the shape will be added to the following equation,

$$\frac{\partial\varphi}{\partial t} + \boldsymbol{u}\cdot\nabla\varphi = \gamma\nabla\cdot\left(e\nabla\varphi - \varphi(1-\varphi)\frac{\nabla\varphi}{|\nabla\varphi|}\right) \tag{4.1}$$

where $\boldsymbol{u}$ is the velocity field, γ is the reinitialization parameter, and e is the parameter controlling the interface thickness where φ changes smoothly from zero to one.

4.2.1 Simulation process

Our simulation approach draws upon established EHD and inkjet printing models sourced from the COMSOL application gallery. These models have been examined and refined to construct our model. In terms of the electrostatic field, our assumption centres on the concentration of charge at the gas-liquid interface. The dispersion of the electric field can then be represented by the subsequent equations,

$$\nabla^2 V = 0 \tag{4.2}$$

$$E = -\nabla V \tag{4.3}$$

$$\nabla\cdot D = \rho_f \tag{4.4}$$

$$D = \varepsilon_0\varepsilon_r E \tag{4.5}$$

In the defined simulation parameters, the electric potential is represented by V, the electric field strength is conveyed by E, the electric displacement field is indicated by D and ρ_f is the charge density. Furthermore, ε_0 denotes the vacuum permittivity, and ε_r corresponds to the permittivity specific to the liquid in question. During our simulation procedures, we have elected to assign a zero-value electric potential to the substrate, whilst attributing a potential of V_0 to the electrode, a value which remains subject to modification in different conditions.

Embedded within the laminar flow model, the Navier-Stokes equation effectively characterizes the dynamics of incompressible fluids. This governing equation encapsulates an array of influential forces; from inertial to pressure forces, from viscous to gravitational forces, and extends to other extrinsic factors such as the volumetric force,

$$\rho(u \cdot \nabla)u = \nabla \cdot \left[-\rho I + \mu(\nabla u + (\nabla u)^T)\right] + F + \rho g \tag{4.6}$$

In this context, 'u' represents velocity, which can be defined with differing magnitudes and forms according to the user's requirements. The term ρ denotes the density of the fluid, user-specified to match the real-world conditions of the system under study. The symbol I stands for the identity matrix, while F signifies the volume force. Given the two-phase nature of the simulation process, variations in viscosity and density across each discrete mesh element are accounted for by the following expressions:

$$\rho = \rho_1 + (\rho_2 - \rho_1)\phi \tag{4.7}$$

$$\mu = \mu_1 + (\mu_2 - \mu_1)\phi \tag{4.8}$$

In the scenario presented, the overall density is denoted by ρ, with ρ_1 and ρ_2 representing the individual densities of the two phases respectively. The total viscosity is represented by μ, while μ_1 and μ_2 indicate the respective viscosities of each phase. The value of ϕ fluctuates depending on the position within the meshed structure, with particular importance in the transition area.

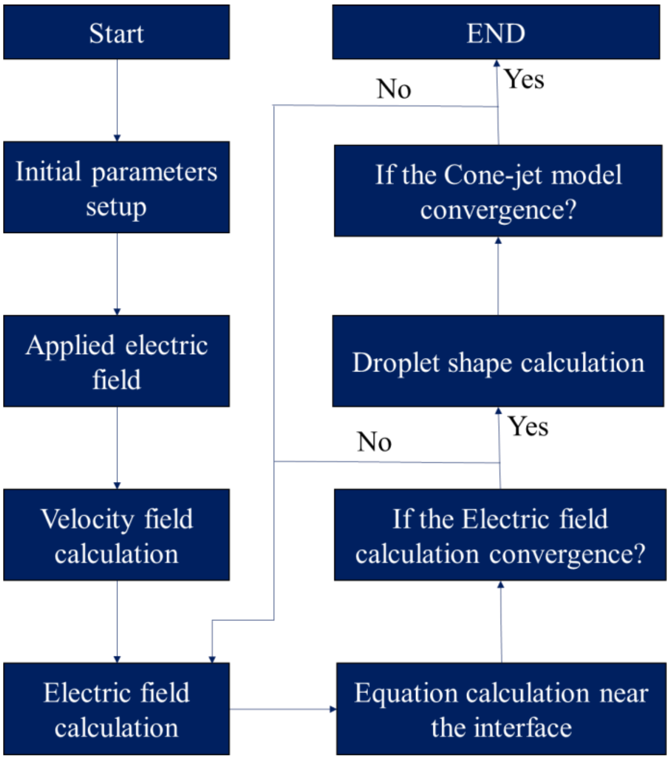

Figure 4.2 Flow chart of the EHD simulation process.

The simulation procedure is visualized in **Figure 4.2**, with a rudimentary model depicted in **Figure 4.3** being employed. The initial delineation of parameters, including geometric and physical attributes needs to be considered in advance. Once these are defined, the module's geometry was carefully crafted to reflect these parameters, simultaneously establishing the electric field. Then, in this initial calculation phase, the velocity field was the primary focus, with the material's initial velocity being applied to simulate the back pressure experienced in the authentic printing process. As a direct consequence of this, the material was thrust out from the nozzle, resulting in the formation of a meniscus at its tip. This forms the basis for the subsequent electric field computation, which ensues only after the velocity calculations have been performed.

A unique feature of this simulation is the utilization of adaptive meshing methodology, capable of accommodating different mesh sizes across varying regions. This nuanced approach allows for localized refinement of the mesh in areas of key interest, ultimately yielding a solution of higher precision without unduly burdening the computational resources, which would be the case with a uniformly fine mesh across the whole computation domain. Specifically, a finer mesh was deployed in the interfacial area between the liquid and air, a choice that necessitates a greater computation time. In contrast, for regions predominantly occupied by air, a coarser mesh suffices.

In recognition of the critical role played by the calculations in the interfacial area, a convergence check was implemented after these computations. Should convergence remain elusive, the electric field parameters and mesh sizes were revisited, and tweaked as necessary, and the calculations repeated until the desired convergence was achieved. This checkpoint sets the stage for the subsequent step - the evaluation of the droplet shape. A second layer of quality control was implemented in the form of a convergence test on the cone-jet model. If this fails to achieve convergence, a similar process of parameter adjustment within the electric field was initiated, with subsequent steps iteratively repeated until the process in its entirety converges.

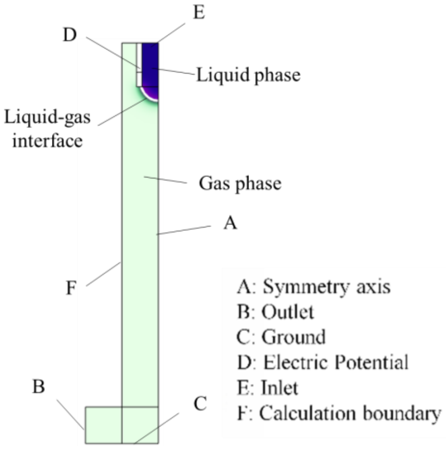

Figure 4.3 The simulation model and the boundary conditions.

While this simulation process involves myriad adjustments, its strengths lie in its relative speed and convenience. The boundary conditions associated with this model are documented in **Table 4.1**. Here, ϕ represents the electrical potential within the electrostatic field. V_0 corresponds to the user-defined initial voltage applied to the electrode, and u signifies the velocity of the liquid.

Table 4.1 Boundary conditions of the electrostatic field and laminar flow field.

Physical field / **boundary**	**Electrostatic**	**Laminar Flow**
B: outlet	Zero charge	$P = 0\ Pa$
C: Ground	$\Phi = 0\ (V)$	$u = 0\ (m/s)$
D: voltage applied	$\Phi = V_0\ (V)$	$u = 0\ (m/s)$
E: inlet	$\Phi = V_0\ (V)$	$u = u_0\ (m/s)$
F: Calculation of boundary	$\Phi = V\ (V)$	$P = 0\ Pa$

Recognizing the highly symmetric nature of our simulation model, we strategically optimized our computational resources by simulating only half of the model in a 2D format. This approach effectively curtails simulation time while retaining the model's essential characteristics. Upon the culmination of the simulation process, the computation results can be visualized both in 2D and 3D forms. The 2D model, depicted in Figure 4.3, defines distinct phases and regions for clarity. The dark blue area signifies the LC material, primed for printing and annotated as the liquid phase within the model. In contrast, the light green region represents the air, indicated as the gas phase in the model. The figure also marks the interface, the crucial boundary between the liquid and gas phases. The white segment within the figure represents the outer wall of the glass nozzle.

In the simulation, we aim to reproduce the dimensions observed in the actual printing process to ensure a high degree of fidelity. The inner diameter of the glass capillary nozzle in the simulation matches the 1 μm diameter utilized in practice. Likewise, the distance separating the tip of the nozzle from the substrate is replicated in the simulation at 11 μm. Given an applied voltage of 0.1 kV, the resulting electric field was approximately 9.1 V/μm. In addition, we also incorporated the material properties of the LC and air into the simulation, as elaborated in **Table 4.2**. Since our simulation focuses solely on electrostatics and the liquid laminar flow field, the critical parameters employed are the density, viscosity, and relative permittivity of each material, along with the surface tension. These carefully selected parameters ensure our simulation accurately captures the physical process of our EHD printing process. One thing to mention is that, in this EHD simulation, a relative permittivity of 18.9 was chosen for the liquid crystal material. This selection is based on the dielectric properties of liquid crystals, such as E7, under specific alignment states. During the EHD printing process, the applied electric field causes the director of E7 to align predominantly along the field direction. Under these conditions, the relative permittivity should reflect the dielectric constant when the long axis of the E7 molecules is parallel to the electric field.

For the boundary conditions, specific boundary conditions were assigned to facilitate an accurate emulation of the actual experimental system. Here, the boundary E is designated as the inlet, where the source material enters our computational domain, reflecting the real-world role of the glass capillary nozzle. To replicate the application of a voltage, we apply it to the upper region of boundary D, simulating the copper tape's function attached to the nozzle with a certain offset from its tip. Further, boundary C corresponds to the ground terminal in the electrostatic field, essentially functioning as the reference point for our voltage measurements. Boundary B is designated as the outlet, serving as the point where the fluid can exit our computational domain, effectively simulating the fluid's ejection onto the substrate in the physical process. Lastly, F delineates the computational boundary, enclosing the region under investigation throughout the simulation process.

Table 4.2 Simulation parameters.

Parameters	Symbols	Values	Units
Nozzle inner radius	r	*1*	μm
Voltage applied	V_0	*10000*	V
Inlet liquid velocity	v	*1.5*	m/s
Surface tension	γ	*0.0235*	N/m
Density (liquid)	ρ_l	*827*	kg/m^3
Density (air)	ρ_a	*1.25*	kg/m^3
Viscosity (liquid)	μ_l	*0.252*	$Pa{\cdot}s$
Viscosity (air)	μ_a	$2e^{-5}$	$Pa{\cdot}s$
The thickness of the level-set interface	t	$1e^{-5}$	m
Relative air permittivity	ε_a	*1*	*[1]*
Relative glass permittivity	ε_g	*5*	*[1]*
Relative liquid permittivity	ε_l	*18.9*	*[1]*

Specifically, the simulation progression was predicated upon the careful employment of velocity and voltage pulses, as illustrated in **Figure 4.4**. The initiation of the voltage pulse lags only a few microseconds behind the velocity pulse.

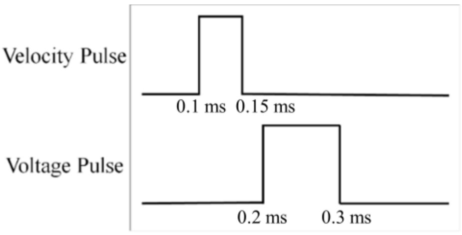

Figure 4.4 Illustration of the velocity pulse and the voltage pulse.

4.2.2 Simulation results

Using the aforementioned parameters, the resultant simulation outcomes are depicted in **Figure 4.5**. The color bar represents the volume fraction of the printed ink, distinguishing between liquid crystal and air. Dark red indicates regions dominated by liquid crystal, while blue represents air. The intermediate colors correspond to varying proportions of liquid crystal and air, reflecting the gradual transition between the two phases. This visualization is based on the level set method, which determines the interface between liquid crystal and air by evaluating their respective volume fractions.

The series of simulation images encapsulates the step-by-step evolution of a liquid meniscus into a droplet, a key stage under the application of an electric field in the process of EHD printing. Initially, the model applies a defined inlet velocity, pushing the liquid to exit the nozzle and subsequently forming a hemispherical meniscus at the nozzle's apex in the procedure. This meniscus formation is the direct outcome of an intricate balance between the exerted pressure and the intrinsic surface tension of the liquid. With the application of voltage between the nozzle and the substrate, the meniscus starts experiencing deformation due to the influence of the ensuing electrostatic field. This applied electric field competes with the surface tension, inducing the meniscus to morph into a structure referred to as a 'Taylor cone'. This conical configuration is a manifestation of the equilibrium struck between the competing electric and capillary forces. This simulation procedure models the entire course of the EHD printing process, capturing the state changes of the liquid under various external conditions. The similarity of these simulated states with the actual printing process described in Chapter 3 is evident. These similarities highlight that the simulation can serve as a useful reference for real-world experiments to a certain extent.

Hence, the simulation serves as a powerful tool for exploring the effects of various parameter adjustments on the printing process. For instance, tweaking parameters like the strength of the electric field or the distance between the nozzle tip and the substrate can provide invaluable insights into their respective impact on the printing outcome. By doing so, we can use the simulation for decision-making, informed by the understanding of the interplay between different process parameters.

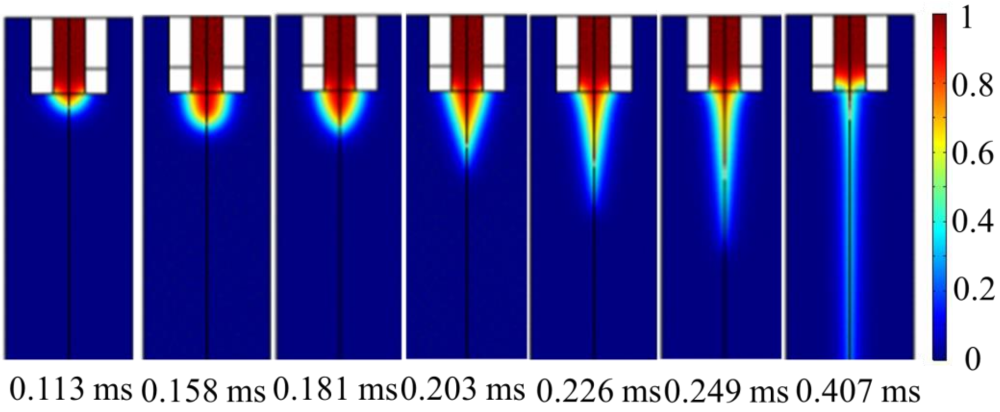

Figure 4.5 Simulation of the dynamic evolution of the droplet formation in the EHD printing model. The colour bar represents the volume fraction of the printed ink which is LC and the air.

4.2.3 Printing parameters

Initial velocity pulse

As previously noted, the initial velocity pulse serves as a surrogate for the back pressure exerted by the system, thereby implying a higher back pressure in the printing system when associated with an increased initial velocity pulse. This relationship is illustrated in **Figure 4.6**, where all other parameters, encompassing material properties and applied voltage, remain constant while the initial velocity pulse varies. Here, the top and bottom rows represent the results corresponding to initial velocity pulses of 1.5 m/s and 2.5 m/s respectively, each for a period of 0.05 ms. An observation from these results is that a higher initial velocity, signifying augmented back pressure, results in an enlarged meniscus. This simulates a heightened flow rate of the liquid that contributes to the meniscus formation. Given the same voltage pulse, the Taylor cone formed from a larger meniscus exhibits greater volume, leading to an enhanced ejection of liquid within an identical voltage pulse duration. Interestingly, this phenomenon does not influence the ultimate radius of the Taylor cone, as no discernible differences were observed. Such insights provide a valuable framework for determining the amount of back pressure to be introduced in a system during practical EHD printing processes, thereby influencing the efficiency and quality of the print.

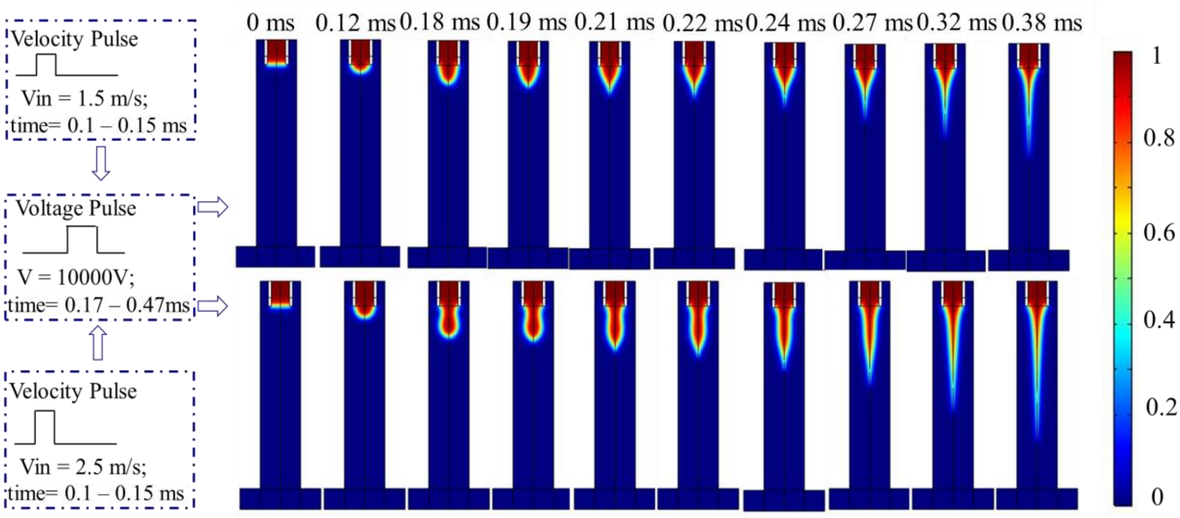

Figure 4.6 The results of the simulation with different initial velocity pulses which are 1.5 m/s and 2.5 m/s.

Applied voltage

During the printing procedure, the voltage applied between the nozzle and the substrate emerges as a vital parameter that significantly influences the outcome of the printing process. As elucidated in Figure 2.21 of Chapter 2, the applied electric field must generate a sufficient Coulomb force to dominate over the surface tension, thus reshaping the meniscus into a Taylor cone. The necessity for a particular electric field strength is profoundly dependent on the surface tension. Consequently, given a particular material property, there exists only a restricted range within which the electric field value can be varied and successful EHD printing obtained. Under such circumstances, if the applied voltage is insufficient, the ejection of the material becomes challenging. Conversely, an excessively high voltage may trigger a multi-jet mode or even cause air breakdown. Therefore, careful regulation of the applied voltage can bring forth substantial modifications in the printing process, emphasizing the critical role of this parameter in defining the final outcomes.

Figure 4.7 illustrates the impact of varying the magnitude of the applied voltage pulse, with all other simulation parameters held constant. The velocity pulse was set to 1.5 m/s for a duration of 0.05 ms. In the top row of Figure 4.7, a voltage of 10 kV is applied, spanning a 0.3 ms time frame. Conversely, the bottom row depicts the jetting process under the influence of an 18 kV applied voltage, also lasting for 0.3 ms. The displayed states at simultaneous time intervals (0 ms, 0.12 ms, 0.18 ms, 0.19 ms, and so forth up to 0.38 ms) correspond to the same elapsed time after the application of a voltage in both scenarios. One can discern that given the identical velocity pulse, a larger initial voltage applied to the meniscus formation results in a thinner Taylor cone. This outcome can be attributed to the amplified normal Coulomb force exerted on the Taylor cone with increasing voltage. A comparison of the states at 0.24 ms, 0.27 ms, 0.32 ms, and 0.38 ms under varying voltage reveals that a higher voltage not only results in a thinner Taylor cone but also promotes a more elongated material ejection, thereby accelerating droplet formation. In practical printing systems, once the operational voltage has been ascertained, minor adjustments around this value can be made to optimize printing speed and achieve desirable diameters for the printed droplets.

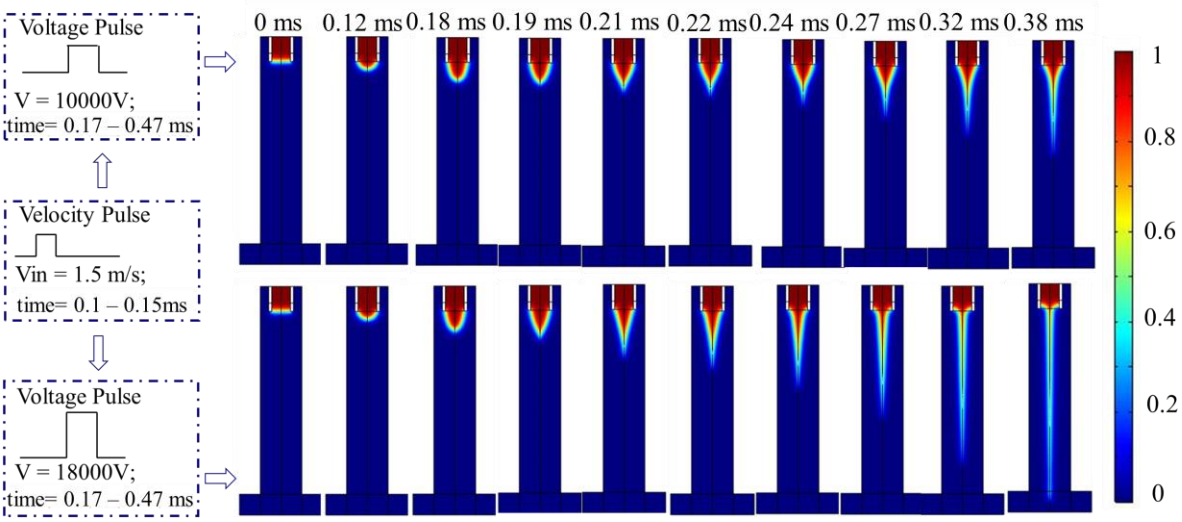

Figure 4.7 The outcomes of the simulations with distinct voltage pulses. Both simulations were conducted under identical initial velocity pulses, set at 1.5 m/s and sustained for 0.05 ms. The upper row of results presents the simulation process under the application of a 10 kV voltage pulse, sustained for a duration of

0.3 ms. In contrast, the lower row portrays the simulation process where an elevated voltage pulse of 18 kV was applied, also for a duration of 0.3 ms.

The effect of nozzle-electrode distance

Another crucial parameter that can influence the printing process is the distance between the nozzle and the electrode. However, any alteration in this distance invariably affects the electric field, making it challenging to discern whether the observed effects result from the distance variation or the consequent changes in the electric field. Therefore, to isolate the influence of distance, it becomes imperative to adjust the applied voltage such that the electric field remains constant. This adjustment ensures any changes in printing can be attributed to the distance between the nozzle and the electrode alone. To investigate the influence of the distance on the printing process, it's critical to ensure that the normal (perpendicular) Coulomb force remains constant, given its dependence on the normal electric field.

The normal electric field near the meniscus has the following relationship with the applied voltage [120],

$$E = \frac{4\,U}{d_n \ln{(8H/d_n)}} \text{ [120]} \tag{4.9}$$

Here, E denotes the electric field at the tip of the generated meniscus, U signifies the applied voltage, d_n is the nozzle diameter, and H represents the distance between the nozzle and the substrate. **Figure 4.8** illustrates the relationship between the applied voltage and the nozzle-to-substrate distance when d_n is 1 µm and E = 2938.55 V/µm.

Figure 4.9 presents simulation results where the distance between the nozzle and the substrate is varied. The top row shows the results for a distance of 10.2 µm, while the bottom row depicts the scenario when this distance was reduced to 7.2 µm. In both simulations, the initial velocity remained constant at 1.5 m/s and persists for 0.05 ms. To maintain the electric field uniformity around the meniscus upon changing the distance, the applied voltage required readjustment; hence, it decreased from 10 kV to 9.49 kV when the distance shrinks from 102 mm to 72 mm.

It is evident that the shape and diameter of the meniscus remained consistent due to the unchanged initial velocity pulse and its duration. However, when the voltage was applied, even with an identical electric field surrounding the newly formed meniscus, the volume of the ejected material increased as the distance between the nozzle and the substrate decreased. This occurrence could be attributed to the potential variations in the electric field distribution around the Taylor cone due to differing nozzle-to-substrate distances. When the gap was narrowed, the electric field discrepancy between the portion of the meniscus closer to the substrate and the portion near the tip of the nozzle intensified. Consequently, this appeared to lead to an amplified material volume being ejected from the nozzle, indicating that a reduced nozzle-to-substrate distance can result in a larger printed droplet.

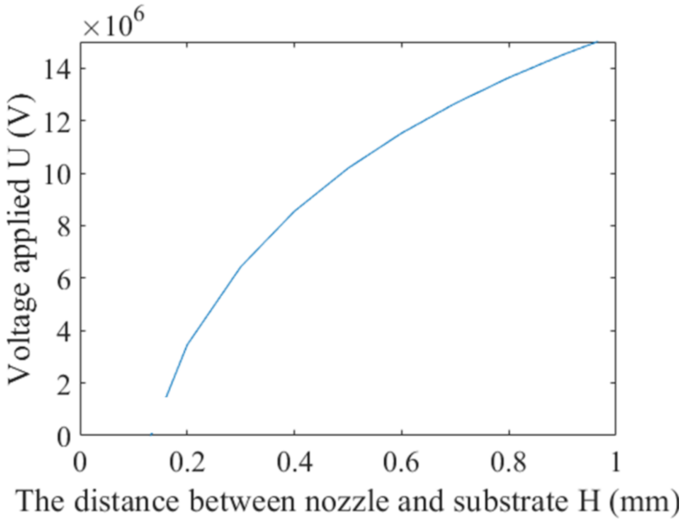

Figure 4.8 The applied voltage *U* as a function of the nozzle-to-substrate distance *H*. The simulation parameters dictate an electric field *E* of 2938.55 V/μm.

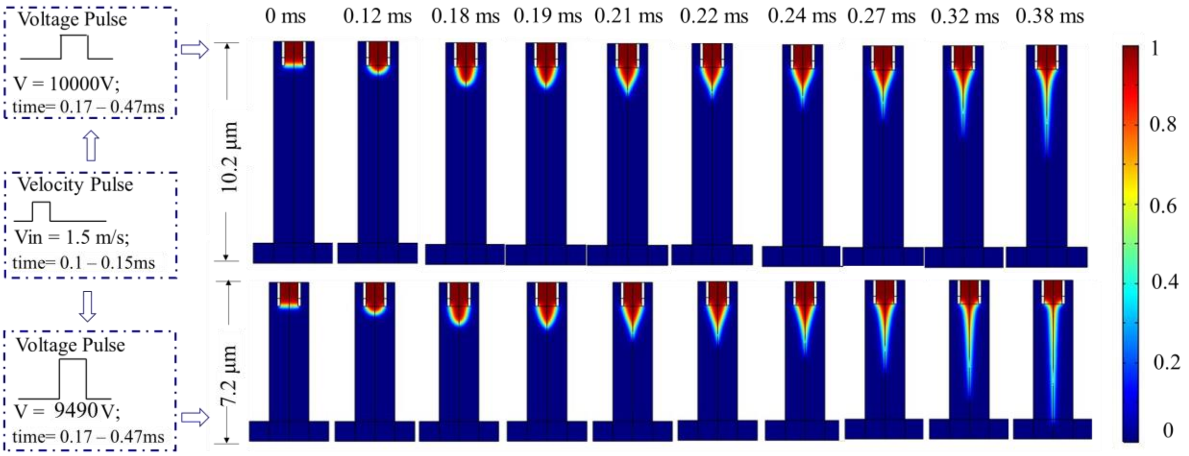

Figure 4.9 Simulations for differing nozzle-to-substrate distances. The top sequence demonstrates a situation where the inter-gap measures 10.2 mm, with an accompanied voltage input of 10 kV. Contrarily, the lower sequence illustrates a reduced distance of 7.2 mm, requiring a decreased voltage of 9.49 kV.

The effect of voltage pulse duration

The duration of the voltage pulse applied has a substantial impact on the printing process. This is demonstrated in **Figure 4.10**, which shows the printing linked to varying lengths of the applied voltage pulse while maintaining a steady initial velocity of 1.5 m/s over 0.05 ms. While the value of the applied voltage pulse remains consistent at 10 kV, the period over which it is sustained varies. In the illustration, the top row shows the results corresponding to a 0.3 ms duration of the applied voltage pulse while the bottom row represents the consequences of a more extended pulse duration of 0.5 ms. Inferences drawn from the simulations show a uniform initial meniscus for both test scenarios, a result of the unchanging initial velocity pulse. As the applied voltage pulse prolongs, the meniscus progressively transitions into the shape of a Taylor cone, ending up noticeably slimmer compared to its state at the conclusion of the shorter voltage pulse. The extended voltage application results in a more significant quantity of material being projected. Once the voltage pulse terminates, the jet produced by the lengthier voltage pulse is considerably extended.

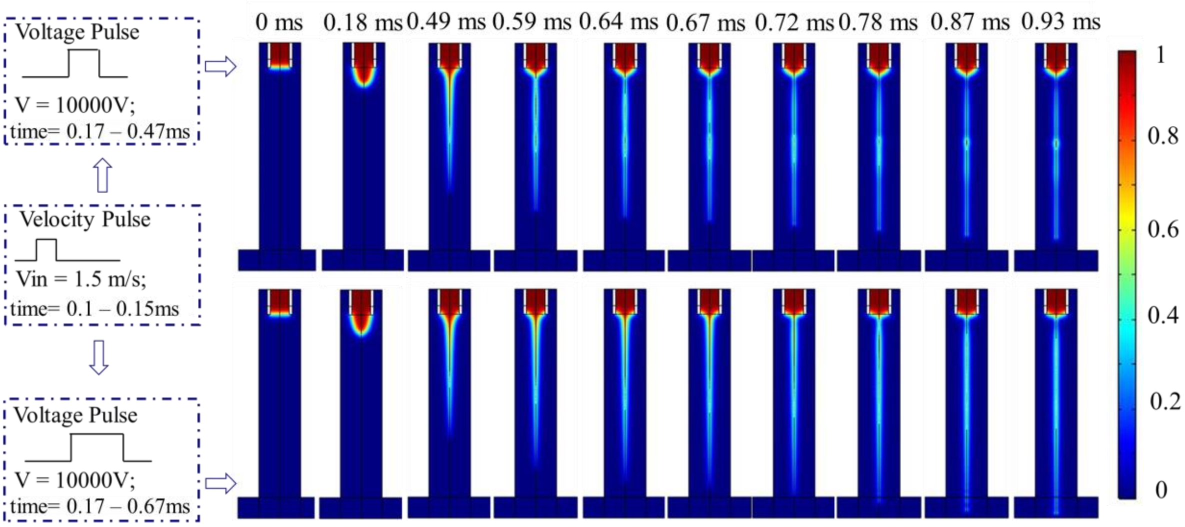

Figure 4.10 Results of simulations, employing varying durations of the voltage pulse. Both simulations maintain a consistent initial velocity pulse of 1.5 m/s throughout 0.05 ms. The upper row illustrates the simulation sequence with an applied voltage pulse of 10 kV sustained over 0.3 ms. Conversely, the lower row depicts the simulation process where the same 10 kV voltage pulse is extended over a longer duration of 0.5 ms.

4.3 Simulations of inkjet printing of nematic liquid crystals

The simulation model described in the previous sections can be effectively tailored to replicate the inkjet printing process by merely adjusting the value of the applied voltage pulse to 0V. The inkjet printing technique employed in this study utilizes a piezoelectric actuator-based printer. When the piezoelectric actuator inside the nozzle is subjected to an electric field, it initiates a reciprocal movement that propels the material out of the nozzle. In this context, this propulsion process is simulated by the application of an initial velocity pulse to the material. Consequently, the printed material is ejected by the influence of the initial velocity pulse.

Just like in the EHD printing process, at the onset of the printing procedure, the material forms a meniscus at the nozzle's tip. However, a notable divergence arises in that the velocity pulse continues to be applied to the material until it is completely ejected from the nozzle, forming a droplet that eventually detaches from the nozzle material. **Figure 4.11** shows the entire process of inkjet printing. It's important to note that the properties of the material employed in the inkjet printing process mirror those used in the EHD printing process, which in this case, is a nematic LC mixture. The initial velocity pulse introduced in this process has a magnitude of 4.5 m/s with a duration of 0.5 ms.

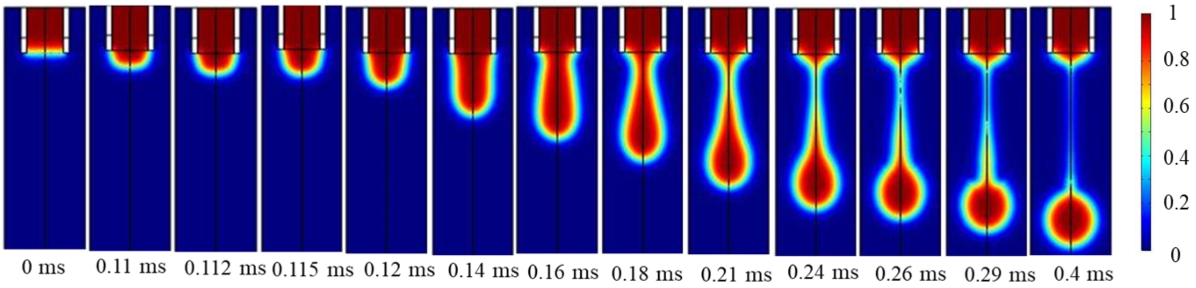

Figure 4.11 The inkjet printing process characterized by an initial velocity pulse of 4.5 m/s and persisting for a duration of 0.5 ms.

In this scenario, the initial velocity pulse stands as the solitary parameter under our control that can be modified. In the practical application, within the domain of piezoelectric actuator-driven inkjet printing, the electric signal, used to stimulate the piezoelectric actuator, can be adjusted. This adjustment allows the piezoelectric actuator to perform a movement with distinct displacements. Consequently, this variation exerts a significant influence on the printing procedure, and more specifically on the size of the resultant droplets. To replicate this process, a corresponding simulation was conducted, keeping all of the parameters constant except for the initial velocity value, which was set at 3 m/s and maintained for 0.5 ms. The results of this simulation are depicted in **Figure 4.12**.

Upon comparison of Figures 4.11 and 4.12, it becomes apparent that an increase in the initial velocity, while holding the duration constant, leads to a larger volume of material being ejected from the nozzle. The direct outcome of this is a printed droplet of a larger diameter. Although these observations may not provide in-depth guidance about how the variation in electric signal designed to trigger the piezoelectric actuator influences the printing process, they nonetheless offer valuable insight into the impact of the piezoelectric actuator's behaviour on the printing process.

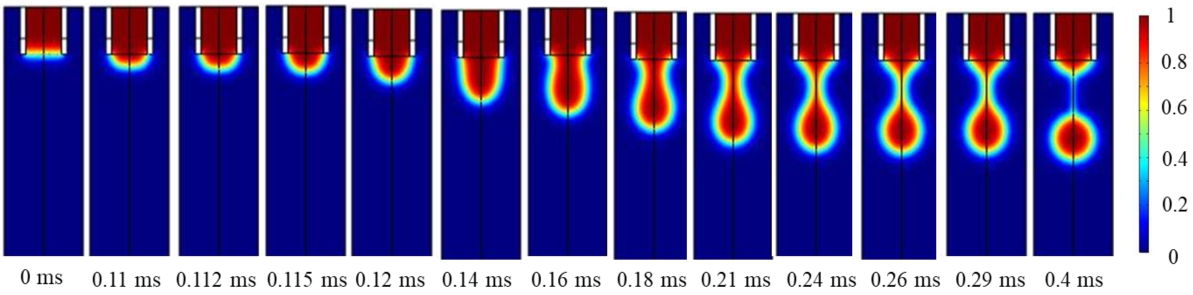

Figure 4.12 The inkjet printing process, facilitated by an initial velocity pulse of 3 m/s, maintained for a brief duration of 0.5 ms.

4.4 Summary

In this chapter, I have described the simulation software COMSOL Multiphysics, along with a walkthrough of the simulation process used in this thesis. The approach harnesses four modules within COMSOL Multiphysics: Electrostatics, Laminar Flow, Level Set, and Multiphysics. It is shown that this versatile model can accommodate simulations for both EHD printing and inkjet printing by adjusting the electric field. The Level Set method was used to delineate the interface between the nematic LC mixture and air, a critical step for accurately modelling two-phase flows. In this context, the properties of the liquid, particularly viscosity and surface tension, exert significant influence on the printing process. For the scope of this chapter, these properties have been configured based on parameters for liquid crystals, allowing us to scrutinize the effects of other parameter settings on the printing outcomes.

For our EHD printing simulations, we investigated variables such as liquid flow rate, applied voltage, nozzle-to-substrate distance, and voltage pulse duration. Our findings revealed a direct correlation between the diameter of the electrofluid jet and the liquid flow rate, while an inverse relationship was observed with the applied voltage. Additionally, if the electric field around the tip of the meniscus remains constant, an increase in the nozzle-to-substrate distance results in a reduced material volume being ejected. Conversely, extending the duration of the voltage pulse leads to an increase in ejected material volume. The insights gained from these simulations can guide our EHD printing experiments in terms of parameter optimization.

For the inkjet printing simulations, our focus lies on the parameter of the initial velocity pulse. Our results showed that a higher initial velocity leads to a greater volume of material being expelled from the nozzle. Therefore, these simulations provide valuable insights for both EHD and inkjet printing processes, serving as a reference point for parameter adjustments in real printing operations to achieve desired droplet diameters with different applications. In the next chapter, this inkjet printing technology will be used in the application of printed LC based smart windows.

CHAPTER 5: Printed Polymer Stabilized Chiral Nematic Liquid Crystal Smart Windows

5.1 Introduction

Smart windows play an important role in managing energy consumption in buildings [121] and automotive vehicles, particularly in environments that experience prolonged periods of extreme temperature conditions [122]. These smart window technologies can help to maintain a comfortable temperature inside both buildings and vehicles whilst at the same time providing privacy features. Specifically, smart windows can prevent solar radiation from either entering or escaping the building depending upon the optical properties of the material used within the window pane [123]. Additionally, spatially patterned smart windows can be fabricated with additional functionality such as the appearance of company logos/signage [124] or the integration of temperature sensors [125].

Liquid crystals (LC) have been particularly popular as the functional material used in smart window technologies because their optical characteristics can be altered either using applied electric fields or remotely using photo-illumination. The LC films that are typically employed often belong to one of the following classes: polymer stabilized LCs (PSLC) [126], polymer dispersed LC (PDLC) [31], or chiral nematic LC (CLC) [127]. Each of these systems can give rise to a light scattering state or a transparent state depending upon the material combination, device architecture and electric field conditions. Polymer-stabilization has also been combined with CLCs (PSCLCs), as first introduced by D.-K. Yang from Kent State University in 1992 [128].

A notable benefit of using PSCLCs in comparison to say PDLCs is that they can exhibit both a conventional mode (whereby the device switches from scattering to a transparent state with AC electric field) and reverse mode (switching from a transparent to a scattering state) by simply changing the photopolymerization conditions rather than having to change the LC material (positive dielectric anisotropy LC for conventional mode [30, 129] and negative dielectric anisotropy LC for reverse mode [130-131]). For example, if the PSCLC is photopolymerized while a voltage of sufficient amplitude is applied to the LC film then it can exhibit an opaque/light scattering state in the voltage off state. However, when a voltage is applied to the LC, the helical structure unwinds forming a nematic LC with a homeotropic alignment [128], which appears transparent. Alternatively, if the photopolymerization process takes place in the absence of an applied voltage then the off state is transparent (as determined by the alignment layer conditions) but the device becomes opaque/scattering when the LC is subjected to an external voltage. Spatially patterned PSCLCs have also attracted interest for a range of reasons and are typically patterned with the aid of a photomask [132]. This process has been used to produce spatial features such as two-dimensional barcodes [133] and temperature indicators [134]. A drawback of this approach is that a new photomask is required every time the design is altered or modified. Moreover, achieving a high spatial resolution and complex pattern on-demand can be challenging.

In this chapter, we first demonstrate the working principle of a PDLC film device, and then we use Drop-on-demand (DoD) inkjet printing to spatially pattern both PDLCs and PSCLCs, and employ this technique to demonstrate prototype smart windows with logos/emblems that can be switched off with the application of an electric field [124]. A key limitation using PDLCs with a positive dielectric anisotropy is that they can only be switched from a scattered state to a transparent state with the applied electric field. However, it would be highly beneficial if, using a kind of printed formulation, one could select either the conventional or reverse-mode functionality by simply changing the photocuring conditions. Here the development of conventional and reverse mode spatially patterned privacy windows fabricated using the DoD printing of PSCLC ink is demonstrated. It is shown that printed patterns can be made to operate in either a conventional or reverse mode configuration depending upon the photopolymerization conditions. The electro-optical properties of printed droplets and arrays are presented and compared with those obtained for standard thin films formed using the same material combinations. Finally, printed PSCLC patterns are presented that demonstrate how images can be embedded into a PSCLC windowpane.

5.2 Printed PDLC smart windows

The polymerization of polymerizable LC mixtures was carried out using an ultraviolet (UV) illumination system. The curing conditions including the exposure time and UV power density were controlled by this system, which influence the resulting properties of the LC film such as the polymer morphology and electro-optic characteristics. In the first stage of my work, I worked jointly on a project to print and characterize PDLC inks. The PDLC formulation contained 60 wt.% of the nematic LC mixture, E7, and 40 wt.% of the Norland Optical Adhesive (NOA65). The mixture formulation was first mixed at 60°C and 300 rpm for 48 hours on a hotplate with a magnetic stirrer. Then the PDLC mixture was filled into a glass cell with an indium tin oxide (ITO) layer on both sides before it was subsequently UV-cured. The exact curing conditions are shown in **Table 5.1**.

Table 5.1 Photopolymerization conditions for four different samples. Each sample contained the same mixture formulation (60 wt.% E7 and 40 wt.% NOA65) filled into glass cells that were 5 μm thick.

Sample	Power Density (mW/cm^2)	Exposure time (min)
1	0.33	4
2	0.33	10
3	1.8	4
4	1.8	10

To study and compare the effects of curing time and curing intensity separately, the same mixture was filled into four separate glass cells and either the exposure time was held constant for different power densities, or the same power density was applied for different exposure times. The results show that the LC droplet size in the mixture varied according to the curing conditions (**Figure 5.1**). The first two columns show polarizing optical microscope images of the optical texture for different curing conditions with and without the application of an external voltage. Also shown are photographs of the cells, showing a scattering state with a voltage off and a clear state with the voltage on. The results indicate that the droplet diameter decreases with increasing power density and exposure time since both affect the polymerization rate. This result is similar to that observed in [135].

In addition to studying the switching of the PDLC films on a polarizing optical microscope, the electro-optic characteristics of the samples were investigated using the system in **Figure 5.2** (a). In this case, a laser was reflected and focused onto the sample by a lens, the light then passed through the sample before it was received by a photodiode so that the transmitted light through the PDLC film can be detected. Another lens was then used to focus the scattered light before it was collected by another photodiode. A modulated ramped waveform shown in Figure 5.2 (b) was used for the measurement. The results presented in Figure 5.2 (c) demonstrate that with increasing voltage, the transmission increases and reaches a maximum of 100 Vpp. In accordance, the scattered light detected by the second photodiode decreased with increasing voltage.

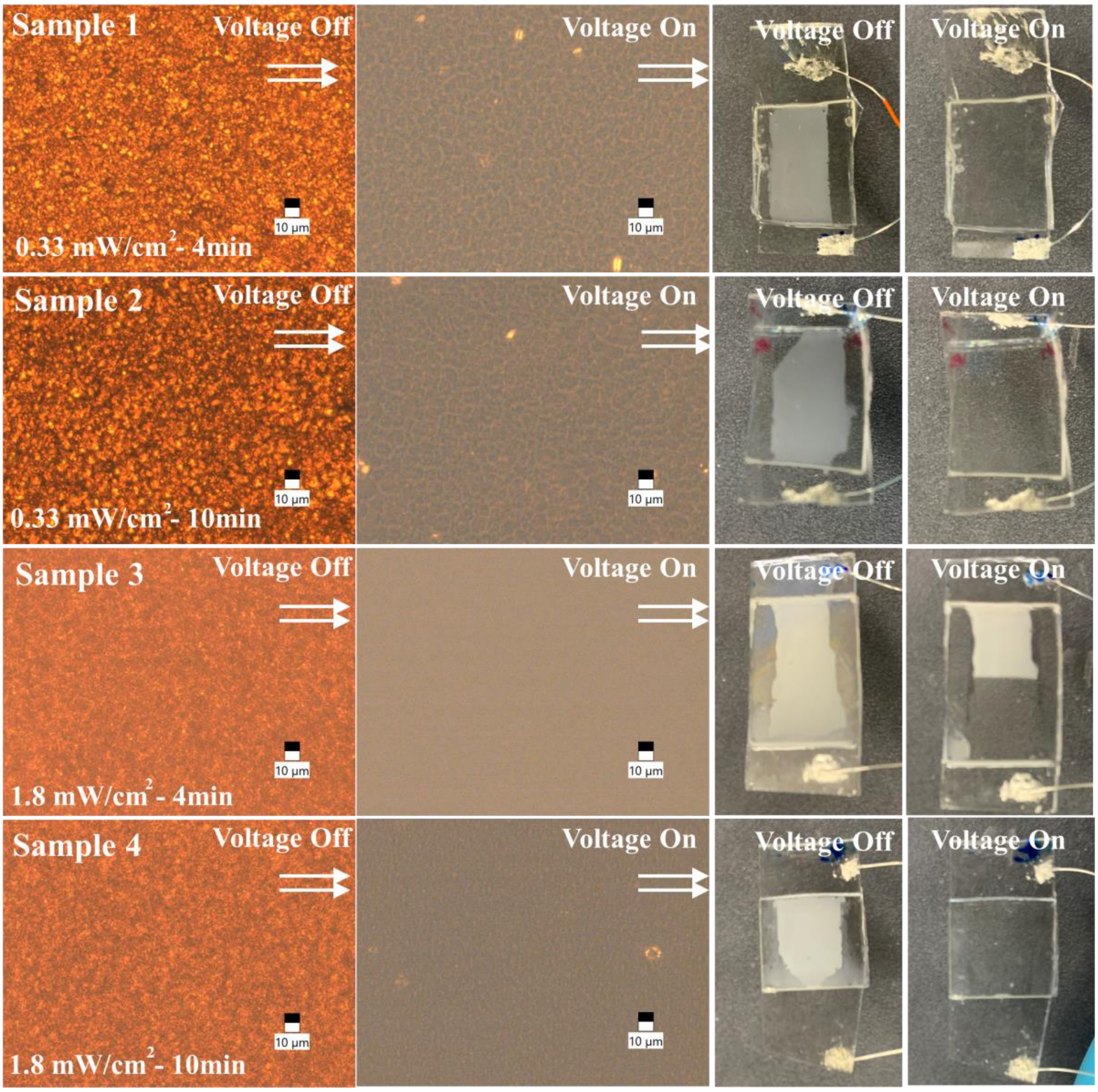

Figure 5.1 Polarizing optical microscope images and photographs of PDLC devices photopolymerized at different power densities and exposure times. The two right-hand columns show photographs of the glass cells containing the PDLC films when switching between a scattering state (voltage off) and a transparent state (60 Vpp voltage on). The scale bar in the microscope images represents a length of 10 μm.

Another system was developed to detect the scattered light as a function of angle. A rotation table was fitted with a lens and photodiode so that the scattered light from an angle of -45° to +45° (**Figure 5.3** (a)) could be collected. For each angle, the scattered light received by the detector was recorded and the results are presented in Figure 5.3 (b). When there is no voltage applied, at 0º the photodiode still receives the highest light intensity but the scattered light varies with the angle in a similar way in both directions and decreases with increasing angle, which indicates that the LC droplet's size and distribution in the mixture are relatively uniformly distributed within the polymer binder. On the other hand, when a voltage is applied, the range of high intensity light narrows and the majority of the light passes directly through the device.

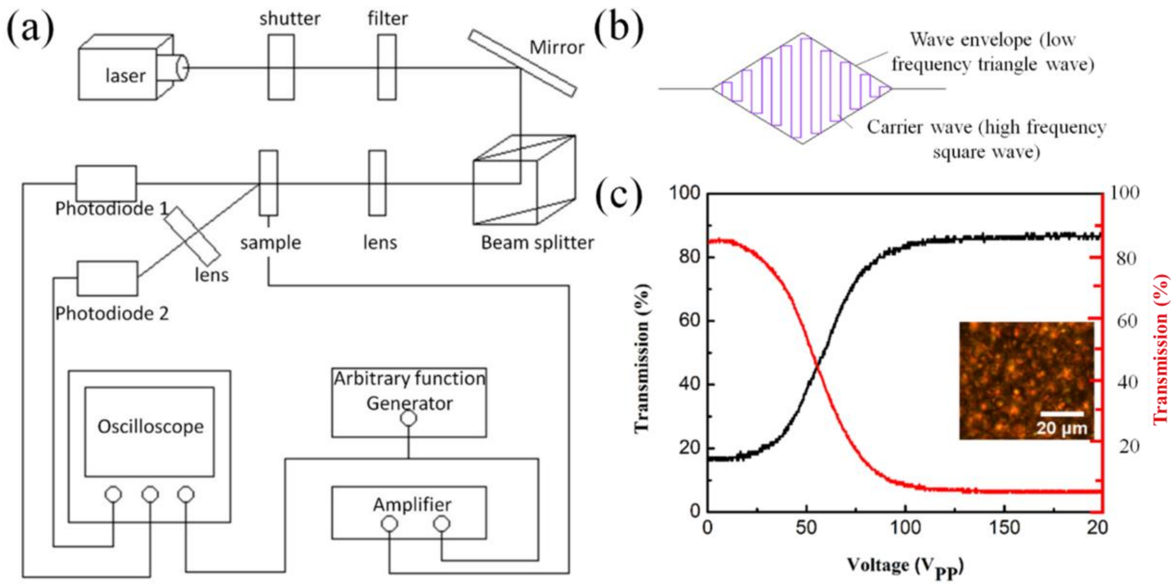

Figure 5.2 (a) Experimental configuration for measuring the transmission and scattering from the PDLC samples. (b) the waveform used in the measurement. (c) transmission and scattering curve as a function of voltage for a 12 µm PDLC film. The red solid line shows the scattered light captured by the second photodiode as a function of the applied voltage to the PDLC sample. The black solid line shows the transmission intensity captured by the first photodiode as a function of the applied voltage to the PDLC sample. The inset in the figure shows a polarizing optical microscope image of the PDLC sample.

A printed PDLC logo showing the Exeter College crest was fabricated as shown in **Figure 5.4**. In the absence of an applied voltage, the patterned LC droplet logo exhibits a scattering appearance. However, upon the application of a 40 Vpp voltage, the droplet logo transitions to a transparent state, hence allowing the underlying 'PDLC' background to be seen.

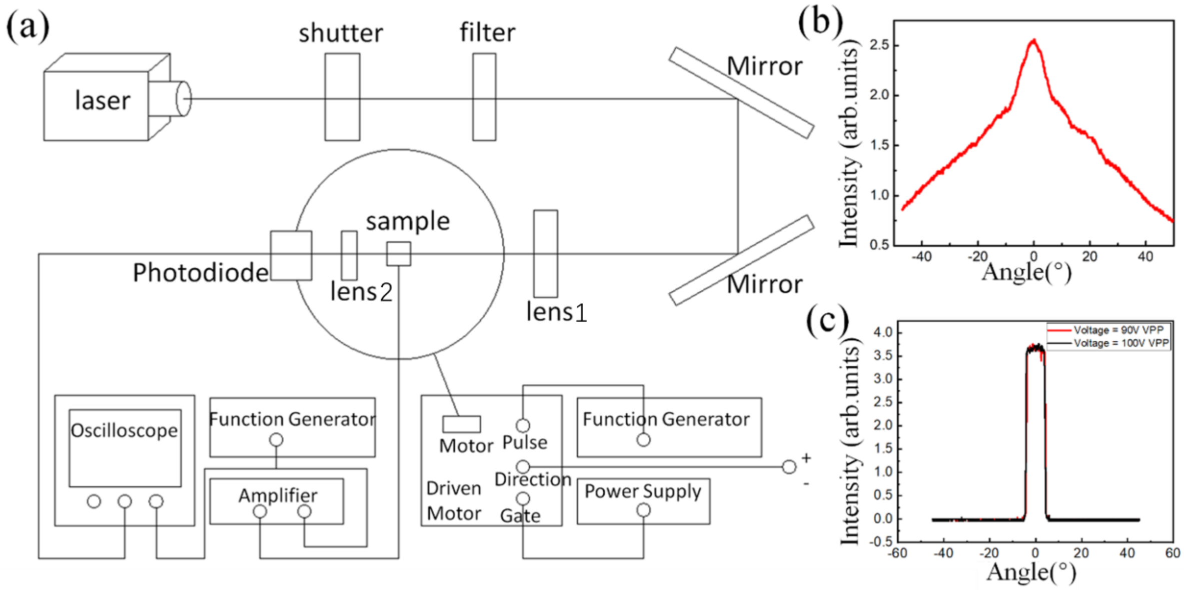

Figure 5.3 (a) Experimental configuration for measuring the angular dependence of the scattering from the PDLC samples. (b) the result of the sample without voltage involved. (c) the results of the sample with 90 Vpp and 100 Vpp applied. The two lenses used in this setup have the focal lengths of 200 mm (Lens 1) and 100 mm (Lens 2). The laser is He-Ne laser (JDS Uniphase, 1122P) with a wavelength of 633 nm.

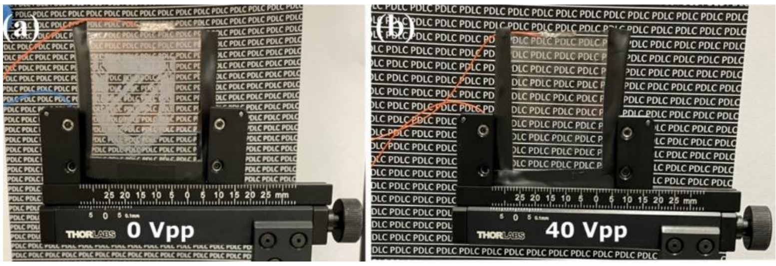

Figure 5.4 Patterned PDLC logo with (a) 0 Vpp applied and (b) 40 Vpp applied.

5.3 Printed polymer-stabilized chiral nematic liquid crystals

5.3.1 Experimental methods

The transmission of light through these thin-film samples was investigated using the experiment configuration presented in **Figure 5.5**. In this case, a He-Ne laser was focused onto the sample by a lens to form a spot size of approximately 60 μm in diameter, which was then received by a detector that recorded the intensity of the light transmitted through the PSCLC film. The detector used to record the intensity was a 4 mm × 4 mm photodiode positioned at a distance of 280 mm from the sample. The collection angle was therefore ±7.14 mrad in the *x* and *y* directions (with the propagation being in the *z*-direction).

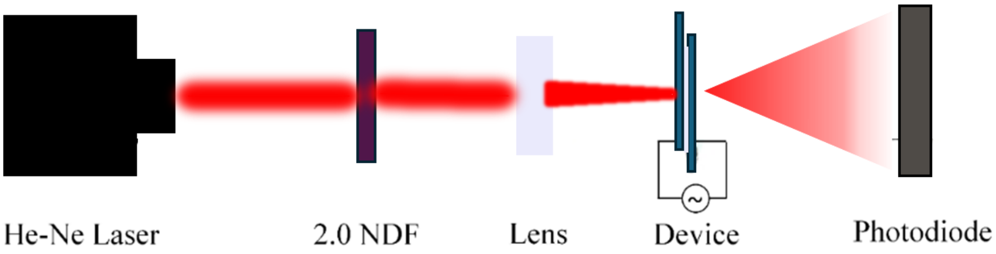

Figure 5.5 Experiment for the measurement of the transmission as a function of electric field amplitude and time for the thin-film and printed droplet devices.

Materials and ink preparation

In this chapter, the room-temperature nematic LC mixture, E7, (obtained from Synthon Chemicals Ltd) was used without further purification. The ordinary and extraordinary refractive indices of the nematic LC are reported to be $n_o = 1.52$ and $n_e = 1.74$, respectively, at a wavelength of 633 nm and a temperature of 20 °C.[136] The high twisting power chiral dopant, BDH1281 (Merck), was added to the nematic LC at a low concentration by weight (3 wt.%) to form a chiral nematic LC. A diacrylate reactive mesogen, 1,4-Bis[4-(3-acryloyloxypropyloxy) benzoyloxy]-2-methylbenzene (RM257 from Synthon Chemicals Ltd) was used in combination with a photoinitiator, IR819 (Ciba-Geigy) in order to form a polymer network inside the chiral nematic LC layer when exposed to UV light. Specifically, the mixture used in this study was composed of 93.5 wt.% E7, 3 wt.% BDH1281, 3 wt.% RM257, and 0.5 wt.% IR819. This formulation was thermally and mechanically mixed at a temperature of 68℃ with a magnetic stirrer at a speed of 300 rpm for 24 hours. This temperature was above the clearing point at which the nematic E7 becomes an isotropic liquid, which is 60℃. The mixture was found to result in a chiral nematic LC with a right-handed helical structure with a reflection band with a central wavelength at 859 nm. The pitch of the PSCLC mixture was measured to be p = 533 nm (from the transmission spectrum of white light in the Grandjean state) and the helical twisting power (β) of the chiral dopant in this mixture was estimated to be $\beta \approx 63\ \mu m^{-1}$.

Characterization

All samples were observed on an Olympus BX51 polarizing optical microscope in transmission mode at various magnifications (4×, 10×, 20×). For the measurement of the transmission and scattering characteristics, as well as the response times, a He-Ne laser (JDS Uniphase, 1122P) was used (λ = 633 nm) to illuminate the PSCLC samples so that the transmitted light could be determined. The transmitted light was detected using a photodiode (Thorlabs PDA36A-EC SI Amplified Detector). In order to generate amplitude modulated (AM) signals to drive the PSCLC films and printed droplets, two function generators (Multicomp Pro MP750065) were used in combination, with the output of one connected to the AM input of the other. Finally, an oscilloscope (Tektronix TDS2004B) was used to capture and display the response recorded by the photodiode.

5.3.2 PSCLC thin-film device

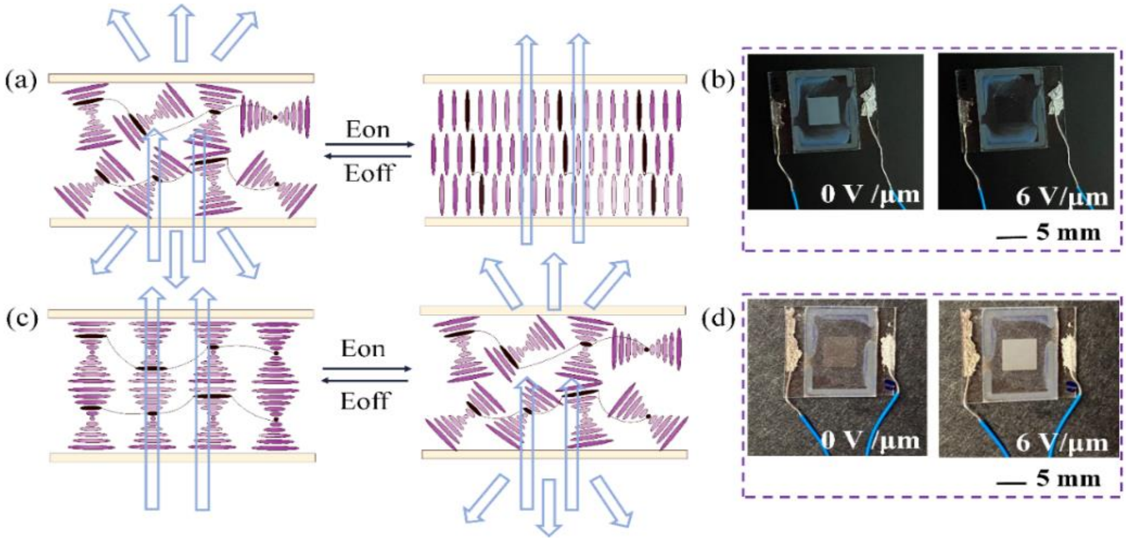

Figure 5.6 Conventional ((a) and (b)) and reverse ((c) and (d)) mode configurations of a 5 μm-thick PSCLC film (93.5 wt% E7, 3 wt% BDH1281, 3 wt% RM257, and 0.5 wt% IR819). In both cases, polymerization was achieved using a UV light source with an intensity of 27 mW/cm^2 for 3 min. (a) Illustration of the conventional mode configuration showing switching from a scattering to a transparent state with the application of an electric field. (b) Photographs of the conventional mode PSCLC film device without (scattering) and with (transparent) an applied electric field. (c) Illustration of the reverse mode configuration showing switching from a transparent to a scattering state with the application of an electric field. (d) Photographs of the reverse mode PSCLC film device without (transparent) and with (scattering) an applied electric field.

The thin-film devices were prepared using commercially sourced glass cells (from Instec) which had two ITO coated glass substrates separated with 5 μm-thick glass spacer beads. The rubbed polyimide alignment layers coated onto the surface of the ITO electrodes were used to form a Grandjean texture whereby the helical axis of the chiral nematic LC was aligned along the normal of the glass cells in the absence of an applied electric field. The LC-reactive mesogen mixture was capillary filled from one side of the cell and wires were attached to the ITO electrodes to enable the application of an electric field. **Figure 5.6** illustrates the switching mechanism and corresponding optical appearance of the thin-film PSCLC devices operating in both conventional and reverse modes.

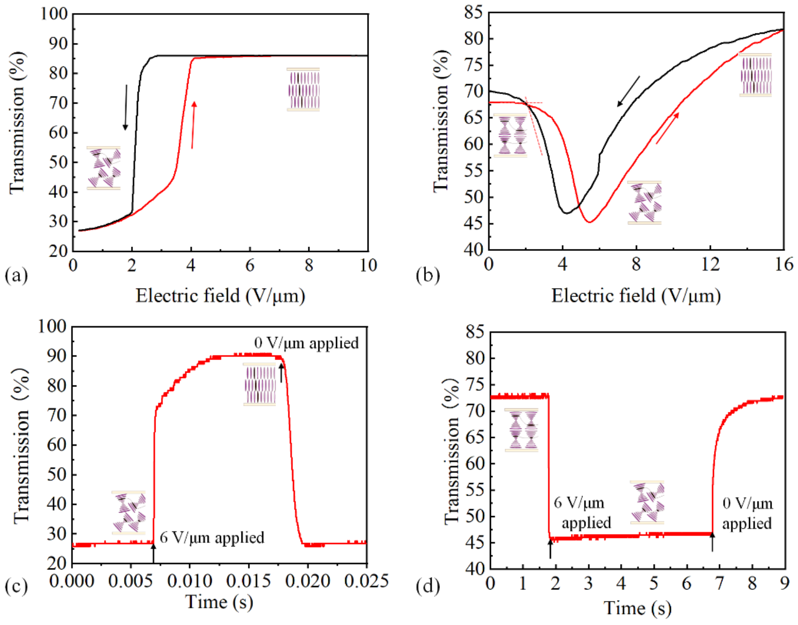

Figure 5.7 Transmission of a He-Ne laser through LC devices as a function of electric field for (a) the conventional mode (scattering to clear) PSCLC sample and (b) the reverse mode (clear to scattering) PSCLC sample. Plots are shown for increasing the electric field amplitude (solid red line) and decreasing the electric field amplitude (solid black line). Both devices consisted of a 5 μm-thick LC layer. Plots (c) and (d) show the change in transmission as a function of time when the PSCLC device was switched on and off with an electric field of 6 V/μm. (c) conventional mode and (d) reverse mode device. All measurements were carried out at a temperature of 25°C.

A plot of the transmission of the laser light from a He-Ne laser through the LC device as a function of the electric field is shown in **Figure 5.7**(a) for the conventional mode and Figure 5.7(b) for the reverse mode. Results are shown for both increasing and decreasing the amplitude of the applied electric field, where various degrees of hysteresis are observed for both the conventional (Figure 5.7(a)) and reverse (Figure 5.7(b)) mode thin films. For each set of data, the signal intensity was then normalized to the signal when no device was present in the system, and then the result was converted to a percentage for plotting.

For the conventional mode, the initial state is the focal conic state since there is no surface treatment and the whole device shows scattering. When the electric field is gradually applied to this device, the director tends to align parallel to the electric field. This process occurs when the electric field is less than 4V/μm. When the electric field reaches 4V/μm, the helical structure disappears, and the director is aligned parallel to the electric field. If the electric field continues to increase, the transmission of the device does not change since the LC director has already reached the maximum rotation angle. In this condition, the transmission of the device has reached the maximum value as shown in Figure 5.7(a). If the electric field is suddenly applied with a value of 6 V/μm, the director needs time to rotate from the helical structure to the homeotropic state following a two-stage switching process as shown in Figure 5.7(b). In the first stage, the director tends to unwind from the helical structure before it then aligns according to the electric field. The whole process will last several microseconds with the applied electric field of 6 V/μm.

For the reverse mode, the initial configuration is in a Grandjean state due to the surface treatment of the glass cell and light is transmitted through the device [128, 137-138]. However, there is still some residual scattering due to imperfections in the alignment of the helical structure. With increasing amplitude, the electric field disturbs the macroscopic helical structure, converting it first to a focal conic state which scatters the incident light before reaching maximum scattering (minimum transmission) at around E = 4V/μm. Increasing the amplitude further results in the electric field becoming strong enough to unwind the macroscopic helix leading to a homeotropic nematic state and even greater transmission through the device [139]. The electric field needed to reach this state was found to be E = 16 V/μm, which was much higher than that found for the conventional mode (E = 4 V/μm). This difference in electric field amplitude is considered to be due to the different initial photopolymerization states for the two modes.

Figures 5.7(c) and Figure 5.7(d) show response time measurements for both the conventional mode and reverse mode samples. From these measurements of the change in the transmission as the device is switched on and off, the rise and fall times can be extracted. For the conventional mode sample, the rise and fall times are found to be 5 ms and 2.5 ms, respectively. For the reverse mode sample, on the other hand, the rise time was found to be 20 ms, which is substantially shorter than the fall time (around 2.2 seconds).

In the electric field on process, the two modes have response times that are roughly comparable in terms of order of magnitude. However, when the voltage is removed, the two modes have very different response times. This is because of the different states from which they must relax when the electric field is removed. For the reverse mode, the focal conic state must relax into a Grandjean state. This requires macroscopic reorganization, including the motion of defects, which takes a relatively long period of time. In contrast, for the conventional mode, when the electric field is removed, the LC only needs to locally form a helix structure upon relaxing from the homeotropic state. But this structure is gradually disordered (see Figure 5.6(a)). Therefore, the conventional mode is much faster for the electric field off process.

From the plot in Figure 5.7(c), an apparent two-stage switching process appears to take place, which was also observed for the printed PSCLC. This two-stage switching property was also observed for an alternative PSCLC mixture with a different LC and chiral dopant (E48 and CB15 respectively) [1]. However, the whole switching process for the conventional mode was relatively fast compared with that of the reverse mode.

5.3.3 PSCLC droplet device

PSCLC droplet device fabrication process

The spatially patterned printed devices were fabricated using ITO coated glass slides (Ossila). The slides were left untreated for the conventional mode device fabrication. For the reverse mode devices, which require a Grandjean (standing helix alignment) in the field off state, the ITO slides were coated with a 5% Polyvinyl Alcohol (PVA) water solution and then dried in an oven for around 2 minutes to form a thin layer of PVA. A rubbing machine was then used to align the PVA layer, resulting in a uniform homogeneous alignment of the LC [140].

The printing process was accomplished using the Jetlab-II printing system (MicroFab Technologies Inc) as described in Chapter 3.3.2, which includes a three-axis translation stage and multiple piezoelectric printheads in a heating module (Eurotherm 2408i). The internal diameter of the printhead's nozzle used was 80 μm (MicroFab MJ-AT-01-80). Backpressure of the printhead was provided by a computerized pneumatic system and was used to control the unperturbed liquid meniscus at the nozzle and to ensure that the dispenser was fully filled with the PSCLC material before printing.

For the printing process, the printhead was heated to a temperature of 68 ℃ to lower the viscosity and surface tension of the PSCLC ink, which ensured a stable jetting process without satellite droplet formation. To observe droplet formation and the printing process, as well as the impact with the substrates, a camera (Omron Sentech STC-MB33USB 18L0203) integrated inside the printing system was used. Arrays of single droplets were printed to form recognizable spatial patterns, for example grids and a logo.

For the conventional mode (scattering to transparent state), the mixture was photopolymerised in the presence of a voltage of 70 Vrms (corresponding to an electric field (E) of $E = 5$ Vμm^{-1}) that forms a polymer network which leads to a scattering state even once the voltage had been removed. The power density of the UV light ($\lambda = 365$ nm) source (CS2010, Thorlabs) used to photopolymerize the LC mixture was 27 mW/cm^2 for 3 minutes [141]. These photopolymerization conditions were used based upon a previous study, where it was found that this power density and exposure time results in a desirable scattering state [141]. The power density was monitored with a handheld power meter (PM100D, Thorlabs) attached to a photodiode (S120VC, Thorlabs). In contrast, for the reverse mode device (transparent to scattering state), the sample was photopolymerized with the same UV power density and duration, but with no applied electric field. This resulted in a Grandjean alignment in the absence of an electric field after fabrication. All steps up to the photopolymerization process were carried out under the illumination of yellow light to prevent premature photoinduced polymerization**.**

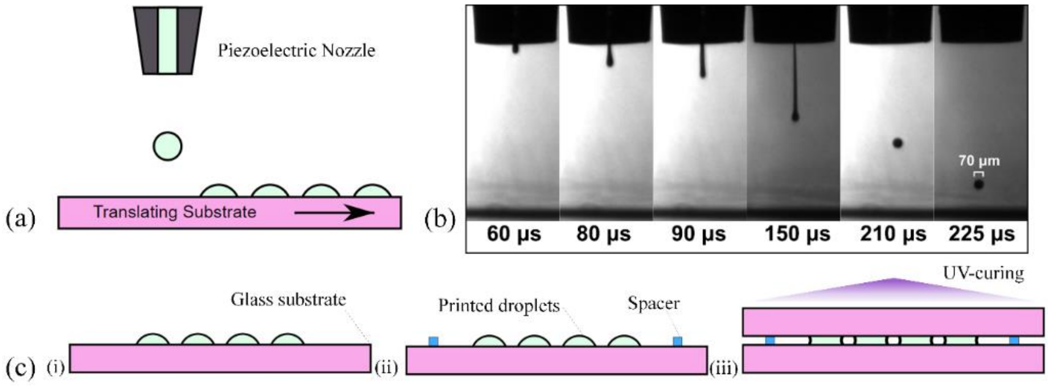

Figure 5.8 (a) Inkjet printing process of the PSCLC mixture (93.5 wt% E7, 3 wt% BDH1281, 3 wt% RM257, and 0.5 wt% IR819). (b) Shadowgraph images of the PSCLC droplet formation process with an 80 µm diameter print-head. For the printing process the print-head was held at a temperature of 68 ℃ to reduce the viscosity and surface tension of the LC ink. (c) Illustration of the device fabrication process including: (i) droplets loaded onto the substrate, (ii) attachment of spacers, (iii) attachment of the top ITO glass slide and photopolymerization process.

Figure 5.8 shows the printing and device assembly processes in detail. Figure 5.8(a) shows an illustration of the deposition of individual picolitre volume droplets onto ITO-coated glass substrate using the DoD printing process with a piezoelectric-driven print head and Figure 5.8(b) shows a sequence of shadowgraph images demonstrating the printing of individual PSCLC droplets that are free from jet break-up and satellite formation. After printing, two spacers (10µm) were attached to the edge of the substrate before another ITO glass slide was applied to form a top substrate (as illustrated in Figure 5.8(c)). The araldite rapid epoxy adhesive was then used to fasten the glass slides together before the device was cured with UV light under different electric field conditions for the conventional and reverse modes. In this fabrication process, although the spacer has a thickness of 10 µm, the entire device is clamped using clips. Both the thickness of the spacer and the clamping force exerted by the clips contribute to the final thickness of the device. As a result, the device fabricated with the 10 µm spacer ultimately has a measured thickness of 14 µm.

Conventional mode printed PSCLC droplet device

For the conventional mode sample, the PSCLC was photopolymerized in the presence of an electric field above the critical electric field required for the chiral nematic-nematic transition to occur. After the photopolymerization process, and when the field was subsequently removed, the film tends to form a scattering state. To obtain a transparent state, an electric field of E = 6 V/µm was applied to unwind the helix and to form a homeotropic nematic alignment whereby the director was aligned along the electric field direction. For this conventional mode sample, the mixture is then in a focal conic state in the field-off configuration because the polymer network favours the homeotropic state, which prevents the Grandjean alignment from forming. Only when an electric field of sufficient amplitude is reapplied will it become transparent again.

Figure 5.9 presents the results of the electro-optical properties of a single printed PSCLC droplet operating in the conventional mode. For the conventional mode, with increasing field amplitude the focal conic (scattering) state switches to a homeotropic nematic LC resulting in a transparent state. The transmission as a function of electric field and time was obtained with the experimental setup presented in Figure 5.5. The diameter of the droplet footprint in the printed case was ≈190 microns and the thickness of the device was ≈14 µm. Figure 5.9(a) shows representative polarizing optical microscope images of a printed PSCLC droplet between parallel polarizers for different electric field amplitudes. In the absence of an applied field, the printed droplet adopted a focal conic state, scattering the light and leading to a dark appearance when viewed in the microscope.

When the electric field was increased to E = 5 V/µm, the helical structure began to unwind as the director inside the droplet aligned with the electric field direction. In all cases, a ring was observed around the droplet that still scattered the light in spite of the applied electric field. This is due to the refraction/reflection of the light at the edge of the droplet, resulting in strong scattering. This effect is illustrated in **Figure 5.10**. Additionally, due to the combined effects of surface alignment and surface tension at the edge of the droplet device, the LC director exhibits some degree of disorder, lacking a regular alignment in this region. This irregularity contributes to the observed dark ring at the edge of the droplet. A line scan taken through the droplet in the microscope images was then used to extract the transmitted intensity for a single printed droplet as the field was increased (Figure 5.9(b)). With increasing field amplitude, it can be seen that the transmission in the circular area that is defined by the droplet increases. For electric field amplitudes ranging from E = 0 to 4.3 V/μm, the transmission remained low, and there was only a small change in the PSCLC configuration for this range of electric field amplitudes. However, upon increasing the amplitude to E = 4.6 V/μm there was a noticeable change in the transmission intensity (as can be seen in both (a) and (b)). For a further increase in the electric field amplitude (E > 5 V/μm) the transmitted intensity across the droplet did not change significantly as can be seen in Figure 5.9(b) (e.g., from E = 5 V/μm to 5.7 V/μm).

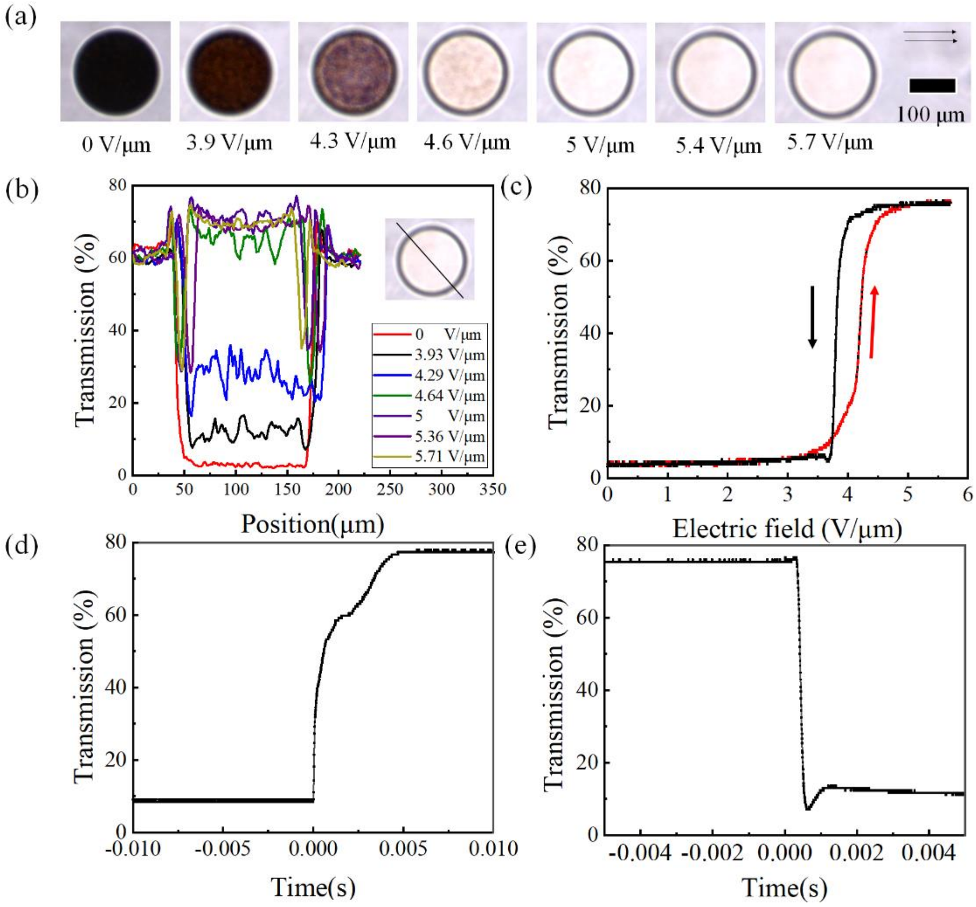

Figure 5.9 Electro-optic characteristics of a printed PSCLC droplet (93.5 wt% E7, 3 wt% BDH1281, 3 wt% RM257, and 0.5 wt% IR819) operating in the conventional mode (scattering to transparent). The droplet was printed at a temperature of 68 °C with an 80 μm diameter nozzle and photopolymerized in the presence of an electric field of E = 5 V/μm at 25°C. The droplet diameter footprint was 190 μm (after device assembly) and the gap between the glass substrates was 14 μm. (a) Polarizing optical microscope images of a printed PSCLC droplet observed between parallel polarizers (indicated by the single-headed black arrows). (b) Line profile of a single printed PSCLC droplet at different electric field amplitudes. (c) Transmission of a He-Ne laser through the printed PSCLC droplet as a function of electric field (for both increasing (red line) and decreasing (black line) amplitudes). Change in transmission as a function of time when the PSCLC droplet was switched on (d) and then off (e) with an electric field of E = 5 V/μm. All measurements were carried out at a temperature of 25°C.

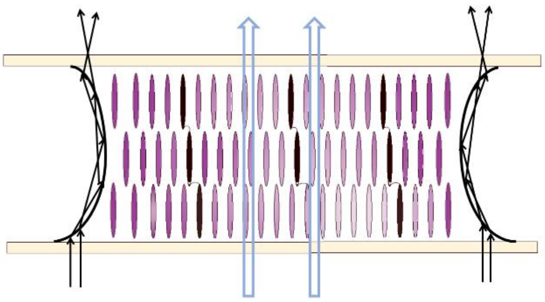

Figure 5.10 Illustration of the formation of a black ring around the printed droplets due to scattering at the edges of the droplet.

Figure 5.9(c) shows the results for the transmitted light intensity as a function of the electric field for both increasing and decreasing amplitude. Here an amplitude modulated signal was applied to the printed PSCLC droplet device to slowly increase the amplitude of the 1 kHz continuous square wave carrier signal. Upon increasing the amplitude of the electric field no change was observed until the amplitude reached approximately E = 3.8 V/µm. Above this value, the transmission increased steeply with a further change in the electric field amplitude, before it increased more gradually above E = 4.7 V/µm corresponding to an unwinding of the helix and the chiral nematic-nematic transition. These results are consistent with the results recorded on the microscope (Figure 5.9(a)) since they both showed a transparent state when the electric field was greater than 4.6 V/µm. Compared with the transmission of the transparent state of the film device (86%, Figure 5.7(a)), the field-on homeotropic state transmission was found to be around 10% lower for the printed droplet device (76%). This is mainly due to the influence of device thickness, but it may also be due to scattering at the edges of the droplets, as well as potentially lower quality alignment in the printed droplets. For the data taken with a microscope (Figure 5.9 (b)) the higher numerical aperture of the condenser and objective will also have an influence. However, for the droplet device, the contrast ratio (CR) improves by nearly a factor of five – being CR = 3.2 for the film device whereas CR = 15.3 for the printed droplet device. This is because the droplet device was much thicker than the film device, which then resulted in a strong scattering state when there was no electric field applied.

Decreasing the electric field amplitude reveals that the transmission begins to decrease at an electric field of E = 4.3 V/µm as the helix begins to reform, and the onset of scattering begins. At an electric field of E = 3.7 V/µm, the transmission reached its minimum value as the focal conic scattering state had been reformed. The results clearly show a degree of hysteresis in the switching when comparing the response for increasing and decreasing the magnitude of the applied electric field. For example, the transmission is midway between its maximum and minimum values at E = 4.2 V/μm on increasing the electric field amplitude, but this same value for the transmission was observed at E = 3.8 V/μm on decreasing the electric field amplitude. Hysteresis in the transmission was therefore observed when increasing and decreasing the field in accordance with previous studies [142-143].

Figures 5.9(d) and 5.9(e) show the rise (scattering to transparent) and fall (transparent to scattering) times for the printed PSCLC droplet, respectively. These results were obtained when the printed droplet was subjected to a square wave signal with a 1 kHz frequency and an electric field of 5 V/μm, which as shown in Figures 5.9(a)-(c) resulted in the printed droplet becoming transparent. Here the rise time was found to take around 4 ms whereas the fall time was completed in approximately 2 ms. These response times are consistent with those obtained for equivalent thin film devices, which were 5 ms for the electric field on and 2.5 ms for the field off (as shown in Figure 5.7). In Figure 5.9(d) it can be seen that a two-stage switching process takes place. In the first stage, the helix is distorted when a voltage is applied, which is a relatively fast process. In the second stage, however, the director needs to unwind from the helix state to form a homeotropic nematic alignment, which takes a relatively long time in comparison. A similar two-stage switching process was observed in the thin-film device (as shown in Figure 5.7(c)).

The results obtained here are within the range of switching times observed by other researchers, although there is very substantial variation in the switching times of polymer stabilized chiral LC devices reported previously, which range from tens of μs [144-145] to tens of ms [128, 146] for the rise time and tens of μs [147] to tens of ms [147] for the fall time. The response time is highly influenced by the ratio of effective viscosity to the effective elastic constant of the LC host and chiral dopant, as well as the pitch [148]. Shorter pitch chiral nematic LC mixtures could result in faster response times. Additionally, the cell gap also influences the response time since in thicker cells, where there is a larger number of chiral pitches across the cell, more time is needed to transfer from one state to another. Further, the polymer network density, morphology, and elasticity, will also strongly influence switching times. Importantly, the thin-film device and the printed droplet device developed here exhibited similar electro-optic characteristics which indicate that the DoD printing fabrication process did not compromise or significantly alter the switching behaviour.

Printed reverse mode PSCLC droplet device

For the printed PSCLC device photopolymerized without the application of an electric field, on the other hand, a Grandjean texture (standing helix alignment) is obtained at E = 0 V/μm. However, when an electric field of sufficient amplitude is subsequently applied the mixture transforms to a focal conic state, resulting in strong light scattering. This is called the reverse mode. If the electric field is then removed, the LC will relax back to the planar aligned (Grandjean) state, which appears transparent as long as the reflection band of the chiral nematic does not coincide with visible wavelengths, as is true for our samples.

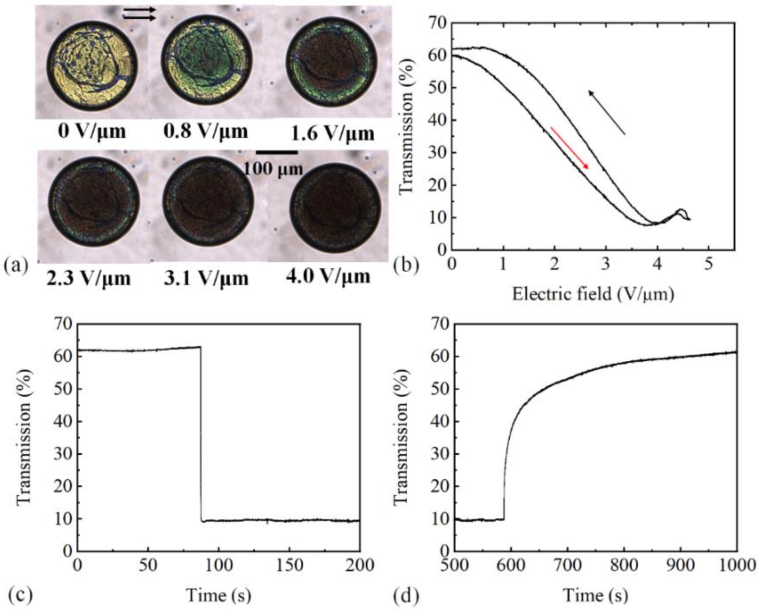

Figure 5.11 Electro-optic characteristics of a printed single PSCLC droplet (93.5 wt% E7, 3 wt% BDH1281, 3 wt% RM257, and 0.5 wt% IR819) operating in the reverse mode (transparent to scattering). The droplet was printed at a temperature of 68 °C and photopolymerized without an applied electric field at a temperature of 25°C. The droplet diameter was 205 μm (after device assembly) and the gap between the glass substrates

was 13 μm. (a) Polarizing optical microscope images of a printed PSCLC droplet viewed with parallel polarizers (indicated by the single-headed black arrows). (b) Transmission of a He-Ne laser through the PSCLC droplet as a function of the applied electric field amplitude (upon increasing (red line) and decreasing (black line) the amplitude). The change in transmission through the printed PSCLC droplet as a function of time when the PSCLC droplet was switched on (c) and then off (d) with an electric field of E = 4 V/μm. All measurements were carried out at a temperature of 25℃.

Results for the electro-optic characteristics of a printed reverse mode PSCLC droplet device are presented in **Figure 5.11**. Figure 5.11(a) shows example microscope images of a printed reverse mode PSCLC droplet viewed between parallel polarizers for a range of different electric field amplitudes. The droplet footprint diameter in this case was 205 μm and the cell gap was 13 μm. The images show that with an increase in the electric field, the printed PSCLC droplet changed from a coloured, polydomain Grandjean texture to a state that appears dark in the centre of the droplet at E = 1.6 V/μm. However, it was found that there was a thin region around the circumference of the droplet which did not appear to change at this electric field amplitude. A further increase in the electric field resulted in the central region of the droplet becoming darker, which was also accompanied by a change in the appearance of the outer ring, with the droplet appearing completely black at around E = 4.0 V/μm. This dark appearance is due to the incident light being strongly scattered by the droplet as well as the out of order LC director alignment in this region. As for the conventional mode, there was no apparent change in the droplet dimensions with the application of the electric field.

For the printed droplet, the Grandjean state was found to have more disclinations and defects when compared with an analogous thin film device. Despite the presence of these disclinations, the droplets still exhibited a relatively good contrast between the initial transparent state (E = 0 V/μm) and the scattering state (E = 4.0 V/μm). The disclinations that are observed are due to the imperfect alignment of the LC director in the Grandjean state. The texture can be further improved by optimizing the substrate treatment and/or the alignment layer. In future commercial applications, it will be possible to use more optimized alignment processes and hence reduce the influence of disclinations and defects on device performance. Additionally, it can be noted that some regions near the droplet edge do not switch fully. This different behaviour at the droplet edge may also be due to some variation in the network formation in this area. The shape of the final droplet is controlled by capillary effects. Light will potentially refract/reflect multiple times at the edges of the droplet, resulting in strong scattering as illustrated in Figure 5.10 which appears as a black ring even when an electric field is applied. This refraction/reflection at the edges of the droplet may also lead to some nonuniformity in the network formation around the edges of the droplets during the UV curing process.

Again, hysteresis was observed upon increasing and decreasing the electric field amplitude (see Figure 5.11(b)). These results were obtained by slowly increasing the amplitude of a 1 kHz square wave carrier until it reached a maximum of E = 4.6 V/μm. As the electric field amplitude increased, the Grandjean texture was distorted by the application of the field which resulted in the growth and formation of a focal conic state, as seen by the transparent to scattering transition. In contrast to the thin-film device, the lowest transmission value was observed at an electric field amplitude of around E = 4 V/μm, which is slightly lower than that observed for the thin-film device. A further increase in the electric field leads to an unwinding of the helical structure as the strength of the field dominates over the twist induced by chirality, forming a second transmission state above the critical unwinding field. This phenomenon is much more obvious in the results presented for the thin-film device as shown in Figure 5.7(b) whereby the transmission begins to increase for field amplitudes above E = 5.4 V/μm. It is worth noting that this second transmission state is surplus to requirements for smart window applications. The highest transmission recorded was found to be ≈62%, which is around 10% lower than for the film device operating in the same mode (70%, Figure 5.7). This is due to the thickness of the PSCLC layer combined with the imperfect alignment of the droplet in the

Grandjean state. Different droplets may have some variation in texture, leading to some droplet-to-droplet variation in optical properties. The printed droplet device also shows a higher contrast ratio compared with the film device because of the influence of the thickness.

The response times for the printed reverse mode PSCLC droplet device were measured when a 1 kHz frequency square wave with an amplitude of E = 4.0 V/μm was applied across the printed PSCLC droplet and subsequently removed. Figures 5.11(c) and (d) show the rise time (transparent to scattering) and the fall time (scattering to transparent), respectively. In this case, the response time for the field on process was found to be 10 ms, but approximately 400 seconds for the field off process.

The dynamic response times recorded here for the field off process are notably different from those recorded for the thin film device (Figure 5.7). One possible reason might be that the printed droplet device was much thicker (by approximately a factor of three) than the thin-film device. The factors that govern the restoration of the standing helix configuration are the surface alignment conditions and the polymer network that was formed in the Grandjean state. Consequently, it is expected that thicker devices result in a slower relaxation process in terms of the recovery of a uniform Grandjean state upon removal of the applied electric field.

Overall, for the reverse mode device, the LC mixture needs to be pre-aligned by the surface alignment to form the Grandjean state. However, in the conventional mode the LC mixture does not require any pre-alignment. In the transparent state, the reverse mode device is in the Grandjean state whereby the LC director aligns parallel to the substrate. Therefore, the transmission of the device in this state highly depends on the alignment of the LC director. On the other hand, for the LC device operating in the conventional mode, the transparent state occurs when the voltage is applied, which forces the LC director to be perpendicular to the substrate. This means that the different states of the LC director then result in some difference in the behaviour of the transmittance.

5.3.4 Printed PSCLC arrays and prototype windows

After successfully identifying the conditions for printing droplets of a PSCLC mixture and characterizing their electro-optic properties, spatial features such as arrays can be printed by digitally printing multiple droplets across the substrate. Utilizing the aforementioned methodology, it is feasible to harness identical materials for the implementation of dual modalities in the smart window configuration, as depicted in **Figure 5.12**. In the absence of an electric field, the display defaults to its conventional mode, exhibiting the 'LC' characters. Conversely, upon the application of voltage, the system transitions to its reverse mode, revealing the 'SMP' characters.

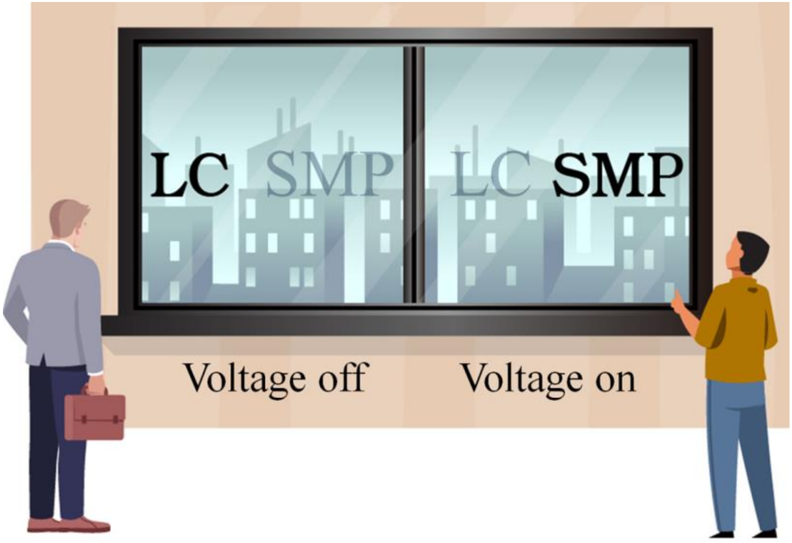

Figure 5.12 The printed smart window's functionality is demonstrated across two distinct states. In the conventional, or reverse mode, which occurs in the absence of an applied voltage, the 'LC' (Liquid Crystal) character is prominently displayed. Conversely, upon the application of an electrical potential, the device transitions into the reverse mode, during which the 'SMP' (Shape Memory Polymer) character is manifested.

Patterning was achieved using the scripting language provided by the Jetlab-II printing system, which can generate arrays and circles, as well as print representations of raster images. Such a system could therefore print customized logos, signs or text. Here we show a window with the letters 'LC' (**Figure 5.13**(a)) operating in the conventional mode The device was fabricated with the same PSCLC ink formulation and the same printing parameters as shown for the single droplet case in Figure 5.9, and the cell gap was 10 μm. It can be clearly seen that the printed droplets scatter light when there is no voltage applied, and so the letters can be seen, while for an applied electric field the droplets become transparent and the letters disappear. Using the same printing parameters, a square array of 25 × 25 droplets was printed on polyimide-coated ITO glass slides and photopolymerized without any electric field to create a reverse mode sample. The results are shown in Figure 5.13(b). The cell gap in this case was 8 μm.

Some regions show variation in droplet sizes in Figure 5.13. This is caused by the top electrode assembly process, when the two electrodes are brought together with a certain amount of pressure, resulting in slight non-uniformities and unevenness which can cause some of the droplets to merge together. In a commercial process, this can be improved by using a highly uniform distributed pressure for the assembly process, together with distributed spacer beads to lead to very well-regulated cell gap control. These combined results indicate that this mixture and the density of the droplets are suitable for a switchable design. Additionally, the printing process can be automatically controlled, and the patterns can be printed in different designs. Using commercial printing processes, this can be further developed to produce large-area switchable patterns and images.

The inkjet printing of a PSCLC mixture for the fabrication of smart windows could achieve that by undergoing both conventional mode and reverse mode switching. The benefit of printing such windows lies in the flexibility in the design, which can produce intricate patterns/logos with excellent print resolution. These printed smart windows are particularly suited to modern architectural design features where they can serve the purpose of being both aesthetically pleasing and energy-saving by controlling the amount of light that is transmitted into or out of a building.

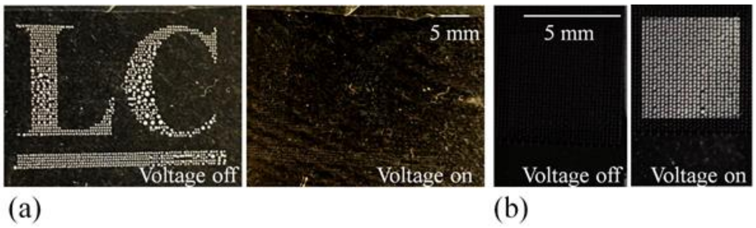

Figure 5.13 Printed patterns and arrays of PSCLC droplets (93.5 wt% E7, 3 wt% BDH1281, 3 wt% RM257, and 0.5 wt% IR819) operating in (a) conventional mode and (b) reverse mode. The droplets were printed at a temperature of 68 °C with an 80 µm nozzle and photopolymerized at 25°C with an electric field of E = 5 V/µm for (a) and without an electric field for (b). The cell gap of the two devices was 10 µm (conventional mode) and 8 µm (reverse mode). The droplet diameters were all approximately 110 µm. These figures were taken indoors under ambient lighting conditions, with a dark background as the backdrop.

5.4 Summary

In this chapter, I have demonstrated the functionality of printed liquid crystal smart windows and discussed the advantages of employing inkjet printing technology over conventional film devices. Initially, a PDLC film-based smart window was presented, which remained in a light scattering state in the absence of a voltage and becomes transparent upon suitable voltage application. In this case, the benefits of printing are demonstrated through the creation of a College crest that can be made to appear or disappear with the application of a voltage.

Drop-on-demand inkjet printing was then used to fabricate polymer-stabilized chiral nematic liquid crystal (PSCLC) privacy windows that can be made to operate in either a scattering to transparent (conventional) or transparent to scattering (reverse) mode by changing the photopolymerization conditions. On the whole, the electro-optic characteristics observed for the printed droplets operating in either mode were found to be comparable to those recorded for the corresponding thin film devices. One key difference was that the fall-time of the printed reverse mode droplets was significantly longer than that recorded for the thin-film devices; this is believed to be due to the difference in the thickness of the printed droplet and thin-film devices.

Printed arrays of PSCLC droplets provide complete freedom of design in terms of the patterning that can be achieved, and this has been used to fabricate demonstrative panels operating in either mode. Specifically, in this work, we used printed alphanumeric characters to demonstrate that they can be made to disappear with the application of an electric field for the conventional mode and that a printed square array can be made to appear with an electric field for the case of the reverse mode. The approach presented in this work could have the potential ability to provide a route towards the fabrication of versatile and bespoke panels that can display images and signage without the need for photomasks and complex lithography processes.

CHAPTER 6 Printed Liquid Crystal Optical Vortex Beam Generators

6.1 Introduction

An optical vortex beam is a type of optical light beam that exhibits a number of remarkable features including helical phase fronts, a region of zero intensity at the centre of the beam, and orbital angular momentum. These unique characteristics have meant that vortex beams can play an important role in a wide gamut of applications such as optical tweezers[149-151], optical communications[152-153], quantum entanglement[154-155], nanotechnology[156], nonlinear optics[157-159], optical machining[160], astronomy[161], microscopy and imaging[162-164], biomedicine and chemistry[165-166], and metrology[167]. These diverse applications have therefore demanded the development of methods with which to generate optical vortex beams. The essence of generating a vortex beam is based upon changing the phase of the input light into one that represents a helical structure. This process can be realized in a number of ways including by using spiral phase plates[168-170], diffractive optical elements[171-172], computer-generated holograms[173-175], segmented deformable mirrors[176-177], nanostructured glass plates[178], spatial light modulators[179-181], mode converters[182-183], helical mirrors[184], dielectric wedges[185], and metasurfaces[186-188].

Liquid crystals (LCs) are a desirable medium for vortex beam generation as they exhibit a natural birefringence, can form complex spatial profiles of the retardance and thus the resulting optical phase, and their internal structure (i.e., the director) and thus the optical properties can be tuned by an applied voltage. Previous demonstrations of vortex beam generation using LCs have included the formation of inhomogeneously aligned nematic LC such as q-plates[189-190] and LC droplets dispersed in other media[190-191] that form vortex beams with different topological charges. Additionally, umbilics[190, 192] formed inside LC cell as well as homeotropic LC light valves (LCLV)[190, 193] have also been shown to form similar structures.

Distinct variants of LC-based vortex beam generators utilize a common operational principle, which involves exploiting the inherent birefringence of LCs. This principle enables the modification of the phase distribution of an incoming Gaussian light beam, facilitating its conversion into a vortex beam. Despite the similarity in operational mechanism, these generators exhibit considerable disparities in terms of their fabrication processes, particularly with respect to their levels of intricacy and the supplemental materials needed for their construction.

6.1.1 Q-plate type LC-based vortex beam generator

In the fabrication process of the aforementioned LC-based q-plates, key steps include the utilization of various polarization-sensitive alignment techniques, such as those involving azo dye or SD1, to form the LC director alignment with specific topological charges, or the employment of multiple LC-based bit cells with electronic regulation[194] for controlled distribution of the LC director. With these approaches, a range of experimental processes have been adopted, such as the integration of sectoral photoalignment[189], with the capability to form intricate light field distributions characterized by a controlled quantity of singularities. Alternatively, other research studies have opted for more straightforward photoalignment methodologies[195], each tailored to the specific requirements.

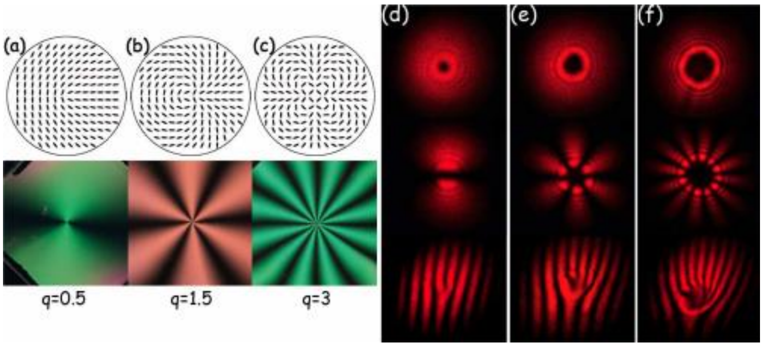

Figure 6.1 (a–c) Examples of LC patterns possessing distinct topological charges, accompanied by photographs of the corresponding samples as observed under crossed polarizers. (d–f) CCD images capture the intensity beam profile, which are generated by the q-plates depicted in (a–c) when they undergo tuning. Both circularly polarized (top) and linearly polarized (middle) input beam polarizations are represented. Additionally, the corresponding interference patterns with a plane wave are included (bottom). [195] Reproduced from ref [195], with permission of Optica Publishing Group. © 2011 Optica Publishing Group.

Figure 6.1 illustrates an application of photoalignment technology to orient the LC director according to specific patterns, as depicted in sections (a-c), each corresponding to a unique topological number. When light passes through these LC configurations, its phase undergoes a modification characterized by different rotational transformations, determined by the topological number. As observed under crossed polarizers, the LC director distribution leads to a rotation of alternating bright and dark stripes, a phenomenon visibly captured in Figure 6.1. The transmitted far-field patterns through the LC-based q-plate are detailed in sections (d-f), each corresponding to a distinct topological number. As a result of this process, the emergent vortex beam displays a characteristic donut-shaped intensity distribution, indicating a direct relationship between the LC director alignment and the resultant beam profile.

Figure 6.2 presents an example of an adjustable q-plate system with n-bits order, a sophisticated design that allows specific optical functionality. For this system, each bit is composed of an LC-based q-plate coupled with a conventional LC-based wave plate. The working principle is centred around the controllability of the phase delay within the LC devices, an aspect that can be manipulated by externally applied voltage. In details, if both the LC-based q-plate and the conventional LC-based wave plate is in full-wave condition, this bit cell won’t change the state of the input light. And if both of the component in half-wave state, this cell bit will then modulate the input light. This control over the phase delay, in turn, determines whether or not the beam modulation occurs and can be selectively governed by the electronic bit units within the system. The order of the q-plate, which is crucial in the formation of vortex beams, can thus be tuned by activating specific bit units. Consequently, this mechanism enables the generation of vortex beams with varied topological numbers, providing a versatile tool for tailoring complex optical fields.

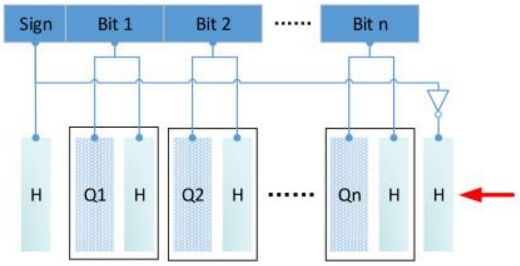

Figure 6.2 A schematic diagram illustrating the system of an adjustable q-plate with n-bits order. [194] Reproduced from ref [194], with permission of Optica Publishing Group. © 2019 Optica Publishing Group.

In general, the q-plate type of vortex beam generator offers the capability to generate vortex beams with various topological numbers. However, this method often necessitates the use of alignment layers such as SD1. Additionally, the implementation of photoalignment equipment or a complex bit voltage control system is required. As a consequence, the fabrication process can be intricate and laborious, or alternatively, the operational mechanism itself may present significant complexity.

6.1.2 LC-based grating vortex beam generator

Vortex beam production can be achieved using a particular grating configuration within the LC layer, a method employed in a range of photonic applications. The two chief gratings used for this function are fork gratings [196]and Dammann gratings[197]. Fork gratings form a unique diffraction pattern featuring anomalies situated at the beam's core, facilitating the formation of spiral phase contours vital for vortex beams. For the LC fork gratings, the fundamental principle lies in manipulating the LC director to emulate a hologram pattern resembling a fork, as illustrated in **Figure 6.3**.

At the dislocation within the centre of the LC layer, a phase dislocation occurs, thereby imparting a helical phase profile to the transmitted or reflected light. This results in the generation of a vortex beam. The fabrication process to achieve this can be implemented through various methods. Initially, a computer-generated hologram is created, as depicted in Figure 6.3. After this step, different techniques can be applied to utilize this hologram in controlling the LC director. One such approach is akin to the method used in q-plates, involving the alignment of SD1 according to the computer-generated pattern through photolithography to form the LC director's alignment layer[198]. This shares a comparable situation with the q-plate, in that the fabrication process is somewhat intricate.

Alternatively, the hologram pattern can be transmuted into a corresponding pattern of ITO electrodes through a process involving photolithography and wet etching. With the application of a voltage to the patterned electrode, the LC director can be controlled to adopt the desired arrangement [199]. This method offers the advantage of eliminating the need for a patterned alignment layer, thus reducing potential defects caused by such layers. The desired arrangement of the LC director can also be achieved by adding azo dyes, such as methyl red (MR), to the LC mixture. The MR molecules will deflect under light exposure, subsequently influencing the orientation of the LC director. By transmitting light through a mask made using the computer-generated hologram, the required LC director configuration can be obtained[200]. This technique centralizes most of the fabrication process on the creation of the mask, making it more suitable for applications that involve repetitive device production.

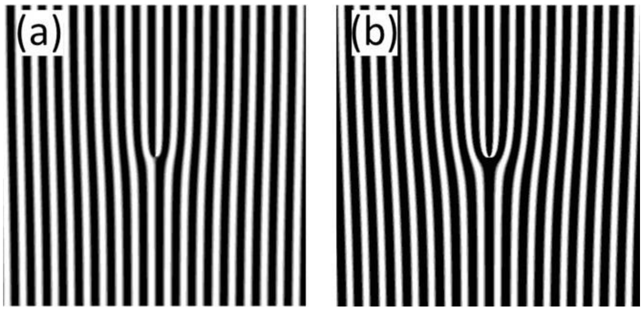

Figure 6.3 Computer-generated holograms with a topological charge of 1 (a) and 2 (b) [198] Reproduced from ref [198], with permission of John Wiley and Sons. © 2013 John Wiley and Sons. All rights reserved.

For the Dammann grating-based vortex beam generator, the capability to generate an optical array with equal energy distribution across its diffraction orders sets it apart. The fabrication process shares similarities with the previously described LC fork grating vortex beam generator. Specifically, it can be manufactured through the use of patterned electrodes, featuring a predesigned configuration that controls the orientation of the LC director when an electric field is applied[197]. Alternatively, the LC director can be directly managed through a photoalignment layer, utilizing the polarization-sensitive properties of sulfonic azo dye SD1[201].

For the grating types of LC-based vortex beam generators, one advantage lies in the ability to control the topological number of the generated vortex beam through computer-generated holograms. However, the fabrication process involves the use of techniques such as photolithography or the incorporation of costly and toxic materials, such as those found in photoalignment layer materials.

6.1.3 Spatial light modulator-based LC vortex beam generator

The LC-based spatial light modulator (SLM) represents a versatile type of vortex beam generator. In its operation, the SLM is programmed with a specific phase pattern that aligns with the desired topological charge of the vortex beam. This phase pattern imparts a helical phase front to the beam, spiralling the phase around the beam axis and inducing a phase singularity at the centre. Various methods can be employed to achieve this process. One such approach utilizes a Vector Optical Field Generator (VOF-Gen), capable of creating arbitrary light beams at the pixel level through a high-resolution reflective LC SLM, independently controlling phase, amplitude, and polarization[202]. Alternatively, the desired spatial phase distribution can be modulated by loading a computer-generated hologram onto the SLM[203]. Regardless of the method employed, the implementation typically involves the construction of a relatively complex optical system.

6.1.4 LC diffractive spiral plate-based vortex beam generator

LC spiral plate-based vortex beam generator represents a distinct category of vortex beam generators, operating on the principle of phase modulation through continuous refractive index variation in the azimuthal direction. This modulation can be accomplished via different techniques, such as employing a LC Diffractive Spiral Axicon (DSA)[204] or utilizing an electronically reconfigurable spiral phase plate[205]. Some of the fabrication process of this type of LC-based vortex beam generator involves the use of direct laser writing technology. This state-of-the-art technique can be applied for electrode patterning or for manipulating a polymer-stabilized LC mixture, thus ensuring the necessary alignment of LC director to achieve the desired phase-change distribution. The integration of these precise control mechanisms allows for the generation of vortex beams with specifically tailored properties, catering to various applications.

6.1.5 Self-assembled defect-based vortex beam generator

Through the intrinsic property of orientational elasticity, LCs have the ability to self-organize. This characteristic, coupled with the spontaneous generation of topological defects when subjected to external fields, paves a natural way for constructing geometric phase optical elements. The study of tunable optical vortex (OV) generators based on grid-patterned LC (GPLC) units utilizes the concept of self-assembled defects for vortex beam creation. This type of vortex beam generator requires a specific orientation of the LC director and is constructed in conjunction with patterned ITO electrodes[206].

6.1.6 LC droplet-based vortex beam generator

The LC droplet is dispersed within water, forming micron-sized spherical droplets. Under the influence of a surfactant (4’-n-pentyl-4-cyanobiphenyl, Aldrich), the LC director in these droplets assumes a radially symmetric 3D spatial structure, centred on the sphere's core. This behaviour stems from the creation of defects at the sphere's centre, leading the LC director to distribute around this defect, as illustrated in **Figure 6.4**. Coupled with the birefringent properties of the LC, this specific distribution gives rise to a helical wavefront, thereby generating a vortex beam. While the fabrication method for this LC droplet-based vortex beam generator is relatively straightforward, controlling the droplet's diameter proves to be a challenge. Consequently, customizing droplets according to different application scenarios is not easily achievable, which may limit the versatility of this approach in various optical engineering contexts.

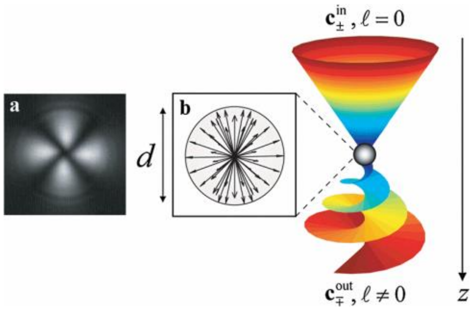

Figure 6.4 Generation of an optical vortex from a radial nematic liquid crystal droplet[191]. Reproduced from ref [191], with permission of the American Physical Society. © 2024 American Physical Society. All rights reserved.

A review of the diverse LC-based vortex beam generators uncovers unique strengths and weaknesses associated with each method. Broadly speaking, the majority of vortex beam generators demand intricate fabrication processes that may include alignment layers or encompass advanced techniques such as photoalignment, lithography, wet etching, and so on.

This category comprises q-plates, diffractive spiral plates, and self-assembled defect-based vortex beam generators. Some designs even require complex optical components, such as SLMs. The exception to this trend is the droplet-based vortex beam generator, which, while simpler to manufacture, does not offer the ability to tailor the droplet diameter to specific requirements.

In this chapter, an innovative technique for fabricating an LC vortex beam generator is presented that employs the use of inkjet printing technology. The vortex beam generator can be activated and deactivated by the application and control of an electric field, respectively. Providing a swift and user-friendly procedure, this approach enables the creation of high-order vortex beam generators and/or arrays. The resulting device is both compact and versatile, with on-demand fabrication and the ability to control beam generation, thus broadening the potential applications of vortex beams and facilitating their integration into various optical systems.

6.2 Device Concept

Based on the preceding description of vortex beam generation, it is evident that the fundamental mechanism revolves around the manipulation of phase distribution as light propagates through the device. The vortex beam generator can be conceptualized as a half-wave plate, as illustrated in **Figure 6.5**. Consider a single pixel within the half-wave plate. When circularly polarized light traverses the device, it undergoes a phase shift, resulting in polarized light with a phase difference of 2θ relative to the input polarized light. For instance, when right circularly polarized (RCP) light is input, the output is left circularly polarized (LCP) light with a 2θ phase shift.

When examining the entire half-wave plate, the polarized light's phase alteration depends on the direction of the fast optical axis. For a structured half-wave plate of order 2, meaning that the fast axis undergoes two full rotations from 0 to π, the input polarized light will be modified by this spatial distribution. As a result, with a predetermined input polarized light, the output will comprise polarized light with varying phase angles, as depicted in the right upper section of Figure 6.5. This output is referred to as a vector beam. In the case where the input light is RCP, the output on each segment of the device is LCP with distinct phase shifts. The resulting beam is termed a vortex beam, and this principle underpins both the device's concept and its operational mechanism.

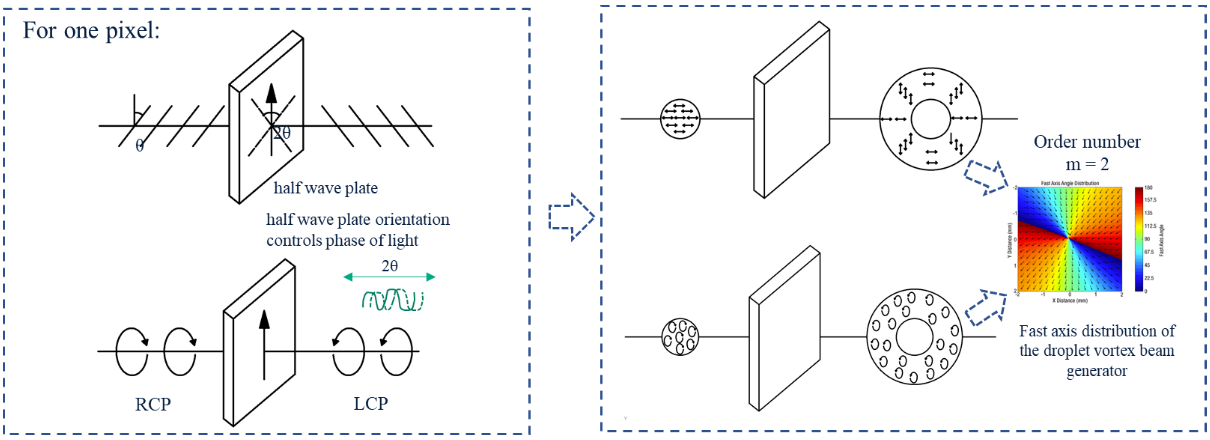

Figure 6.5 Device concept of the vortex beam generator. The left box demonstrates that for one point on the droplet device, when the input light is linear polarized light, the output is linear polarized light with 2θ shift. When the input light is left-handed circular polarized light, the output is right-handed circular polarized light with 2θ shift. The right box shows the whole device can be considered as a halfwave plate with order number of 2.

6.3 Simulation of printed LC droplet vortex beam generators

For the simulations, a two-pronged approach was adopted. Initially, the device was treated as a half-wave plate that produced promising far-field simulation results. Subsequently, this half-wave plate was substituted with the simulation of the LC director distribution, facilitating the computation of both the retardance and fast axis distribution. The procedure begins with the configuration of predefined variables, encompassing the Gaussian laser beam's traits, peak field constituents, and the Gaussian beam's location. The next step involved generating the Gaussian beam that served as the input light field. The beam's amplitude profile was carefully set up over the computed area, utilizing a looping mechanism that covered each point in the input *x-y* plane. Subsequently, the propagation of this light wave through a half-wave plate was simulated.

The Jones matrix, a mathematical framework, represented this layer's optical properties. The Jones matrix was computed at each field point, incorporating the orientation profile of the LC droplet that generated the vortex. Following this, the overall output field and light transmission through the waveplate structure were computed to model the optical system's performance. Afterwards, the far-field patterns were calculated by transforming the data into the spatial frequency domain. The process concluded with the generation of a visual representation, illustrating the total intensity of the input light field, the structure's transmission between crossed polarizers, the far-field intensity components, and the total output intensity.

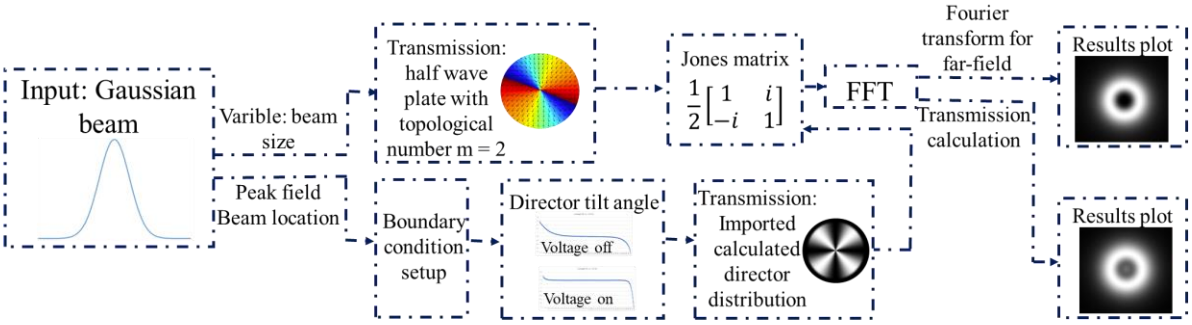

Figure 6.6 The two processes for the far-field simulation. For each simulation, the input light beam is a Gaussian beam with changeable beam size, peak field and beam location. The first row is the demonstration of using the half wave plate as the device. The second row demonstrates using the simulated LC director in the process.

This model was further modified by using the simulated LC director distribution. The retardance and fast axis distribution were then calculated from this LC director distribution. The simulation procedure was based on the definition of certain constants, which included the elastic constants of the LC and the applied electric field. Following the initial setup, grid points were defined in both the axial and radial directions while specifying the number of relaxation iterations and the corresponding parameter. These selections influence the simulation grid's structure and the characteristics of the relaxation process, subsequently impacting the accuracy and convergence properties of the simulation.

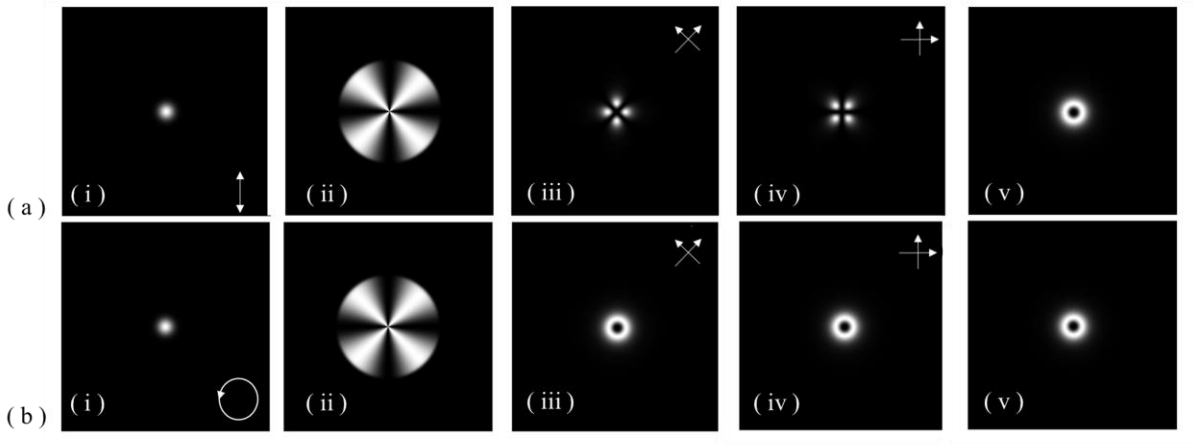

Figure 6.7 Simulation results when the device was treated as a half-wave plate, showing the generation of both vector and vortex beams. (a) vector beam generation: (i) The input light is linearly polarized. (ii) The retardance distribution of the half-wave plate is shown. (iii) The simulated far-field distribution is presented with a linear polarizer placed in front of the far-field. (iv) The simulated far-field distribution is depicted with a linear polarizer, rotated 90° from the orientation in (iii), placed in front of the far-field. (v) The simulated far-field results are shown without a polarizer placed in front. (b) vortex beam generation: (i) The input light is circularly polarized. (ii) The retardance distribution of the half-wave plate is illustrated. (iii) The simulated far-field distribution is shown with a linear polarizer positioned in front of the far-field. (iv) The simulated far-field distribution is exhibited with a linear polarizer, rotated 90° from the configuration in (iii), placed in front of the far-field. (v) The simulated far-field results are showcased without a polarizer positioned in front.

After configuring these parameters, two-dimensional arrays were created to monitor the evolution of the tilt across the grid points throughout the iteration process. Next, we set up the initial state for the tilt variable over the simulation grid, imposing specific boundary conditions at designated grid points to simulate real-world experimental scenarios. The simulation then advances through a relaxation procedure, involving a nested iteration scheme that traverses all grid points over a predetermined number of iterations. In the course of each iteration, the second derivatives of the tilt variable were calculated via a finite difference approach, and the torque elements related to the elastic and field components were determined. Upon the completion of these computations, the values of the tilt variable were revised based on the evaluated torque, marking the conclusion of a relaxation iteration. The updated values were subsequently transferred to the previously defined arrays for use in the ensuing iterations.

Figure 6.7 illustrates the simulation results discussed in the previous section, where the device was modelled as a half-wave plate. The top row displays results for a linearly polarized input beam. The corresponding far-field images are presented in the subsequent portions of this row. A simulation was conducted with a polarizer positioned in front of the far-field image plane that was rotated by 90°, the results are depicted in Figure 6.7(a) (iii) and (iv). These results indicate the generation of a vector beam. The bottom row, in contrast, shows the results for a circularly polarized input beam. The corresponding far-field images are depicted in the subsequent sections of this row. Again, a simulation was carried out with a polarizer placed in front of the far-field image plane that was rotated by 90° and the results are presented in Figure 6.7 (b)(iii) and (iv). These results confirm the generation of a vortex beam.

Figure 6.8 presents the simulation results obtained using the modelled LC director field. These results display a high degree of consistency when the device was approximated as a half-wave plate. By employing linearly polarized light as the input, as shown in Figure 6.8(a), and circularly polarized light, as depicted in Figure 6.8(b), simulations confirm the generation of vector and vortex beams, respectively. These results can be compared with those that will be displayed later that were obtained from experiments. Notably, there is a remarkable similarity between the two sets of results. Given the circumstances, a strong coherence between the two sets of simulation outputs and the experimental findings can be asserted.

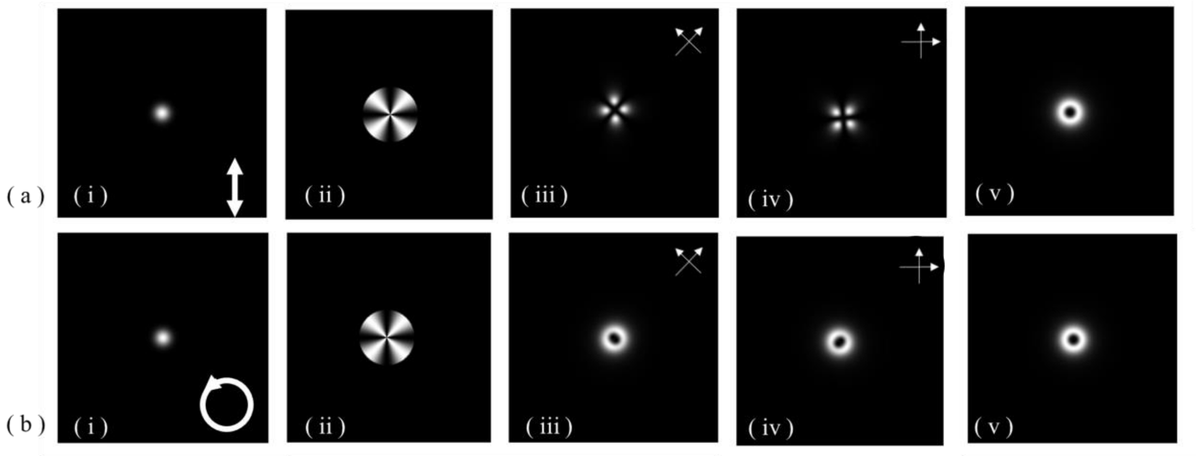

Figure 6.8 Simulation results derived from the modelled LC director distribution, highlighting the generation of vector and vortex beams. (a) vector beam generation: (i) The input light is linearly polarized. (ii) The retardance distribution of the half-wave plate is displayed. (iii) The simulated far-field distribution is shown with a linear polarizer situated in front of the far-field. (iv) The simulated far-field distribution appears with a linear polarizer, rotated 90° from its position in (iii), positioned in front of the far-field. (v) The simulated far-field results are depicted without a polarizer placed in front. (b) vortex beam generation: (i) The input light is circularly polarized. (ii) The retardance distribution of the half-wave plate is represented. (iii) The simulated far-field distribution emerges with a linear polarizer set in front of the far-field. (iv) The simulated far-field distribution is displayed with a linear polarizer, rotated 90° from its setup in (iii), placed in front of the far-field. (v) The simulated far-field outcomes are illustrated without a polarizer located in front.

6.4 Experimental Procedure

6.4.1 Materials

The nematic LC mixture, E7 from Synthon Chemicals Ltd with ordinary refractive index, n_o = 1.52, and extraordinary refractive index, n_e = 1.74, at a wavelength of 633 nm and a temperature of 20 ℃, was the primary material used in this vortex beam generator. Lecithin from Merck was diluted into a 1 wt.% solution in an isopropanol (IPA) solvent from Merck, that was used to align the LC director homeotropically. Polyvinyl alcohol (PVA) was purchased from Merck and dissolved in deionized water (DI water) at a temperature of 100 ℃ with magnetic stirring for 6 hours to obtain a 10 wt.% PVA solution.

6.4.2 Fabrication process

The whole vortex beam generator fabrication process is shown in **Figure 6.9**. ITO-coated glass slides (Ossila) were cleaned with acetone (VWR Chemicals), IPA, and DI water successively.

Lecithin solution (1% by weight in isopropanol) was then spin coated on the surface of the clean ITO-coated glass slide at 800 rpm for 2 min and left for a period of time to allow for the solvent to evaporate (Steps i to iii). The deposition of the lecithin solution was needed to ensure a homeotropic alignment of the nematic LC droplet at the LC/glass substrate. This treated substrate then served as a platform for the printing of the nematic LC droplet.

The printing procedure was executed utilizing a Jetlab-II system (MicroFab Technologies Inc), equipped with a three-axis translation platform that facilitated precise positioning of the LC droplets. An integrated camera provided real-time monitoring of the droplet shape and quality. Using a nozzle with an 80 μm inner diameter (MicroFab MJ-AT-01-80), the system printed LC droplets with in-flight and landed footprint diameters measuring 70 μm and 95 μm, respectively. The physical properties of the printed ink such as the viscosity and the surface tension can have much influence on the printing process. We investigated printing with a smaller nozzle than that presented here, with a 50 μm inner diameter. However, the printing process using such a nozzle is not very stable, due in particular to the combination of viscosity and surface tension of the LC. We therefore chose the 80 μm inner diameter nozzle to realize a stable and uniform printing process. The clearing temperature for E7 is 60 ℃ as introduced in Chapter 3.4.3. Therefore, if the temperature is above 60 ℃, the LC will be in the isotropic phase which is substantially less viscous than at room temperature. For these printing conditions, by printing 32 times at the same location, droplets with a footprint diameter of 280 μm were obtained. (Step iv).

Two spacers were attached to the sides of the slide. A second glass substrate spin-coated with a 10 wt.% wet polyvinyl alcohol (PVA) solution at 800 rpm for 30s (Steps v to vii)) was positioned over the printed LC droplet to make sure the PVA solution was in a wet state when attached to the other side. The device was then sealed with a UV-curable glue (NOA65). The whole device was then placed in a UVP Crosslinker (analytikjena) for 20 mins of UV illumination. After being sandwiched by the two ITO-coated glass slides, the thickness of the device was 27 μm and the diameter of the printed LC droplet was found to be 360 μm. This particular diameter was chosen based on our findings that the diameter of the droplet can influence the operational performance of the printed LC droplet device.

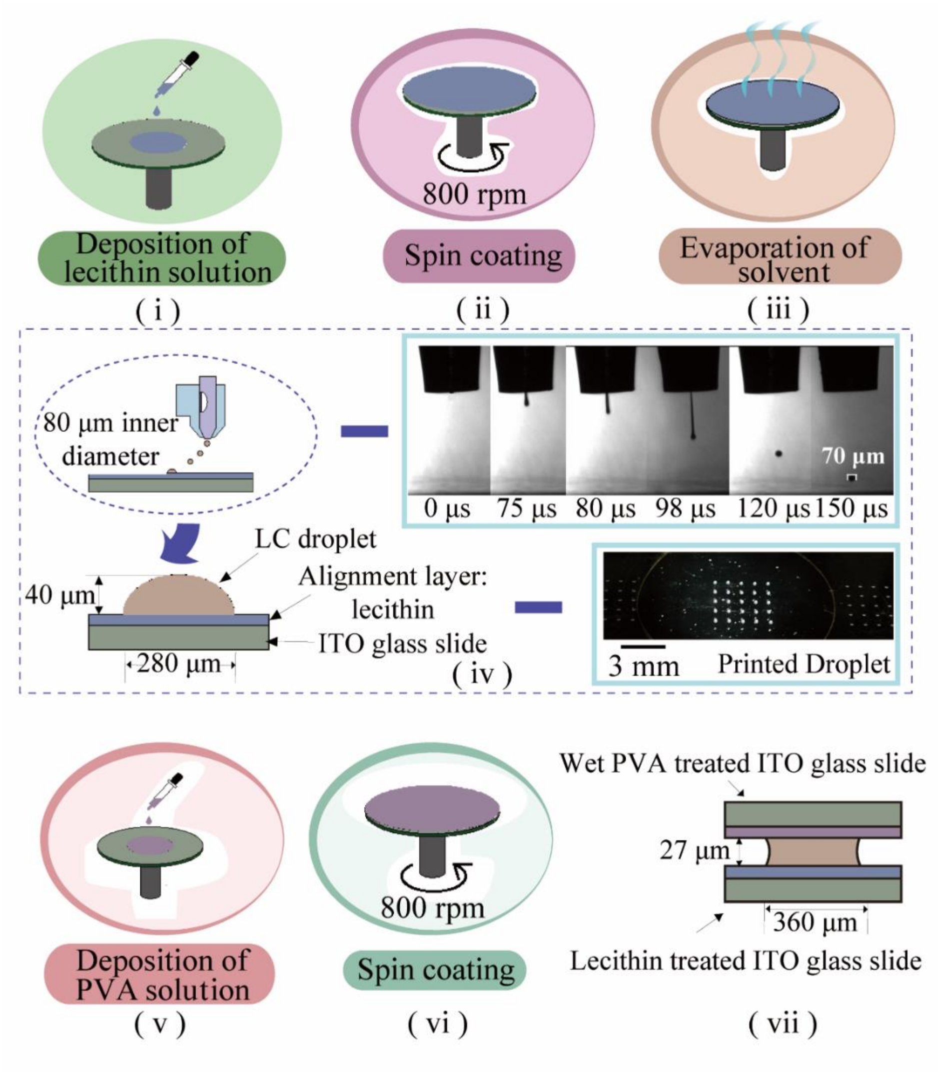

Figure 6.9 Fabrication process of the inkjet-printed LC vortex beam generators. (i) – (iii), deposition and spin-coating of the lecithin solution for the homeotropic alignment. (iv) process for printing LC droplets (and arrays thereof) onto the lecithin treated substrate. This includes an illustration of the side profile of a printed droplet, shadowgraphy images showing the deposition of the LC, and a photograph of a 5 × 5 array of printed LC droplets. The inner diameter of the printhead used in this work was 80 μm. 32 droplets were printed onto the same location on the substrate resulting in a final footprint diameter of the droplet of 280 μm. The height of the droplet was 40 μm. (v) – (vi) deposition and spin-coating of the wet PVA solution onto the top substrate to promote a radial alignment of the LC directly. (vii) Illustration of the inkjet-printed LC vortex beam generator device with a diameter of 360 μm and a height of 27 μm. The nematic LC in this case was the eutectic mixture, E7.

6.4.3 Retardance and Fast Axis Characterization

A Mueller matrix (MM) polarimeter was employed to assess the optical attributes of the devices, including retardance and fast axis orientation[207]. The method was based on the use of a polarization state generator (PSG), and a polarization state analyzer (PSA). Both the PSG and the PSA consisted of a polarizer and a motor-controlled quarter-wave plate, which allowed for rotation of these components. A set of 30 images were captured based on varying combinations of the PSG and PSA states. From these images, the MM of the devices was computed, subsequently enabling the decomposition of the retardance and fast axis distribution.

6.4.4 Far-field Images

The experimental assembly used to record the images in the far-field is shown in **Figure 6.10**. The process begins with a Helium-Neon laser, which acts as the principal source of light, generating a coherent and focused beam. The filter functions to uniformly diminish the laser beam's intensity across the whole light spectrum, thereby providing a layer of protection for the subsequent optical elements. Post-filter, a carefully aligned reflective mirror was employed to guide the attenuated beam towards a quarter-wave plate. The quarter-wave plate was a critical instrument in controlling the beam's polarization state. By rotating the plate's fast-axis, it generated the required input for the experiment - either linearly or circularly polarized light.

Once the light had passed through the quarter-wave plate, it encountered a lens. The lens was positioned to focus the incident laser beam onto the device., which ensured that the beam radius was contracted to be smaller than the device's diameter, enabling the entire device to be evenly illuminated. The device itself was linked to a function generator which applied an electric field. This field was increased in steps of 0.1 V_{PP} until it peaked at 9.12 V_{PP} which provided an electric field of E = 0.17 V/ µm. When subjected to this electric field, the device responded by producing a vortex beam.

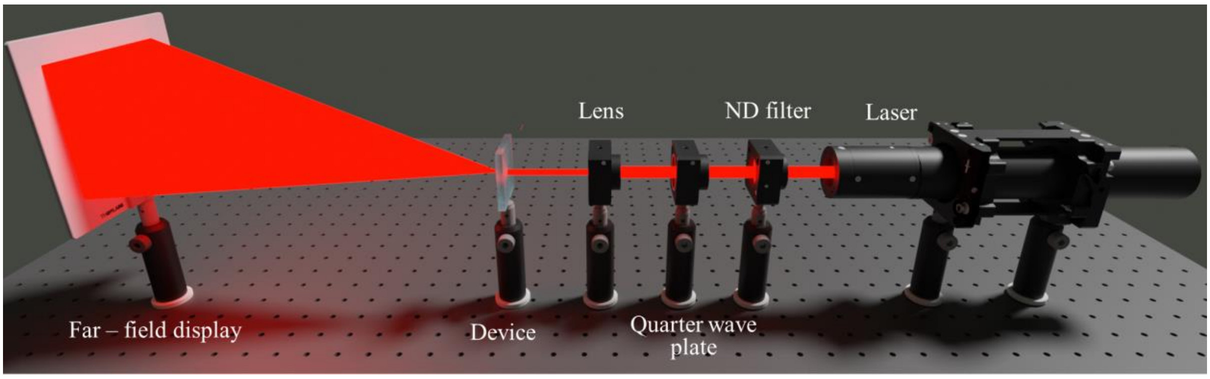

Figure 6.10 The optical configuration used to capture far-field images. The system consists of a laser source, a neutral density (ND) filter, a quarter wave plate, a lens and a white screen on which the far-field pattern can be observed.

6.5 Experimental results

Figure 6.11 illustrates the optical characteristics of a printed LC droplet on a lecithin-coated glass substrate (Figure 6.11(a)) as well as that for the printed LC vortex beam generator devices without (Figure 6.11(b)) and with (Figure 6.11(c)) an applied voltage. For each device, the series of images in each row is as follows: the initial image is of the optical texture on a polarizing optical microscope (POM) with crossed polarizers, followed by an image that depicts the optical retardance of the device. The third image in the sequence represents the fast axis distribution, and the sequence concludes with a schematic representation of the director distribution within the droplet/device. The changes observed in the optical properties when the droplet was assembled into a device and a voltage was applied can be attributed to changes in the distribution of the LC director within the droplet/device.

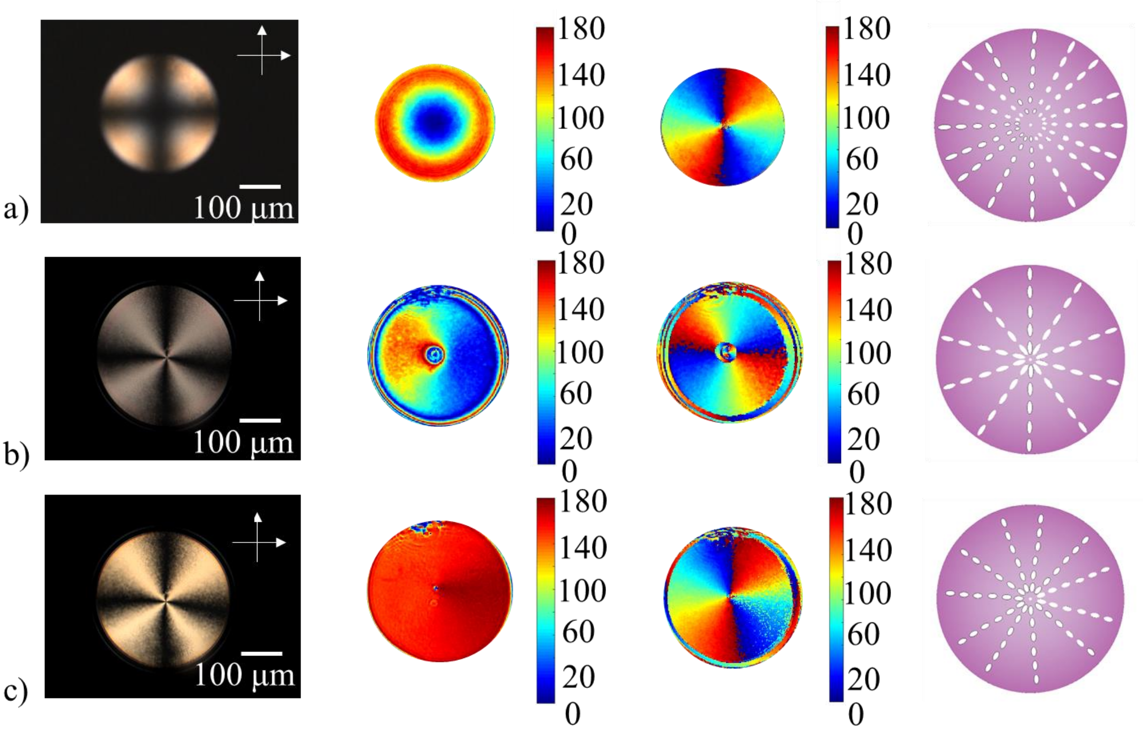

Figure 6.11 A comparison of the optical properties of a printed LC vortex beam generator. a) nematic LC droplet printed onto a lecithin-treated glass substrate; b) the printed LC vortex beam generator (i.e., printed LC droplet between a PVA-coated glass substrate and the lecithin-coated glass substrate) with no applied electric field; c) the printed LC vortex beam generator with an applied electric field of E = 0.17 V/µm (square wave, frequency = 1 kHz). The images in each row are as follows: the first image in this sequence is a polarizing optical microscope image (white single-headed arrows denote the orientations of the polarizer and analyzer) while the second image shows the corresponding retardance extracted from Mueller Matrix (MM) polarimetry. The third image shows the fast axis distribution (also obtained from MM polarimetry) and the fourth image illustrates the corresponding internal director distribution. The nematic LC was the mixture E7 and the measurements were carried out at a temperature of 25℃. The thickness of the device was 27 µm. The unit of the retardance and fast axis distribution is degree (°).

The optical properties (namely the retardance and orientation of the fast axis) were characterized using an MM polarimeter. This specific type of polarimetry based on the determination of the MM is capable of evaluating the anisotropic optical attributes of microstructures, including the birefringence and diattenuation[207]. When LC droplets were deposited onto lecithin-treated ITO slides, the LC director within the droplet generally aligned homeotropically, i.e., perpendicularly to the substrate surface and the air interface. However, due to surface tension, the director alignment shifted to become perpendicular to the interface of the LC droplet and the air inside the droplet. This resulted in the formation of a distinctive dark cross pattern under crossed polarizers, as depicted in Figure 6.11(a). These director distribution characteristics and the inherent birefringence properties of nematic LCs cause the droplet's retardance to increase to the highest value and then decrease at the edge of the droplet along the radius from the centre point to the edge.

When another ITO-coated glass slide, coated with a PVA layer, was introduced on top of the droplet, the director orientation altered to align parallel to the surfaces, at this interface thereby forming a 'windmill'-like director distribution structure. The corresponding retardance, demonstrated in Figure 6.11, exhibits marked differences compared to the pre-sandwiched LC droplet. However, the phase shift induced by the new LC director distribution still does not suffice to convert the incident linearly polarized light into a vortex beam. It is only when an appropriate electric field is applied normally to the glass substrates that a vortex beam is observed in the far-field. With the application of an electric field, the LC director tilts, causing the device to function as a half-wave plate with a vortex beam order number $m = 2$.

A comparative analysis of the retardance (2nd column in Figure 6.11) reveals that both the original (without an applied electric field, Figure 6.11b)) and the field-tuned device (with an electric field, Figure 6.11c)) display relatively uniform retardance distribution, albeit with different values. The field-off configuration displays a markedly uneven retardance, resulting in a broad range of values, whereas the field-on condition demonstrates a retardance ranging from 140° to 180°. This can be directly attributed to the tilt angle of the LC director within the device. Further discussion on the simulation of the director distribution will follow shortly. The fast axis (3rd column in Figure 6.11) undergoes a 2π shift in the azimuthal direction.

In the context of Figure 6.11(b), which shows the sandwiched device in a state without an applied voltage, a 90° shift was observed in the fast axis distribution. This shift arises from the algorithm employed for the calculation of the MM, as well as the subsequent decomposition process for the retardance and the fast axis distribution results. During data processing, the algorithm was designed to induce a flip when the retardance exceeded π, concurrently causing the fast axis to undergo a 90° shift. This phenomenon was not isolated to the case presented but also manifests in the outer ringing of the retardance in Figure 6.11(b) and the fast axis distribution in both Figure 6.11(b) and 6.11(c). The circular pattern in the central region of the field-off condition, as seen in both the retardance and fast axis orientation diagrams, can be attributed to a non-uniform director alignment in this area. This central region was minimized with the application of an electric field. Another phenomenon observed in this device is illustrated in Figure 6.11b). The POM image does not appear to be entirely consistent with the retardance measurements. This discrepancy can be attributed to the relationship between retardance and transmission intensity. In Figure 6.11b) and c), the retardance values are unwrapped within the range of 0 to 180 degrees. However, the actual retardance of the device is much higher than this range suggests. According to the Michel-Levy Birefringence Chart, when the retardance is very high, as in this case, the transmission intensity does not vary significantly despite changes in retardance. This limited variation in transmission intensity could lead to the apparent inconsistency between the POM image and the retardance data, as observed in Figure 6.11. For our droplets, the switching relaxation time is around 0.4s. The reason is that the response time of LC devices is generally controlled by the length scale of the structure formed, together with the elastic and viscous properties of the material. In our structures, the key length scale is the thickness of the LC layer. Therefore, the switching speed of our devices is very similar to that of a hybrid aligned nematic layer of 27 μm thickness. With E7, such a layer has a relaxation time of ~0.4s.

For a more comprehensive understanding of the changes in the tilt angle of the LC director under the influence of an electric field, simulations were conducted based on continuum theory as introduced in Chapter 2.2.4. As previously discussed, this theory takes into account the elastic free energy, which describes the correlation between energy and the distortion that results from any external influences. The free energy per unit volume (F_{v}) for an achiral nematic LC can be written as

$$F_v = \frac{1}{2} K_1[\nabla \cdot \hat{\boldsymbol{n}}]^2 + \frac{1}{2} K_2[\hat{\boldsymbol{n}} \cdot (\nabla \times \hat{\boldsymbol{n}})]^2 + \frac{1}{2} K_3|\hat{\boldsymbol{n}} \times (\nabla \times \hat{\boldsymbol{n}})|^2 \tag{6.1}$$

where $\boldsymbol{n}$ represents the director while K_1, K_2, and K_3 are constants representing the splay, twist and bend distortions of the director, respectively. These three constants describe the "rigidity" of the LC to director distortion. In this simulation, a 2-D model was employed utilizing a cylindrical coordinate system defined by the radial coordinate r, measuring the distance from the origin, and z across the device thickness. The angular coordinate θ, signifies the tilt angle between the positive x-axis and the line segment connecting the origin to the point. Following a minimization of the Euler-Lagrange equation we obtain,

$$\begin{aligned}
&\frac{\partial}{\partial\theta} - \frac{\partial}{\partial r}\left(\frac{\partial}{\partial\left(\frac{\partial\theta}{\partial r}\right)}\right) - \frac{\partial}{\partial z}\left(\frac{\partial}{\partial\left(\frac{\partial\theta}{\partial z}\right)}\right) = -\frac{2K_1}{r^2}\cos\theta\sin\theta + (K_3 - \\
&K_1)\sin\theta\cos\theta\left(\frac{\partial\theta}{\partial r}\right)^2 + (K_1 - K_3)(\cos\theta^2 - \sin\theta^2)\frac{\partial\theta}{\partial r}\frac{\partial\theta}{\partial z} - (K_1\sin\theta^2 + \\
&K_3\cos\theta^2)\frac{\partial^2\theta}{\partial r^2} + 2(K_1 - K_3)\sin\theta\cos\theta\frac{\partial^2\theta}{\partial r\partial z} + (K_1 - K_3)\sin\theta\cos\theta\left(\frac{\partial\theta}{\partial z}\right)^2 + \\
&(K_3\sin\theta^2 - K_1\cos\theta^2)\frac{\partial^2\theta}{\partial z^2}
\end{aligned} \tag{6.2}$$

A complete derivation is provided in the appendix. Simulations were carried out including parameters such as the diameter and height of the droplet vortex beam generator as well as the physical parameters of the nematic LC mixture, E7. As discussed, the optical properties of these devices are intrinsically influenced by the distribution of the LC director.

Figure 6.12 illustrates the director distribution in a cross-section of the droplet/droplet device, alongside their respective simulation results, including the retardance from the central point of the droplet device to the peripheral ring. Figure 6.12(a) presents the results for an LC droplet printed onto the lecithin-treated glass substrate before the assembly of the vortex beam generator device. Subsequently, Figure 6.12(b) displays the vortex beam generator device in the absence of any applied electric field, while Figure 6.12(c) shows the behaviour when an electric field was applied that was of the amplitude required for the director distribution to generate a vortex beam output. Each row in the figure presents a distinct set of sub-figures corresponding to different states. The first sub-figure in each row illustrates schematically the director distribution for the respective state. This is followed by a second sub-figure that depicts a 2D simulation of the LC director, extending from the central point to the outer ring. Subsequently, the third sub-figure shows the simulation results for the retardance, derived from the simulated director distribution diagram, thereby shedding light on the link between director distribution and the resultant retardance. The fourth sub-figure in each row presents the corresponding simulated fast axis distribution, which complements the preceding retardance simulation.

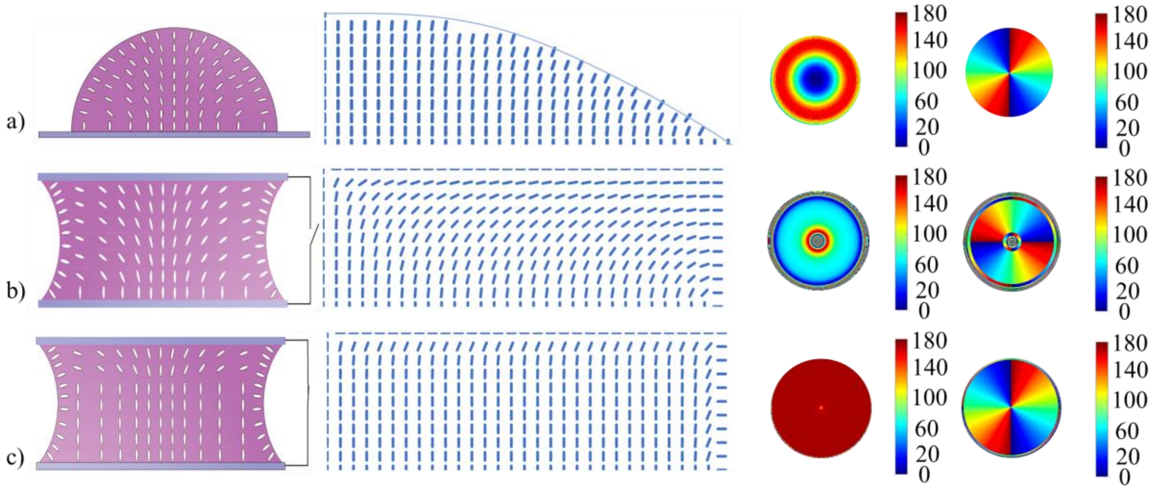

Figure 6.12 Simulations of the director distribution within the vortex beam generator. a) results for a single LC droplet printed onto a lecithin-treated glass substrate. b) vortex beam generator where no electric field is applied. c) vortex beam generation under conditions of appropriate electric field amplitude. For each depicted device, the sequence of images begins on the far left with a side view schematically illustrating the director distribution, then the respective director simulation results (ranging from the centre to the outermost ring), followed by the simulated retardance (3rd column) and fast axis profiles (4th column). The unit of the retardance and fast axis distribution is degree (°).

Considering the tilt angle of the LC director from the centre point to the outer boundary of the droplet reveals that different devices display distinct average tilt angles. For the single LC droplet printed onto the lecithin glass substrate, the tilt angle was found to continuously change. Using the average tilt angle of the LC director to represent the director distribution from the centre point to the outer boundary reveals that different devices display distinct average tilt angles. The retardance was calculated via the following equation:

$$R = 2\pi \int \left(\frac{n_e \cdot n_o}{\sqrt{n_o^2 \cdot cos^2\theta + n_e^2 \cdot sin^2\theta}} - n_o \right) \cdot \frac{dz}{\lambda} \tag{6.3}$$

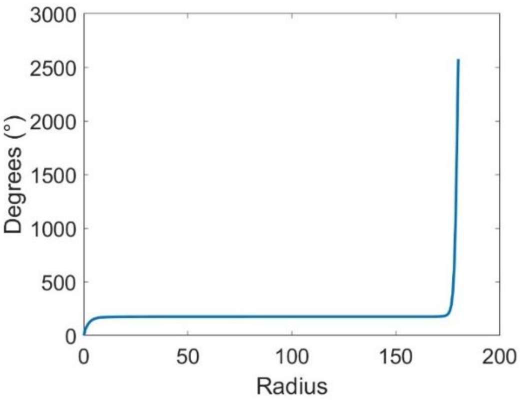

Figure 6.13 The accumulated retardance distribution along the radius of the printed droplet device with the electric field applied.

In the equation, the integral is taken along the z-direction, representing the cumulative optical effect across the physical thickness of the droplet device.; λ is the wavelength of the incident Gaussian beam; θ is the tilt angle of the LC director; n_e is the extra ordinary refractive index; and n_o is the ordinary refractive index of the LC. Therefore, the retardance is decided not only by the tilt angle of the LC director, but also by the thickness of the droplet device. For the single LC droplet printed onto the lecithin glass substrate, the average tilt angle was observed to change continuously. When the retardance was calculated based on this LC director distribution, it also varied, as demonstrated by the subsequent retardance image. This variability in retardance does not meet the requirements for vortex light generation. In the context of the vortex beam generator that operates without the application of an external electric field, the LC tilt angle distribution initially decreases, then stabilizes at a certain value before dropping to zero. However, when a suitable amplitude of the electric field was applied, the trend in terms of changes in the LC tilt angle remained the same, but the overall maintained value remained relatively high. This resulted in a different retardance profile. Nonetheless, as the LC director only tilts within the vertical plane, the direction of the director's minor axis remains in the annular direction.

One thing to note is that in the process of mapping retardance, the values were constrained to a range of 0 to 180°. This was done in order to be consistent with the images of retardance extracted from the Mueller Matrix (MM) polarimetry, which cannot measure the total accumulated retardance. The total accumulated retardance values under the application of an electric field are presented in **Figure 6.13.**

An analysis of the retardance and fast axis distributions, derived from the simulated director profile, indicates a strong correlation between the simulation results presented in Figure 6.12 and the experimental data obtained using a MM polarimeter as depicted in Figure 6.11, validating the efficacy of the modelling approach. There is evidently greater uniformity exhibited in the simulation results, particularly in terms of retardance, whereas it can be seen that there is some non-uniformity in the retardance in the experimental results. This discrepancy primarily stems from imperfections in the alignment layer leading to non-ideal LC director alignment. When an electric field was applied, the LC director reoriented under the influence of the electric field, resulting in relatively uniform retardance, and thus very good agreement between the results from simulations and experiments.

The simulation procedure was graphically presented in Figure 6.6. As previously introduced, the simulation commences with the introduction of a Gaussian beam as the input light, which be manipulated in terms of dimensions, peak intensity, polarization state and spatial positioning, thereby facilitating the investigation of the influence of these parameters on the eventual outcome. The Gaussian beam subsequently passes through a phase distribution zone, which was prescribed by the director distribution identified earlier. This zone plays a pivotal role in forming the input light into a vortex beam.

Following the determination of the phase distribution, the far-field pattern of the vortex beam can be ascertained through the deployment of the Fourier transform techniques. This computation offers a view of the manifested vortex beam, revealing its size, intensity, and location. In the final step, the simulation outcome is visually depicted as the resultant vortex beam, thus providing a representation of the entire process. This illustrative tool serves as a valuable resource for further exploration of vortex beam properties and the underlying processes governing their generation.

To relate these simulations of the far-field pattern, a set of experimental procedures were executed as detailed in the schematic presented in Figure 6.10. Examination of the device with a single printed LC droplet vortex beam generator, in both the non-electric field and non-optimal electric field conditions, revealed an absence of vortex light manifestation in the far-field. It was solely in the instance of the application of the electric field of the appropriate amplitude to the vortex beam generator device that a vortex beam, bearing the characteristic doughnut shape, emerged in the far field (Figure 6.7).

Results from the experiments are showcased in **Figure 6.14** for different input polarizations. Both vector and vortex beams can be generated depending on the characteristics of the incident light. For example, with linearly polarized incident light, a vector beam was created, as shown in Figure 6.14(a). Conversely, when the incident light was circularly polarized, it resulted in the formation of a vortex beam, demonstrated in Figure 6.14(b). A laser beam with a wavelength of 633 nm, when transmitted through the device, resulted in the formation of a vector beam, illustrated in Figure 6.14(a) (v), in the far-field. The corresponding far-field images, as seen in Figure 6.14(a) (iii) and (iv), were obtained by positioning a polarizer at a relative orientation of 90° between the device and the far-field. This exemplifies the generation process of the vector beam.

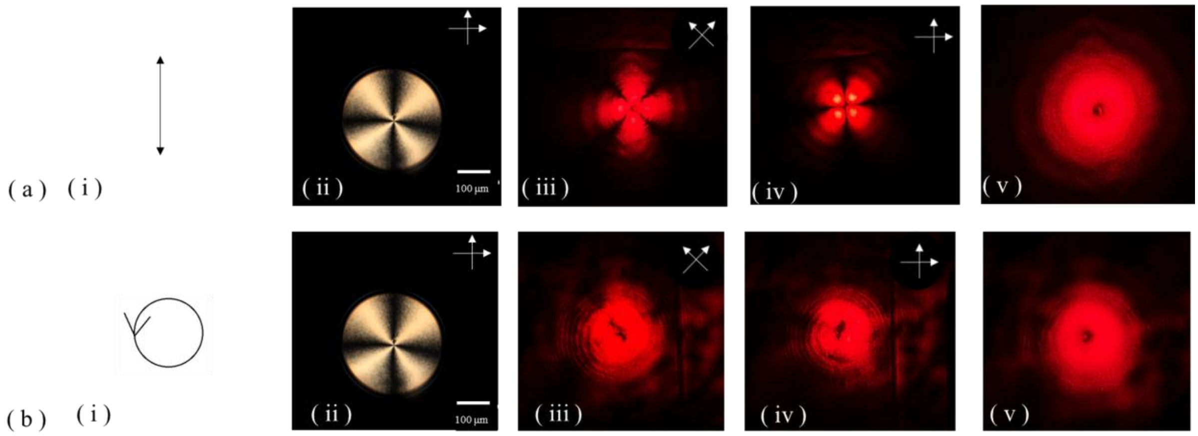

Figure 6.14 Generation of the far-field vector beam (with linearly polarized input light) a) and the vortex beam (with circularly polarized input light) b) for a printed LC device. (i) indicates that the input light is linearly polarized, and (ii) shows the vortex beam generation device on a POM with crossed polarizers and an electric field of $E = 0.17$ V/µm. (iii) and (iv) display the far-field images when the polarizer between the device and the far-field were set at angles of 0° and 90°, respectively. (v) demonstrates the far-field in the absence of a polarizer. For the vortex beam generation, (i) represents the circularly polarized input light, and (ii) shows the vortex beam generator device on a POM with crossed polarizers and an electric field of $E =$ 0.17 V/µm. (iii) and (iv) represent far-field images for orientations of the polarizer of 0° and 90°, respectively. (v) depicts the far field without a polarizer between the device and the far field.

In contrast, when the input light was circularly polarized, a vortex beam appeared in the far-field. Utilizing the same methodology, the two decomposed far-field intensities in mutually perpendicular directions are demonstrated in Figure 6.14(b)(iii) and (iv), which were obtained by introducing a polarizer and rotating it by 90° between the device and the far-field. The complete far-field intensity results, displayed in Figure 6.14(b)(v), represent a vortex beam. This elucidates the generation process of the vortex beam.

One thing needs to be considered is that the diameter of the droplet device will influence the generation of the vortex beam. The working principle for the vortex beam generator is based on the area of radial orientation of the LC director's alignment. Therefore, the working area is the area between the centre point and the outer area where the retardance is around π. As illustrated in **Figure 6.15**, for a very small droplet the director distortion extends over a large proportion of the area and the working area is too small to generate vortex beam. And for rather large droplets, the LC flow at the wet PVA surface during assembly means that the surface anchoring may not be able to form radial alignment over the entire droplet area. Following preliminary experiments, the 360 μm droplet device was chosen to generate the vortex beam generator as described in this paper.

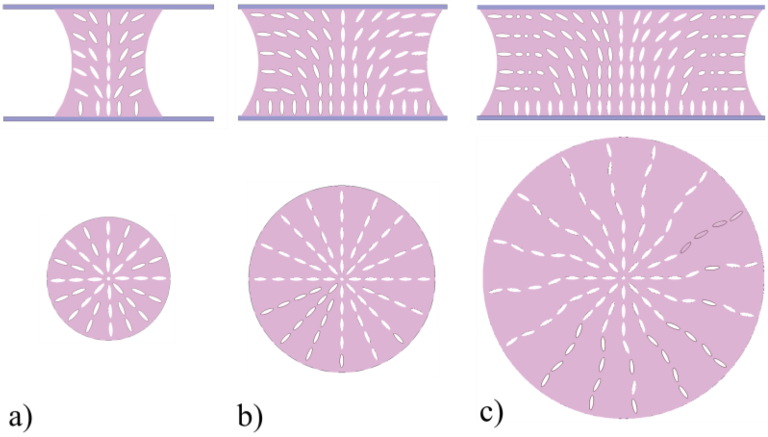

Figure 6.15 Demonstration of the influence of the device droplet diameter.

In this fabrication process, the LC director aligns in a specific way. When the LC is first printed on the lecithin treated substrate, it provides vertical alignment of the LC director at the substrate interface. Because of the surface tension, the LC director tends to align perpendicular to the interface of LC and the air as shown in Figure 6.12(a). When the wet PVA coated substrate is attached on the top of the printed droplet, due to the pre tilt of the LC director (caused by the surface tension), the LC director tends to align parallel to the wet PVA coated substrate along the pre tilt direction. This is because unlike rubbed PVA, the wet PVA provides planar alignment with no prior preferred direction. This provides the LC director configuration as shown in Figure 6.12(b) which following voltage application becomes the director profile shown in Figure 6.12(c).

In summary, the printed device offers an alternative and straightforward method for fabricating switchable vortex beam generators. Details comparing different vortex beam generators are available in **Table 6.1**. With drop-on-demand inkjet printing technology, the device we have reported here features a customizable design with a low thickness. This compact form provides the possibility for the generator to be integrated into various complex optical systems.

Table 6.1 A comparison of different optical vortex beam generators.

Optical elements	Fabrication technology	Topological number	Diameter of the device	Ref.
Spiral phase plate	Electron-beam lithography	1	-	143
	Direct laser writing	1,2,3	-	144
	femtosecond 3D direct laser writing	±1, ±2, ±3	diameter of 40 μm and a height of a few microns	145
Diffractive optical elements	3D printing of photosensitive resin material	0, ±1, ±2	Diameter:101.6mm height:6.997mm	146
	3D printing of rigid opaque material	0, ±1, ±2, ±3	76.2 mm	147
Computer-generated holograms	Analog camera	0, ±2, ±4, ±6	-	148
	Electron beam lithography	1	-	149
	Lithography	1, 2, 3	Around 100 μm	150
Segmented deformable mirrors	37-segment deformable mirror	1	-	151
	Deformable mirror	1,6,10	-	152
Nanostructured glass plates	Femtosecond laser writing	±1, ±2	1.2mm	153
Mode converters	Acoustically induced fibre grating	±1	-	157

	Mode selective coupler and an inner elliptical cladding fibre	±1	-	158
Helical mirror	PZT tubular actuator and mirror	1,2,3,4	25mm	159
Dielectric wedges	a stack of wedges	2,3,4	More than 1 mm	160
Metasurfaces	Electron beam evaporation	2	-	161
	The unit cell (two varactor diodes and three copper layers)	±1	10mm X 10mm	162
	Meta-atom (three metallic layers and two F4B dielectric layers)	1	11mm X 11mm	163
Our device	Inkjet printing	2	360 µm	-

6.6 Summary

In this chapter, we discuss a vortex beam generator, a critical tool in advanced optics. Various methodologies exist for fabricating such generators, although in this chapter discussion is focused those based on LC technology. LC-based vortex beam generators can be categorized into six distinct types: q-plates, gratings, spatial light modulators (SLM), diffractive spiral plate-based, self-assembled defects-based, and droplet-based. These different designs were considered, comparing their respective merits and drawbacks.

Following this comparative analysis, the chapter then delves into the design concept of the printed LC-based vortex beam generator presented in this thesis. The working principle and functionality of the design were substantiated through simulations and empirical measurements. Details of the device fabrication process were outlined along with the materials used and the precise methodologies employed for performance evaluation.

The results demonstrate an efficient and practical methodology for the generation of vortex beams utilizing a device that contains a sub-millimeter size LC droplet that has been fabricated using drop-on-demand inkjet printing technology. The representative device, possessing a footprint diameter of 360 µm and a thickness of 27 µm, can generate both vector and vortex beams upon the application of an electric field with an amplitude of $E = 0.17$ V/µm. The type of beam produced depends upon the polarization state of the incident light. The fabrication process of this device is highly versatile, with the added advantage of enabling customization in terms of the dimensions of the device and the ability to create arrays of vortex beam generators of different configurations. The technique can be readily translated to mass production for applications that potentially demand high volumes such as optical communications.

Through our discussion of vortex beam generation, we have explored both the working principles and applications of this technology. Building on this, the next chapter will delve into another crucial measurement tool: the Stokes polarimeter, which shows that printed LC droplet devices can be used for precise polarimetric analysis.

CHAPTER 7 Printed Liquid Crystal Droplet for Stokes Polarimetry

7.1 Introduction

A polarimeter is a scientific technique used to measure and analyse the polarization properties of light. A polarimeter provides offers additional information beyond the intensity of light, enabling a more comprehensive understanding of light properties and their interactions with materials or objects. The polarization data obtained through a polarimeter reveals crucial details about the composition, structure, optical characteristics, and environmental factors. This knowledge contributes to advancements in various fields such as biomedical research[208-209], material science[210], and environmental studies[210], encompassing diverse substances like cancerous tissue[211], bulk tissues[212], nanohole lattice[213] righthanded α-quartz[214], soil[215], and urban/manmade materials[216].

Among the different polarimeter measurements, the methods predominantly employed are the Stokes polarimeter[217-218] and Mueller Matrix polarimeter measurement[219-220]. The Stokes polarimeter was named after the Irish physicist George Gabriel Stokes[221], who made significant contributions to the understanding of light polarization. The primary function of a Stokes polarimeter is to measure the Stokes parameters, which provide a complete description of the polarization state of light.

7.1.1 Polarized light

Polarized light refers to light waves in which the direction of the oscillation of the electric field light vector remains constant or varies in a certain well-defined pattern. Only transverse waves have polarization properties. E.L. Malus discovered the polarization property of light in 1808[222]. Different objects have different effects on the polarization state of light. For example, when light passes through or reflects off different surfaces or passes through materials, the polarization state of the light can change. By detecting this change, information about the measured object can be obtained.

Polarized light can be represented in many different ways, including as a trigonometric function, a Jones vector[223], Stokes vector[224], on a Poincaré sphere [225], etc. Here, we mainly focus on the Jones vector and Stokes vector methods. For the Jones vector method, polarized light of any state is represented by two linearly polarized components with mutually perpendicular vibration directions. The arbitrary polarized light can be expressed as:

$$\begin{bmatrix} E_x \\ E_y \end{bmatrix} = \begin{bmatrix} E_{0x}\mathrm{e}^{j\delta_x} \\ E_{0x}\mathrm{e}^{j\delta_y} \end{bmatrix} \tag{7.1}$$

Separately, the Stokes vector, which was introduced by Stokes in 1954, consists of four parameters that can be represented as

$$S = \begin{bmatrix} I \\ Q \\ U \\ V \end{bmatrix} = \begin{bmatrix} S_0 \\ S_1 \\ S_2 \\ S_3 \end{bmatrix} = \begin{bmatrix} I_0 + I_{90} \\ I_0 - I_{90} \\ I_{45} - I_{135} \\ I_L + I_R \end{bmatrix} \tag{7.2}$$

where S_0represents the total intensity of the light; S_1 represents the difference between the polarization components in two orthogonal directions, horizontal and vertical; S_2 represents the difference between the linear polarization components in the two directions of -45° and 45°. S_3 represents the difference between the left-handed circular polarization component and the right-handed circular polarization component. Compared with the Jones matrix which can only represent completely polarized light, the Stokes vector can represent both completely polarized light and unpolarized light.

For fully polarized light

$$S_0^2 = S_1^2 + S_2^2 + S_3^2 \tag{7.3}$$

For unpolarized light

$$S_0^2 > S_1^2 + S_2^2 + S_3^2 \tag{7.4}$$

For natural sunlight

$$S_1^2 = S_2^2 = S_3^2 \tag{7.5}$$

Figure 7.1 shows different states of polarized light that are represented by the Stokes vector. For unknown light, the degree of polarization (DOP) is introduced to define the proportion of polarized light in this beam, which can be calculated as follows,

$$P = \frac{I_{\text{Pol}}}{I_{\text{tol}}} = \frac{\sqrt{S_1^2+S_2^2+S_{13}^2}}{S_0} (1 \geq P \geq 0) \tag{7.6}$$

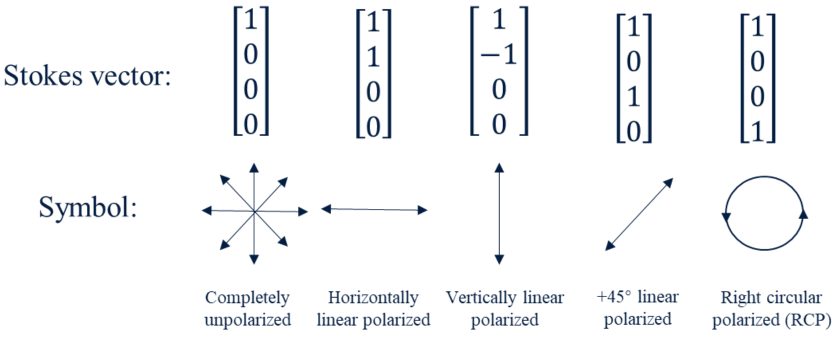

Figure 7.1 Stokes vector for different states of polarized light.

Aside from the DOP, the degree of circular polarization (DOCP) can also be used to represent the percentage of the circular polarization of the light that can be shown as follows,

$$DOCP = \frac{S_3}{S_0} \tag{7.7}$$

The degree of linear polarization (DOLP) defines the ratio of the intensity of linearly polarized light to the intensity of the entire polarized light,

$$OLP = \frac{\sqrt{S_1^2 + S_2^2}}{S_0} \tag{7.8}$$

7.1.2 Mueller Matrix Polarimeter

The Mueller matrix is a 4 × 4 matrix that can represent the polarization properties of a material or system. It can be used to analyze the polarization properties of various materials, such as polymer materials[226], biological tissues[227-229], and optical components[230]. The Mueller Matrix Polarimeter is a powerful tool in the field of polarization optics and can be used in a wide range of applications, including remote sensing[231-233], biomedical imaging[212, 234-236], and material analysis[214, 237-239].

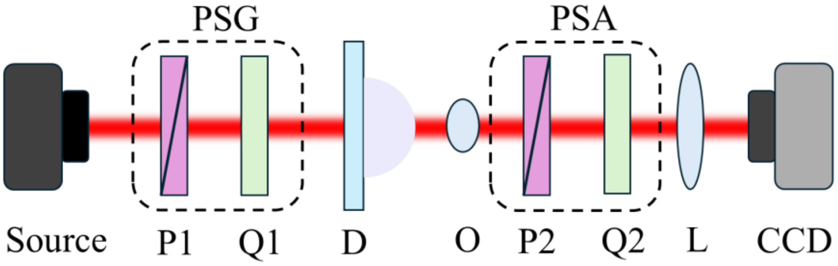

Figure 7.2 The typical experimental arrangement for the Mueller Matrix polarimeter when measuring the printed droplet device. L: lens; Q1, Q2: quarter wave plate; P1, P2: polarizer; D: the droplet device; O, objective lens. Light source: red LED with a central wavelength of 625 nm.

Figure 7.2 shows the experimental system of the Mueller Matrix polarimeter used in this work. In this setup, the Polarization State Generator (PSG) is used to generate polarized light with different states of polarization by rotating the quarter wave plate. The Polarization State Analyzer (PSA) is used to analyze the light beam that passes through the printed droplet device. The combination of the PSG and PSA can help to measure the state of the polarization of the light that passes through the droplet, enabling the polarization properties of the printed droplet device to be determined.

7.1.3 Stokes Polarimeter

A Stokes polarimeter is used to measure the state of polarization (SOP) of the light. When performing the measurements, generally four equations are required to be obtained so as to solve for the four parameters to obtain the polarization properties of the unknown beam. Therefore, the working principle of the polarimeter is to obtain four sets of equations in different ways, which need to generate incident light with four different polarization states, so that four sets of different light intensities are detected by the detector after passing through the measurement system.

There are two main types of polarimeters depending upon whether the data acquisition is time sequential or there is a simultaneous detection of Stokes parameters. Both types of polarimeter have advantages and disadvantages. For the time sequential data acquisition Stokes polarimeter, rotation of the component[240-241], photoelastic modulators[242], LC variable retarders[243] are the three main types that are used. Most of these are simple and easy to use but they can only provide static measurements and are time-consuming. Additionally, the photoelastic modulation polarimeter requires a high voltage although the switching speed for the phase retardance is fast compared with LC variable retarder polarimeters.

For the other type of polarimeter that enables simultaneous measurement of the parameters, these can be divided into division-of-amplitude polarimeter (DoAmP)[244-246], Division of aperture polarimeter (DoAP)[247-248], Division of wavefront polarimeter (DoWP)[249-251], and Division of focal plane polarimeter (DoFP)[252-254]. The DoAmP generally uses a polarizing beam splitter or other optical components to divide the incident light beam into four sub-beams which pass through different optical components and are received by four detectors. It does not need mechanical movements or electric signal addressing and offers a high-processing efficiency method. However, the optical system is complex and multiple CCD detectors are needed, which makes the whole system be bulky and expensive. DoAP also divides the light beam into four parts, but in this case the uses an objective lens and collimation optics to form the image of the objective lens aperture onto a mini-lens array which is then followed by a

CCD detector. Even though the DoAP only needs one detector, the optical system design is still complicated, and its implementation costs are high.

Aside from DoAmP and DoAP, DoWP is also an important type of Stokes polarimeter. To use the DoWP technique, it is necessary to first expand the incident light. After that, the light should be split into four separate beams, each of which will pass through different optical components. Typically, two of the channels will contain a linear polarizer (LP), while another channel will have a quarter wave retarder (QWR) followed by a linear polarizer. The remaining channel will be left clear of any components. However, this system has a high-quality requirement for the incident light. It must exhibit uniform polarization across its entire cross-sectional area. Additionally, the light that is transmitted from the sample being measured must illuminate each photodetector equally. In order to ensure accurate measurements, the absolute responses of all the photodetectors must be identical. Alternatively, the system can be calibrated to account for any differences in response. The experiment configuration used in this chapter is based on this later type of polarimeter (DoWP).

Finally, DoFP is a type of polarimeter that integrates micro-polarizer arrays onto the detector. Each group of four micro-polarizers includes polarizers oriented in four different directions (0, 45, 90, 135). This system is small in size and light in weight and is also easy to integrate into other optical systems. In addition to the polarimeters introduced above, there is also a type of polarimeter based on spectral modulation. This type of polarimeter has the capability to manipulate the polarization properties of the incoming light and map them onto the spectral dimension of the light wave. This results in the generation of a sinusoidal curve that exhibits regular variations in both the degree and angle of linear polarization. By applying demodulation techniques, it becomes possible to extract important parameters such as the degree of linear polarization, angle of linear polarization, spectral information, and intensity of the light.

The polarization of light transmitted through or reflected by an object can carry information related to it. Analyzing the information through the polarization state carried by the beam could help gain more information. For example, it could be used in atmospheric remote sensing [255], including the characterization of aerosol particles[256], scattering properties of the atmosphere and the cloudbow features[257]. Besides, in the target detection field, the Stokes polarimeter could help to analyze the characteristics of complex distributed targets. In addition, the Stokes polarimeter can be used for biomedical diagnosis[258-260]. It is a non-invasive, non-destructive *in vitro* detection method. Moreover, for the application of the earth's land surface detection, it could provide large-scale real-time monitoring by the help of a Global Navigation Satellite System which can provide information related to soil moisture, vegetation cover, etc[261]. Consequently, a Stokes polarimeter is a crucial measurement tool for a large variety of fields.

7.2 Division of Wavefront Polarimeter (DoWP)

As previously introduced, the operation of a wavefront polarimeter resides in the partitioning of incident light within the cross-sectional plane of the optical beam. Subsequently, the partitioned light beams are individually directed into distinct polarization analysis channels. Normally, each of these polarization analysis channels necessitates bespoke optical elements and a minimum of four such channels are imperative. The operational concept of the Degree of Polarization (DoWP) is illustrated in **Figure 7.3**. Defined by four Stokes parameters, the solution of the indeterminate parameters requires a minimum of four distinct equations, thus entailing four measurements. The variable "M" within the illustration signifies the varied optical characteristics inherent to the optical components traversed by the incident light, imparting potential alterations upon the polarization state of the incoming light. The symbol "D" within the diagram designates the detector located within each channel, exclusively capable of recording the light's intensity, denoted as "i". The inclusion of four channels in the system introduces a layer of complexity that not only complicates calibration but also has the potential to induce additional errors.

In this chapter, we explore a single-shot measurement method that leverages the unique properties of printed LC droplets. As indicated in Chapter 6 (Figure 6.12), the LC director distribution within the droplet gives rise to spatial variations in optical retardance and fast axis orientation across the droplet area. It follows that each point on the droplet possesses distinct optical characteristics capable of altering the polarization state of incident light. Consequently, it is potentially feasible to achieve comprehensive polarization measurements by employing just four strategically selected points on the printed LC droplet device.

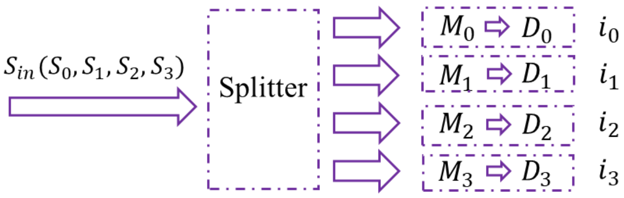

Figure 7.3 The working principle of a Division of Wavefront Polarimeter (DoWP).

The experimental setup is depicted in **Figure 7.4**., which consists of a PSG that includes a collimating lens, a bandpass filter, a polarizer, and a quarter-wave plate. These components are utilized to generate various states of polarization (SOP) which are used to mimic the unknown input polarized in the measurement procedure. It is not a part of the polarimeter. The LC droplet polarimeter, another component of the setup, comprises a printed LC droplet, an imaging lens, a polarizer, and a camera. The LC droplet plays a crucial role in analyzing the polarization state of the incident light. The imaging lens helps to image the light onto the LC droplet, while the polarizer allows the selection of different intensities of different SOP on its polarization orientation. The camera captures the transmitted light and facilitates the measurement and analysis of the polarization state.

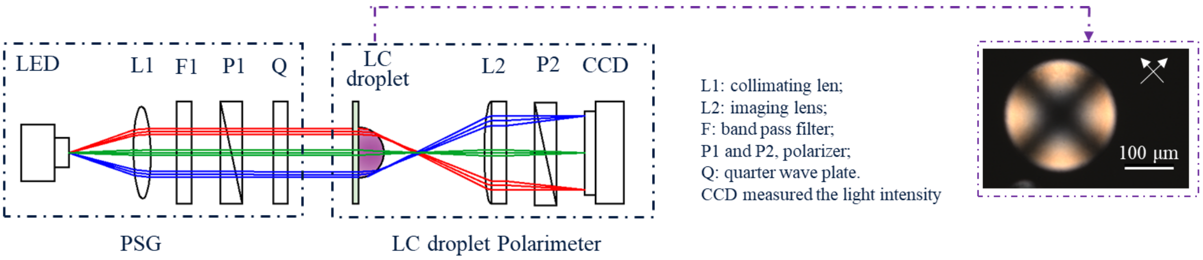

Figure 7.4 Experimental setup of the printed LC droplet Stokes DoWP. The diameter of the printed droplet is 365 μm. L1 is a collimating lens; F1 is a band pass filter; P1 and P2 are polarizers; Q is a half wave plate; LC droplet is the printed device; L2 is an imaging lens. Light source: red LED with a central wavelength of 625 nm.

The polarimeter, based on the printed LC technology that is the subject of this thesis, comprises a mere four components: a printed LC droplet, a lens, a polarizer, and a CCD camera. This streamlined design obviates the need for mechanical manipulation of the optical elements, the division of light paths into multiple beams, or the incorporation of an electrical control module. As a result, the configuration is both cost-effective and elegantly simple.

7.3 Droplet device fabrication and characterization

Figure 7.5 illustrates the fabrication process of the inkjet-printed LC droplet Stokes Polarimeter, which was carried out using a computer-controlled Microfab Jetlab II printer for automated printing, as described in Chapter 3.3.2. The process commenced by spin-coating a lecithin solution, composed of 0.02% lecithin and 99.98% Isopropyl Alcohol, onto glass slides that were previously cleaned with acetone, at a spin rate of 1200 revolutions per second. This layer encourages a homeotropic alignment of the LC director, as depicted in the upper left corner of Figure 7.5. During the printing phase, a nozzle with an inner diameter of 80 μm was utilized. The lower portion of Figure 7.5 features shadowgraph imagery that captures the entire printing process, from meniscus formation to the production of an individual droplet and its eventual deposition onto the pretreated substrate.

The smallest achievable droplet diameter in mid-air was found to be about 70 μm, but it expands to approximately 100 μm upon contact with the substrate, in accordance with the observations presented in the previous chapters. To create a larger droplet, a technique of depositing 62 droplets at a single point was employed, resulting in a droplet with a final diameter of 365 μm as described in Chapter 6.4.2. The image of the printed LC droplet can be seen in the bottom right of Figure 7.5, showcasing the uniform diameter of the droplets. Additionally, a side view of the printed LC droplet is represented in the figure above it. The upper right corner of Figure 7.5 details the specific printing parameters used. A wave of 50 Vpp was applied to trigger the piezoelectric actuator within the printhead, with the entire process lasting 43 seconds.

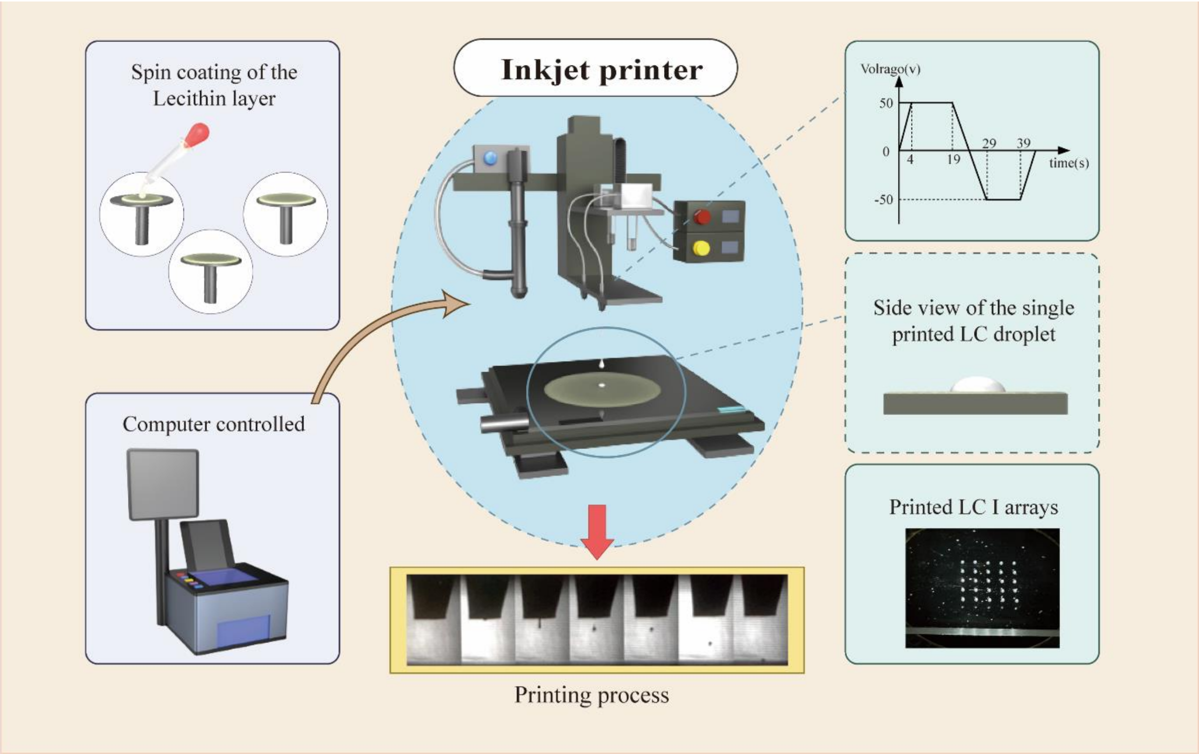

Figure 7.5 The device fabrication process of the printed LC Stokes DoWP. Central in the figure is the Microfab JetLab II printing system, which is operated through computer control to facilitate automated printing. In the upper left quadrant of the figure, we observe the pre-treatment of glass slides, a step crucial for fostering homeotropic alignment in the LC director. The upper right portion of the figure presents the printing parameters that are instrumental in actuating the piezoelectric element within the printing nozzle. These parameters are vital for driving the internal piezoelectric component of the printhead. Situated at the bottom of the figure is the shadowgraph imagery, providing a visual account of the inkjet printing process. Finally, the lower right corner showcases an array of printed LC droplets.

Figure 7.6 depicts a printed LC droplet as viewed on a polarizing optical microscope with crossed polarizers. The diameter of the printed droplet is 365 μm. As elaborated upon in Chapter 6, the LC director is oriented perpendicularly to both the substrate and the droplet surface. This specific alignment of the LC director, combined with the birefringent property of the LC, gives rise to unique optical effects. Specifically, regions where the LC director aligns with the direction of the polarizers tend to block light transmission, resulting in a black appearance. Conversely, other areas of the droplet permit the passage of light with varying intensities, leading to a display of different brightness levels or intensities when observed under the microscope.

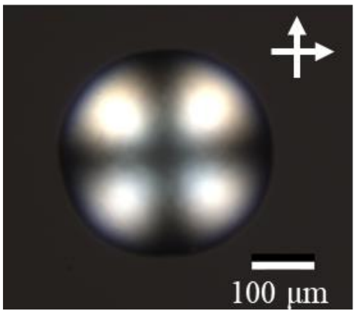

Figure 7.6 The printed LC droplet on a polarizing optical microscope with crossed polarizers (indicated by the single-headed white arrows). The diameter of the droplet is 365 μm.

7.4 Results and discussion

As discussed, each point on the droplet can be considered as a wave plate with a distinct fast axis direction and retardance. Then the whole printed LC droplet device can be considered as having *n* identical sub-beams incident on *n* miniature wave plates. In theory, measuring four points on the droplet would suffice since the Stokes parameters contains four unknown parameters. However, increasing the number of measurement points reduces the potential error.

Figure 7.7 shows the patterns of retardance and the orientation of the fast axis within the printed LC droplet. This was measured with a Mueller matrix polarimeter as introduced in

Chapter 5. The retardance gradually increases from zero at the central points to 180° when moving along the radial direction, and then decreases back to zero at the outer edge of the droplet. Simultaneously, the orientation of the fast axis undergoes two cycles of increasing from zero to 180° in the azimuthal direction. The principle of this configuration can be described as follows: A paraxial beam, characterized by a consistent SOP, enters the initial face of the apparatus, which can be conceptualized as a series of *n*/2 diminutive wave plates with varying degrees of retardance and fast axis orientation owing to the symmetrical construction of the device. This interaction culminates in the generation of distinguishable patterns observable on the CCD.

Given that both the wave plates and polarizers are representable via the Mueller matrix, the Stokes parameters of the incident light can be determined. This process is facilitated by measuring the intensity of the light beam as detected by the CCD, which fluctuates in response to the diverse SOPs that emerge from distinct sections of the droplet device. **Figure 7.8** displays the images captured by the CCD, corresponding to standard input SOPs. These include linearly polarized light at 0° (H), 90° (V), 45° (P), and 135° (M), as well as left-hand circular polarized light (L) and right-hand circular polarized light (R).

If we denote the input light as $S_{in} = \left(s_{in_0}, s_{in_1}, s_{in_2}, s_{in_3}\right)$, and the light beam captured by the CCD as $S_{out} = \left(s_{out_0}, s_{out_1}, s_{out_2}, s_{out_3}\right)$, with '$M_P$' representing the Mueller matrix of the polarizer and '$M_{droplet}$' representing the Mueller matrix of the droplet device, we can express their interrelationship through the following equation,

$$S_{out} = M_p \cdot M_{droplet} \cdot S_{in} \tag{7.9}$$

However, it's important to note that the CCD can only register the intensity of the received light beam. As a result, only the first row of the Mueller matrix can be utilized for computation. Hence, the first row of M_p is denoted as

$$M_P(1,:) = \left(T_t, T_t, 0, 0\right) \tag{7.10}$$

where T_t signifies the transmission ratio along the transmission axis, disregarding the transmission ratio along the extinction axis.

As previously discussed, the Mueller matrix of the droplet device can be conceptualized as n small waveplates where n is the pixels of the image captured by the CCD, each with different retardance δ_n and fast axis θ_n. The measurement process allows us to obtain results in a single, direct attempt. In light of this, we can express '$M_{droplet}$' as follows:

$$M_{droplet} \approx \begin{bmatrix} 1, & 0, & 0, & 0 \\ 0, & \cos^2 2\theta_n + \sin^2 2\theta_n \cos\delta_n, & 0.5\sin 4\theta_n\left(1-\cos\delta_n\right), & -\sin 2\theta_n \sin\delta_n \\ 0, & 0.5\sin 4\theta_n\left(1-\cos\delta_n\right) & \sin^2 2\theta_n + \cos^2 2\theta_n \cos\delta_n & \cos 2\theta_n \sin\delta_n \\ 0, & \sin 2\theta_n \sin\delta_n & -\cos 2\theta_n \sin\delta_n & \cos\delta_n \end{bmatrix} \tag{7.11}$$

If Equation (7.10) and Equation (7.11) are brought into Equation (7.9), the following result can be obtained

$$s_{out_{0n}} = T_t \cdot s_{in_0} + T_t \cdot \left(\cos^2 2\theta_n + \sin^2 2\theta_n \cos\delta_n\right) s_{in_1} + 0.5 T_t \cdot \sin 4\theta_n \left(1-\cos\delta_n\right) s_{in_2} - T_t \cdot \sin 2\theta_n \sin\delta_n s_{in_3}, \tag{7.12}$$

The $s_{out_{0n}}$ represents the intensity of the nth pixel recorded by the CCD. Therefore, the total intensity could be expressed as follows,

$$I = \left(s_{out_{01}}, s_{out_{02}}, s_{out_{03}}, s_{out_{04}}, \ldots, s_{out_{0n}}\right)^T \tag{7.13}$$

First, by using a set of SOPs with known Stokes parameters, the instrument matrix *A* could be defined as follows,

$$A = I \cdot S^{-1} \tag{7.14}$$

where *A* is a matrix with *n* rows and 4 columns. Given that *n* should exceed 4, there are more than 4 equations involved in the calculation process. Consequently, we utilized the least squares method to address the over-determined systems, ensuring the most optimal fit for the instrument matrix. Then for an unknown SOP, the Stokes parameters could be calculated with the following equations,

$$S = A^{-1} \cdot I \tag{7.15}$$

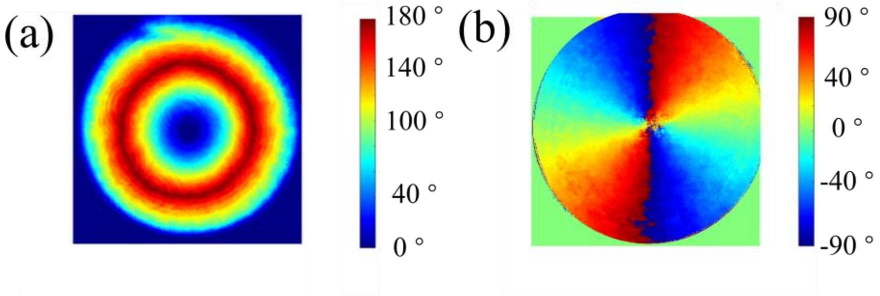

Figure 7.7 The optical properties of the printed droplet (a) the retardance of the printed LC droplet device and (b) the fast axis orientation.

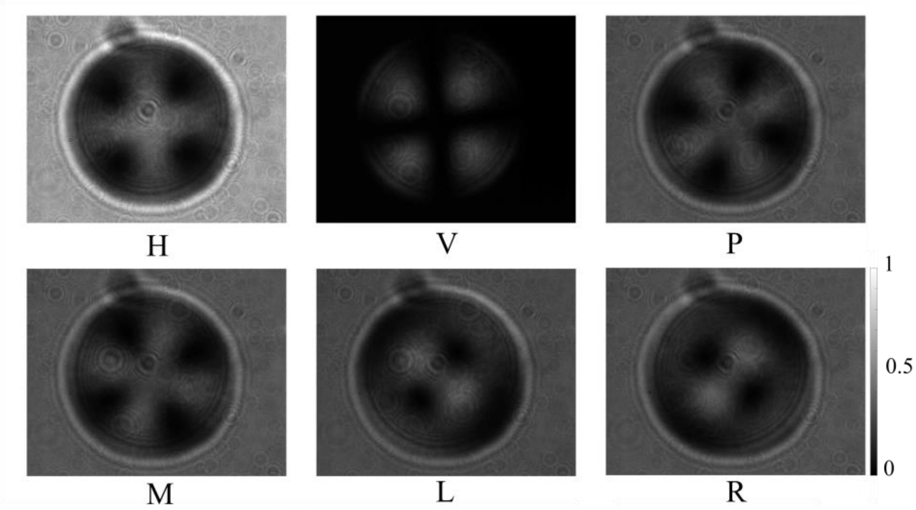

Figure 7.8 CCD-captured images for typical input SOPs, measureing linear polariszd light at 0° (H), 90° (V), 45° (P), and 135°(M), along with left-handed (L) and right-handed (R) circularly polarized light.

The measurement optimization process employed the use of three separate methodologies. As described before, in theory, only four distinct points on the printed LC droplet are required for a comprehensive analysis, given that the Stokes parameters consist of four components. The selection of these four points greatly influences the measurement accuracy, making it imperative to choose them with care to minimize errors. Prior studies on optimizing the Stokes polarimeter have tackled this challenge by identifying four optimal points based on criteria that the fast axis orientations should be at 15.12°, 51.69°, 128.31°, and 164.88°, with the retardance at these points being 132°[217]. This strategy ensures minimization of the measurement errors and enhances the precision of polarization analysis. The first method that is considered in this chapter uses the four selected special points on the droplet device. However, there are actually four series of points that actually meet these requirements so this is the second method that is considered. For the third method, all the points on the droplet are selected for the measurement.

7.4.1 Method 1

Drawing from existing research that optimized the computational procedure through the application of a condition number[217], the retardance was set at 132°. Meanwhile, the fast axis angle was designated at 15.12°, 51.69°, 128.31°, and 164.88°. By selecting four points on the droplet device that satisfy these conditions, we can obtain results with acceptable errors. This is because these specific parameters produce the minimum condition number, as described in detail in [262]. **Figure 7.9** displays the four chosen points, which were subsequently utilized to calculate the instrumentation matrix using the previously introduced method.

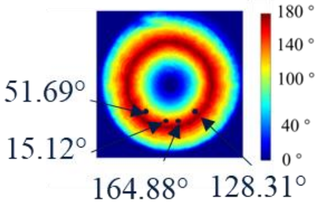

Figure 7.9 The four selected points are characterized by a retardance of 132° and fast axis angles at 15.12°, 51.69°, 128.31°, and 164.88°.

Figure 7.10 presents the experimental outcome, illustrating the measurement process as follows: initially, the instrument matrix A is measured. The polarizer is then rotated from 0° to 180° in 4° increments, encompassing a total of 45 steps. This results in the generation of 45 unique linearly polarized light beams. Subsequently, with the polarizer fixed at zero, the quarter-wave plate undergoes another 45 rotations from 0° to 180°, producing 45 distinct elliptically polarized light variations. The camera then captures the intensities of these 90 different polarization states, from which the instrument matrix of the four specific points is calculated. Using this computed matrix, a new set of SOPs is generated and introduced into the device to simulate the unknown polarization of the incoming light.

In Figure 7.10(a), a polarizer is depicted rotating from 5° to 175° in 10° increments, totalling 18 steps and creating 18 different linearly polarized light beams. After normalization with S_0, the lines in the plot signify the simulated results, while the points represent the experimental data, displaying a remarkable consistency. Turning our attention to Figure 7.10(b), with the polarizer fixed at zero, the quarter-wave plate performs 18 rotations from 0° to 180°, giving rise to 18 unique elliptically polarized light forms. It is evident that the experimental and simulation results exhibit similar overall trends, but not all individual polarization measurements yield satisfactory outcomes. Specifically, the measurement of S_3 depicted in Figure 7.10(a) is not very consistent with the simulation results.

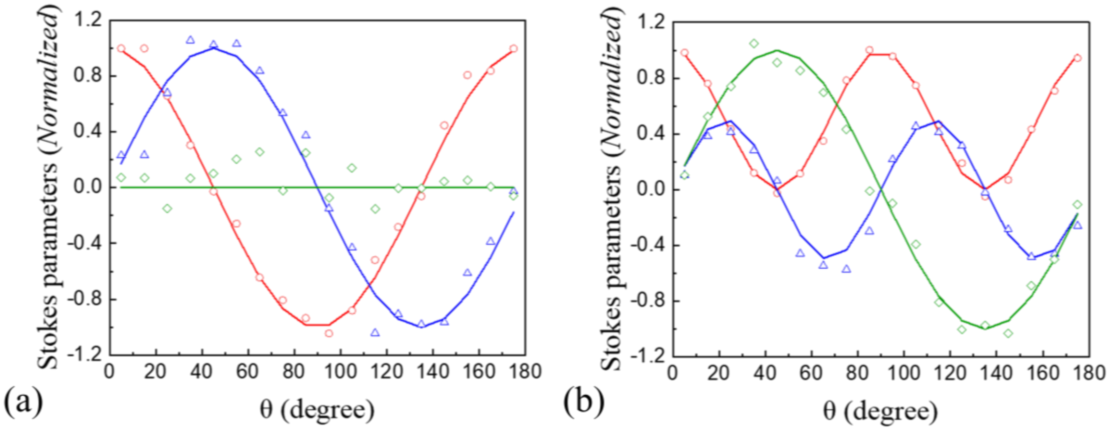

Figure 7.10 Experimental results for the method using four special points on the printed LC droplet (represented by circle markers for s_1, triangle markers for s_2, and square markers for s_3) as well as the calculated results (depicted by a red line for s_1, blue line for s_2, and green line for s_3) of the Stokes parameters. These measurements were obtained for different incident States of Polarization (SOPs). (a) In the polarization state generator (PSG), the polarizer was rotated in 18 equal steps spanning 180° to achieve varying incident SOPs. (b) The Polarization State Generator (PSG) was set with a fixed 0° polarizer, and the quarter-wave plate rotated in 18 in even increments across 180° to achieve diverse incident SOPs.

7.4.2 Method 2

It is widely understood that, without considering efficiency, selecting more points typically yields better results. Given that there are more than four points that satisfy the condition for a lower condition number, we have chosen four series of points for the measurement and calibration process. **Figure 7.11** demonstrates these four selected series of points. The same procedure was repeated to capture a total of 90 images for measurement and 36 images for calibration, as detailed in the previous section.

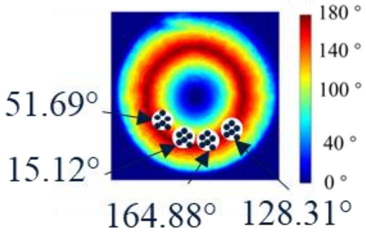

Figure 7.11 The four chosen series of points satisfy the criteria of having a retardance of 132°, and individual fast axis angles at 15.12°, 51.69°, 128.31°, and 164.88°.

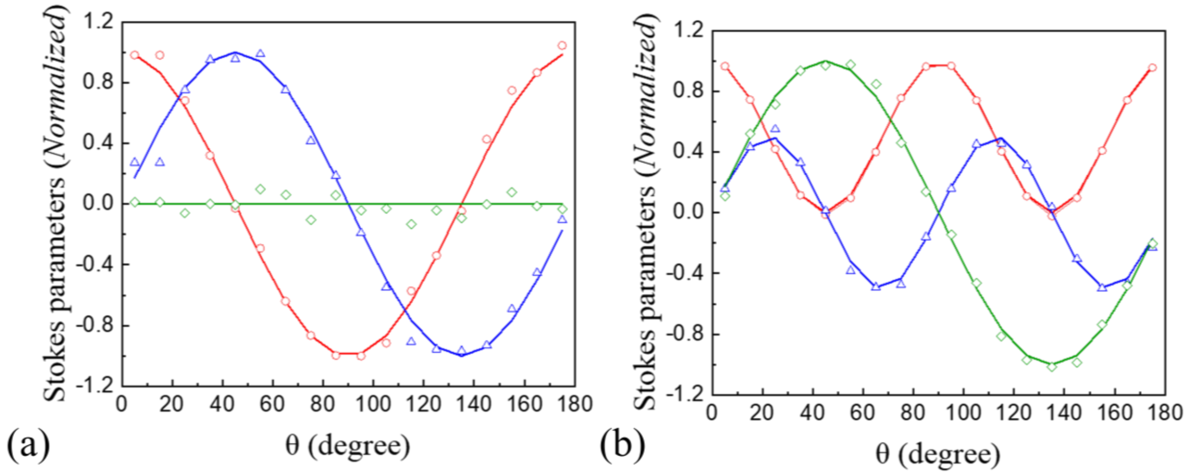

Figure 7.12 Experimental results for using the selected four series of special points (represented by circle markers for s_1, triangle markers for s_2, and square markers for s_3) as well as the calculated results (depicted by a red line for s_1, blue line for s_2, and green line for s_3) of the Stokes parameters. These measurements were obtained for different incident States of Polarization (SOPs). (a) In the polarization state generator (PSG), the polarizer was rotated in 18 equal steps spanning 180° to achieve varying incident SOPs. (b) The Polarization State Generator (PSG) was set with a fixed 0° polarizer, and the quarter-wave plate rotated in 18 even steps across 180° to achieve diverse incident SOPs.

Figure 7.12 presents the corresponding results obtained using these four selected series of points. The data plotting method remains unchanged. When compared to the results derived from only four points, these results show improved accuracy. The experimentally obtained data points are closely scattered around the simulated curves, exhibiting relatively small errors, whether the incident light is linearly polarized or circularly polarized.

7.4.3 Method 3

The third approach considered in this chapter involves utilizing all the points on the printed droplet device, as depicted in **Figure 7.13** within the region demarcated by the white lines. The remaining measurement procedures and data plotting processes align with those of the two preceding methods.

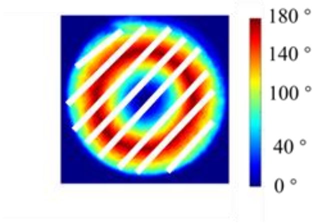

Figure 7.13 All the points on the printed droplet are selected for the measurement.

Figure 7.14 presents the results obtained from the experiment. Based on the experimental observations, the experimental results are nicely aligned with the simulation result line, with hardly any discernible discrepancies. Among the three methods, this approach exhibits the best performance, regardless of whether the simulated incident light is linearly polarized or circularly polarized. Only when the incidence angle is 15° for linearly polarized light does some small error manifest, but in the grand scheme of things, its impact is negligible.

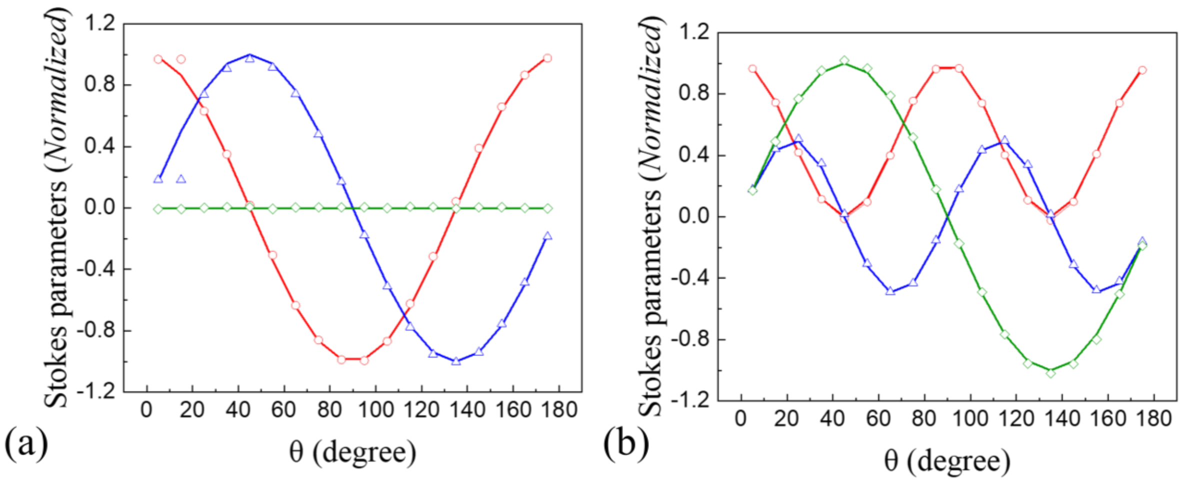

Figure 7.14 Experimental results using all the points on the printed droplet device (represented by circle markers for s_1, triangle markers for s_2, and square markers for s_3) as well as the calculated results (depicted by a red line for s_1, blue line for s_2, and green line for s_3) of the Stokes parameters. These measurements were obtained for different incident States of Polarization (SOPs). (a) In the polarization state generator (PSG), the polarizer was rotated in 18 equal steps spanning 180° to achieve varying incident SOPs. (b) The Polarization State Generator (PSG) was set with a fixed 0° polarizer, and the quarter-wave plate rotated in 18 even steps across 180° to achieve diverse incident SOPs.

The results depicted in **Table 7.1** presents an error analysis corresponding to the three methodologies elucidated above. These results were obtained under illumination with a 625 nm red LED. Different polarized light states were generated using various polarization state generators (PSGs) for the measurements. The calculation of the error is shown as follows,

$$error = \frac{|s_{simu\_1} - s_{mea\_1}| + |s_{simu\_2} - s_{mea_2}| \dots + |s_{simu\_n} - s_{mea\_n}|}{n} \tag{7.16}$$

where s_{simu} represents the simulation and the s_{mea} represents the measurement results. These results primarily encompass three of the Stokes parameters, normalizing the parameter S_0. The analysis reveals that employing all pixels captured by the CCD delivers superior outcomes with each parameter's error of approximately 1% or even less. Four sets of data, each with a retardance of 132°, yield errors around the 2% mark. Nevertheless, the error resulting from computations using solely four points ascends to roughly 4%. This evidence suggests that employing all points provides the best accuracy for the Stokes polarimeter. However, it should be noted that this computational process generally demands more time relative to the other two methods. Thus, there is merit in contemplating the balance between measurement precision and computational efficiency.

Table 7.1 Error comparison for the three different methods considered in this chapter.

Error Analysis	4 points (%)	4 series points (%)	All points (%)
S_1	2.20	1.81	0.62
S_2	4.02	2.02	0.61
S_3	4.17	2.12	0.47

The above results demonstrate the efficacy of the LC droplet device, affirming its successful implementation as a Stokes polarimeter with an impressive error margin of approximately 1% for each Stokes parameter. The entire measurement process can be accomplished in a singular, simultaneous test, offering an efficient and time-saving approach to Stokes parameter measurement. Moreover, the system configuration, composed of a glass slide bearing a printed LC droplet, an imaging lens, a polarizer, and a CCD, maintains a level of simplicity that promotes easy integration into other optical systems. The measurement process is free from any mechanical movements or additional electrically triggered components, further streamlining the system in comparison to conventional Stokes polarimeters. Additionally, the diameter of the printed LC droplet can be readily customized to cater to various application requirements, enhancing the device's versatility and broadening its range of potential applications. The design of this system is ease of use, reducing economic and technical barriers to accessibility. The system's unique blend of cost-effectiveness and simplicity makes it a desirable choice for a wide variety of Stokes parameter measurement applications. Future explorations could concentrate on incorporating various optical functions within the same framework, aiming to develop a versatile, multi-purpose sensing system.

One important point to note is that throughout the measurement process, the polarized light was used which was generated by a polarization state generator (PSG). This approach allowed us to conveniently compare the measurement results with the known Stokes parameters of the generated polarized light, ensuring consistency and reliability. For future research, it would be beneficial to incorporate incoherent or unpolarized light into the measurement process. This addition would provide a more comprehensive evaluation of the system's performance and broaden the applicability of the experimental results, making the study more complete.

7.5 Summary

The focus of the discussion in this chapter centres on the development of a new Stokes polarimeter rooted in the DoWP mechanism that uses printed nematic LC droplets. For our measurements, we adopted three distinct methodologies. Initially, we employed merely four points, each adhering to predefined retardance and fast axis angle conditions. Our subsequent approach expanded this to four series of points that conformed to the same criteria. Lastly, we encompassed all available points on the printed LC droplet.

Our findings coupled with error analyses indicate a discernible trend. Utilizing the entirety of the CCD-captured pixels culminates in the best precision, with most parameters' errors dropping to around 1% or even less. Conversely, when relying on four distinct data sets with a consistent retardance, errors hover around 2%. Relying on only four distinct points for computation escalates this error to an approximately 4%. These observations underscore the efficacy of leveraging all available data points for optimal accuracy in Stokes polarimetry. However, it's worth noting that this comprehensive computational approach necessitates a more prolonged duration in comparison to its counterparts, underlining the trade-off between precision and efficiency.

CHAPTER 8 Conclusions and Future Work

This chapter summarises the key findings from the work presented in this thesis and proposes topics and experiments that could be explored in the future.

In this thesis, drop-on-demand (DoD) printing has been investigated, encompassing both inkjet and electrohydrodynamic (EHD) methodologies. The principal printing ink explored was that based upon liquid crystalline mixtures and variants thereof. The overarching objective of this research was to harness the potential of DoD printing to innovate optical components suitable for an array of applications. Contrasted with conventional fabrication methods such as lithography, laser writing, and wet etching typically employed in microstructure creation, DoD printing emerges as an efficient, time-conservative, and cost-effective alternative.

Two distinct inkjet printers were employed in this research. The first, sourced from Microfab, offers high automation, controlled via computer interfaces, facilitating intricate pattern printing. In contrast, the second apparatus, a bespoke creation by a senior member of the research group, boasts flexibility. Its modular design ensures adaptability, allowing us to customize each component. Within our group, a senior member and I pioneered the construction of the EHD printing system. To the best of our knowledge, it is the first instance where EHD printing has been harnessed to dispense nematic liquid crystals (LCs), achieving droplets with diameters as small as approximately 1 μm. In the upcoming sections, I will provide an overview of the key achievements and findings presented in this thesis. Additionally, potential avenues for future research will be described.

8.1 Concluding remarks

This thesis presents results on the application of a new EHD printing system for the dispensation of LC mixtures. When compared with the inkjet printing system, EHD, given identical nozzle diameters, typically achieves smaller diameters of the printed droplets. To further refine the droplet diameter and furnish automated control over printing patterns, the system has been enhanced to include temperature and position regulation features. Our findings reveal that the incorporation of a heating element, when used with a metal printhead, can further decrease the droplet's diameter. Additionally, with the implementation of the position control model, intricate patterns such as the word “Oxford" can be rendered. This offers an efficient method for producing patterns with exceptionally fine droplet diameters.

To glean a deeper understanding of the interplay of various parameters in the printing process, simulations were employed utilizing COMSOL Multiphysics. This model aptly simulated both the inkjet and EHD printing processes; the latter was emulated by simply deactivating the electric field. In terms of the inkjet printing process, the impact of back pressure was explored which could influence the diameter of the printed droplet. Exploration of EHD printing using simulations encompassed multiple parameters: the inlet flow rate of the printing ink, the imposed voltage, the nozzle-to-substrate distance, and the voltage pulse duration. Through these analyses, we discerned how such parameters influence the diameter of printed droplets. Such insights stand to greatly streamline our efforts in actual printing, enabling us to achieve the desired droplet diameter with enhanced precision and efficiency.

The first application demonstrated within this thesis was dedicated to smart window technology. Historically, research on smart windows predominantly revolved around film devices. However, we have used printing to demonstrate the patterning of smart windows, offering functionalities such as signage for guidance and other purposes. Working with a senior colleague I have demonstrated printed PDLC smart windows, characterized by their ability to scatter when light when devoid of voltage, transitioning to a transparent optical state under an applied electric field. Following on from this work, the thesis reports the use of polymer-stabilized chiral nematic LCs for patterned smart window applications. Intriguingly, this smart window's behaviour can be inverted based on the fabrication process, which cannot be readily achieved using PDLCs. In its conventional mode, the device scatters light without a voltage and becomes transparent under an appropriate electric field. Conversely, in the reverse mode, the default state of the device is optically transparent, becoming scattering upon the application of a sufficient electric field. Remarkably, the composition of the printing material remains consistent across both modes. This innovation in patterned smart windows broadens the spectrum of potential applications. Their dual-mode functionality, paired with customization capabilities, presents a potential game-changer in the smart window application arena.

Future research avenues in the realm of smart window applications have a range of possibilities. While the current focus primarily centres on harnessing the electrooptical properties of LCs, the thermotropic nature of these materials—where temperature can induce a phase change from anisotropy to isotropy—presents a potential avenue for temperature indication. Moreover, the present design for patterned smart windows employs rigid glass slides, which inherently lack flexibility. Transitioning to more pliable substrates, such as ITO-coated PET film, could pave the way for printed flexible smart window applications. Such innovations and explorations have the potential to further expand the scope and versatility of smart windows grounded in printed LC technology and its mixtures.

Following the demonstration of printed polymer-stabilized chiral nematic LCs for use in dual-mode smart window applications, the thesis then considered the potential of printed LCs in other optical components. The first new component investigated was a vortex beam generator formed using printed LC droplets. Standard methodologies for producing vortex beam generators using LCs have typically necessitated intricate fabrication processes, including lithography, direct laser writing, or the use of photoalignment materials such as SD1 to align the LC director. As a novel alternative, the thesis reports a vortex beam generator crafted using printing technology, offering an economical and straightforward fabrication process.

The thesis outlines the fabrication process and has examined the resulting optical properties using simulations of the LC director distribution and the vortex beam generation process, which were then compared with the results from experiments. Empirical evidence revealed the capability of the printed droplets to generate both vector and vortex beams with a topological number of 2, accomplished by changing the input light beam from linearly polarized light to circularly polarized light. Notably, there was a match between our experimental and simulation results, underscoring the validity and potential of our innovative approach.

In future work, there is potential to refine and advance our approach further. At present, our concept for the vortex beam generator requires the use of electric fields to manipulate the director distribution, facilitating the generation of vortex or vector beams. Utilizing an external electric field in this manner, however, might not be the most cost-effective or efficient. As an alternative, incorporating UV-sensitive LC polymers into the LC droplet device may be worthy of further study. Upon applying the appropriate electric field and achieving optimal vortex beam generation, the mixture could be exposed to UV light, inducing polymerization and thereby "locking" the LC director in place. This would obviate the need for a sustained electric field in subsequent beam generation processes. This approach represents an energy-conserving method, albeit without the flexibility of toggling the vortex beam generation on or off. Such a static mode might be particularly apt for scenarios where constant vortex beam generation is desired, especially if there is a requirement to keep the droplet device affixed to experimental equipment without frequent removal or adjustment.

Drawing on prior experiences in optical device applications, the next optical component was the use of the printed droplets in a new Stokes polarimeter. It was shown that the printed LC droplet exhibits varied retardance and fast axis values across different regions of the droplet, which provides a means of measuring the Stokes parameters, eliminating the need for external electrical input or components that require mechanical adjustment. Such a system promises swift, efficient, and straightforward Stokes parameter measurements.

The calibration process considered three distinct measurement methodologies. The first involved using four specific points, which had to fulfil certain conditions: a retardance of 132° coupled with fast axis angles of 15.12°, 51.69°, 128.31°, and 164.88°. The second methodology expanded on the first by using a series of points that conformed to the previously mentioned criteria. Lastly, the third method employed every point present on the printed droplet device. These approaches are all based on preceding research geared towards optimizing a Stokes polarimeter. All methods delivered promising results, with the third method standing out as it achieved an error margin of less than 1%. However, this precision does come at the cost of extended processing time. The optimal method can be tailored to fit specific application scenarios and requirements.

Moving forward, the realm of Stokes polarimetry presents a plethora of opportunities for research exploration. At present, our accomplishments are centred around point sensing, allowing us to measure Stokes parameters at a singular point. However, the introduction of printed LC droplet arrays could pave the way for imaging capabilities, adding potential possibility to further application. Furthermore, the potential to develop the Stokes polarimeter for biomedical applications is vast. For instance, it could be instrumental in gauging the polarization of light as it traverses through biomedical tissues, providing insights into tissue properties and health.

In terms of materials, while our current model employs a nematic LC, diversifying the types of LC used could be beneficial. Exploring materials with varied refractive indices, or even experimenting with larger dimensions for the printed droplets, could lead to a range of retardances, potentially enhancing the device's capabilities and precision. Each step forward could contribute to the refinement and augmentation of this already promising technology.

8.2 Future work

8.2.1 Gratings (LC array)

The main applications explored in the thesis are achieved by using the inkjet printing technique. In the meantime, I have also explored some other applications using the EHD printing technique since it could achieve a droplet diameter of only 1 μm.

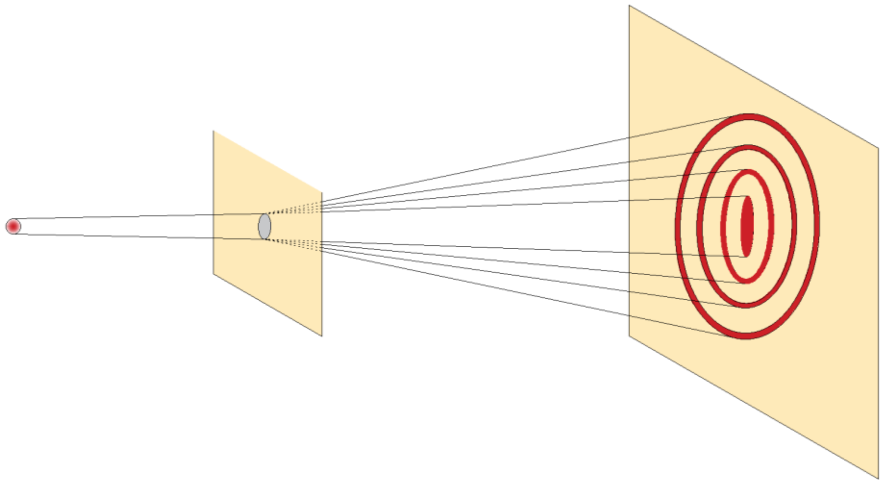

Figure 8.1 Circular aperture diffraction.

For example, the printed LC droplet arrays could be used as diffraction gratings. Diffraction is an optical phenomenon describing the propagating of a light wave[263]. As shown in **Figure 8.1**, when a light wave is potentially obscured, it will form different waves when it passes through the hole which could cause different light intensity distributions in the far-field. Consequently, as light propagates and encounters specific components, termed diffraction gratings, there is a resultant alteration in its phase front. Diffraction gratings consist of periodic microstructures that can alter the phase front or the amplitude of the incident light. Therefore, based on the modulation, diffraction gratings can be categorized into phase gratings and amplitude gratings. However, diffraction can also occur when light does not encounter an obstruction but instead passes through diffraction gratings made of materials with varying refractive indices.

At present, a plethora of methodologies exist for making dielectric gratings. Noteworthy among these are photolithography[264], electron beam lithography[265], interference lithography[266], nanoimprint lithography[267], ion beam lithography[268], direct laser writing[269], focused ion beam techniques[270], chemical etching[271], and laser ablation[272], to enumerate a few. These methodologies are used across a range of materials, encompassing photoresists[273], SiO_2[274], polysilicon[275], thermoplastic polymers[276], metallic constituents[277], semiconductors[278-279], and so on.

Liquid crystals also play an important role in diffraction gratings. For example, LCs have already been used with a direct laser writing process to fabricate stretchable gratings[280] and Dammann gratings[281] within my group. In this section, the utilization of EHD printing technology is explored for the fabrication of a particular category of dielectric grating. The fundamental principle behind this device hinges on producing micro-droplet structures atop a glass slide substrate, thereby establishing a region with distinct dielectric disparities around a designated area. When the light passes through this area, the printed droplet device can serve as a diffraction grating.

Figure 8.2 illustrates the experimental apparatus deployed for the described procedure. A laser emitting at 635 nm was first passed through a Neutral Density (ND) filter to attenuate its power. Subsequently, the light beam was directed through a lens to constrict its diameter, ensuring it remains narrower than the size of the array of the printed droplet diffraction gratings. Lastly, the screen shows the replay field pattern observed from the diffraction grating.

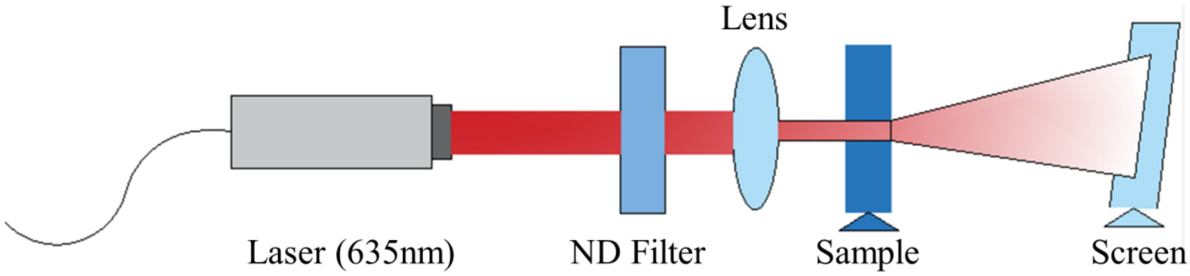

Figure 8.2 Schematic of the experimental setup for characterizing the printed droplet diffraction gratings.

Figure 8.3 is a simple demonstration that the EHD printed LC droplet array device could be used as a diffraction grating. A 10 × 10 droplet array with 1 micron in diameter was printed on a lecithin treated glass slide. Although from the result of the replay field pattern, the first diffraction spot is quite obvious, it still shows strong potential for the EHD printing technology used in the fabrication of optical components. The EHD printed droplet diffraction gratings could be used for the splitting of the light beam into a number of diffracted light beams which could be used in a large variety of applications.

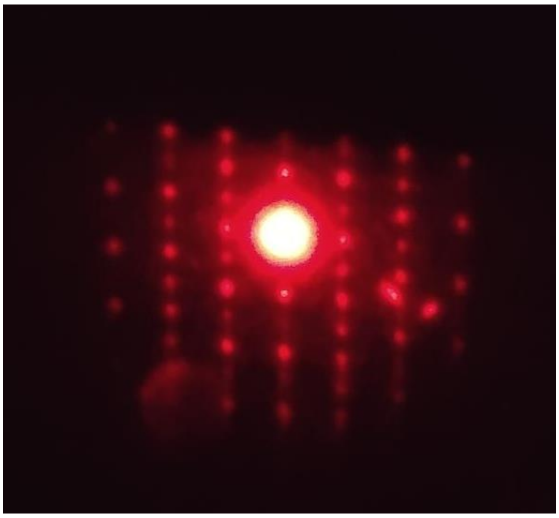

Figure 8.3 The replay field pattern observed from the screen with the EHD printed droplet array device.

In summary, this ability of EHD printing to deposit highly precise, micron-scale droplets offers a straightforward and efficient method for the fabrication of LC gratings. Looking forward, the thesis suggests avenues for future research, including the development of stretchable LC gratings. This would involve depositing 1 μm LC droplets onto a flexible substrate, a process that promises to be relatively simple yet innovative, potentially providing a simple process for microstructure fabrication.

8.2.2 Optical Skyrmion Generator

Skyrmions, conceived by Tony Skyrme in the nuclear physics realm of the 1960s[282], are topological solitons distinguished by attributes of stability, minimal energy consumption, and swift dynamics, features that have elicited interest within condensed matter physics. Recently, the exploration of skyrmions has extended beyond their traditional domain and permeated into the field of photonics. Within this new realm, skyrmions manifest as confined wave packets within select optical materials. This venture into the optical domain heralds a deeper comprehension of skyrmions and inaugurates a multitude of novel application opportunities. Furthermore, research on skyrmions has transcended beyond evanescent fields[283] and encapsulated diverse domains such as structured media[190, 284-285], free space[286-287], space-time[288], and momentum space[289]. The multifaceted exploration promises profound advancements in numerous applications, including optical tweezers, microscopy, displacement metrology, optical communications, and quantum entanglement.

Concurrently, the study of optical topological quasiparticles that share similarities with skyrmions has emerged as a captivating frontier within photonics. This burgeoning domain encompasses entities such as merons[290], bimerons[291], hopfions[292], bimeroniums[290], skyrmionium[290], skyrmion bags[293-294], skyrmion bundles[295], skyrmion braids[296], torons[297], and heliknotons[284], each demonstrating distinctive topological structures and characteristics. For instance, merons and bimerons, acclaimed for their intricate polarization and phase distribution patterns, lend themselves to advancements in information encoding and processing. Furthermore, three-dimensional quasiparticles like hopfions could potentially revolutionize optical data storage and manipulation. Moreover, complex composite entities, namely bimeroniums and skyrmioniums, displaying sophisticated spatial structures, hold promise for the crafting of resilient and adaptable photonic devices. These quasiparticles can be brought into existence by leveraging vectorial structured light beams, created through methods incorporating gradient-index lenses[298], polarization interferometers[299], metasurfaces[300], and more. This work specifically dwells on the generation of skyrmions in optical fields utilizing inkjet-printed LC droplets.

In this work, I have considered the use of printed LC droplet arrays as a mechanism to facilitate the generation of higher-order optical skyrmions, as well as intricate higher-order optical skyrmionium and meronium arrays. There are basically three different types of skyrmions as shown in **Figure 8.4**. Figure 8.4(a) depicts a skyrmion structure, where varying colours represent different vector orientations in space. For instance, black represents the vector that is perpendicular and points upwards, while white signifies the vector that, although perpendicular, directs downwards. The intermediate colours illustrate a gradual transition in spatial orientation. However, due to the varying spatial distribution of vectors, skyrmions are generally categorized as one of the following: Neel-type, Bloch-type, and Anti-type, as depicted in Figure 8.4(b), (c), and (d).

As Figure 8.4(a) shows, the structure's northern point is characterized by a vertically oriented vector pointing upwards, which is delineated by a white hue. Conversely, at the southern point, there exists a vertically oriented vector pointing downwards, manifested with a black hue. These specific attributes have been employed to translate this three-dimensional skyrmion structure into a two-dimensional schematic. Within this illustration representation, a consistent colouration is indicative of vectors located within the same longitudinal plane, while gradations in the said colour imply vectors positioned at varied latitudinal coordinates.

In Figure 8.4(b), a Neel-type skyrmion is illustrated. Within this figure, i) illustrates the 2D structure. For clarity and simplification, one might opt to utilize solely hue variations to signify the vectors at different spatial positions, as presented in ii). Furthermore, iii) provides insight into the vector distribution confined within the delineated dashed box. In Figure 8.4(c), an analogous illustration is presented for the Bloch type, while Figure 8.4(d) offers a congruent depiction for the corresponding Anti-type of the optical skyrmion. As described in the figure, the vectors of distinct skyrmion types exhibit varied spatial distributions. For instance, certain distinctions become evident upon examining the vector distributions within the delineated dash boxes for each skyrmion type.

In the Neel type, the vector undergoes a 360-degree rotation co-planar with the distribution plane. Conversely, in the Bloch-type skyrmion, the vector completes a 360-degree rotation in a plane perpendicular to the distribution plane. The Anti-skyrmion presents a more complex behaviour, seemingly amalgamating characteristics from both Neel and Bloch types at different regions. Normally, the skyrmion number is used to describe how many times the vector wraps around the unit sphere. All types of skyrmions shown in Figure 8.4 have the skyrmion number of 1.

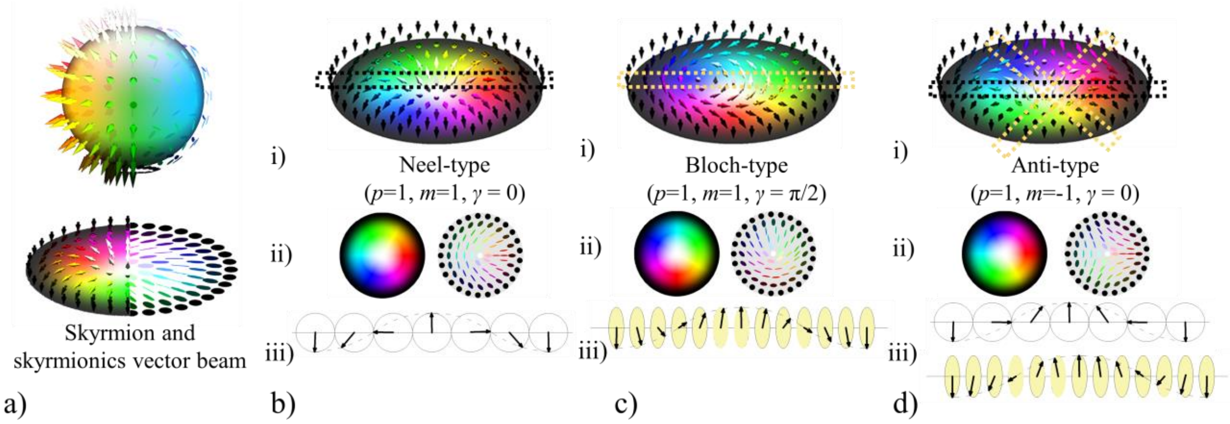

Figure 8.4 a) Illustration of the skyrmion translation from a 3D structure to 2D structure with hue colour. b) Neel type skyrmion. c) Bloch type skyrmion. d) Anti type skyrmion. In each figure, i) is the vector distribution, ii) is the corresponding hue colour representation for the vector distribution. iii) is the vector distribution in the dashed box (in the corresponding figure (i)) for each type.

Aside from the skyrmion number, there are three characters that could be used to characterize the different vector orientations. Here, we could use polarity, vorticity and helicity to describe these three types. The concept of polarity is employed to characterize the orientation of the central vortex nucleus. When the vector at the nucleus' focal point is orientated vertically and directed upwards, the polarity is assigned a value of positive one (+1). Conversely, when the vector is oriented vertically and directed downwards, the polarity is denoted as negative one (-1).

The types of skyrmion listed in **Figure 8.5** have a polarity of 1 which could be represented as p = 1. Vorticity is a term applied to delineate the rotational direction of a vector distribution along a given radius, symbolized by the variable 'm'. Should the vector rotate in a clockwise direction, the vorticity is considered positive. In contrast, a counterclockwise rotation of the vector is indicative of negative vorticity. The magnitude of the vorticity is determined by the number of complete rotations executed by the vector. Helicity is utilized to quantify the vector's own rotational disposition within the plane tangential to the circle's centre. By establishing an orthogonal coordinate system for each vector with one axis along the radius and the other orthogonal to it, the vector component aligned with the radial axis would possess an angle of 0, which can be represented as $\gamma = 0$. For vectors exhibiting a direction antithetical to the aforementioned orientation, the resultant helicity value would be $\gamma = \pi$. Furthermore, depending on the specific distribution of the vectors, helicity can assume angular values of -π/2 and π/2, respectively.

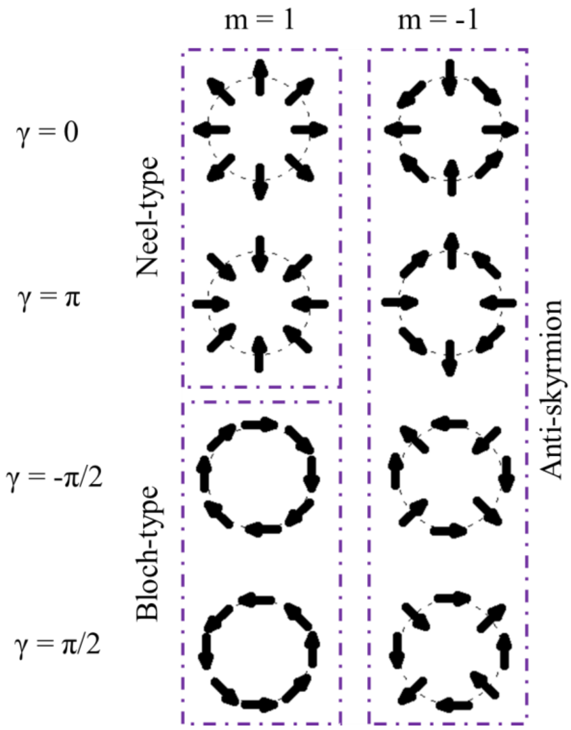

Figure 8.5 The demonstration of the Neel- type, Bloch-type and Anti-skyrmion type with different values of vorticity and helicity.

Printed LC droplets could potentially facilitate the generation of higher-order optical skyrmions, alongside intricate multi-bimerons and hybrid states. The fabrication process of this device would be the same as that of the Stokes Polarimeter as described in Chapter 7. The experimental setup for the generation of an optical skyrmion is shown in **Figure 8.6.** In the generation process, the quarter wave plate rotates to generate different SOP. The component C in the setup representing the quarter waveplate or half waveplate is added depending on the generation of different types of optical skyrmion.

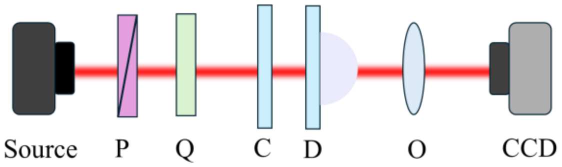

Figure 8.6. The setup for the generation of an optical skyrmion. P: polarizer; Q: quarter waveplate; C is either a quarter waveplate or half waveplate; O: objective lens; D: droplet device.

To demonstrate the efficacy of the LC droplet device in generating optical skyrmions, a comparative analysis was conducted between the skyrmions produced by the printed device and a theoretical simulation, both represented with hue coding for clarity. The skyrmion generated by the LC droplet device, as depicted in **Figure 8.7**(a)i), is identified as a high-order skyrmionium with an order number of 2. Similar to Figure 8.1 a), black represents vectors that are perpendicular and point upward, while white corresponds to vectors that are perpendicular but point downward, with the intermediate colors illustrating a smooth spatial transition. This use of different colors effectively represents the three-dimensional skyrmion in a two-dimensional format. Accordingly, in Figure 8.7 (a) i), the black core region signifies vectors oriented perpendicularly upward. The gradual color shift from black to white and then back to black along the radial direction reflects the continuous spatial reorientation of vectors, symbolizing the skyrmionium's formation process.

Comparatively, using MATLAB, illustrated in Figure 8.7(a)ii), exhibits a similar structural arrangement, particularly in the core region where the vectors are directed upwards, and in the outer ring where a white colour signifies downward perpendicular vectors. This resemblance validates the accuracy of the printed LC droplet-generated skyrmions against theoretical models. Additionally, a future avenue for research could be the generation of another optical skyrmion variant known as bimeronium, which comprises four sub-bimerons.

Differing from traditional skyrmions, a bimeron can be conceptualized as a soliton, essentially constituting half of a skyrmion.

In the specified configuration of this bimeronium, the presence of four distinct bimerons is observable. When these observed entities are compared to the simulation results, there is a coherence between the bimerons that were generated and their simulated counterparts. Theoretical considerations suggest that the transition of a skyrmion from its original three-dimensional structure to a two-dimensional form can be envisaged as an unwinding process from a polar origin, either from the southern or northern extremity. The optical skyrmions produced through our printed LC droplet method exhibit remarkable agreement with the theoretical simulations. These two instances demonstrate that the LC droplet device could be employed as a generator of optical skyrmions.

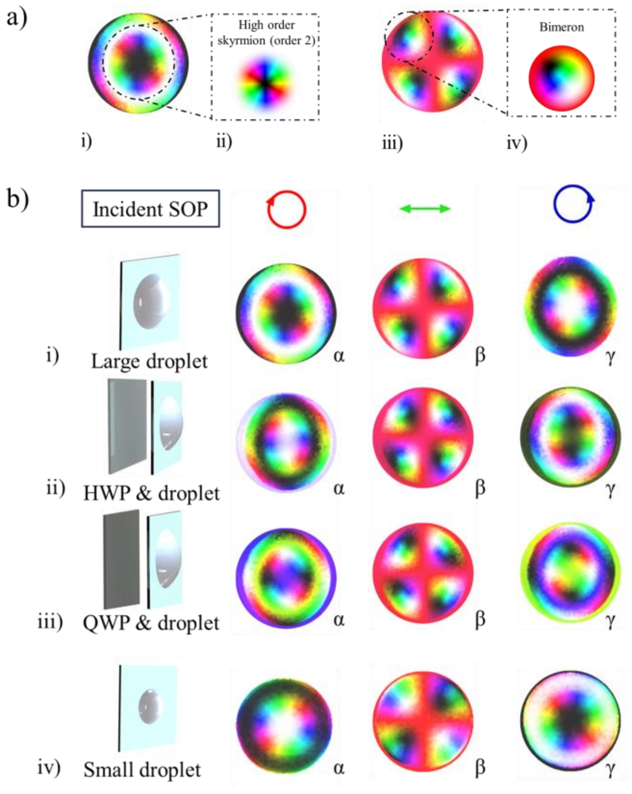

Figure 8.7 Optical skyrmion generation based on a printed LC droplet device. a) A comparison of generated Skyrmionium by the printed LC droplet device with a large droplet diameter (420 μm) and the corresponding simulation. i) Experimentally generated skyrmionium with input SOP corresponding to left-handed circular polarised light. ii) The corresponding simulation results of the inner part of i). iii) The experimentally-

generated skyrmionium with input SOP corresponding to linear polarised light. iv) The corresponding simulation results of one quarter of iii). b) Generation of different Skyrmion beams via different input SOPs and different combinations of the printed LC droplet device. i) Optical skyrmionium generated using a printed LC droplet device with a footprint diameter of 420 μm. ii) Optical skyrmionium generated via the combination of a half wave plate and the printed LC droplet device with a footprint diameter of 420 μm. iii) Optical skyrmionium generated via the combination of a quarter wave plate and printed LC droplet device with a footprint diameter of 420 μm. iv) Optical skyrmionium generated with a printed LC droplet device with a smaller droplet diameter of 260 μm. In each row, α represents the input SOP that is left-handed circular polarized light; β represents the input SOP that is linear polarized light, and γ represents the input SOP that is right-handed circular polarized light.

By changing the different SOPs as the input, the optical skyrmion and skyrmion field generated after passing through the device also differs, and the results vary according to the diameter of the printed LC droplets. Figure 8.7(b) shows the results. The first line demonstrates the different incident SOPs from the left-handed circular polarized light, linear polarized light, and right-handed circular polarized light. The generated results are shown in Figure 8.7(b) i) α and β are discussed before in Figure 8.7(a).

Upon integrating the thin film droplet device with a half-wave plate and a quarter-wave plate, diverse optical skyrmions can be generated contingent upon the incident SOPs. This predicts that our LC thin film-based droplet device holds promise as a generator for optical skyrmions. Notwithstanding, all generated optical skyrmions consistently exhibit a flux value of zero, which presents challenges for its immediate application in optical communications. There is a pressing need for further investigation to adapt it effectively for communication applications. Nonetheless, this serves as a testament to the potential of the LC thin film-based droplet device in producing optical skyrmions. This insight suggests that through meticulous control over droplet size and alterations in the assembly of optical components, one can tailor-made skyrmion structures. These custom formations are potentially advantageous for a broad spectrum of applications or research inquiries, indicating a promising frontier for optical manipulation and photonic device innovation.

This chapter has summarized the key achievements of the thesis, initially outlining the main technologies utilized—specifically, inkjet printing and Electrohydrodynamic (EHD) printing—and then providing the principal findings from each chapter. The thesis describes the application of these printing technologies using LC mixtures as the ink, offering a straightforward and environmentally sustainable method for the creation of functional droplet-based devices. Furthermore, it presents two potential areas for future research: LC droplet array gratings and optical Skyrmions, thereby broadening the scope of possibilities in the field of printed functional droplet-based devices.

Appendix

The process of formula derivation is involved in the simulation mentioned in the thesis.

In this simulation, the LC director is considered in a polar coordinate system which is described with the angle θ with axis r.

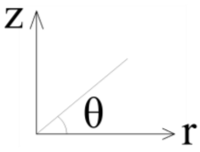

$$n_r = \cos\theta \tag{A.1}$$

$$n_z = \sin\theta \tag{A.2}$$

$$n_\emptyset = 0 \tag{A.3}$$

$$\nabla \cdot \mathbf{n} = \frac{1}{r}\frac{\partial}{\partial r}(r \cdot n_r) + \frac{1}{r}\frac{\partial n_\emptyset}{\partial \emptyset} + \frac{\partial n_z}{\partial z} = \frac{1}{r}\frac{\partial}{\partial r}(r\cos\theta) + \frac{\partial(\sin\theta)}{\partial z} = \frac{1}{r}\cos\theta - \sin\frac{\partial\theta}{\partial r} + \cos\theta\frac{\partial\theta}{\partial z} \tag{A.4}$$

$$\nabla \times \mathbf{n} = (\frac{\partial n_r}{\partial z} - \frac{\partial n_z}{\partial r})\widehat{\mu_\emptyset} + (\frac{1}{r}\frac{\partial n_z}{\partial \emptyset} - \frac{\partial n_\emptyset}{\partial z})\widehat{\mu_r} + \frac{1}{r}[\frac{\partial}{\partial r}(rn_\emptyset) - \frac{\partial n_r}{\partial \emptyset}]\widehat{\mu_z} = (-\sin\theta\frac{\partial\theta}{\partial z} - \cos\theta\frac{\partial\theta}{\partial r})\widehat{\mu_\emptyset} \tag{A.5}$$

$$\mathbf{n} \cdot (\nabla \times \mathbf{n}) = \begin{pmatrix} \cos\theta & \widehat{\mu_r} \\ \sin\theta & \widehat{\mu_z} \\ 0 & \widehat{\mu_\emptyset} \end{pmatrix} \cdot \begin{pmatrix} 0 & \widehat{\mu_r} \\ 0 & \widehat{\mu_z} \\ \left(-\sin\theta\frac{\partial\theta}{\partial z} - \cos\theta\frac{\partial\theta}{\partial z}\right) & \widehat{\mu_\emptyset} \end{pmatrix} \equiv 0 \tag{A.6}$$

$$(\nabla \cdot \mathbf{n})^2 = (\frac{1}{r}\cos\theta - \sin\theta\frac{\partial\theta}{\partial r} + \cos\theta\frac{\partial\theta}{\partial z})^2 = (\sin\theta\frac{\partial\theta}{\partial r} - \cos\theta\frac{\partial\theta}{\partial z})^2 + \frac{1}{r^2}\cos^2\theta - \frac{2}{r}\sin\theta\cos\theta\frac{\partial\theta}{\partial r} + \frac{2}{r}\cos^2\theta\frac{\partial\theta}{\partial r}\frac{\partial\theta}{\partial z} \tag{A.7}$$

$$\mathbf{n}\times(\nabla\times\mathbf{n})=\mathbf{n}\times\left(-\sin\theta\frac{\partial\theta}{\partial z}-\cos\theta\frac{\partial\theta}{\partial r}\right)\widehat{\mu_{\emptyset}}=\begin{pmatrix}\sin^2\frac{\partial\theta}{\partial r}+\sin\theta\cos\theta\frac{\partial\theta}{\partial r}\\ 0\\ -\sin\theta\cos\theta\frac{\partial\theta}{\partial z}-\cos^2\theta\frac{\partial\theta}{\partial r}\end{pmatrix}\quad\text{(A.8)}$$

$$[\mathbf{n}\times(\nabla\times\mathbf{n})]^2=\left[\sin^4(\frac{\partial\theta}{\partial z})^2+\sin^2\theta\cos^2\theta\,(\frac{\partial\theta}{\partial r})^2+2\sin^3\theta\cos\theta\frac{\partial\theta}{\partial r}\frac{\partial\theta}{\partial z}\right]+$$
$$[\sin^2\theta\cos^2\theta\,(\frac{\partial\theta}{\partial z})^2+\cos^4(\frac{\partial\theta}{\partial r})^2+2\sin\theta\cos^3\theta\frac{\partial\theta}{\partial z}\frac{\partial\theta}{\partial r}]=[\cos\theta\,(\frac{\partial\theta}{\partial r})+\sin\theta\,(\frac{\partial\theta}{\partial z})]^2\quad\text{(A.9)}$$

$$f=\tfrac{1}{2}K_1(\nabla\cdot\mathbf{n})^2+\tfrac{1}{2}K_2[\mathbf{n}\cdot(\nabla\times\mathbf{n})]^2+\tfrac{1}{2}K_3[\mathbf{n}\times(\nabla\times\mathbf{n})]^2=\tfrac{1}{2}K_1[(\sin\theta\frac{\partial\theta}{\partial r}-\cos\theta\frac{\partial\theta}{\partial z})^2+$$
$$\tfrac{1}{r^2}\cos^2\theta-\tfrac{2}{r}\sin\theta\cos\theta\frac{\partial\theta}{\partial r}+\tfrac{2}{r}\cos^2\theta\frac{\partial\theta}{\partial r}\frac{\partial\theta}{\partial z}]+\tfrac{1}{2}K_3[\cos\theta\,(\frac{\partial\theta}{\partial r})+\sin\theta\,(\frac{\partial\theta}{\partial z})]^2\quad\text{(A.10)}$$

Within this equation,

$$\frac{\partial}{\partial\theta}=\tfrac{K_1}{2}[2(\sin\theta\frac{\partial\theta}{\partial r}-\cos\theta\frac{\partial\theta}{\partial z})(\cos\theta\frac{\partial\theta}{\partial r}+\sin\theta\frac{\partial\theta}{\partial z})-\tfrac{2}{r^2}\cos\theta\sin\theta-\tfrac{2}{r}\tfrac{\partial\theta}{\partial r}(\cos^2\theta-$$
$$\sin^2\theta)-\tfrac{4}{r}\cos\theta\sin\theta\frac{\partial\theta}{\partial z}]+\tfrac{K_3}{2}[2(\sin\theta\frac{\partial\theta}{\partial z}+\cos\theta\frac{\partial\theta}{\partial r})(\cos\theta\frac{\partial\theta}{\partial z}-\sin\theta\frac{\partial\theta}{\partial r})]\quad\text{(A.11)}$$

$$\frac{\partial}{\partial(\frac{\partial\theta}{\partial r})}=\tfrac{1}{2}K_1[2\left(\sin\theta\frac{\partial\theta}{\partial r}-\cos\theta\frac{\partial\theta}{\partial z}\right)\sin\theta-\tfrac{2}{r}\sin\theta\cos\theta]+\tfrac{K_3}{2}[2(\sin\theta\frac{\partial\theta}{\partial z}+\cos\theta\frac{\partial\theta}{\partial r})\cos\theta]$$
$$\text{(A.12)}$$

$$\frac{\partial}{\partial r}(\frac{\partial\theta}{\partial r})=\tfrac{1}{2}K_1\{2\left[\cos\theta\left(\frac{\partial\theta}{\partial r}\right)^2+\sin\theta\frac{\partial^2\theta}{\partial r^2}+\sin\theta\frac{\partial\theta}{\partial z}\frac{\partial\theta}{\partial r}-\cos\theta\frac{\partial^2\theta}{\partial r^2}\right]\sin\theta+2\left(\sin\theta\frac{\partial\theta}{\partial r}-\right.$$
$$\left.\cos\theta\frac{\partial\theta}{\partial z}\right)\cos\theta\frac{\partial\theta}{\partial r}+\tfrac{2}{r^2}\sin\theta\cos\theta-\tfrac{2}{r}(\cos^2\theta-\sin^2\theta)\frac{\partial\theta}{\partial r}\}+\tfrac{1}{2}K_3\{2[\cos\theta\frac{\partial\theta}{\partial z}\frac{\partial\theta}{\partial r}+$$
$$\sin\theta\frac{\partial^2\theta}{\partial z\partial r}-\sin\theta\left(\frac{\partial\theta}{\partial r}\right)^2)+\cos\theta\frac{\partial^2\theta}{\partial r^2}]\cos\theta-2(\sin\theta\frac{\partial\theta}{\partial z}+\cos\theta\frac{\partial\theta}{\partial r})\sin\theta\frac{\partial\theta}{\partial r}\}\quad\text{(A.13)}$$

$$\frac{\partial}{\partial(\frac{\partial\theta}{\partial z})}=\frac{K_1}{2}[-2(\sin\theta\frac{\partial\theta}{\partial r}-\cos\theta\frac{\partial\theta}{\partial z})\cos\theta+\frac{2}{r}\cos^2\theta]+\frac{K_3}{2}[2(\sin\theta\frac{\partial\theta}{\partial z}+\cos\theta\frac{\partial\theta}{\partial r})\sin\theta]$$

$$\frac{\partial}{\partial z}(\frac{\partial\theta}{\partial z}) = \frac{K_1}{2}\{-2[\cos\theta\frac{\partial\theta}{\partial r}\frac{\partial\theta}{\partial z} + \sin\theta\frac{\partial^2\theta}{\partial r\partial z} + \sin\theta\left(\frac{\partial\theta}{\partial z}\right)^2 - \cos\theta\frac{\partial^2\theta}{\partial z^2}]\cos\theta + 2(\sin\theta\frac{\partial\theta}{\partial r} - \cos\theta\frac{\partial\theta}{\partial z})\sin\theta\frac{\partial\theta}{\partial z} - \frac{4}{r}\cos\theta\sin\theta\frac{\partial\theta}{\partial z}\} + \frac{K_3}{2}\{2[\cos\theta\left(\frac{\partial\theta}{\partial z}\right)^2 + \sin\theta\frac{\partial^2\theta}{\partial z^2} - \sin\theta\frac{\partial\theta}{\partial z}\frac{\partial\theta}{\partial r} + \cos\theta\frac{\partial^2\theta}{\partial r\partial z}]\sin\theta + 2(\sin\theta\frac{\partial\theta}{\partial z} + \cos\theta\frac{\partial\theta}{\partial r})\cos\theta\frac{\partial\theta}{\partial z}\} \tag{A.14}$$

Euler-Lagrange equation:

$$\frac{\partial}{\partial\theta} - \frac{\partial}{\partial r}(\frac{\partial}{\partial\left(\frac{\partial\theta}{\partial r}\right)}) - \frac{\partial}{\partial z}(\frac{\partial}{\partial\left(\frac{\partial\theta}{\partial z}\right)}) = \frac{K_1}{2}\{-\frac{4}{r^2}\cos\theta\sin\theta + 2(\cos^2\theta - \sin^2\theta)\frac{\partial\theta}{\partial r}\frac{\partial\theta}{\partial z} - 2\sin\theta\cos\theta\left(\frac{\partial\theta}{\partial r}\right)^2 - 2\sin^2\theta\frac{\partial^2\theta}{\partial r^2} + 4\sin\theta\cos\theta\frac{\partial^2\theta}{\partial r\partial z} + 2\sin\theta\cos\theta\left(\frac{\partial\theta}{\partial z}\right)^2 - 2\cos^2\theta\frac{\partial^2\theta}{\partial z^2}\} + \frac{K_3}{2}[2(\sin^2\theta - \cos^2\theta)\frac{\partial\theta}{\partial z}\frac{\partial\theta}{\partial r} - 4\sin\theta\cos\theta\frac{\partial^2\theta}{\partial r\partial z} + 2\sin\theta\cos\theta\left(\frac{\partial\theta}{\partial r}\right)^2 - 2\cos^2\theta\frac{\partial^2\theta}{\partial r^2} - 2\sin\theta\cos\theta\left(\frac{\partial\theta}{\partial z}\right)^2 - 2\sin^2\theta\frac{\partial^2\theta}{\partial z^2}] = -\frac{2K_1}{r^2}\cos\theta\sin\theta + (K_3 - K_1)\sin\theta\cos\theta\left(\frac{\partial\theta}{\partial r}\right)^2 + (K_1 - K_3)(\cos^2\theta - \sin^2\theta)\frac{\partial\theta}{\partial r}\frac{\partial\theta}{\partial z} - (K_1\sin^2\theta + K_3\cos^2\theta)\frac{\partial^2\theta}{\partial r^2} + 2(K_1 - K_3)\sin\theta\cos\theta\frac{\partial^2\theta}{\partial r\partial z} + (K_1 - K_3)\sin\theta\cos\theta\left(\frac{\partial\theta}{\partial z}\right)^2 + (K_3\sin^2\theta - K_1\cos^2\theta)\frac{\partial^2\theta}{\partial z^2} \tag{A.15}$$

These equations were used for the simulation process.

Reference

[1] M. A. Shah, D.-G. Lee, B.-Y. Lee, S. Hur, *IEEE Access* **2021**, 9, 140079.

[2] H. Wijshoff, *Physics reports* **2010**, 491, 77.

[3] T. Boland, T. Xu, B. Damon, X. Cui, *Biotechnology Journal: Healthcare Nutrition Technology* **2006**, 1, 910.

[4] P. G. Campbell, L. E. Weiss, *Expert Opin Biol Ther* **2007**, 7, 1123.

[5] W. Zhu, X. Ma, M. Gou, D. Mei, K. Zhang, S. Chen, *Curr Opin Biotechnol* **2016**, 40, 103.

[6] V. Beedasy, P. J. Smith, *Materials* **2020**, 13, 704.

[7] L. Nayak, S. Mohanty, S. K. Nayak, A. Ramadoss, *Journal of Materials Chemistry C* **2019**, 7, 8771.

[8] Z. Yin, Y. Huang, N. Bu, X. Wang, Y. Xiong, *Chinese Science Bulletin* **2010**, 55, 3383.

[9] R. Daly, T. S. Harrington, G. D. Martin, I. M. Hutchings, *International journal of pharmaceutics* **2015**, 494, 554.

[10] D. R. Serrano, A. Kara, I. Yuste, F. C. Luciano, B. Ongoren, B. J. Anaya, G. Molina, L. Diez, B. I. Ramirez, I. O. Ramirez, *Pharmaceutics* **2023**, 15, 313.

[11] B. Derby, *Annual Review of Materials Research* **2010**, 40, 395.

[12] Z. Yin, D. Wang, Y. Guo, Z. Zhao, L. Li, W. Chen, Y. Duan, *InfoMat* **2024**, 6, e12505.

[13] V. J. Alino, P. H. Sim, W. T. Choy, A. Fraser, K.-L. Yang, *Langmuir* **2012**, 28, 17571.

[14] C. K. Chang, C. M. Bastiaansen, D. J. Broer, H. L. Kuo, *Advanced Functional Materials* **2012**, 22, 2855.

[15] D. J. Davies, A. R. Vaccaro, S. M. Morris, N. Herzer, A. P. Schenning, C. W. Bastiaansen, *Advanced Functional Materials* **2013**, 23, 2723.

[16] M. Mitov, *Chemphyschem* **2014**, 15, 1245.

[17] I. W. Hamley, *Introduction to soft matter: synthetic and biological self-assembling materials*, John Wiley & Sons, **2007**.

[18] J. W. Goodby, P. J. Collings, T. Kato, C. Tschierske, H. Gleeson, P. Raynes, V. Vill, *Handbook of liquid crystals, 8 volume set*, Vol. 1, Informa UK Limited, **2017**.

[19] D. Mulder, A. Schenning, C. Bastiaansen, *Journal of Materials Chemistry C* **2014**, 2, 6695.

[20] A. Sengupta, *Topological microfluidics: nematic liquid crystals and nematic colloids in microfluidic environment*, Springer Science & Business Media, **2013**.

[21] P. J. Collings, J. W. Goodby, *Introduction to liquid crystals: chemistry and physics*, PLSclear, **2019**.

[22] G. Babakhanova, O. D. Lavrentovich, presented at *Modern Problems of the Physics of Liquid Systems: Selected Reviews from the 8th International Conference "Physics of Liquid Matter: Modern Problems", Kyiv, Ukraine, May 18-22, 2018 8*, **2019**.

[23] J. Ericksen, *Archive for Rational Mechanics and Analysis* **1959**, 4, 231.

[24] S. Fujii, O. Henrich, *Physical Review E* **2021**, 103, 052704.

[25] E. Parry, D.-J. Kim, A. A. Castrejón-Pita, S. J. Elston, S. M. Morris, *Optical Materials* **2018**, 80, 71.

[26] M. Oh-e, M. Yoneya, K. Kondo, *Journal of applied physics* **1997**, 82, 528.

[27] G. W. Gray, V. Vill, H. W. Spiess, D. Demus, J. W. Goodby, *Physical properties of liquid crystals*, John Wiley & Sons, **2009**.

[28] G. Grinstein, *Directions in condensed matter physics: memorial volume in honor of Shang-keng Ma*, Vol. 1, World Scientific, **1986**.

[29] Y. Garbovskiy, A. Glushchenko, presented at *Liquid Crystals XXII*, **2018**.

[30] A. K. Jain, R. R. Deshmukh, *Liq. Cryst. Disp. Technol* **2020**, 1.

[31] D. Cupelli, F. P. Nicoletta, S. Manfredi, M. Vivacqua, P. Formoso, G. De Filpo, G. Chidichimo, *Solar Energy Materials and Solar Cells* **2009**, 93, 2008.
[32] J.-Y. Park, H.-K. Kim, *RSC advances* **2018**, 8, 36549.
[33] J. W. McCargar, R. Ondris-Crawford, J. L. West, *Journal of Electronic Imaging* **1992**, 1, 22.
[34] Y. J. Liu, X. Ding, S. C. S. Lin, J. Shi, I. K. Chiang, T. J. Huang, *Advanced materials* **2011**, 23, 1656.
[35] M. Jamil, F. Ahmad, J. Rhee, Y. Jeon, *Current Science* **2011**, 1544.
[36] M. Date, T. Hisaki, N. Naito, A. Nakadaira, S. Suyama, H. Tanaka, K. Uehira, Y. Koshiishi, presented at *SID Symposium Digest of Technical Papers*, **2000**.
[37] K. Takizawa, H. Kikuchi, H. Fujikake, M. Okada, *Applied physics letters* **1990**, 56, 999.
[38] K. Takizawa, H. Kikuchi, H. Fujikake, Y. Namikawa, K. Tada, *Japanese journal of applied physics* **1994**, 33, 1346.
[39] R. Plamont, F. Lancia, A. Ryabchun, *Liquid crystals* **2020**, 47, 1569.
[40] M. Kamarudin, A. Khan, E. Tan, G. Rughoobur, S. Said, M. Qasim, T. Wilkinson, *RSC advances* **2017**, 7, 31989.
[41] H. Zhang, S. K. Moon, *ACS Applied Materials & Interfaces* **2021**, 13, 53323.
[42] E. Antonopoulou, O. Harlen, M. Walkley, N. Kapur, *Physical Review Fluids* **2020**, 5, 043603.
[43] J. Peakall, J. Warburton, *Journal of Hydrology (New Zealand)* **1996**, 199.
[44] J. Tai, H. Y. Gan, Y. N. Liang, B. K. Lok, presented at *2008 10th Electronics packaging technology conference*, **2008**.
[45] J. Fromm, *IBM J Res Dev* **1984**, 28, 322.
[46] N. Reis, B. Derby, *MRS Online Proceedings Library (OPL)* **2000**, 625, 117.
[47] D. B. Bogy, F. Talke, *IBM J Res Dev* **1984**, 28, 314.
[48] H.-C. Wu, T.-R. Shan, W.-S. Hwang, H.-J. Lin, *Materials transactions* **2004**, 45, 1794.
[49] H. Gan, X. Shan, T. Eriksson, B. Lok, Y. Lam, *Journal of micromechanics and microengineering* **2009**, 19, 055010.
[50] Y.-F. Liu, M.-H. Tsai, Y.-F. Pai, W.-S. Hwang, *Applied physics A* **2013**, 111, 509.
[51] Z. Esa, M. Abid, J. H. Zaini, B. Aissa, M. M. Nauman, *Applied Physics A* **2022**, 128, 780.
[52] N. Mkhize, H. Bhaskaran, *Small Science* **2022**, 2, 2100073.
[53] S.-H. Lee, X. H. Nguyen, H. S. Ko, *Journal of mechanical science and technology* **2012**, 26, 1403.
[54] Y. Han, J. Dong, *Journal of Micro-and Nano-Manufacturing* **2018**, 6, 040802.
[55] J. Fernández de La Mora, *Annu. Rev. Fluid Mech.* **2007**, 39, 217.
[56] M. Yu, K. H. Ahn, S. J. Lee, *Materials & Design* **2016**, 89, 109.
[57] M. S. Onses, E. Sutanto, P. M. Ferreira, A. G. Alleyne, J. A. Rogers, *Small* **2015**, 11, 4237.
[58] A. R. Nassrah, I. Jánossy, T. Tóth-Katona, *Journal of Molecular Liquids* **2020**, 312, 113309.
[59] C. Multiphysics, *COMSOL Multiphysics, Burlington, MA, accessed Feb* **1998**, 9, 32.
[60] O. Khrystoslavenko, R. Grubliauskas, presented at *Proceedings of the 20th Conference for Junior Researchers „Science–Future of Lithuania*, **2017**.
[61] N. H. Schiller, M. G. Jones, B. Bertolucci, presented at *23rd AIAA/CEAS aeroacoustics conference*, **2017**.
[62] Z. Wei, L. K. Weavers, *Ultrason Sonochem* **2016**, 31, 490.
[63] R. Jiang, L. Mei, Q. Zhang, *Mrs Advances* **2016**, 1, 1755.
[64] M. Vajdi, F. S. Moghanlou, F. Sharifianjazi, M. S. Asl, M. Shokouhimehr, *Journal of Composites and Compounds* **2020**, 2, 35.

[65] V. Gerlich, K. Sulovská, M. Zálešák, *Measurement* **2013**, 46, 2003.

[66] V. Suarez, J. H. Wong, U. Nogal, A. Calderón, J. B. Rojas-Trigos, A. Juárez, E. Marín, *Applied Radiation and Isotopes* **2014**, 83, 260.

[67] J. Tyson, T. Rahman, S. Boden, **2019**.

[68] B. Drawert, S. Engblom, A. Hellander, *BMC Syst Biol* **2012**, 6, 76.

[69] P. P. Kothmire, Y. J. Bhalerao, V. M. Naik, R. M. Thaokar, V. A. Juvekar, *Chem Eng Res Des* **2020**, 154, 273.

[70] M. K. Patel, T. Sharma, M. K. Nayak, C. Ghanshyam, *International Journal of Computer Applications* **2015**, 124.

[71] M. Q. Fadhil, A. A. Abdullah Albakry, A. J. Sultan, presented at *AIP Conf Proc*, **2023**.

[72] D. M. Ekanath, N. Badi, A. Bensaoula, presented at *Excerpt from the proceedings of the COMSOL conference in Boston*, **2011**.

[73] B. Sheeparamatti, P. D. Hanasi, V. Aibbigeri, N. Meti, presented at *Excerpt from the Proceedings of the COMSOL Conference in Pune*, **2015**.

[74] L. Yu-Xing, Y. Yan, B. Xue-Yang, L. Kai, G. Bo, presented at *2022 4th International Conference on Smart Power & Internet Energy Systems (SPIES)*, **2022**.

[75] H. Benguesmia, N. M'ziou, A. Boubakeur, *Diagnostyka* **2018**, 19, 41.

[76] A. Banik, A. Mukherjee, S. Dalai, *Electrical Engineering* **2018**, 100, 533.

[77] H. Benguesmia, B. Bakri, S. Khadar, F. Hamrit, N. M'ziou, *Diagnostyka* **2019**, 20.

[78] M. Kumar, B. Mukherjee, S. Sen, *Communications in Nonlinear Science and Numerical Simulation* **2021**, 96, 105690.

[79] A. Acheli, R. Serhane, presented at *AIP Conf Proc*, **2015**.

[80] M. V. Garud, R. Pratap, *Journal of Microelectromechanical Systems* **2020**, 29, 592.

[81] J. C. Blecke, G. G. Parker.

[82] A. Washington, Z. Olsen, J. Su, K. J. Kim, *Journal of Physics Communications* **2022**, 6, 085007.

[83] N. Sivakumar, H. Kanagasabapathy, H. Srikanth, *Materials today: proceedings* **2018**, 5, 11516.

[84] E. Leroy, R. Hinchet, H. Shea, *Advanced Materials* **2020**, 32, 2002564.

[85] J. De Amicis, A. Cammi, L. P. Colombo, M. Colombo, M. E. Ricotti, *Prog Nuclear Energy* **2014**, 76, 206.

[86] W. A. F. W. Ali, J. Yunas, A. A. Hamzah, B. Y. Majlis, presented at *2017 IEEE Regional Symposium on Micro and Nanoelectronics (RSM)*, **2017**.

[87] O. Ulkir, O. Girit, I. Ertugrul, *Journal of Nanomaterials* **2021**, 2021, 1.

[88] P. Rajput, *Turkish Journal of Computer and Mathematics Education (TURCOMAT)* **2021**, 12, 1650.

[89] M. Z. Islam, Y. Y. Tsui, *Sensors* **2016**, 16, 1639.

[90] M. G. Abdelmageed, A. M. F. El-Bab, A. Abouelsoud, *Microelectron J* **2019**, 86, 105.

[91] S. Zhang, P. Li, Y. Zhong, J. Xiang, *CMES-Comput Model Eng Sci* **2014**, 101, 17.

[92] M. Afrasiabi, M. Roethlin, K. Wegener, *Computer Methods in Applied Mechanics and Engineering* **2018**, 336, 667.

[93] H. A. Amiri, A. A. Hamouda, *International Journal of Multiphase Flow* **2013**, 52, 22.

[94] H. Li, T. Kondoh, P. Jolivet, K. Furuta, T. Yamada, B. Zhu, K. Izui, S. Nishiwaki, *Appl Math Model* **2022**, 101, 276.

[95] W. B. Zimmerman, *Multiphysics modeling with finite element methods*, Vol. 18, World Scientific Publishing Company, **2006**.

[96] R. Mahdavi, S. Hashemi-Najafabadi, M. A. Ghiass, C. B. Adiels, *Med Biol Eng Comput* **2024**, 62, 121.

[97] T. Adam, U. Hashim, *Advanced Materials Research* **2014**, 832, 511.

[98] J. Towne, N. Carter, D. J. Neivandt, *Biomed Eng Online* **2021**, 20, 60.

[99] S. Taco-Vasquez, C. A. Ron, H. A. Murillo, A. Chico, P. G. Arauz, *Processes* **2022**, 10, 1144.
[100] B. S. Adji, Y. Muharam, S. Kartohardjono, *Int. J. Eng. Res. Sci. Technol* **2019**, 12, 2592.
[101] J. Xie, Y.-A. Cui, Y. Luo, L. Zhang, H. Chen, presented at *Journal of Physics: Conference Series*, **2023**.
[102] D. Papaioannou, A. Heinig, **2017**.
[103] N. Ullah, L. Huang, M. R. Amirzada, A. Ullah, M. L. Haider, M. K. Ehsan, Y. Khan, *Elektronika ir Elektrotechnika* **2022**, 28, 72.
[104] J. E. Pilliod Jr, E. G. Puckett, *Journal of Computational Physics* **2004**, 199, 465.
[105] R. Comminal, J. Spangenberg, J. H. Hattel, *Journal of computational physics* **2015**, 283, 582.
[106] T. Maric, H. Marschall, D. Bothe, *arXiv preprint arXiv:1305.3417* **2013**.
[107] R. R. Nourgaliev, T. G. Theofanous, *Journal of Computational Physics* **2007**, 224, 836.
[108] C. Günther, M. Meinke, W. Schröder, *Computers & Fluids* **2014**, 102, 182.
[109] S. Shin, J. Chergui, D. Juric, L. Kahouadji, O. K. Matar, R. V. Craster, *Journal of Computational Physics* **2018**, 359, 409.
[110] M. Herrmann, *annual research briefs* **2005**, 3.
[111] D. She, R. Kaufman, H. Lim, J. Melvin, A. Hsu, J. Glimm, in *Handbook of Numerical Analysis*, Vol. 17, Elsevier, 2016.
[112] M. R. Pivello, M. M. Villar, R. Serfaty, A. M. Roma, A. d. Silveira-Neto, *International Journal of Multiphase Flow* **2014**, 58, 72.
[113] Y. Sun, C. Beckermann, *Journal of Computational Physics* **2007**, 220, 626.
[114] A. Fakhari, M. Geier, D. Bolster, *Computers & Mathematics with Applications* **2019**, 78, 1154.
[115] A. Zhang, J. Du, Z. Guo, Q. Wang, S. Xiong, *Physical Review E* **2019**, 100, 023305.
[116] K. Ling, S. Zhang, W. Liu, X. Sui, W. Tao, *Frontiers in Energy Research* **2021**, 8, 526035.
[117] K. Ling, S. Zhang, P.-Z. Wu, S.-Y. Yang, W.-Q. Tao, *International Journal of Heat and Mass Transfer* **2019**, 143, 118565.
[118] D. Guo, D. Sun, Z. Li, W. Tao, *Numerical Heat Transfer, Part A: Applications* **2011**, 59, 857.
[119] D. Sun, W. Tao, *International Journal of Heat and Mass Transfer* **2010**, 53, 645.
[120] L. Guo, Y. Duan, Y. Huang, Z. Yin, *Micromachines* **2018**, 9, 522.
[121] Y. Ke, C. Zhou, Y. Zhou, S. Wang, S. H. Chan, Y. Long, *Advanced functional materials* **2018**, 28, 1800113.
[122] Y. Ke, J. Chen, G. Lin, S. Wang, Y. Zhou, J. Yin, P. S. Lee, Y. Long, *Advanced Energy Materials* **2019**, 9, 1902066.
[123] S. Nundy, A. Mesloub, B. M. Alsolami, A. Ghosh, *Journal of Cleaner Production* **2021**, 301, 126854.
[124] W. Kamal, M. Li, J. D. Lin, E. Parry, Y. Jin, S. J. Elston, A. A. Castrejón-Pita, S. M. Morris, *Advanced Optical Materials* **2022**, 10, 2101748.
[125] Y. Guo, H. Shahsavan, M. Sitti, *Advanced Optical Materials* **2020**, 8, 1902098.
[126] A. Y. G. Fuh, S. Y. Chih, S. T. Wu, *Liquid Crystals* **2018**, 45, 864.
[127] C.-W. Chen, A. N. Brigeman, T.-J. Ho, I. C. Khoo, *Optical Materials Express* **2018**, 8, 691.
[128] D. K. Yang, L. C. Chien, J. Doane, *Applied physics letters* **1992**, 60, 3102.
[129] M.-Y. Chen, J.-Y. Lee, *Journal of the Chinese Institute of Engineers* **2014**, 37, 793.
[130] V. Sharma, P. Kumar, Chinky, P. Malik, K. Raina, *Journal of Applied Polymer Science* **2020**, 137, 48745.

[131] S.-H. Hwang, K.-J. Yang, S.-H. Woo, B.-D. Choi, E.-H. Kim, B.-K. Kim, *Molecular Crystals and Liquid Crystals* **2007**, 470, 163.

[132] X. Li, X. Du, P. Guo, J. Zhu, W. Ye, Q. Xu, Y. Sun, *Polymers* **2018**, 10, 884.

[133] W.-S. Li, Y. Shen, Z.-J. Chen, Q. Cui, S.-S. Li, L.-J. Chen, *Applied Optics* **2017**, 56, 601.

[134] R. Hikmet, R. Polesso, *Advanced Materials* **2002**, 14, 502.

[135] F. Ahmad, M. Jamil, J. W. Lee, S. R. Kim, Y. J. Jeon, *Electronic Materials Letters* **2016**, 12, 685.

[136] J. Li, *Refractive indices of liquid crystals and their applications in display and photonic devices*, University of Central Florida, **2005**.

[137] I. Dierking, *Advanced Materials* **2000**, 12, 167.

[138] F. Ahmad, M. Jamil, Y. J. Jeon, *Journal of Molecular Liquids* **2017**, 233, 187.

[139] L. Natarajan, E. Beckel, V. Tondiglia, R. Sutherland, T. White, J. Voss, T. Bunning, *Molecular Crystals and Liquid Crystals* **2009**, 502, 143.

[140] K. Ha, J. L. West, *Liquid Crystals an international journal of science and technology* **2004**, 31, 753.

[141] X. Hu, X. Zhang, W. Yang, X. F. Jiang, X. Jiang, L. T. de Haan, D. Yuan, W. Zhao, N. Zheng, M. Jin, *Journal of Applied Polymer Science* **2020**, 137, 48917.

[142] R. Yamaguchi, K. Goto, S. Sakurai, L. Xiong, T. Tomono, *Journal of Photopolymer Science and Technology* **2015**, 28, 319.

[143] Y.-H. Lin, H. Ren, Y.-H. Fan, Y.-H. Wu, S.-T. Wu, *Journal of applied physics* **2005**, 98, 043112.

[144] H. Sun, Z. Xie, C. Ju, X. Hu, D. Yuan, W. Zhao, L. Shui, G. Zhou, *Polymers* **2019**, 11, 694.

[145] J.-H. Woo, T.-H. Choi, B.-G. Jeon, T.-H. Yoon, *Crystals* **2017**, 7, 260.

[146] Y. Jiang, G. Qin, X. Xu, L. Zhou, S. Lee, D.-K. Yang, *Optics Express* **2018**, 26, 32640.

[147] L. Weng, P.-C. Liao, C.-C. Lin, T.-L. Ting, W.-H. Hsu, J.-J. Su, L.-C. Chien, *AIP advances* **2015**, 5.

[148] K.-H. Chang, V. Joshi, L.-C. Chien, *Physical Review E* **2017**, 95, 042701.

[149] Y. Liang, Y. Cai, Z. Wang, M. Lei, Z. Cao, Y. Wang, M. Li, S. Yan, P. R. Bianco, B. Yao, *Applied optics* **2018**, 57, 3618.

[150] A. Yakimenko, Y. M. Bidasyuk, O. Prikhodko, S. Vilchinskii, E. Ostrovskaya, Y. S. Kivshar, *Physical Review A* **2013**, 88, 043637.

[151] V. Kotlyar, A. Kovalev, A. Porfirev, *Journal of Applied Physics* **2016**, 120.

[152] Z. Wang, N. Zhang, X.-C. Yuan, *Optics Express* **2011**, 19, 482.

[153] W. Shao, S. Huang, X. Liu, M. Chen, *Optics Communications* **2018**, 427, 545.

[154] R. Gauthier, presented at *Journal of Physics: Conference Series*, **2019**.

[155] G. S. Agarwal, J. Banerji, *J Phys A: Math Gen* **2006**, 39, 11503.

[156] P. Miao, Z. Zhang, J. Sun, W. Walasik, S. Longhi, N. M. Litchinitser, L. Feng, *Science* **2016**, 353, 464.

[157] A. Mamaev, M. Saffman, A. Zozulya, *Physical review letters* **1996**, 77, 4544.

[158] H. Singh, *Optica Applicata* **2017**, 47.

[159] D. Mihalache, *Romanian Reports in Physics* **2007**, 59, 515.

[160] F. Takahashi, K. Miyamoto, H. Hidai, K. Yamane, R. Morita, T. Omatsu, *Scientific reports* **2016**, 6, 21738.

[161] S. Wei, T. Lei, L. Du, C. Zhang, H. Chen, Y. Yang, S. Zhu, X.-C. Yuan, *Optics Express* **2015**, 23, 30143.

[162] J. Park, P. Eames, D. Engebretson, J. Berezovsky, P. Crowell, *Physical Review B* **2003**, 67, 020403.

[163] C. Zhang, C. Min, L. Du, X.-C. Yuan, *Applied Physics Letters* **2016**, 108.

[164] A. Popiołek-Masajada, J. Masajada, M. Szatkowski, *Optics and Lasers in Engineering* **2018**, 105, 201.
[165] Y. Shen, X. Wang, Z. Xie, C. Min, X. Fu, Q. Liu, M. Gong, X. Yuan, *Light: Science & Applications* **2019**, 8, 90.
[166] X. Zhuang, *Science* **2004**, 305, 188.
[167] S. Syubaev, A. Zhizhchenko, A. Kuchmizhak, A. Porfirev, E. Pustovalov, O. Vitrik, Y. Kulchin, S. Khonina, S. Kudryashov, *Optics Express* **2017**, 25, 10214.
[168] W. Lee, X.-C. Yuan, W. Cheong, *Optics letters* **2004**, 29, 1796.
[169] S. N. Khonina, A. V. Ustinov, V. I. Logachev, A. P. Porfirev, *Physical Review A* **2020**, 101, 043829.
[170] H. Wei, A. K. Amrithanath, S. Krishnaswamy, *IEEE Photonics Technology Letters* **2019**, 31, 599.
[171] Y. Yang, X. Ye, L. Niu, K. Wang, Z. Yang, J. Liu, *Optics Express* **2020**, 28, 1417.
[172] C. Liu, X. Wei, L. Niu, K. Wang, Z. Yang, J. Liu, *Optics express* **2016**, 24, 12534.
[173] A. V. Carpentier, H. Michinel, J. R. Salgueiro, D. Olivieri, *American Journal of Physics* **2008**, 76, 916.
[174] B. Terhalle, A. Langner, B. Päivänranta, V. A. Guzenko, C. David, Y. Ekinci, *Optics letters* **2011**, 36, 4143.
[175] S. Li, Z. Wang, *Applied Physics Letters* **2013**, 103.
[176] R. K. Tyson, M. Scipioni, J. Viegas, *Applied optics* **2008**, 47, 6300.
[177] M. Scipioni, R. K. Tyson, J. Viegas, *Applied optics* **2008**, 47, 5098.
[178] M. Beresna, M. Gecevičius, P. G. Kazansky, T. Gertus, *Applied Physics Letters* **2011**, 98.
[179] S. N. Khonina, S. V. Karpeev, M. A. Butt, *Sensors* **2021**, 21, 2988.
[180] A. S. Ostrovsky, C. Rickenstorff-Parrao, V. Arrizón, *Optics letters* **2013**, 38, 534.
[181] Y. He, H. Ye, J. Liu, Z. Xie, X. Zhang, Y. Xiang, S. Chen, Y. Li, D. Fan, *IEEE Photonics Journal* **2017**, 9, 1.
[182] J. Lu, L. Meng, F. Shi, X. Liu, Z. Luo, P. Yan, L. Huang, F. Pang, T. Wang, X. Zeng, *Optics letters* **2018**, 43, 5841.
[183] R. Chen, J. Wang, X. Zhang, J. Yao, H. Ming, A. Wang, *Opto-Electronic Advances* **2018**, 1, 180003.
[184] D. P. Ghai, *Applied Optics* **2011**, 50, 1374.
[185] Y. Izdebskaya, V. Shvedov, A. Volyar, *Optics Letters* **2005**, 30, 2472.
[186] F. Yue, D. Wen, J. Xin, B. D. Gerardot, J. Li, X. Chen, *ACS photonics* **2016**, 3, 1558.
[187] B. Liu, Y. He, S. W. Wong, Y. Li, *Advanced Optical Materials* **2021**, 9, 2001689.
[188] S. Tang, X. Li, W. Pan, J. Zhou, T. Jiang, F. Ding, *Optics express* **2019**, 27, 4281.
[189] E. Melnikova, D. Gorbach, S. Slussarenko Sr, A. Muravsky, A. Tolstik, S. Slussarenko Jr, *Optics Communications* **2022**, 522, 128661.
[190] R. Barboza, U. Bortolozzo, M. Clerc, S. Residori, E. Vidal-Henriquez, *Advances in Optics and Photonics* **2015**, 7, 635.
[191] E. Brasselet, N. Murazawa, H. Misawa, S. Juodkazis, *Physical review letters* **2009**, 103, 103903.
[192] R. Barboza, T. Sauma, U. Bortolozzo, G. Assanto, M. Clerc, S. Residori, *New Journal of Physics* **2013**, 15, 013028.
[193] R. Barboza, U. Bortolozzo, M. Clerc, S. Residori, E. Vidal-Henriquez, *Philosophical Transactions of the Royal Society A: Mathematical, Physical and Engineering Sciences* **2014**, 372, 20140019.
[194] S. Zheng, L. Zha, J. Lu, X. Zeng, Y. Li, S. Xu, D. Fan, *Optics Express* **2019**, 27, 16103.
[195] S. Slussarenko, A. Murauski, T. Du, V. Chigrinov, L. Marrucci, E. Santamato, *Optics express* **2011**, 19, 4085.

[196] P. Chen, B.-Y. Wei, W. Ji, S.-J. Ge, W. Hu, F. Xu, V. Chigrinov, Y.-Q. Lu, *Photonics Research* **2015**, 3, 133.

[197] S.-J. Ge, P. Chen, L.-L. Ma, Z. Liu, Z.-G. Zheng, D. Shen, W. Hu, Y.-Q. Lu, *Optical Materials Express* **2016**, 6, 1087.

[198] B. y. Wei, W. Hu, Y. Ming, F. Xu, S. Rubin, J. g. Wang, V. Chigrinov, Y. q. Lu, *Advanced Materials* **2014**, 26, 1590.

[199] S.-J. Ge, W. Ji, G.-X. Cui, B.-Y. Wei, W. Hu, Y.-Q. Lu, *Optical Materials Express* **2014**, 4, 2535.

[200] P. Soleimani, H. Khoshsima, M. Yeganeh, *Scientific Reports* **2022**, 12, 21271.

[201] H. Zhang, W. Duan, T. Wei, C. Xu, W. Hu, *Crystals* **2020**, 10, 882.

[202] J. Chen, Y. Wang, C. Wan, K. Lu, Y. Liu, Q. Zhan, *Optics Communications* **2021**, 495, 127112.

[203] M.-Q. Cai, Z.-X. Wang, J. Liang, Y.-K. Wang, X.-Z. Gao, Y. Li, C. Tu, H.-T. Wang, *Applied Optics* **2017**, 56, 6175.

[204] J. Pereiro-García, M. García-de-Blas, M. A. Geday, X. Quintana, M. Caño-García, *Scientific Reports* **2023**, 13, 2385.

[205] X. QUINTANA, M. GEDAY.

[206] D. Lee, H. Lee, L. Migara, K. Kwak, V. P. Panov, J. K. Song, *Advanced Optical Materials* **2021**, 9, 2001604.

[207] H. He, R. Liao, N. Zeng, P. Li, Z. Chen, X. Liu, H. Ma, *Journal of Lightwave Technology* **2018**, 37, 2534.

[208] C. He, H. He, J. Chang, B. Chen, H. Ma, M. J. Booth, *Light: Science & Applications* **2021**, 10, 194.

[209] J. Chue-Sang, M. Gonzalez, A. Pierre, M. Laughrey, I. Saytashev, T. Novikova, J. C. Ramella-Roman, *Journal of biomedical optics* **2019**, 24, 030901.

[210] V. V. Tuchin, *Coherent-Domain Optical Methods: Biomedical Diagnostics, Environment and Material Science*, Springer Science & Business Media, **2004**.

[211] C. He, J. Chang, P. S. Salter, Y. Shen, B. Dai, P. Li, Y. Jin, S. C. Thodika, M. Li, A. Tariq, *Advanced Photonics* **2022**, 4, 026001.

[212] S. Alali, A. Vitkin, *Journal of biomedical optics* **2015**, 20, 061104.

[213] O. Arteaga, S. M. Nichols, J. Antó, *Applied Surface Science* **2017**, 421, 702.

[214] O. Arteaga, B. Kahr, *JOSA B* **2019**, 36, F72.

[215] I. Hajnsek, E. Pottier, S. R. Cloude, *IEEE Transactions on Geoscience and Remote Sensing* **2003**, 41, 727.

[216] D. H. Goldstein, presented at *Polarization: Measurement, Analysis, and Remote Sensing VIII*, **2008**.

[217] A. Peinado, A. Lizana, J. Vidal, C. Iemmi, J. Campos, *Applied optics* **2011**, 50, 5437.

[218] A. Peinado, A. Lizana, J. Vidal, C. Iemmi, J. Campos, *Optics express* **2010**, 18, 9815.

[219] S. Tripathi, K. C. Toussaint, *Optics express* **2009**, 17, 21396.

[220] C. He, J. Chang, Q. Hu, J. Wang, J. Antonello, H. He, S. Liu, J. Lin, B. Dai, D. S. Elson, *Nature communications* **2019**, 10, 4264.

[221] J. F. De Boer, T. E. Milner, *Journal of biomedical optics* **2002**, 7, 359.

[222] M. W. Davidson, *Microscopy Today* **2011**, 19, 52.

[223] P. S. Theocaris, E. E. Gdoutos, P. S. Theocaris, E. E. Gdoutos, *Matrix Theory of Photoelasticity* **1979**, 20.

[224] A. Singh, *Optical Engineering* **2020**, 59, 090901.

[225] E. Collett, B. Schaefer, *Applied optics* **2008**, 47, 4009.

[226] S. Batool, M. Nisar, F. Mangini, F. Frezza, E. Fazio, *Results in Optics* **2021**, 4, 100102.

[227] H. He, N. Zeng, D. Li, R. Liao, H. Ma, *Journal of Innovative Optical Health Sciences* **2012**, 5, 1250017.

[228] N. Ghosh, J. Soni, M. Wood, M. Wallenberg, I. Vitkin, *Pramana* **2010**, 75, 1071.
[229] D. N. Ignatenko, A. V. Shkirin, Y. P. Lobachevsky, S. V. Gudkov, *Applied Sciences* **2022**, 12, 5258.
[230] G. López-Morales, M. d. M. Sánchez-López, Á. Lizana, I. Moreno, J. Campos, *Crystals* **2020**, 10, 1155.
[231] W.-M. Boerner, H. Mott, E. Luneburg, presented at *IGARSS'97. 1997 IEEE International Geoscience and Remote Sensing Symposium Proceedings. Remote Sensing-A Scientific Vision for Sustainable Development*, **1997**.
[232] S. Zhang, H. Jiang, H. Gu, X. Chen, S. Liu, *The International Archives of the Photogrammetry, Remote Sensing and Spatial Information Sciences* **2020**, 43, 607.
[233] M. El-Shenawee, *JOSA A* **2003**, 20, 183.
[234] W. Sheng, W. Li, J. Qi, T. Liu, H. He, Y. Dong, S. Liu, J. Wu, D. S. Elson, H. Ma, presented at *Photonics*, **2019**.
[235] T. Novikova, J. Rehbinder, S. Deby, H. Haddad, J. Vizet, A. Pierangelo, P. Validire, A. Benali, B. Gayet, B. Teig, presented at *Clinical and Translational Biophotonics*, **2016**.
[236] A. Sdobnov, V. A. Ushenko, L. Trifonyuk, O. Bakun, M. Garazdyuk, I. V. Soltys, O. Dubolazov, O. G. Ushenko, Y. A. Ushenko, A. Bykov, *Journal of Biomedical Optics* **2023**, 28, 102903.
[237] S. A. Hall, M.-A. Hoyle, J. S. Post, D. K. Hore, *Analytical chemistry* **2013**, 85, 7613.
[238] L. L. Deibler, M. H. Smith, *Applied Optics* **2001**, 40, 3659.
[239] M. Kupinski, L. Li, *Electronic Imaging* **2020**, 33, 1.
[240] J.-F. Lin, *Optik* **2010**, 121, 2144.
[241] N. Gu, Y. Xiao, L. Huang, C. Rao, *Optics Express* **2022**, 30, 3497.
[242] S. Alali, T. Yang, I. A. Vitkin, *Optics letters* **2013**, 38, 2997.
[243] S. Firdous, M. Ikram, presented at *European Conference on Biomedical Optics*, **2007**.
[244] C. Negara, Z. Li, T. Längle, J. Beyerer, presented at *Photonics and Education in Measurement Science 2019*, **2019**.
[245] R. Azzam, *Optica Acta: International Journal of Optics* **1982**, 29, 685.
[246] R. Azzam, *Optica Acta: International Journal of Optics* **1985**, 32, 1407.
[247] T. Mu, C. Zhang, R. Liang, *Journal of Optics* **2015**, 17, 125708.
[248] J. L. Pezzaniti, D. B. Chenault, presented at *Polarization Science and Remote Sensing II*, **2005**.
[249] G. R. Soto, P. Smith, *Revista Mexicana de Física* **1998**, 44, 392.
[250] H. Gao, C. Zhang, Y. Wang, M. Li, J. Feng, presented at *Second International Conference on Photonics and Optical Engineering*, **2017**.
[251] H. Gao, C. Zhang, presented at *Optical Measurement Systems for Industrial Inspection IX*, **2015**.
[252] R. Perkins, V. Gruev, *Optics express* **2010**, 18, 25815.
[253] X. Tu, S. McEldowney, Y. Zou, M. Smith, C. Guido, N. Brock, S. Miller, L. Jiang, S. Pau, *Applied optics* **2020**, 59, G33.
[254] T. York, V. Gruev, *Applied optics* **2012**, 51, 5392.
[255] F. Snik, J. Craven-Jones, M. Escuti, S. Fineschi, D. Harrington, A. De Martino, D. Mawet, J. Riedi, J. S. Tyo, *Polarization: measurement, analysis, and remote sensing XI* **2014**, 9099, 48.
[256] O. Dubovik, Z. Li, M. I. Mishchenko, D. Tanré, Y. Karol, B. Bojkov, B. Cairns, D. J. Diner, W. R. Espinosa, P. Goloub, *Journal of Quantitative Spectroscopy and Radiative Transfer* **2019**, 224, 474.
[257] M. D. Alexandrov, B. Cairns, A. P. Wasilewski, A. S. Ackerman, M. J. McGill, J. E. Yorks, D. L. Hlavka, S. E. Platnick, G. T. Arnold, B. Van Diedenhoven, *Remote Sensing of Environment* **2015**, 169, 20.

[258] J. C. Ramella-Roman, A. Nayak, S. A. Prahl, *Journal of biomedical optics* **2011**, 16, 047001.
[259] J. Chang, H. He, C. He, H. Ma, presented at *Dynamics and Fluctuations in Biomedical Photonics XIII*, **2016**.
[260] P. Lemaillet, J. C. Ramella-Roman, presented at *Photonic Therapeutics and Diagnostics VII*, **2011**.
[261] J. F. Munoz-Martin, N. Rodriguez-Alvarez, X. Bosch-Lluis, K. Oudrhiri, *Remote Sensing of Environment* **2023**, 287, 113491.
[262] J. Chang, H. He, C. He, Y. Wang, N. Zeng, R. Liao, H. Ma, *Applied Optics* **2015**, 54, 7424.
[263] A. W. Snyder, J. D. Love, A. W. Snyder, J. D. Love, *Optical Waveguide Theory* **1983**, 189.
[264] K. S. Schanze, T. S. Bergstedt, B. T. Hauser, C. S. Cavalaheiro, *Langmuir* **2000**, 16, 795.
[265] U. D. Zeitner, M. Oliva, F. Fuchs, D. Michaelis, T. Benkenstein, T. Harzendorf, E.-B. Kley, *Applied Physics A* **2012**, 109, 789.
[266] S. Lee, Y. Ma, J. Park, B. Shin, *Japanese Journal of Applied Physics* **2021**, 60, 105001.
[267] C.-H. Lin, Y.-M. Lin, C.-C. Liang, Y.-Y. Lee, H.-S. Fung, B.-Y. Shew, S.-H. Chen, *Microelectronic engineering* **2012**, 98, 194.
[268] B. Xu, S. Smith, D. Smith, D. Chargin, presented at *PROCEEDINGS OF THE ANNUAL TECHNICAL CONFERENCE-SOCIETY OF VACUUM COATERS*, **2007**.
[269] T. Kohoutek, M. A. Hughes, J. Orava, M. Mastumoto, T. Misumi, H. Kawashima, T. Suzuki, Y. Ohishi, *JOSA B* **2012**, 29, 2779.
[270] Y. Inada, S. Yamashita, S. Murakami, K. Takahashi, T. Yamao, S. Hotta, *Japanese Journal of Applied Physics* **2021**, 60, 120901.
[271] A. Kamenskii, I. Reduto, V. Petrikov, A. Lipovskii, *Optical Materials* **2016**, 62, 250.
[272] M. Flores-Arias, A. Castelo, C. Gomez-Reino, G. De La Fuente, *Optics communications* **2009**, 282, 1175.
[273] L. Mashev, S. Tonchev, *Applied Physics A* **1981**, 26, 143.
[274] J. Song, N. Zhu, *Electronics Letters* **2008**, 44, 1.
[275] D. Sene, V. Bright, J. Comtois, J. Grantham, *Sensors and Actuators A: Physical* **1996**, 57, 145.
[276] V. Kalima, J. Pietarinen, S. Siitonen, J. Immonen, M. Suvanto, M. Kuittinen, K. Mönkkönen, T. Pakkanen, *Optical Materials* **2007**, 30, 285.
[277] R. Boyd, J. Britten, D. Decker, B. Shore, B. Stuart, M. Perry, L. Li, *Applied optics* **1995**, 34, 1697.
[278] N. A. Ivliev, S. N. Khonina, V. V. Podlipnov, S. V. Karpeev, presented at *Photonics*, **2023**.
[279] I. Z. Indutnyi, I. I. Robur, P. F. Romanenko, A. V. Stronski, presented at *Computer and Optically Generated Holographic Optics; 4th in a Series*, **1991**.
[280] B. Chen, Z. Zhao, C. Nourshargh, C. He, P. S. Salter, M. J. Booth, S. J. Elston, S. M. Morris, *Crystals* **2022**, 12, 1340.
[281] Z. Zhao, B. Chen, P. S. Salter, M. J. Booth, D. O'Brien, S. J. Elston, S. M. Morris, *Advanced Materials Technologies* **2023**, 8, 2200861.
[282] T. H. R. Skyrme, *Proceedings of the Royal Society of London. Series A. Mathematical and Physical Sciences* **1961**, 260, 127.
[283] P. Shi, L. Du, X. Yuan, *Nanophotonics* **2021**, 10, 3927.
[284] J.-S. Wu, I. I. Smalyukh, *Liquid Crystals Reviews* **2022**, 1.
[285] J. i. Fukuda, A. Nych, U. Ognysta, S. Žumer, I. Muševič, *Annalen der Physik* **2022**, 534, 2100336.

[286] Y. Shen, E. C. Martínez, C. Rosales-Guzmán, *ACS Photonics* **2022**, 9, 296.
[287] W. Lin, Y. Ota, Y. Arakawa, S. Iwamoto, *Physical Review Research* **2021**, 3, 023055.
[288] Y. Shen, Y. Hou, N. Papasimakis, N. I. Zheludev, *Nature communications* **2021**, 12, 5891.
[289] C. Guo, M. Xiao, Y. Guo, L. Yuan, S. Fan, *Physical review letters* **2020**, 124, 106103.
[290] Y. Shen, Q. Zhang, P. Shi, L. Du, X. Yuan, A. V. Zayats, *Nature Photonics* **2023**, 1.
[291] Y. Shen, *Optics Letters* **2021**, 46, 3737.
[292] C. Wan, Y. Shen, A. Chong, Q. Zhan, *eLight* **2022**, 2, 1.
[293] D. Foster, C. Kind, P. J. Ackerman, J.-S. B. Tai, M. R. Dennis, I. I. Smalyukh, *Nature Physics* **2019**, 15, 655.
[294] D. Foster, C. Kind, P. J. Ackerman, J.-S. B. Tai, M. R. Dennis, I. I. Smalyukh, *arXiv preprint arXiv:1806.02576* **2018**.
[295] R. Gutiérrez-Cuevas, E. Pisanty, *Journal of Optics* **2021**, 23, 024004.
[296] Y. Shen, Q. Zhang, P. Shi, L. Du, A. V. Zayats, X. Yuan, *arXiv preprint arXiv:2205.10329* **2022**.
[297] P. J. Ackerman, Z. Qi, I. I. Smalyukh, *Physical Review E* **2012**, 86, 021703.
[298] Y. Shen, C. He, Z. Song, B. Chen, H. He, Y. Ma, J. A. Fells, S. J. Elston, S. M. Morris, M. J. Booth, *Physical Review Applied* **2024**, 21, 024025.
[299] H.-J. Wu, B.-S. Yu, Z.-H. Zhu, W. Gao, D.-S. Ding, Z.-Y. Zhou, X.-P. Hu, C. Rosales-Guzmán, Y. Shen, B.-S. Shi, *Optica* **2022**, 9, 187.
[300] J. W. You, Z. Lan, Q. Ma, Z. Gao, Y. Yang, F. Gao, M. Xiao, T. J. Cui, *Photonics Research* **2023**, 11, B65.